

Barrier layers in the tropical Atlantic Ocean: Growth and decay mechanisms and impact of Amazon river runoff

Dissertation

with the aim of achieving a doctoral degree
at the Faculty of Mathematics, Informatics and Natural Sciences
Department of Earth Sciences
at Universität Hamburg

submitted by

Aurpita Saha

from Mumbai, India

Hamburg, 2020

Accepted as Dissertation at the Department of Earth Sciences

Day of oral defense: *26th October 2020*

Reviewers: Prof. Dr. Detlef Stammer
Dr. Nuno Serra

Chair of the Subject Doctoral Committee: Prof. Dr. Dirk Gajewski

Dean of Faculty of MIN: Prof. Dr. Heinrich Graener

Abstract

A barrier layer is a water layer forming in the upper ocean under certain conditions, separating the surface well-mixed layer from the permanent strongly stratified thermocline. The barrier layer starts at the base of the shallower, homogeneous in density, mixed layer (termed mixed layer depth - MLD) and extends to the base of a deeper-reaching, homogeneous in temperature, isothermal layer (termed isothermal layer depth - ILD), and therefore its thickness (termed barrier layer thickness - BLT) is the difference between the ILD and the MLD. Barrier layers are significant because their existence limits the interaction between the surface mixed layer and the deep ocean. Studies have shown that enhanced surface freshwater input, e.g., through river runoff or rainfall in the Intertropical Convergence Zone (ITCZ), can result in barrier layer formation.

In this thesis I identify and investigate the mechanisms governing the growth and decay of barrier layers in the tropical Atlantic Ocean at seasonal and short timescales and analyze how the tropical ocean responds to changes in the Amazon river freshwater discharge.

To this end, the impact of small-scale ocean processes embedded in the regional circulation on the evolution of barrier layers was investigated using output from a fully eddy-resolving, 4 km resolution numerical model simulation forced by an atmospheric reanalysis. The simulation reproduces well the temporal and spatial patterns of BLT estimated with Argo and CTD in situ profiles. As seen from an analysis of the vertical gradient of the salinity and temperature balances, localized barrier layers larger than 80 m form inside North Brazil Current (NBC) rings during late-June to July because of an enlarging of the ILD in the rings due to horizontal temperature advection, stretching of isotherms and tilting of temperature fronts. These barrier layers decay when the ILD reduces due to again the above mechanisms. Further to the north, along the North Equatorial Current (NEC), thick winter (January to early-March) barrier layers (> 90 m) locally grow as the MLD shoals mainly due to a tilting of the salinity fronts. The short-term barrier layers in this case decay due to a deepening of the MLD, whereas they get completely eroded in spring by a shoaling of the ILD due to surface temperature stratification. In the open ocean, in the central tropical Atlantic, the migrating ITCZ has sporadic episodes of strong rainfall. Turbulent mixing of surface freshwater lenses drastically reduces the MLD, forming large sporadic barrier layers (~ 60 m) mostly in winter and summer. A deepening of the MLD due to turbulent salt mixing, along with a tilting of salinity fronts into the vertical, destroys those barrier layers. In the eastern tropical Atlantic, the largest BLT (~ 60 m) exists from September to October, formed by shoaling of the MLD due to tilting of salinity fronts at the Niger river plume and turbulent mixing of rainwater from the ITCZ, combined with a deepening of the ILD due to turbulent heat mixing. A shoaling of the ILD, also by turbulent mixing, mostly leads to the decay of those barrier layers.

To understand the impacts of the Amazon river discharge on the northern tropical Atlantic barrier layer variability, and on the regional and larger-scale ocean circulations, a set of sensitivity experiments were carried out using an 8 km resolution version of the above numerical model, including realistic (based on observed runoff data) and extreme idealized changes in the mean or amplitude of the Amazon runoff. With an excess of freshwater, sea surface salinity (~ -10 psu), ILD (~ -42 m) and MLD (~ -50 m) decrease, while the sea surface temperature ($\sim +1^\circ\text{C}$) and BLT ($\sim +42$ m) increase. The maximum differences to the control experiment (closest to reality) occur during summer and autumn, for two extreme cases: no river runoff and 100% increase in mean river runoff. In most regions, the above variables are more sensitive to a 20% change in mean runoff than to a 40% change in seasonal amplitude.

Looking at the changes in the dynamics, the mean kinetic energy explains a large part of the total kinetic energy differences, with eddy kinetic energy changes being present only in the highly nonlinear areas of the NBC rings, the retroreflection into the North Equatorial Countercurrent (NECC) and the Loop Current. Introducing more freshwater intensifies the western boundary currents and weakens, with a marginal northward shift and more meandering, the NBC retroreflection and the NECC. On the other hand, the ocean dynamics are more insensitive when freshwater is decreased, but without any runoff a clear opposite response is retained. Furthermore, in presence of more freshwater, the ocean top 50 m volume transport of the tropical western boundary currents have larger amplitudes of interannual fluctuations. Corroborating previous studies, that suggest that the Amazon runoff and the Atlantic Meridional Overturning Circulation (AMOC) are anti-correlated, my results further indicate that variations of BLT are anti-correlated with the top-to-bottom Florida Current transport and the AMOC.

This work highlights that barrier layers are localized phenomena, which can form and grow at times because of simply ocean dynamics, like surface and subsurface currents, subduction, eddies and filaments, without the presence of a local surface freshwater influx. In absence of complete observational data, a comprehensive study identifying the growth and decay mechanisms of tropical Atlantic barrier layers, not addressed in earlier studies, was possible using numerical simulations. The growth and decay mechanisms discussed here can be translated into other regions of the World Ocean, where similar physical conditions for barrier layer existence are prevalent. This knowledge about the tropical Atlantic barrier layers and the response of the upper ocean, in terms of salinity, temperature and regional and large-scale circulation, to possible future changes of the Amazon discharge, can aid a further understanding of the role of barrier layers in air-sea interaction and of their climatic impacts, like the prediction of tropical cyclone intensification, of the AMOC and of atmospheric teleconnections.

Zusammenfassung

Eine Barrierschicht ist eine Wasserschicht, die sich im oberen Ozean unter bestimmten Bedingungen bildet und die gut durchmischte Oberflächenschicht von der permanent stark geschichteten Temperatursprungschicht (Thermokline) trennt. Die Barrierschicht beginnt an der Basis der flacheren, in der Dichte homogenen, durchmischten Schicht (bezeichnet als gemischte Schichttiefe - MLD) und erstreckt sich bis zur Basis einer tiefer reichenden, in der Temperatur homogenen, isothermen Schicht (bezeichnet als isotherme Schichttiefe - ILD). Ihre Dicke (bezeichnet als Barrierschichtdicke - BLT) entspricht daher der Differenz zwischen der ILD und der MLD. Barrierschichten sind bedeutend, weil ihre Existenz die Wechselwirkung zwischen der gemischten Oberflächenschicht und dem tiefen Ozean beschränkt. Studien haben gezeigt, dass ein erhöhter Süßwassereintrag, z.B. durch Flusseintrag oder Regenfälle in der intertropischen Konvergenzzone (ITCZ), zur Bildung von Barrierschichten führen kann.

In dieser Arbeit identifiziere und untersuche ich die Mechanismen, die das Wachstum und den Zerfall von Barrierschichten im tropischen Atlantischen Ozean auf saisonalen und kurzfristigen Zeitskalen steuern, und analysiere, wie der tropische Ozean auf Veränderungen des Süßwassereintrags aus dem Amazonasfluss reagiert.

Zu diesem Zweck wurde der Einfluss kleinskaliger, in die regionale Zirkulation eingebetteter Ozeanprozesse auf die Entwicklung von Barrierschichten untersucht. Dafür habe ich die Ergebnisse einer vollständig wirbelaufösenden numerischen Modellsimulation mit einer Auflösung von 4 km verwendet, die durch eine atmosphärische Reanalyse angetrieben wurde. Die Simulation reproduziert gut die zeitlichen und räumlichen Muster der BLT, die mit Argo- und CTD-In-situ-Profilen geschätzt wurden. Wie aus einer Analyse des vertikalen Gradienten der Salinitäts- und Temperaturbilanzen hervorgeht, bilden sich in den Ringen des Nordbrasilianischen Stroms (NBC) von Ende Juni bis Juli Barrierschichten mit mehr als 80 m Dicke aufgrund einer Vergrößerung der ILD. Das Anwachsen der ILD wird durch horizontale Temperaturadvektion, Dehnung der Isothermen und Neigung von Temperaturfronten hervorgerufen. Dieselben Mechanismen sorgen dafür, dass sich die ILD wieder reduziert und damit die Barrierschichten zerfallen. Weiter nördlich, entlang des Nord-Äquatorialstroms (NEC), bilden sich im Winter (Januar bis Anfang März) lokal Barrierschichten von mehr als 90 m Dicke durch eine Abnahme der MLD, die hauptsächlich durch eine Neigung der Salzgehaltsfronten bedingt ist. Die Barrierschichten zerfallen in diesem Fall aufgrund einer Vertiefung der MLD, während sie im Frühjahr durch eine aufgrund der Schichtung der Oberflächentemperatur verringerte ILD vollständig erodiert werden. Im offenen Ozean, im zentralen tropischen Atlantik, treten in der wandernden ITCZ sporadisch Episoden von starken Regenfällen auf. Die turbulente Einmischung der Süßwasserlinsen in die Oberflächenschicht reduziert die MLD drastisch und bildet dort vor allem im Winter und Sommer starke sporadische Barrierschichten (ca. 60 m). Eine Vertiefung der MLD zerstört diese Barrierschichten durch turbulente Salzvermischung und einer Neigung der Salzgehaltsfronten in die Vertikale. Im Osten des tropischen Atlantiks gibt es von

September bis Oktober die stärkste Barrierschicht (ca. 60 m). Die Ursachen sind eine Verringerung der MLD durch eine Neigung der Salzgehaltsfronten an der Flussfahne des Niger und einer turbulenten Durchmischung des Regenwassers aus der ITCZ, sowie eine Vertiefung der ILD aufgrund der turbulenten Durchmischung. Zumeist werden diese Barrierschichten durch eine von turbulenter Durchmischung hervorgerufene Verringerung der ILD zersetzt.

Um die Auswirkungen des Amazonas-Flusseintrages auf die Variabilität der nördlichen tropisch-atlantischen Barrierschichten sowie auf die regionalen und großräumigen Ozeanzirkulationen zu verstehen, wurde eine Reihe von Sensitivitätsexperimenten mit einer 8 km-Auflösungsversion des obigen numerischen Modells durchgeführt, einschließlich realistischer Flusseintragsraten (basierend auf Messungen) und extremer, idealisierter Änderungen des Mittelwertes oder der Amplitude des Amazonas-Flusseintrages. Bei einem Überschuss an Süßwasser nehmen der Salzgehalt an der Meeresoberfläche (um ca. 10 psu), ILD (um ca. 42 m) und MLD (um ca. 50 m) ab, während die Temperatur der Meeresoberfläche (um ca. 1°C) und BLT (um ca. 42 m) ansteigt. Die größten Unterschiede zum Kontroll-Experiment, welches der Realität am nächsten kommt, treten im Sommer und Herbst auf, und zwar in zwei Extremfällen: kein Flusseintrag und 100%iger Anstieg des mittleren Flusseintrages. In den meisten Regionen reagieren die oben genannten Variablen empfindlicher auf eine Veränderung des mittleren Eintrages um 20% als auf eine Veränderung der jahreszeitlichen Amplitude um 40%.

Betrachtet man die Veränderungen in der Dynamik, so erklärt die mittlere kinetische Energie einen großen Teil der Unterschiede in der gesamten kinetischen Energie, wobei Änderungen der kinetischen Wirbelenergie nur in den hochgradig nichtlinearen Bereichen der NBC-Ringe, der Rückkopplung in den nordäquatorialen Gegenstrom (NECC) und des Schleifenstroms auftreten. Die Einführung von mehr Süßwasser verstärkt die westlichen Randströme, schwächt die NBC-Retrofektion sowie den NECC, die mehr mäandern und marginal nach Norden verschoben werden. Andererseits ist die Ozeandynamik unempfindlicher, wenn das Süßwasser abnimmt, aber ganz ohne Abfluss bleibt eine deutlich entgegengesetzte Reaktion erhalten. Darüber hinaus hat der Volumentransport in den oberen 50 m des Ozeans bei Vorhandensein von mehr Süßwasser größere Amplituden bei den zwischenjährlichen Fluktuationen der tropischen westlichen Randströmungen. Diese Ergebnisse bestätigen frühere Studien, die darauf hindeuten, dass der Amazonas-Flusswassereintrag und die Atlantische Meridionale Umwälzbewegung (AMOC) antikorreliert sind. Des Weiteren deuten meine Ergebnisse auf eine Antikorrelation der Änderung der BLT mit dem Transport durch den Floridastrom (integriert über die gesamte Ozeantiefe) sowie der AMOC hin.

Diese Arbeit zeigt, dass Barrierschichten lokalisierte Phänomene sind, die sich zuweilen aufgrund der Dynamik des Ozeans bilden und wachsen können (z.B. durch Strömungen in der Oberflächen- oder oberflächennahen Schicht, Subduktion, Wirbel und Filamente), ohne dass ein lokaler Oberflächen-Süßwasserzufluss vorliegt. In Ermangelung vollständiger Beobachtungsdaten war eine umfassende Studie zur Identifizierung der Wachstums- und Zerfallsmechanismen von Barrierschichten im tropischen Atlan-

tik mithilfe numerischer Simulationen möglich. Die hier untersuchten Wachstums- und Zerfallsmechanismen können auf andere Regionen des Weltozeans übertragen werden, in denen ähnliche physikalische Bedingungen für die Existenz von Barrierschichten vorherrschen. Diese Kenntnisse über Barrierschichten im tropischen Atlantik und die Reaktion des oberen Ozeans (hinsichtlich des Salzgehaltes, der Temperatur sowie regionaler und großskaliger Zirkulationen) auf mögliche zukünftige Änderungen des Amazonaseintrags, können zu einem besseren Verständnis der Rolle der Barrierschicht in der Ozean-Atmosphären-Wechselwirkung und ihrer klimatischen Auswirkungen beitragen, wie die Vorhersage der Intensivierung tropischer Wirbelstürme, der AMOC und der atmosphärischen Fernverbindungen.

Contents

Abstract	i
Zusammenfassung	iii
1 Introduction	1
1.1 Motivation	1
1.2 State of the art	7
1.3 Objectives of the study	12
1.4 Outline of the thesis	13
2 Ocean numerical simulations	15
2.1 Model setup and experiments	15
2.1.1 Atlantic-Arctic ocean simulations	15
2.1.2 Amazon runoff experiments	17
2.2 Simulated circulation patterns in the tropical Atlantic	17
3 Observed and simulated barrier layers	23
3.1 Observational data	23
3.2 Seasonal variability of observed and simulated BLT	24
4 Barrier layer growth and decay mechanisms in the tropical Atlantic Ocean	33
4.1 Introduction	33
4.2 Balance equations and governing mechanisms	35
4.3 Barrier layer in the NBC rings region	38
4.3.1 Seasonal evolution	41
4.3.2 Short timescale events	47
4.4 Barrier layer in the NEC region	58
4.4.1 Seasonal evolution	59
4.4.2 Short timescale events	63
4.5 Barrier layer in the ITCZ region	72
4.5.1 Seasonal evolution	73
4.5.2 Short timescale events	74
4.6 Barrier layer in the ETA region	81

4.6.1	Seasonal evolution	81
4.6.2	Short timescale events	88
4.7	Summary and discussion	96
5	Impact of Amazon river runoff on the western tropical Atlantic Ocean	103
5.1	Introduction	103
5.2	Description of experiments	104
5.3	Relation between Amazon runoff and upper ocean salinity, ILD, MLD and BLT	107
5.3.1	Time mean differences	113
5.3.2	Seasonal variability of differences	117
5.4	Relation between Amazon runoff and the NBC/NECC and related eddy activity	122
5.4.1	Time mean differences	122
5.4.2	Seasonal variability of differences	124
5.5	Relation between Amazon runoff and the large-scale north Atlantic cir- culation	128
5.5.1	Amazon runoff/BLT and the western boundary current transports	128
5.5.2	Amazon runoff/BLT and the AMOC	134
5.6	Summary and discussion	136
6	Conclusions and outlook	143
6.1	What are the mechanisms responsible for the BLT variability in the tropical Atlantic?	143
6.2	What is the impact of changing the Amazon river runoff on BLT and larger-scale circulation?	145
6.3	Future work	148
	References	xv
	List of Abbreviations	xvii
	List of Figures	xxvii
	List of Tables	xxix
	Acknowledgements	xxxix

Chapter 1

Introduction

1.1 Motivation

The upper ocean connects surface forcings from winds, heat and freshwater with the deep ocean. Penetration of sun's radiation, evaporation, freshening of surface due to rainfall, ice melt, and river runoff, and mixing due to winds and waves, all occur at the surface of the ocean (Figure 1.1). Those momentum, energy and mass fluxes interchanged in the surface layer of the ocean can have impacts on the heat and salt budgets, local and large-scale oceanic circulations, and on the atmosphere-ocean coupling. This can have repercussions on the everyday weather and long-term climate. The upper ocean thus affects not only the climatic conditions and weather patterns over the ocean, but also on land, given it has an integral role to play in natural calamities like flooding due to intense monsoons, sea-level rise or tropical cyclones. Apart from having physical impacts, being the photic or sunlit zone, the surface layer of the ocean supports photosynthesis and thus is a thriving ecosystem and habitat to many life forms. It is the most tangible segment of the ocean, being in direct contact with an integral part of the anthroposphere through coastal settlements, fishery and other industries and serving as a mode of transportation. A change in the upper ocean can thus have a palpable affect on many spheres. Therefore, it is essential to understand the upper ocean structure, its variability and the underlying processes.

The uppermost layer of the ocean is the mixed layer, which spans from the surface up to the depth where the density remains constant (the so called "mixed layer depth" (MLD)). Within the mixed layer, the salinity, temperature, and density are vertically uniform. The pycnocline is where the density increases strongly with depth, after being uniform in the mixed layer. The MLD marks the top of the pycnocline (black curve in Figure 1.2). The homogeneous mixed layer forms due to the vigorous turbulent mixing processes which are active in the upper ocean, like wind-stirring, waves, turbulence generated by vertical shear or night time convective mixing (Figure 1.1). The transfer of mass, momentum, and energy between the atmosphere and this homogeneous layer

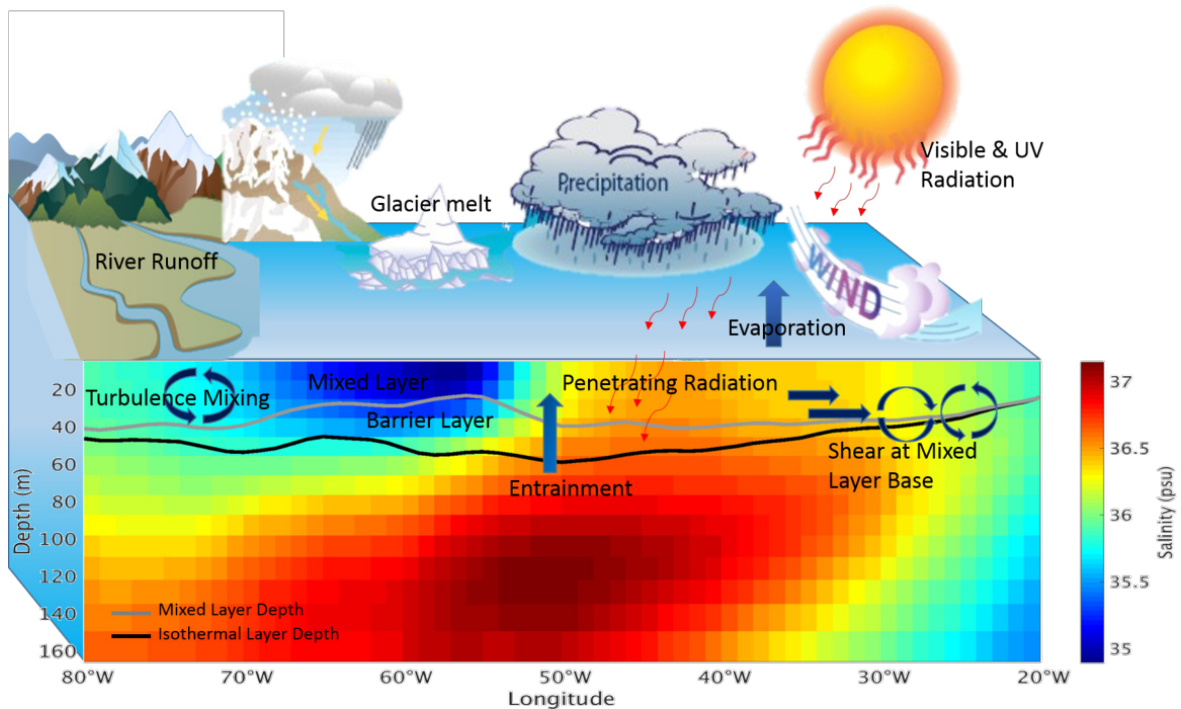


Figure 1.1: Schematic of the upper ocean processes and its external forcings along a salinity section at 15°N in the Atlantic Ocean (observations from the EN4 database). Adapted and expanded from an illustration by Jayne Doucette, Woods Hole Oceanographic Institution.

occurring at short timescales, is the source of most oceanic motions. The thermal and mechanical inertias of the upper ocean are determined by the depth of the mixed layer.

The "isothermal layer depth" (ILD) is the depth (counted from the surface) up to which the temperature remains constant. It marks the top of the thermocline, which is the large vertical gradient of decreasing temperature. Further below, the water temperature reduces more gradually to greater depths (red curve in Figure 1.2). The ILD is dependent only on temperature, while the MLD is dependent on density, and therefore on salinity and temperature. Cooling and evaporation cause convective mixing and overturning, deepening the ILD and MLD. On the other hand, heating re-stratifies the isothermal layer and the mixed layer; freshening re-stratifies just the latter. Heavy precipitation in the tropics, river runoff and melting of glaciers and ice/snow from land into the ocean can cause a surface-trapped fresh water pool that induces a strong halocline (and therefore pycnocline) in the top few meters, leading to the MLD being shallower than the ILD (Figure 1.1). The upper mixed layer, limited by the salt stratification, is thinner and thus more reactive than the deeper isothermal layer (de Boyer Montégut et al., 2007). The intermediate layer that separates the base of the shallower mixed layer from the top of the thermocline is called "barrier layer".

Following Sprintall and Tomczak (1992), de Boyer Montégut et al. (2004), de Boyer Montégut et al. (2007), Breugem et al. (2008), Mignot et al. (2012) and

Drushka et al. (2014), I define ILD as the depth at which temperature has dropped by a value of $\Delta T = 0.2^\circ\text{C}$ relative to the temperature at a reference depth of 2.5 m, the first depth level in the simulation used in the present work. MLD is defined as the depth at which potential density σ_θ has increased with respect to its value at the reference depth by an amount $\Delta\sigma_\theta$. Here $\Delta\sigma_\theta$ is the potential density change equivalent to the above temperature change at the local salinity:

$$\Delta\sigma_\theta = \sigma_\theta(T_{ref} - \Delta T, S_{ref}, P_0) - \sigma_\theta(T_{ref}, S_{ref}, P_0) \quad (1.1)$$

where T_{ref} and S_{ref} are the temperature and salinity at the 2.5 m reference depth and P_0 is the pressure at the ocean surface. The thickness of the barrier layer, i.e., the barrier layer thickness (BLT) is defined as the positive difference between the ILD and the MLD:

$$BLT = ILD - MLD \quad \text{for } ILD > MLD. \quad (1.2)$$

This definition of MLD ensures that, in the absence of haline stratification, i.e. in the absence of barrier layers, the MLD and ILD are identical ($BLT = 0$). Also, this definition of ILD takes care of temperature inversions that may be present in the barrier layer (Mignot et al., 2012).

Barrier layers are significant as they prevent mixing between the thermocline and the mixed layer, thus diminishing the forcing of the thermocline by surface freshwater, heat and momentum fluxes, and enhancing their impacts on surface temperature and salinity. Furthermore, they also limit large effects of turbulent processes at the mixed layer base and prevent entrainment of cold water from the deep ocean up above the thermocline (Sprintall and Tomczak, 1992; Drushka et al., 2014). As a consequence, the barrier layers can trap heat inside and above them, featuring a temperature inversion (Balaguru et al., 2012a; Mignot et al., 2012) (Figure 1.2b), thus increasing the sea surface temperature and causing potential intensification of tropical cyclones passing over the barrier layers (de Boyer Montégut et al., 2007; Balaguru et al., 2012b). Barrier layers therefore play a significant role in the upper ocean heat and salt budgets as well as in air-sea interaction (Vialard and Delecluse, 1998). They also affect currents by trapping momentum input from the wind in the shallow mixed layer, thereby producing strong surface flows (Drushka et al., 2014). On the other hand, weakening of the barrier layers can enhance primary productivity by allowing greater injection of nutrients from below into the mixed layer (Sarmiento et al., 2004; Doney, 2006; Dave and Lozier, 2013).

Figure 1.2a illustrates an example from the north-eastern tropical Atlantic, of the typical structure of the upper ocean in the absence of a barrier layer, when the MLD and the ILD are equal. An example of the upper ocean structure from the western tropical Atlantic, during the presence of a barrier layer is shown in Figure 1.2b. Within the barrier layer there is a halocline and pycnocline where the salinity and density increase

respectively as we go deeper below the mixed layer (Figure 1.1 and Figure 1.2). Thus, salinity variability plays an important role in the physics of barrier layers.

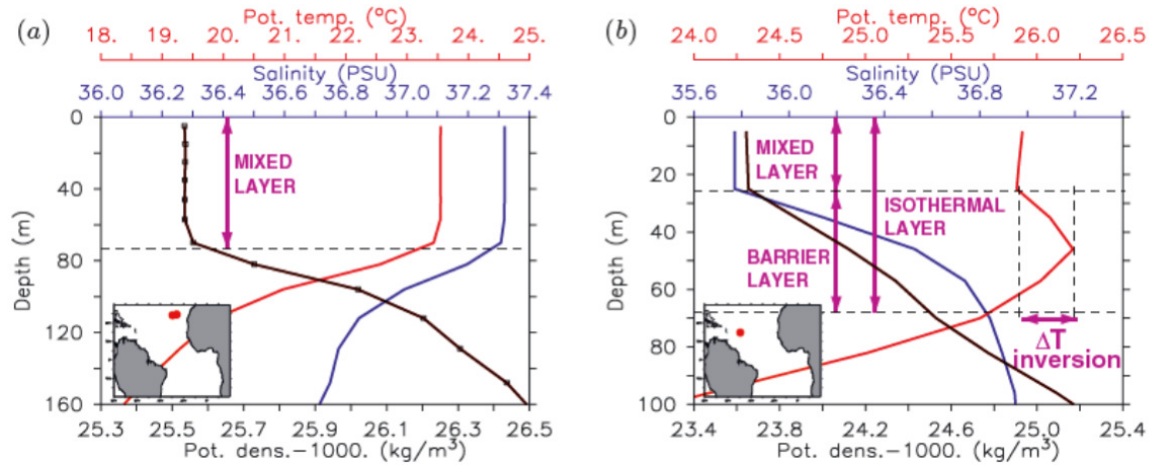


Figure 1.2: Examples of vertical stratification in the tropical Atlantic Ocean (a) without and (b) with a barrier layer. The profiles were taken from Simple Ocean Data Assimilation (SODA) reanalysis at the location of the red dot in the insert (25°N , 30°W and 15°N , 50°W , respectively). The black, red and blue lines depict, respectively, potential density (kg/m^3), potential temperature ($^{\circ}\text{C}$), and salinity (psu). Reproduced from Breugem et al. (2008).

The ocean surface salinity is strongly influenced by the water exchanges with the atmosphere via evaporation and precipitation, sea ice formation and melt, as well as inputs from river runoffs and iceberg melting (Figure 1.1). Salinity plays key dynamical roles in the ocean circulation and in recent or past climate variability, in addition to being a tracer of ocean circulation. Salinity provides an independent insight into atmospheric moisture transport, interactions between the terrestrial and oceanic water cycles through river runoff, inter-ocean freshwater exchanges and variability associated with oceanic features such as planetary waves, fronts and eddies, all of which affect the upper ocean. The spatial distribution of barrier layers in the tropics resembles the spatial distribution of the surface freshwater flux (Thadathil et al., 2008).

Large values of BLT are typically found in the tropics and at high latitudes around both poles. Figure 1.3a shows a map of the annual maximum BLT using observations of temperature and salinity spanning the years 1967-2006. The annual maximum of the monthly BLT shows values of up to 80 m in the tropics and much larger values above 100 m in the latitude bands $50\text{-}90^{\circ}$ around the north and south polar ice caps. Exceptions are the mid-latitude bands ($25\text{-}45^{\circ}$) in both the hemispheres, where the BLT vanishes. It is noticeable that even though the largest global values of BLT are found in parts of the Arctic and Southern Ocean, the tropics (highlighted in the pink box in Figure 1.3) have large regions with BLT existing for more than 6 months, like in the warm western and equatorial tropical Atlantic and Pacific Oceans, and in the Bay of Bengal and eastern equatorial Indian Ocean. Those barrier layers in the tropics are distinguished because of the strongest air-sea coupling taking place in the tropics.

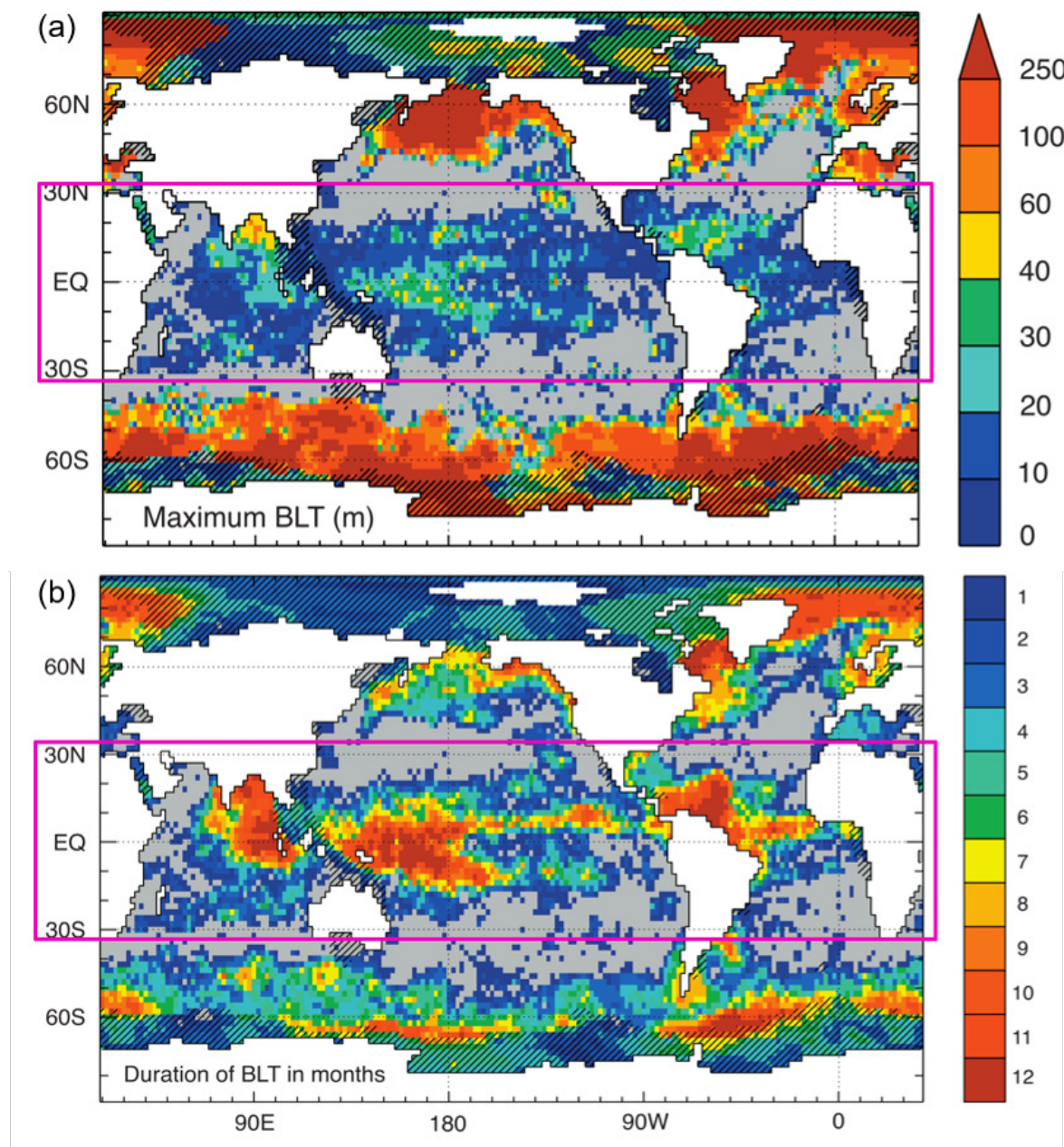


Figure 1.3: (a) Annual maximum of the monthly BLT, showing the maximum BLT in meters and (b) number of months during which the percentage of the BLT relative to ILD exceeds 10%. Areas where the relative thickness never exceeds 10% are in light grey. Areas where data are not available over a whole annual cycle are hatched. Adapted from de Boyer Montégut et al. (2007).

The Amazon River, with an average annual discharge of about 0.2 Sv close to the equator in the western tropical Atlantic, has the largest river discharge in the world. The Amazon discharge constitutes 20% of the global riverine discharge to the ocean (Moura et al., 2016). The magnitude of this Amazon freshwater source is important in the salinity balance of the tropical Atlantic, as the discharged volume is seen to

reach double the net Evaporation-minus-Precipitation budget over the northwestern tropical Atlantic (Ferry and Reverdin, 2004). In the presence of this fresh river water capping of the upper ocean, due to the resulting density stratification, large BLT is produced (Sprintall and Tomczak, 1992; Paillet et al., 1999; Masson and Delecluse, 2001; Silva et al., 2005; Sato et al., 2006; Mignot et al., 2007; Breugem et al., 2008; Balaguru et al., 2012a; Mignot et al., 2012). Apart from the freshwater discharge from the Amazon and Orinoco rivers in the western tropical Atlantic, precipitation under the Intertropical Convergence Zone (ITCZ), discharge from the Niger River in the eastern tropical Atlantic and several oceanographic processes also facilitate the formation of the barrier layers in the tropical Atlantic.

Located in the northwestern tropical Atlantic, the quasi-permanent barrier layers present throughout the year (occurring for 12 months in Figure 1.3b) (Mignot et al., 2012) are likely more prominent and important than other barrier layers of the World Ocean (Foltz et al., 2004; Mignot et al., 2007; Mignot et al., 2012). Balaguru et al. (2012b), Reul et al. (2014) and Fournier et al. (2017) highlight the importance of the Amazon plume's fresh and warm water and of resulting barrier layers in the development and intensification of the devastating tropical cyclones, prevalent in the northwestern tropical Atlantic. Since barrier layers prevent the surface momentum fluxes from going beyond the base of the mixed layer and prevent the entrainment of cold deep water from reaching into the isothermal layer, the ocean surface and the barrier layers heat up. Additionally, the northwestern tropical Atlantic barrier layers feature one of the largest temperature inversions (Figure 1.2b). Temperature inversions can exist within barrier layers since the solar radiative flux penetrates below the mixed layer inducing the development of unique subsurface temperature maxima and the barrier layers trap the warm water until much later. Also warm surface water from summer is trapped until autumn and winter in the barrier layers here (Balaguru et al., 2012a; Mignot et al., 2012). This warm reservoir below the mixed layer can potentially be eroded by intense atmospheric momentum forcing and also contribute to further heating of the surface temperatures. The increased surface temperature can cause potential intensification and sustenance of the tropical cyclones passing over the thick barrier layers in the northwestern tropical Atlantic (Balaguru et al., 2012b).

Locally, salinity anomalies can induce changes in the tropical surface mixed layer and consequently in the position and strength of the equatorial and off-equatorial currents (Mignot and Frankignoul, 2010). Masson and Delecluse (2001) concluded that the circulation at the northern Brazilian continental shelf is primarily forced by the seasonal cycle of the Amazon runoff. Such freshwater anomalies in the tropical Atlantic generated mainly by Amazon runoff, evaporation and/or precipitation changes due to ITCZ position variations and intensification, African monsoon variability, etc., have the potential to alter the properties of the waters involved in the upper limb of the Atlantic Meridional Overturning Circulation (AMOC) and further north crucially change the water stability in the convection sites of the subpolar gyre, therefore contributing to low-frequency ocean variability. Mignot et al. (2012) suggested that the barrier layer

system of the northwestern tropical Atlantic is located on the path of the surface branch of the AMOC, so its formation and seasonality could also be linked to remote oceanic conditions and influence the whole Atlantic climate through modified oceanic conditions.

The above characteristics of the upper-ocean barrier layer phenomenon, and in particular the important impacts of barrier layers in the tropical Atlantic, emphasize the relevance and significance of their study and served as motivation for this thesis work.

1.2 State of the art

The upper ocean was originally thought to have just a thermally-mixed layer that is now termed isothermal layer. This mixed layer theory based on just temperature was developed by Kraus and Turner (1967) and later extended by Denman (1973). This model was then further extended by Miller (1976) to include the effects of salinity on the upper ocean. The presence of an isohaline layer shallower than the isothermal layer was first observed in the tropical Atlantic Ocean by Defant (1961) during the Meteor cruises of 1936, and later, it was observed during the Barbados Meteorological and Oceanographic Experiment (BOMEX) cruises in May, June, and July of 1969 also in the tropical Atlantic (Elliott, 1974). Later with the observations from a series of cruises by the Western Equatorial Pacific Ocean Study (WEPOCS) and Tropical Ocean and Global Atmosphere (TOGA) programs, the presence of a shallower pycnocline than thermocline was reported in the western equatorial Pacific by Delcroix et al. (1987), Lindstrom et al. (1987), Godfrey and Lindstrom (1989), Lukas and Lindstrom (1991) and You (1995). This distance separating the top of the pycnocline from the top of the thermocline was given the term "barrier layer" (Eq. 1.2) by Godfrey and Lindstrom (1989) and by Lukas and Lindstrom (1991). Soon after, one of the pioneering discoveries of barrier layers in the World Ocean was made in the tropics by Sprintall and Tomczak (1992), which described also the tropical Atlantic barrier layers. Following that, Pailler et al. (1999) conducted a focused study of the western tropical Atlantic barrier layers based on observation profiles.

The thick barrier layers associated with temperature inversions occurring within the Atlantic Warm Pool (AWP) in the northwestern tropical Atlantic south of the subtropical gyre (Figure 1.4a) are believed to originate primarily from advection of fresh Amazon and Orinoco river water and ITCZ precipitation by the northwestward moving North Brazil Current (NBC) and associated rings (Fratantoni and Glickson, 2002; Ferry and Reverdin, 2004), in combination with surface cooling during boreal autumn and winter (Sato et al., 2006; Breugem et al., 2008; Mignot et al., 2012; Balaguru et al., 2012a). Poleward transport of those fresh equatorial waters by northward Ekman currents and equatorward sub-surface transport of the Salinity Maximum Water

(SMW) may also contribute to the formation of barrier layers in this region (Sprintall and Tomczak, 1992; Foltz et al., 2004; Sato et al., 2006; Mignot et al., 2007; Balaguru et al., 2012a). The relevance of the above ideas for the local barrier layer growth and decay still need clarification. Henceforth, I address those barrier layers in the equatorial flank of the subtropical gyre as the barrier layers along the North Equatorial Current (NEC), as this is the dominant current there.

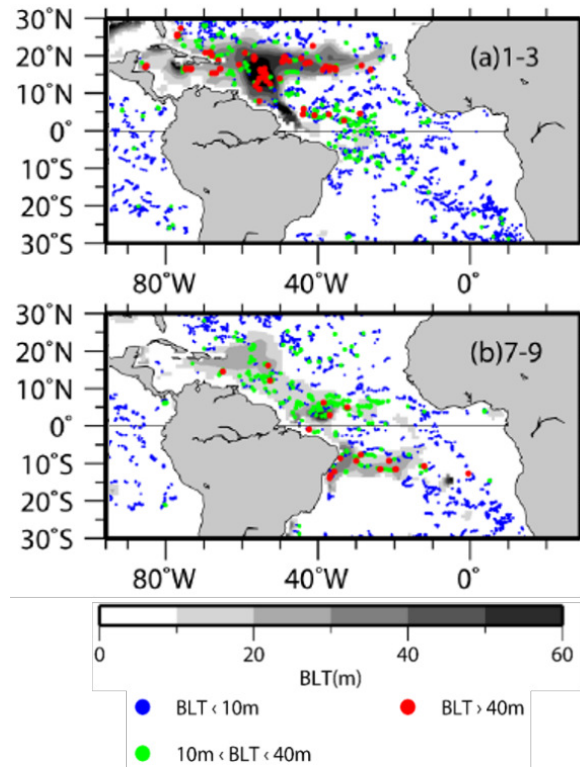


Figure 1.4: Seasonal distribution of profile data obtained with Argo floats from January 2000 to June 2005: (a) January-March and (b) July-September. The BLT at each profile is denoted by colored points. Background shadings denote the BLT calculated from the corresponding seasonal World Ocean Atlas 2001. Adapted from Sato et al. (2006).

In the southern hemisphere, in the south western tropical Atlantic between 10-20°S there exist smaller magnitude barrier layers for around three months in a year (Figure 1.3, Figure 1.4b) during the boreal summer months. The causes of their formation are suggested to be, like in the northwestern tropical Atlantic, mainly the fresher equatorial water being transported southward at the surface while the saline water from the southern subtropical gyre flows towards the equator in the subsurface (Mignot et al., 2007; Veneziani et al., 2014). Those southern hemisphere barrier layers, are simulated in the model used in this thesis work, and are out of the scope of this study as their major formation mechanisms are similar to the northwestern tropical Atlantic barrier layers along the NEC, and they are smaller and less frequent than the latter.

The seasonal cycle of BLT north of the Amazon mouth close to the equator (Figure 1.4b) is different from the seasonal cycle of the BLT along the NEC in the northwest-

ern tropical Atlantic. Masson and Delecluse (2001) studied the formation of barrier layers in the western tropical Atlantic (from 10°S to 10°N) by performing sensitivity experiments with an Ocean General Circulation Model (OGCM). They explained that the temporal evolution of the sea surface salinity (SSS) is controlled by the dynamics: in summer the NBC and North Equatorial Countercurrent (NECC) systems advect the fresh water north- and northeastward and create large Amazon plumes three months after the Amazon flood in May-June. This creates thick barrier layers at the Amazon mouth from March to June (Silva et al., 2005) and in the north and east of the Amazon mouth from June to October (Pailler et al., 1999; Masson and Delecluse, 2001). My study corroborates this finding and shows specifically that the NBC rings carry the conditions for barrier layer growth.

Freshwater influx from precipitation due to ITCZ is hypothesized to be responsible in general for the existence of barrier layers in the central tropical and equatorial Atlantic (Figure 1.4) (Sprintall and Tomczak, 1992; Pailler et al., 1999; Sato et al., 2006; Mignot et al., 2007; de Boyer Montégut et al., 2007). The Niger River's freshwater plume in the eastern tropical Atlantic also generates smaller magnitudes of BLT, which have not been much explored, though their existence based on in situ data, and their seasonality using climatological outputs from a numerical simulation have been reported in a recent study (Dossa et al., 2019). This region is reported to have large barrier layers in September-October and in February, which are suggested to be formed due to Niger runoff and ITCZ precipitation.

Therefore, it is widely accepted that precipitation and river discharge are the main causes for the existence of barrier layers. However, ocean dynamics play a significant role in their formation, evolution and decay (Agarwal et al., 2012). Coles et al. (2013), using a $1/6^{\circ}$ model and data from three research cruises (in May-June 2010, September-October 2011, and July 2012), identified four Amazon plume pathways of freshwater transport and found that the role of currents and advection is more important than river discharge in maintaining plume properties. The current state of knowledge with respect to the above barrier layers in the tropical Atlantic highlights the need for a better understanding and a clarity of the mechanisms governing the generation, evolution and decay of these barrier layers, on seasonal and short-term periods, especially those related to local circulation patterns and small-scale processes.

In an analysis of Argo observations from January 2000 to June 2005, Sato et al. (2006) noticed patchy and thick barrier layer structures, which were explained by large-scale and small-scale (100 km) subduction processes in the subtropical gyres of the World Ocean. As those synoptic thick barrier layers appear in areas where the quasi-permanent climatological barrier layer is also thick, the climatological barrier layer is claimed to be a spatially and temporally smoothed picture of the synoptic barrier layers (Sato et al., 2006; de Boyer Montégut et al., 2007; Mignot et al., 2007; Katsura and Sprintall, 2020), as shown in Figure 1.4 for the tropical Atlantic. According to the authors, since the Argo floats sample mesoscale features but do not resolve them,

the role of mesoscale eddies to describe the barrier layer formation process needs to be assessed. In a study using the most recent Argo data on the formation mechanisms of barrier layers in the Southern Ocean, Pan et al. (2018) noted that, due to the lack of high resolution data, effects of mesoscale eddies and filaments, and the entrainment into barrier layers remain to be studied. This is a research gap that exists for most of the barrier layers in the World Ocean, and is addressed in this thesis for the above described tropical Atlantic barrier layers.

In some earlier modeling studies (Ferry and Reverdin, 2004; Mignot et al., 2012; Da-Allada et al., 2013; Sommer et al., 2015; Camara et al., 2015) and in a reanalysis and observational study (Foltz and McPhaden, 2008), the contribution of several processes to the salinity budget, which are responsible for SSS changes in the tropical Atlantic, have been identified. But the processes that are responsible for the formation, evolution and decay or erosion of the barrier layers in this region have not been identified or defined before. Using the vertical derivative of salinity and temperature balance equations, Cronin and McPhaden (2002) provided a qualitative description of the relevant mechanisms by which barrier layers can form, grow and dissipate in the tropical Pacific under the influence of westerly wind bursts. A quantitative analysis was not possible in their case due to inadequate observational data. A qualitative or quantitative analysis of these mechanisms governing the evolution of barrier layers in the tropical Atlantic has not been performed yet, which leaves a large gap in the understanding of the growth and decay of these barrier layers. The present work aims at closing that gap.

Observational (Pailler et al., 1999; Silva et al., 2005) and modelling (Masson and Delecluse, 2001) studies showed the importance of the seasonally-varying Amazon river discharge for maintaining the summer barrier layers in the western tropical Atlantic. Using two 1-year-long numerical integrations of the ROMS model, one with a seasonal river discharge and another with no river discharge, Varona et al. (2019) investigated the potential local impact of the Amazon and Para rivers on the western tropical Atlantic. Coles et al. (2013) suggested that the inclusion of a river plume significantly enhances the eddy variability and mixing in the model simulations. By performing experiments with a constant time mean Amazon river discharge and one with a seasonal cycle, Romanova et al. (2011) pointed out that including seasonal runoff forcing helps reproduce the seasonal cycle of barrier layers in the Amazon domain and the freshwater transport in the tropical Atlantic. They suggested that based on the strong seasonal response of one of the major rivers like the Amazon, one can assume that the seasonal variability of all rivers in the world partly modify the ocean current system. Thus, the importance of including a river plume for simulating a realistic eddy variability and mixing and having a seasonal cycle in the Amazon river discharge for reproducing the observed BLT and freshwater transport in the tropical Atlantic was so far identified in previous studies. However, there is limited understanding of the impacts of changes in the seasonal amplitude and mean of the Amazon river discharge on the physical state of the ocean, in particular on the upper ocean stratification, and also on the large-scale

circulation.

Mignot and Frankignoul (2010) investigated the sensitivity of the AMOC and of the north Atlantic climate to freshwater anomalies in the tropical Atlantic using a state-of-the-art Atmosphere-Ocean General Circulation Model (AOGCM), with an emphasis on temperature and salinity adjustments, oceanic and atmospheric pathways towards the high latitudes, and possible feedbacks. They compared these climatic effects to those associated with the natural decadal AMOC variations and with the AMOC shutdown induced by freshwater release at high latitudes. They showed that, by forcing the tropical Atlantic (15°S - 15°N) with negative freshwater forcing (-0.4 Sv), i.e., removing freshwater from the tropical Atlantic, the AMOC intensified after 15-20 years since the year of perturbation. The higher salinity and cold sea surface temperatures (SST) causes the MLD to deepen in the tropics, this propagates to higher latitudes, reaching the Labrador Sea and the regions with positive freshwater flux due to ice melt, and counteracts, to some extent, the dampening (slowing down) of the AMOC caused by the stratification and mixed layer shoaling at the higher latitude regions of ice melt.

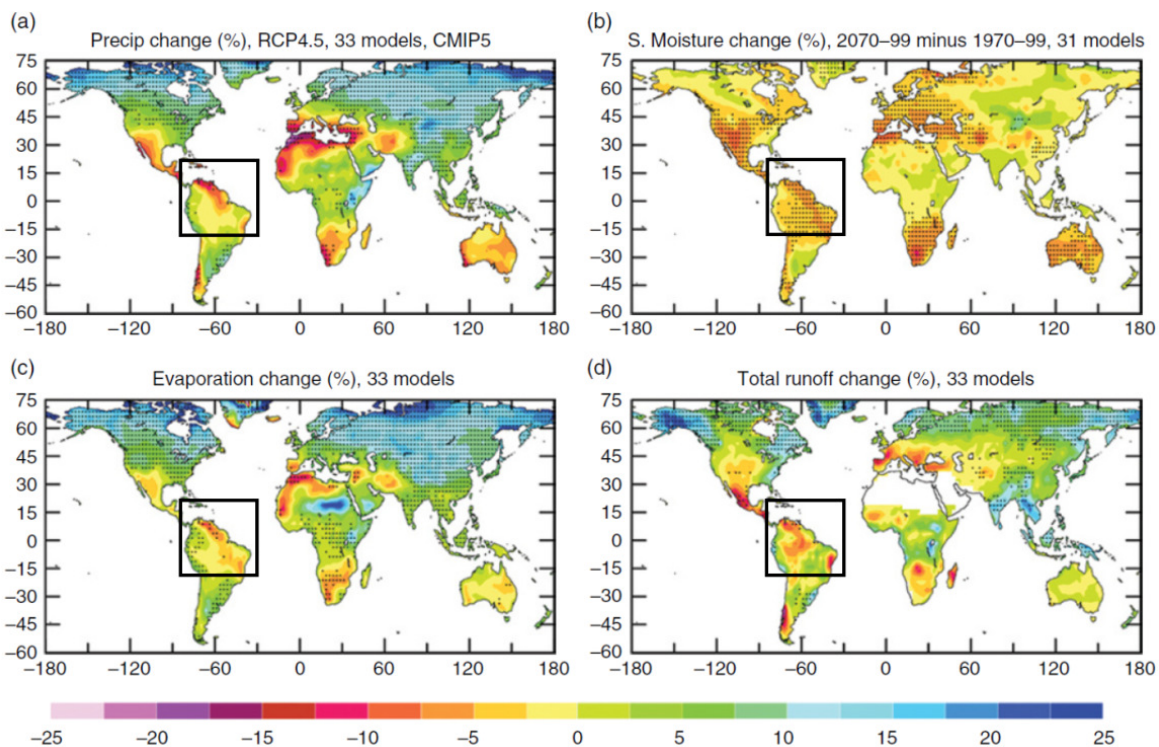


Figure 1.5: Multimodel mean long-term percentage changes from 1970-1999 to 2070-2099 (under a moderate RCP4.5 scenario) over land in annual (a) precipitation, (b) soil moisture content in the top 10 cm layer, (c) surface evapotranspiration, and (d) total runoff, from 31-33 CMIP5 models. The stippling indicates at least 80% of the models agree on the sign of change. The change patterns are similar to those shown by Collins et al. (2013). Figure adapted from Dai (2016).

From a past perspective, a review of the historical and future changes in streamflow and continental runoff by Dai (2016) notes that, from about 1950 to 2012, precipitation

and runoff have decreased over parts of Brazil (Figure 2.7 in Dai (2016)) including the Amazon River's catchment area (drainage basin), probably because of global warming (Gu and Adler, 2013). From a future perspective, they point out that over the Amazon River's catchment area, CMIP5 models generally predict decreased precipitation and runoff by 5-15% from 1970-1999 to 2070-2099 (Figure 1.5), i.e. in the 21st century, under the moderate emissions scenario RCP4.5. Also under the RCP8.5 high emissions scenario, daily mean streamflow is projected to decrease by 5-50% (Figure 2.12 from Dai (2016) also from Koirala et al. (2014)). Recent studies of Jahfer et al. (2017) and Jahfer et al. (2020) investigated the climatic impacts of having no Amazon river runoff and doubled runoff with a coupled AOGCM. They showed, in agreement with Mignot and Frankignoul (2010), that no Amazon river runoff causes the AMOC to strengthen while doubling the runoff causes it to weaken. The IPCC considers it very likely that the AMOC will weaken as a result of climate change, a conclusion which is mainly based on model calculations. As mentioned in Mignot and Frankignoul (2010) there is an argument that in global warming conditions, increased salinity in the tropical Atlantic might compensate for the freshening of the Atlantic high latitudes (Latif et al., 2006), and that would be true only if the tropical negative freshwater forcing is strong enough. Using a coupled model of intermediate complexity, Goelzer et al. (2006) estimated that freshwater forcing in the tropics and in the high northern latitudes have comparable impacts on the AMOC maximum when the tropical forcing is about 1.5 times larger. They also suggested that the compensation would be limited in a more realistic condition. Therefore, such a strong tropical forcing, as considered in Mignot and Frankignoul (2010), Jahfer et al. (2017) and Jahfer et al. (2020), would be unrealistic. Seen earlier in the motivation section, lying on the upper limb of the AMOC, the northwestern tropical Atlantic barrier layers may have an impact on the AMOC (Mignot et al., 2012). The freshwater variability and transport in the tropical Atlantic basin was suggested in previous studies to have an impact on the large-scale AMOC, however, the relation between the upper ocean phenomenon of barrier layer and the large-scale AMOC is not known. Further understanding of the role that the realistic and extreme changes in the Amazon runoff and the resulting barrier layers play in the physics and dynamics of the tropical Atlantic Ocean as well as the large-scale circulation is therefore of crucial importance and is addressed in the present work.

All of the above pointed research gaps motivate the objectives of this thesis.

1.3 Objectives of the study

In this study I will detect and demarcate the growth and decay mechanisms of barrier layers in all the above introduced areas in the tropical Atlantic and discuss them in relation to ocean circulation features, like the regional current systems (the NBC/NECC and NEC), and certain other local small-scale processes like eddies and fronts. The oceanic response and sensitivity of the BLT to realistic and extreme increase/decrease

in the mean and amplitude of the Amazon runoff, will be investigated with sensitivity experiments incorporating modified runoff. Along with temperature and salinity observations, outputs from eddy resolving simulations at 8 km and 4 km resolutions forced by fluxes computed with the National Centers for Environmental Prediction (NCEP) RA1 and the European Centre for Medium-Range Weather Forecasts (ECMWF) ERA-Interim reanalyses respectively, facilitate this study of the finer details of the upper ocean dynamics. The results give an insight into what impact a predicted drought/flood condition over the Amazon basin could have on the ocean state, BLT and possibly on the larger-scale circulation.

The answers to the following key questions posed in the present thesis will provide a more comprehensive understanding of the above aspects and give some new insights into upper ocean dynamics and its larger climatic impacts.

The key questions to be addressed in the present thesis are:

- Q.1. What are the mechanisms responsible for the growth and decay of barrier layers and their variability in the tropical Atlantic Ocean?
- Q.2. What is the impact of changing the Amazon river runoff on the tropical Atlantic barrier layers and on the local and large-scale Atlantic circulations?

1.4 Outline of the thesis

The remaining thesis is organized as follows:

Chapter 2 describes the details of the model set-up and provides an overview of the simulated oceanic circulation patterns and atmospheric freshwater forcing in the tropical Atlantic.

In **Chapter 3** the model simulations are validated against observations, with regard to the spatial and seasonal variability of barrier layers.

In **Chapter 4** the physical mechanisms responsible for the growth and decay of barrier layers are studied in detail. The mechanisms governing the growth and decay of four localized barrier layers are identified and examined in the tropical Atlantic: barrier layers in the NBC rings in the western tropical Atlantic, barrier layers along the NEC further to the north, barrier layers in the central and eastern tropical Atlantic region, and finally barrier layers in the Niger river plume in the eastern tropical Atlantic. Discussion of the results along with a discussion of the similarities and differences between all the regions is presented at the end of this chapter.

Chapter 5 explores the impacts on the western tropical Atlantic of changes in the Amazon river discharge by increasing/decreasing the mean runoff and its seasonal amplitude. The experiments performed with the varying Amazon runoff are described

in detail in this chapter. The resulting changes in upper ocean salinity, temperature, density, ILD, MLD, BLT, changes in the local currents (NBC/NECC system) and in the eddy activity are addressed. The chapter finally examines if and how the changes in the Amazon discharge and the resulting barrier layers further influence the large-scale circulation. Results are summarized and discussed at the end of the chapter.

Chapter 6 summarizes the conclusions of the thesis, and gives an outlook on possible future work.

Chapter 2

Ocean numerical simulations

2.1 Model setup and experiments

2.1.1 Atlantic-Arctic ocean simulations

The analysis presented in this thesis are based on two different integrations of the Massachusetts Institute of Technology general circulation model (MITgcm) (Marshall et al., 1997) covering the Arctic Ocean and the Atlantic Ocean north of 33°S, together featuring a hierarchy of horizontal resolutions: 8 km (equivalent to 1/12° at the equator) and 4 km (equivalent to 1/24° at the equator). The simulations will be henceforth termed ATL8km and ATL4km. In each case, the model was set up with a bipolar curvilinear grid, with one pole located over North America and the other over Europe. In the vertical, the model configurations use 50 levels (ATL8km) or 100 levels (ATL4km) of varying depth, from 10 m (ATL8km) and 5 m (ATL4km) in the upper ocean to 456 m (ATL8km) and to 185 m (ATL4km) in the deep ocean. The model uses a z-coordinate vertical grid. Bottom topography is derived from the ETOPO 2-min resolution database (ETOPO2). The initial conditions are derived from the annual mean temperature and salinity from the World Ocean Atlas 2005 (Boyer et al., 2005) in the case of ATL8km. The ATL4km model integration starts in year 2002 from initial conditions derived from ATL8km 1948-2015 model integration. The vertical mixing parametrization employed in the simulations uses the KPP formulation. Background coefficients of vertical diffusion are set to $10^{-5} m^2/s$ and of vertical viscosity to $10^{-4} m^2/s$. Horizontally, biharmonic diffusion and viscosity represent unresolved eddy mixing, with coefficients of horizontal diffusion and viscosity set to $5 \times 10^9 m^4/s$ (ATL8km), and $1 \times 10^9 m^4/s$ (ATL4km).

The model simulations are forced at the surface by fluxes of momentum, heat, and freshwater computed using bulk formulae and either the 1948-2009 6-hourly atmospheric state from the NCEP RA1 reanalysis (Kalnay et al., 1996) (in case of ATL8km) or the 1989-2009 ECMWF ERA-Interim reanalysis (Dee et al., 2011) (in

case of ATL4km). At the volume-balanced open northern and southern boundaries, the model is forced by the output of a 1° resolution global solution of the MITgcm forced by the NCEP reanalysis. A barotropic net inflow of 0.9 Sv ($1\text{Sv} = 10^6 \text{ m}^3/\text{s}$) into the Arctic is prescribed at Bering Strait, the model's northern open boundary, which balances a corresponding outflow through the southern boundary at 33°S . The model includes a dynamic-thermodynamic sea ice model, which solves for sea ice parameters, realistically simulating the impact of respective surface freshwater fluxes in the Arctic Ocean (Koldunov et al., 2014) and along the coasts of Greenland (Köhl and Serra, 2014). An annual averaged river runoff derived from Fekete et al. (1999) is imposed in the model by adding a corresponding freshwater flux to the Precipitation-minus-Evaporation field at grid points adjacent to river mouths. The model dynamics are then responsible for distributing this low salinity signal into the ocean interior. Details about the model performance and detailed validations against observations can be found in Serra et al. (2010), Köhl and Serra (2014), Koldunov et al. (2014), Sena Martins et al. (2015) and Biri et al. (2016).

The validation analysis presented in Chapter 3 and the study in Chapter 4 are based on daily and monthly output from the ATL4km simulation for the period 2003-2011. The high spatial and temporal resolution simulated data is essential to carry out the analysis presented in Chapter 3 and Chapter 4 because of the following reasons:

- It helps to identify the true nature and characteristics of the barrier layers.
- It helps to study the short-term events of localized barrier layers in the tropical Atlantic.
- It is needed for a better understanding of the mechanisms governing the generation, evolution and decay of the tropical Atlantic barrier layers, specially those related to small-scale processes, eddies and fronts, the objective of Chapter 4.
- Observations complete in four-dimensions and at high resolution are not easy to obtain.

The growth and decay mechanisms of the barrier layers have never been quantified before in previous studies, though Cronin and McPhaden (2002) discuss these mechanisms qualitatively for the barrier layers in the western tropical Pacific. They mention that a data field having space, depth and time dimensions is needed in order to study barrier layers, which was not the case with the observation data they used. Cronin and McPhaden (2002) quote, "...to perform a quantitative analysis of barrier layer formation, temperature, salinity, and currents must be resolved from the surface through the top of the thermocline. Likewise, because zonal and meridional advection appear to be a critical element of barrier layer formation, horizontal salinity and temperature gradients must be resolved, as well as their variations with depth. Finally, because there is substantial temporal and spatial variability in the formation of barrier layers, these measurement systems must be correctly placed in time and space."

The ATL4km daily output data is therefore essential in my study in order to resolve the small-scale processes and compute the terms of the salinity and temperature vertical gradient balance equations, which quantify the mechanisms responsible for the growth and decay of barrier layers. These equations and mechanisms are explained in detail in Chapter 4 and they help to quantify the formation, growth and decay mechanisms, identified and investigated for the tropical Atlantic barrier layers in that chapter.

2.1.2 Amazon runoff experiments

Regarding the second objective of the thesis, the corresponding analysis being presented in Chapter 5, the aim is to understand how increasing/decreasing the mean and amplitude of the Amazon river runoff can impact the barrier layers and the dynamics in the western tropical Atlantic Ocean. To obtain this, a series of numerical experiments were performed, now with the above described eddy-resolving ATL8km configuration. The only difference between the experiments is in the forced Amazon runoff in each experiment, which is derived based on the actual observed past behavior of the discharge (Dai, 2016; Dai, 2017).

Experiments were performed with 10, 20 and 100% increased/decreased mean runoff. Experiments with a 40% amplified and attenuated seasonal runoff amplitude, an experiment having a constant mean runoff, an experiment having zero runoff, and a control experiment having the mean and seasonal cycle of the Amazon river runoff were also conducted. An experiment similar to the control experiment but with 10⁻⁴% increase in mean runoff was conducted to test the significance and robustness of the obtained results. Details of the experiments and validation of the control run are described in Chapter 5. Apart from learning the sensitivity of the tropical Atlantic to the Amazon river discharge, the results obtained from these experiments help give an insight into what impact a predicted drought/flood condition (reduced/increased mean runoff) in this region could have on the ocean state and on the larger-scale circulation.

2.2 Simulated circulation patterns in the tropical Atlantic

Before comparing the simulated BLT from ATL4km and the observed BLT, which are presented in Chapter 3, in this section I examine the simulated surface ocean circulation and Evaporation-minus-Precipitation-minus-Runoff (E-P-R) field with a focus on the northern tropical Atlantic. As Figure 2.1 illustrates, the simulated NBC advects the mixed layer properties (salinity in this case) towards the northwest in winter and spring and towards the northwest and east in summer and autumn (NBC/NECC system). The latter case is supported by the development of the NECC starting in May-June and persisting until December (Figure 2.1b-f).

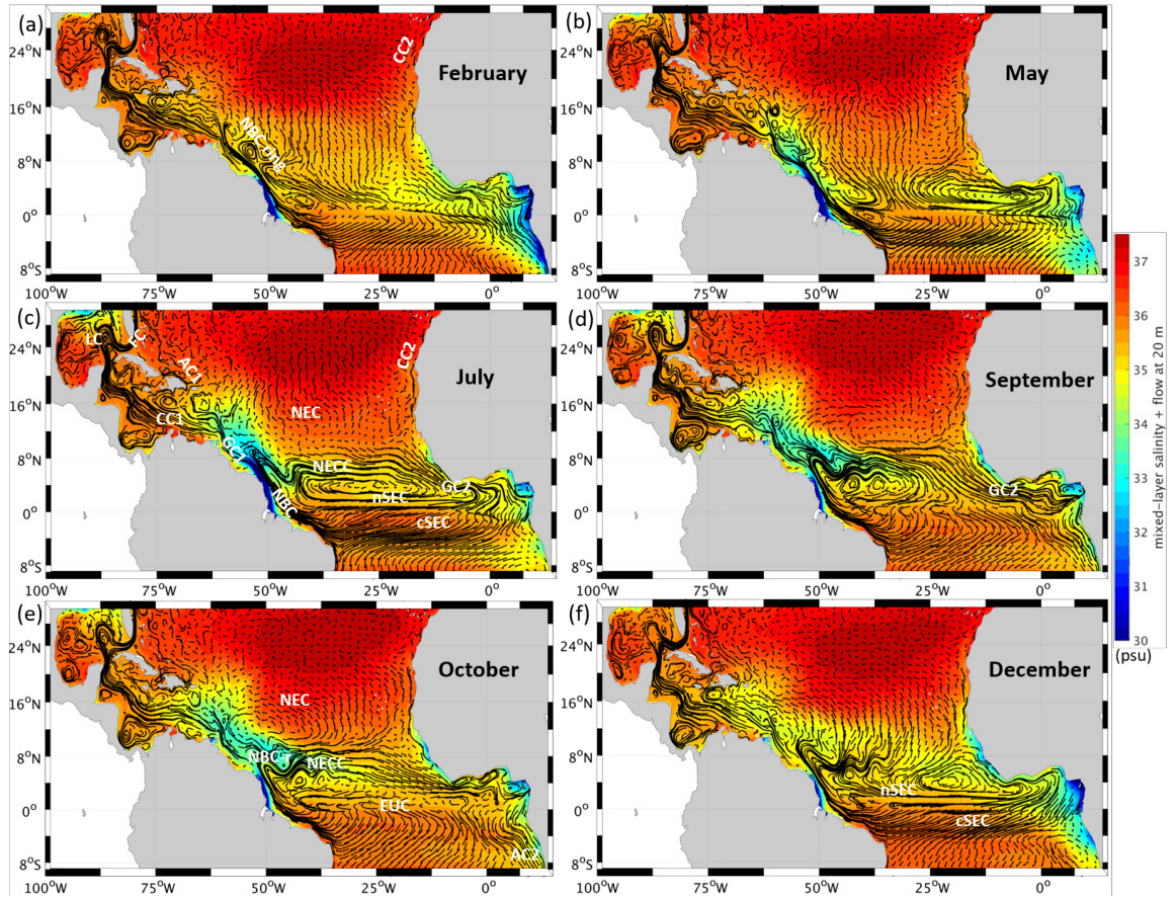


Figure 2.1: Climatology of simulated mixed-layer salinity (psu) and simulated flow at 20 m depth for the months of (a) February, (b) May, (c) July, (d) September, (e) October and (f) December. The flow trajectories result from a 30-day integration of particles using the climatological three-dimensional ocean velocity of the respective month. Labeled are the North Brazil Current (NBC), the North Brazil Current retroflection (NBC-r), the North Equatorial Countercurrent (NECC), the North Brazil Current ring (NBC ring), the Guiana Current (GC1), the Caribbean Current (CC1), the Loop Current (LC), the Florida Current (FC), the Antilles Current (AC1), the North Equatorial Current (NEC), the Canary Current (CC2), the Guinea Current (GC2), the South Equatorial Current (SEC) with the northern (nSEC) and central (cSEC) branches, the Equatorial Undercurrent (EUC) and the Angola Current (AC2).

The western boundary NBC is strongest in July (Figure 2.1c) transporting the maximum Amazon river freshwater discharged in May and the precipitation water due to the ITCZ further northwestward (Figure 2.2b,c), thus expanding the Amazon plume northward in summer-autumn (Figure 2.1c-e). In these months starting from June, the NBC spawns prominent and bigger anticyclones called the NBC rings along the northeastern coast of south America. These NBC rings (Figure 2.1a) are prevalent throughout the year and carry the freshwater northwestward.

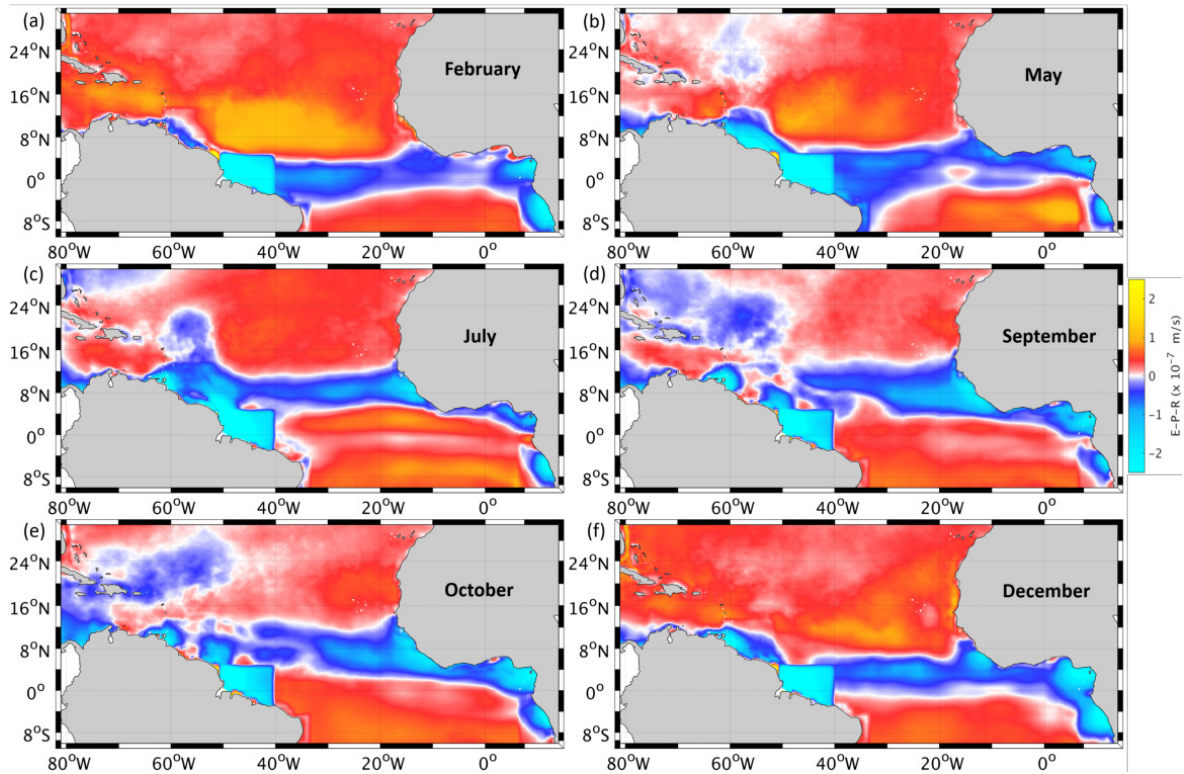


Figure 2.2: Climatology of simulated E-P-R ($\times 10^{-7}$ m/s) for the months of (a) February, (b) May, (c) July, (d) September, (e) October and (f) December.

Around the same time in May-June, the NBC starts to bifurcate in an eastward limb at the retroflection (NBC-r in Figure 2.1e) around 5-7°N, driven by wind, and feeds the NECC (Figure 2.1c-e) (Fonseca et al., 2004). During this time the ITCZ is in its northward position (Figure 2.2b,c). In August-October the NECC has maximum intensity and consequently transports the freshwater eastward forming the maximum eastward freshwater plume in autumn (Figure 2.1d-e). In addition to the freshwater from the Amazon River, the ITCZ rainfall reaches its northernmost position in summer-autumn (around 14°N) (Figure 2.2d), resulting in higher relative humidity, lower wind speed (Foltz et al., 2004; Foltz and McPhaden, 2008), and less evaporation in the northwest tropical Atlantic. This reduces the mixed layer salinity as well in these months (Figure 2.1c-e).

The seasonal variability of mixed layer salinity in the tropical Atlantic follows the migration of the ITCZ (Figure 2.1 and Figure 2.2). Thus after reaching the maximum northward extent in September, the rainfall is maximum on the eastern tropical Atlantic, along the west coast of Africa during the entire autumn and in early winter when the ITCZ is on its return path back southward (Figure 2.2e,f) (Figure 1 of Foltz and McPhaden (2008) and of Xie and Carton (2004); Figure 3 of Stramma and Schott (1999); Waliser and Gautier (1993); Foltz et al. (2004); Wang and Fu (2007)). All this freshwater is carried eastward along the African continent by the Guinea Current (GC2 in Figure 2.1c,d), which exists throughout the year (Figure 2.1) and the simulated GC2

shows a similar pattern as in Stramma and Schott (1999). The Angola Current (AC2 in Figure 2.1e), which joins the Angola Dome south of the equator in the eastern tropical Atlantic, carries the freshwater further south along the western African coast, peaking in September-October in the simulation (Figure 2.1d,e). A part of this freshwater is also transported westward by the northern branch of the South Equatorial Current (SEC) (northern branch is nSEC in Figure 2.1c,f) (described in Stramma and Schott (1999)), present throughout the year (Figure 2.1). It is located immediately south of the eastward moving NECC.

In February the ITCZ reaches its southernmost position around 5°S latitude (Figure 2.2a) and the salinity reduces in the equatorial Atlantic, especially in the west (Figure 2.1a, see also Figure 1 of Foltz and McPhaden (2008) and of Xie and Carton (2004)). In the southern hemisphere there exists the central branch of the SEC (cSEC in Figure 2.1c,f) (described in Figure 4 in Stramma and Schott (1999)) carrying the equatorial freshwater from east to west around 5°S . On the northern hemisphere, during winter (November-February) the evaporation is maximum north of 8°N , and easterly Trade Winds also are the strongest. Thus the increasing northeast Trade Winds and decreasing humidity northward from the equator cause the water to be saline. Sinking of the cold saline water and strong winds cause the winter-convection and deepening of MLD and ILD. The excess evaporation at the northern subtropical gyre always maintains the SMW at the gyre.

The Canary Current (CC2 in Figure 2.1c,a) situated in the northeast of the subtropical gyre carries the saline subtropical gyre water from north to south. The NEC situated around $12\text{-}20^{\circ}\text{N}$ (Figure 2.1c, having maximum speed of 0.15 m/s in summer (Arnault, 1987)) carries this saline water from the CC2 to the west (Stramma and Schott, 1999) throughout the year. These two currents form the eastern and the southern limbs of the subtropical gyre, respectively. Most of the NEC waters flow westward and feed the Guiana Current (GC1 in Figure 2.1c) and the Caribbean Current (CC1 in Figure 2.1c) (Bourlès et al., 1999a; Bourlès et al., 1999b). The GC1, along with the NBC rings, transports part of the fresh water from the Amazon, Orinoco and ITCZ into the Caribbean Sea. This freshwater is further carried by the CC1 (Figure 2.1c) in the Caribbean Sea, carried by the Loop Current (LC in Figure 2.1c) in the Gulf of Mexico and out of the Gulf of Mexico by the Florida Current (FC in Figure 2.1c) passing through the Florida Strait. By the end of winter, the freshwater on the surface reaches the farthest northern extent. Some of the mixed fresh and saline water east of the Antilles Islands travel along the Antilles Current (AC1 in Figure 2.1c) northwestward. These currents are well simulated and illustrated in Figure 2.1.

In April-May the ITCZ has its peak rainfall in the west near the Amazon mouth, while it is on its way northward again, thus completing an annual cycle (Figure 2.2b). At the equator there is the Equatorial Undercurrent (EUC in Figure 2.1e,b,d,a) moving from west to east, flanked by the branches of SEC moving east to west in the north and south. EUC is seen in the simulation as well but not so prominent in Figure 2.1,

as this current has its highest intensity only below 20 m depth. Also, the southern SEC in the southern hemisphere below 10°S (not shown) feeds the western boundary North Brazil Undercurrent (NBUC) at 100-500 m depth around $11-6^{\circ}\text{S}$ with saline mid-Atlantic southern hemisphere water which later feeds the western boundary NBC at the surface (Stramma and Schott, 1999).

From comparisons with published work (Schott et al., 1998; Stramma and Schott, 1999; Fratantoni et al., 2000; Fonseca et al., 2004; Stramma et al., 2005), the major regional circulation features of the tropical north Atlantic, like the NEC, the NBC and the NECC, and the other circulation features too were seen to be well reproduced in the model. As previously shown in Biri et al. (2016), the ATL4km model simulates well the observed patterns of Atlantic eddy kinetic energy (EKE). The eddy activity related to the NBC is also realistic in the simulation, with about seven large rings being formed per year from the NBC retroflection. Comparing with previous literature (Figure 1 of Foltz and McPhaden (2008) and of Xie and Carton (2004); Figure 3 of Stramma and Schott (1999); Waliser and Gautier (1993); Foltz et al. (2004); Wang and Fu (2007)) we see that the E-P-R field is well reproduced as well. All this gives confidence in using the model to correlate the variability of barrier layers with ocean dynamical features.

Chapter 3

Observed and simulated barrier layers

In this chapter, the climatological barrier layers in the tropical Atlantic Ocean computed from the monthly and daily outputs of the ATL4km simulation are validated against and compared with the observed barrier layers.

3.1 Observational data

The observational data set EN4.2.1 at $1^\circ \times 1^\circ$ spatial resolution is used in this study. It is made available by the Met Office Hadley Centre (<https://www.metoffice.gov.uk/hadobs/>). Both the observed subsurface ocean temperature and salinity individual profiles including data quality information, and the monthly-averaged objective analyzed fields (henceforth called EN4) are used. To make correct use of the profile data, the quality control flags indicating elimination of temperature and salinity observations due to vertical stability checks, track checks and vertical outlier checks were applied. Elimination of a profile was carried out if the profile is on the altimetry quality control suspect list, the profile appears to be on land, the profile is at exactly 0° latitude and longitude, the profile is on the Argo grey list, the profile is on the EN3 reject list, if there were no background values for this profile, or if over half its levels were rejected. About 88% of the total observed profiles were available for use after elimination through quality control. Details of the quality control flags are given on the above website. Details of how the data set was constructed is provided in Good et al. (2013). The data set version with the Gouretski and Reseghetti (2010) bias correction is used in the present study.

In some comparisons, I additionally use the climatology of observed BLT (de Boyer Montégut et al., 2004), available from 1961-2008 at $2^\circ \times 2^\circ$ spatial resolution from the IFREMER/LOS Mixed Layer Depth Climatology website (<http://www.ifremer.fr/cerweb/deboyer/mld/>) (henceforth termed DeBoyer climatology).

3.2 Seasonal variability of observed and simulated BLT

In the following, the average BLT computed from monthly EN4 temperature and salinity profiles and EN4 objective analyzed fields is compared with the BLT computed from daily and monthly ATL4km output. Selected months from climatological averages are shown in Figure 3.1. In the case of the model, the number of days that a barrier layer was present in that given month is shown in the last respective panel (Figure 3.1d,h,l,p) as an average over the 9-year period. This helps to locate the places where barrier layers are of common occurrence in the model.

The northwestern tropical Atlantic is the region with largest barrier layer coverage existing almost throughout the year. The ATL4km simulation and the EN4 analyzed fields show similar spatial patterns in the distribution of BLT, but there are some large differences as well. Maximum spatial coverage in the northwestern tropical Atlantic occurs in February (Figure 3.1a-d) and minimum in May (Figure 3.1e-h).

Overall, EN4 has larger BLT than the simulation. Since spurious barrier layers could be generated by spatial and temporal interpolation of the sparsely available temperature and salinity profiles, the individual in situ profiles are here used to validate the BLT found in EN4 and model. BLTs computed from available Argo and CTD individual profiles of temperature and salinity show that barrier layers are a very localized phenomenon. The sparsely observed (in space and time) BLT distribution (Figure 3.1b,f,j,n) is consistent with the results from the simulation (Figure 3.1c,d,g,h,k,l,o,p) and other data sets, but not enough profiles are available for a detailed comparison for each month in the period 2003-2011. Due to the small amount of data, it is not clear if the visible discrepancy in barrier layer spatial coverage between model and the EN4 analyzed fields is due to model deficiencies or due to interpolation of in situ profiles to regions with no information. Indeed, the EN4 results should be interpreted with some care. In fact, some signals seen in EN4-derived BLT have no correspondence in the profiles that serve as basis for the objective analysis. I take therefore the EN4 results as being only illustrative rather than giving true BLT amplitudes. I conclude that the results from the profiles give a closer look at what has been observed regarding barrier layers. The results from the profiles indicate that coherence of barrier layers is less than what the EN4 analysis shows. When taking only the profiles into account, the model BLT amplitude and spatial variability seem realistic.

In February, BLT goes up to 75 m in EN4 and up to 55 m in the DeBoyer climatology (not shown) and in ATL4km. Compared to the other data sets, EN4 has a larger spatial coverage of high BLT than the simulation. The reason for this is a deeper simulated winter mixed layer compared to observations (Figure 3.2a,b), what could be attributed to unrealistic forcing or to missing/unresolved mixed layer processes in the model. During February (and in general during winter), the model generates barrier layers mostly at the Amazon mouth region and further north along the NEC and

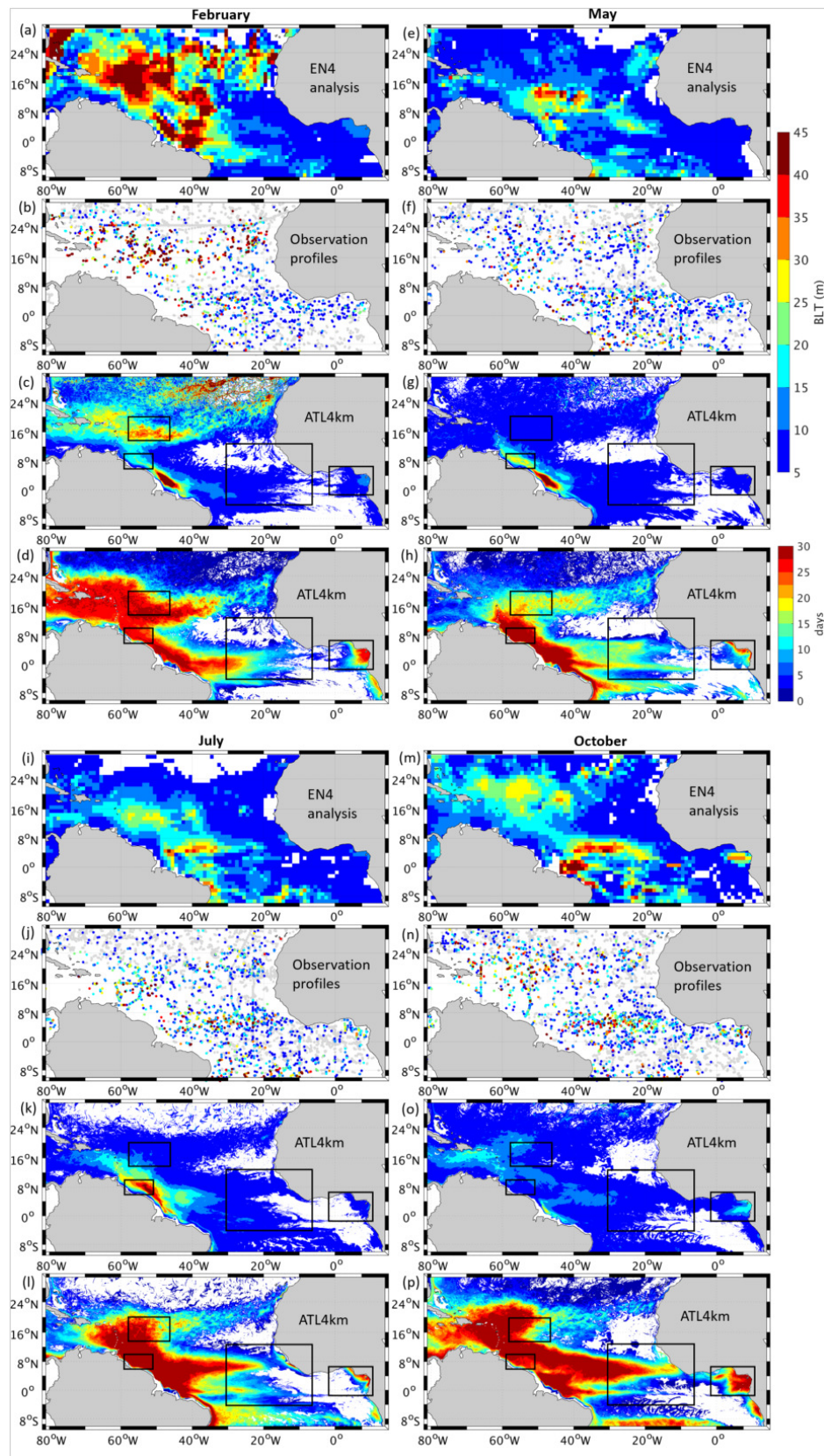


Figure 3.1: Spatial variability of BLT in February (top-left), May (top-right), July (bottom-left) and October (bottom-right) computed from monthly EN4 objective analyzed fields (a,e,i,m), in situ profiles (b,f,j,n) and ATL4km daily model output (c,g,k,o). The average number of days BLT was present in the period 2003-2011 is shown (d,h,l,p). The black boxes delimit the areas of large BLT studied in the present work: NBC-box (6-10°N, 51-59°W), NEC-box (14-20°N, 46-58°W), ITCZ-box (4°S-13°N, 6-30°W) and ETA-box (1°S-7°N, 11°E-1°W).

AC1 (Figure 3.1c) (currents denoted in Figure 2.1 in Chapter 2). The reasons for the growth and decay of those latter barrier layers (northern black NEC-box) are explored in section 4.4 of Chapter 4. Between the two regions, there is a stripe of moderately large BLT (southern black NBC-box), which the model shows to be supported by the presence of NBC eddies. That BLT signal is investigated in section 4.3 of Chapter 4. There is a comparatively smaller magnitude of BLT in the central tropical Atlantic, with a small localized region having 15 m BLT in the model and 25 m in EN4 immediately south of the equator, whose position corresponds to the ITCZ migration (central ITCZ-box). In February, 15-20 m BLT also exists at the Niger river mouth in the eastern tropical Atlantic (ETA) along the African coast in the model, EN4 and in the observation profiles (eastern black ETA-box). The formation and erosion mechanisms of the BLT in the last two regions are explored in sections 4.5 and 4.6 of Chapter 4, respectively.

In May, BLT is only up to 35 m in EN4 in the northwestern tropical Atlantic and most of the signal along the NEC and AC1 is not present. On the other hand, during May, maximum Amazon discharge near the coast gives rise to a freshwater plume there with consequent large barrier layers, as seen in the simulation. The large signal in the region adjacent to the Amazon mouth is not visible in the EN4 analysis, however, when inspecting the actual in situ profiles, large BLT is seen in the same locations as in the model simulation. The BLT there is smaller in EN4 because of a smaller ILD (Figure 3.2c,d) than the one simulated. The simulation of eddies and retroreflection captures the finer details leading to a more realistic result, which are not captured in the EN4 analysis but are captured in the in situ profiles. The ATL4km shows 10 m and EN4 shows around 20 m BLT in the central ITCZ-box, mostly also because of a larger simulated MLD, like in February. Both observations and model show very small BLT in the ETA-box in May.

During July (Figure 3.1i-l), the discharged Amazon freshwater spreads northwestward and eastward, leading to barrier layers being present, when compared to May, along eastern limb of the Amazon plume and further north to the east of the smaller Antilles and in the NBC-box. This is due to the presence of the NECC, bringing the Amazon low salinity water into the ocean interior, and the NBC transporting freshwater northwestward. The model reproduces this tendency seen in the observations. The model presents still a strong BLT signal offshore of the Amazon mouth (6-10°N, 51-59°W NBC-box), not seen in the EN4 analysis, the reason being, same as described for May, a larger simulated ILD (Figure 3.2e,f). However, there are a few profiles with barrier layers in that region during the months of May and July (Figure 3.1,f,j). The small BLT in the central tropical Atlantic shifts more north in July, captured in the model, as the ITCZ moves further north from May. The BLT in the ETA in July is not very different from that in May.

In October, the BLT distribution from the EN4 analysis resembles still the one in July, with a further intensification along the NECC and the emergence of large BLT

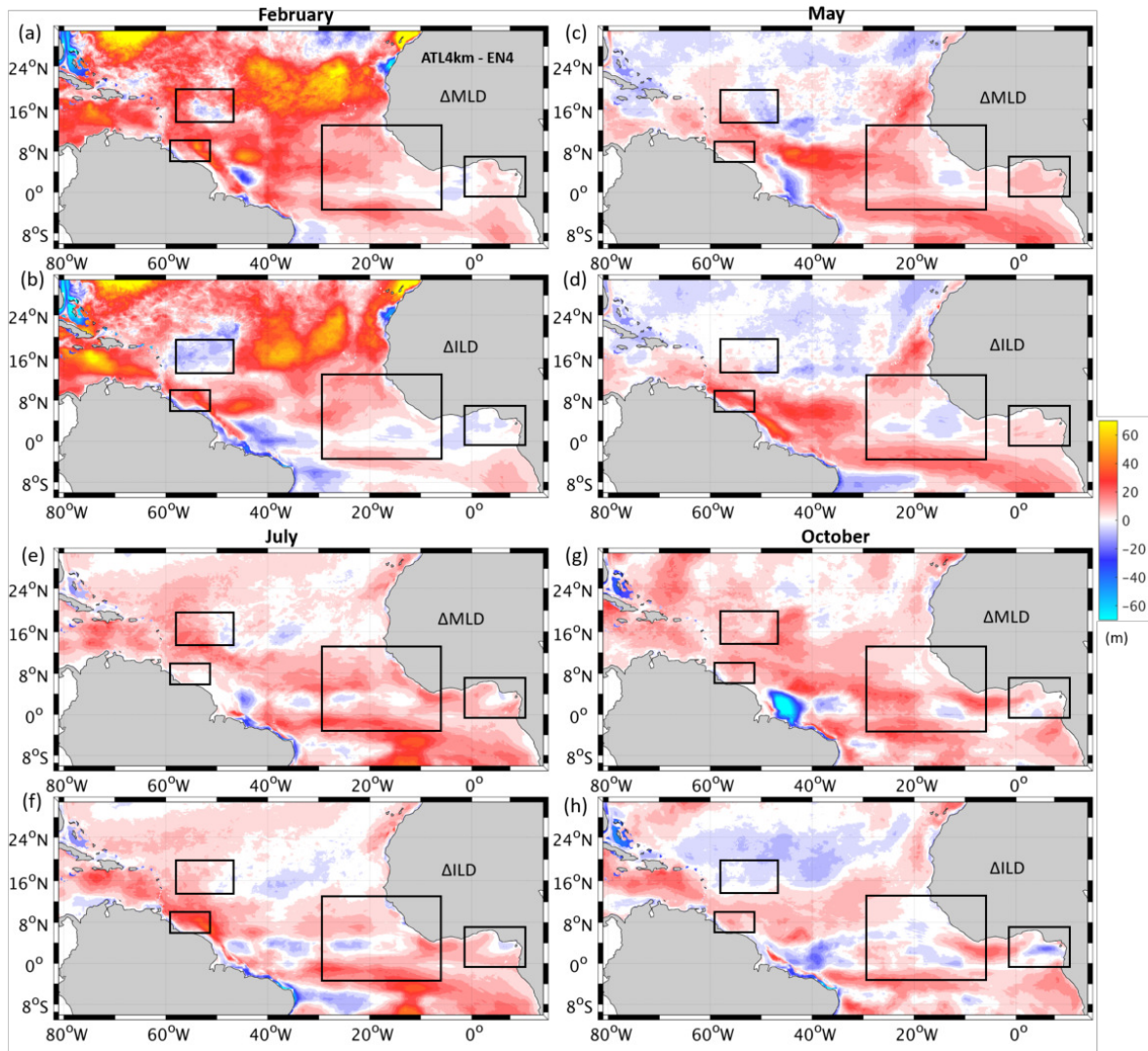


Figure 3.2: Spatial variability of the difference in MLD (a,c,e,g) and ILD (b,d,f,h) between ATL4km and EN4 in February (top-left), May (top-right), July (bottom-left) and October (bottom-right).

north of 16°N , a region which is gaining importance towards winter. The model BLT distribution for October shows the largest amplitude discrepancy compared with EN4 profiles, with the model underestimating the observed BLT. Still, a tendency is seen towards increasing BLT in the northern NEC-box. This discrepancy is attributable again to the larger simulated MLD (Figure 3.2g,h). In the ITCZ-box, the BLT in the simulation and in the observations are similar to their patterns in July, but are larger along the western coast of Africa. At the Niger river plume, October (and autumn in general) has the largest seasonal BLT of this region, with 35 m in EN4 and comparatively smaller in the model.

The model provides, however, more details than the observations about the spatial variability of barrier layers. Judging by the number of days per month with barrier lay-

ers (Figure 3.1d,h,l,p), it is concluded that barrier layer formation is a common feature, albeit most of the times with small amplitudes. In those frequency distributions, it is seen how the winter (February) barrier layers are frequent in the Lesser and Greater Antilles regions and how they extend along the NEC, along the equator, and in the Niger river plume. In May, the equatorial and off-equatorial currents show barrier layer formation, with the NEC and ETA regions losing importance. In summer (July), the large impact of the NECC and of NBC eddies (more on this in section 4.3 of Chapter 4) is seen, making barrier layers frequent at NBC-box, along NECC and east of the Lesser Antilles. These tendencies continue through the autumn (October), until the NEC region starts to develop large BLT again. Barrier layers are frequent along the African coast in the central ITCZ-box in July, which increase in autumn. The ETA-box near the Niger plume has a large frequency of occurrence of barrier layers in autumn.

As seen in the simulation, barrier layer formation is a highly variable phenomenon, sometimes made up of sporadic events. Therefore, an average over the whole time series is not a good indicator of typical BLT magnitudes, since a barrier layer absence will locally bias the mean BLT estimate towards zero. In Figure 3.3, a time average of BLT is presented, taking into account only values larger than two standard deviations of the local time series. The regions where large barrier layers form are now more visible. In all months except October, the model forms large barrier layers in the region immediately adjacent to the Amazon mouth. In February there are large barrier layers occurring to the north of 12°N (Figure 3.3a), but only around 16°N are they often forming (Figure 3.3b). In May large BLT (>25 m) is mostly confined to the South American coast (Figure 3.3c). In July, the region of large BLT extends towards the Caribbean Sea and to the east along the NECC (Figure 3.3e). The frequency of occurrence plot for July illustrates in particular the latter extension (Figure 3.3f). During October, the Caribbean Sea remains with large BLT and the NECC region fades compared to July (Figure 3.3g). The pattern of occurrence in October shows a shift to the north, but corresponds to only more moderate barrier layers (Figure 3.3h). It can be also noticed that the southern NBC-box area indeed shows large barrier layers most of the year; however they are only present less than 15 days in an average month. The localized barrier layers in the central tropical Atlantic ITCZ-box are well captured in all the months, the frequency of occurrence of those barrier layers being less than 15 days. In the Niger plume region the frequency of occurrence and the large magnitude BLT (up to 30 m) patterns correspond to each other, both being large in October and February. The overall BLT magnitude in the central and eastern regions are smaller than in the western tropical Atlantic. Comparing with Figure 3.1, the BLT values in Figure 3.3 better approach the ones from observations, probably suggesting that a large undersampling is present in the observational estimate.

Four localized regions in the tropical Atlantic were identified, which have large BLT peaking in different months. These are enclosed in the four boxes in Figures 3.1, Figures 3.2 and 3.3 and will be further discussed in this work. In the northern NEC-box ($14\text{-}20^{\circ}\text{N}$, $46\text{-}58^{\circ}\text{W}$) BLT is large in the months December-March, with largest

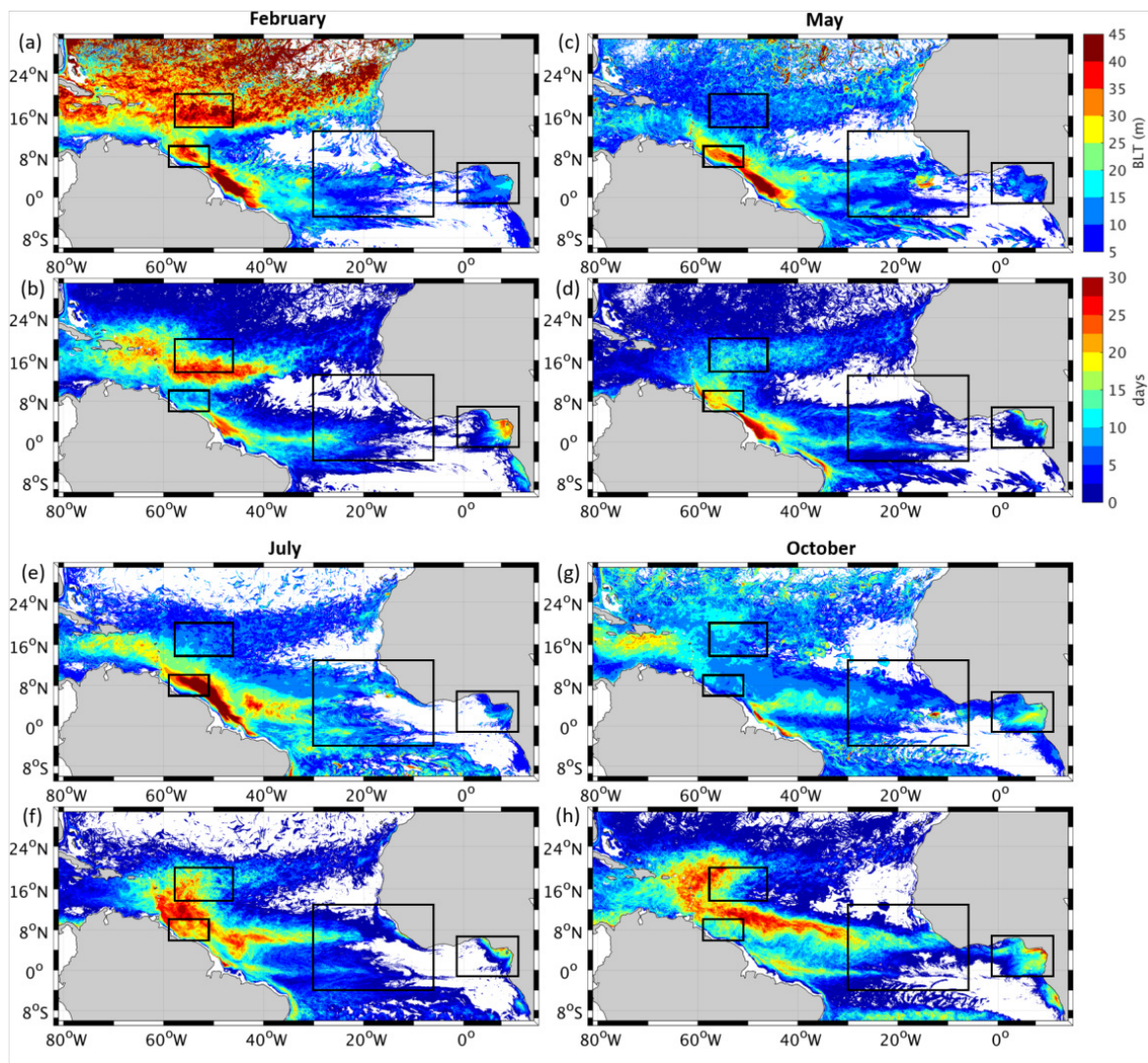


Figure 3.3: Spatial variability of the largest simulated BLT (average over values of the BLT larger than 2 standard deviations) in (a) February (top-left), (c) May (top-right), (e) July (bottom-left) and (g) October (bottom-right). The corresponding average number of days in the period 2003-2011 is shown in (b,d,f,h).

spatial coverage and magnitude in February-early March (Figure 3.3a,b), and weak in the months May-September, with the smallest spatial coverage and magnitude in May (Figure 3.3c,d). In the NBC-box ($6-10^{\circ}\text{N}$, $51-59^{\circ}\text{W}$), BLT peaks in June-July (Figure 3.3e,f) decreasing towards October. During winter and spring BLT in the NBC-box is still large, but more sporadic. The ITCZ-box ($4^{\circ}\text{S}-13^{\circ}\text{N}$, $6-30^{\circ}\text{W}$) which is the largest, encompasses all the localized short-lived barrier layers in the central tropical Atlantic, whose occurrences are seen to follow the ITCZ. The BLT there peaks in different months in different locations, with the maximum spatial extent and occurrence around 8°N in summer-autumn (Figure 3.3e-h). The peak in BLT moves to the south until end of winter and again to the north in spring-summer. In the ETA-box ($1^{\circ}\text{S}-7^{\circ}\text{N}$, $11^{\circ}\text{E}-1^{\circ}\text{W}$) covering the Niger plume, the largest annual spatial extent and magnitude

is in September-October, and again in February, while the spatial extent is the smallest in July and the magnitude is the smallest in May.

The seasonal cycle of the area-averaged BLT for the NBC-box (Figure 3.4a) shows that BLT peaks in the model in the summer months of June-July, with a tendency for an overestimation when using monthly instead of daily profiles. The EN4 analysis, in contrast, shows a maximum in March decreasing towards September, completely missing the simulated summer peak BLT. The DeBoyer climatology shows an overall constant value throughout winter and spring. The EN4 profiles, on the other hand, corroborate the existence of a maximum in June (being seen in 80% of the profiles). There are however only 5 profiles in this region in June (and in general not many over the whole year), making the observational estimates rather uncertain. For this box, the seasonality and spatial distribution of BLT in the model and observations (Figures 3.1, 3.3 and 3.4) found in my results also agrees with the findings of Pailler et al. (1999) and Masson and Delecluse (2001) for the region south of 10°N , where the NBC rings and the Amazon and Orinoco river plumes are at their peak in summer.

The seasonal cycle of area-averaged BLT in the NEC region using the ATL4km, DeBoyer climatology, and EN4 analysis and profiles is presented in Figure 3.4b. In this box, there is a good agreement between all data sets in terms of temporal evolution. As was seen in the spatial comparisons, the temporal plot also shows large BLT occurring during winter months of December-March, when the EN4 analysis and profiles show larger values compared to the rest of the data sets, which in turn peak in February-March. A seasonal minimum is seen in May. The ATL4km simulation agrees well with the DeBoyer climatology but seems to underestimate the EN4 estimates. This can be partly due to the above discussed tendency to lower the estimates when complete coverage in space and time is taken into account.

Figure 3.4c shows the seasonal cycle of the area-averaged BLT for the ITCZ-box using model and observations. All the datasets show a tendency of having large BLT values in autumn-winter from September-February, while the BLT values are smaller in the rest of the year. The EN4 analysis has the largest BLT in September and a second large peak in May. The temporal variability in ATL4km agrees well with the EN4 profiles and the DeBoyer climatology, but again seems to underestimate the EN4 estimates. The ATL4km, profiles and DeBoyer climatology peak in December, followed by a second peak in September. The minimum BLT is in spring from March-April in all datasets. A large number of profiles sample this box, so some confidence in the temporal behavior is ensured.

The seasonal cycle of BLT in the model and observations for the ETA-box at the Niger river plume is shown in Figure 3.4d. A good agreement between the EN4 analysis, observation profiles, DeBoyer climatology and the ATL4km simulations can be seen in terms of temporal variations. The magnitude of BLT in ATL4km is closer to the profiles and DeBoyer climatology and is underestimated compared to EN4 analysis estimates, for the same reason stated before. The largest BLT occurs in September in

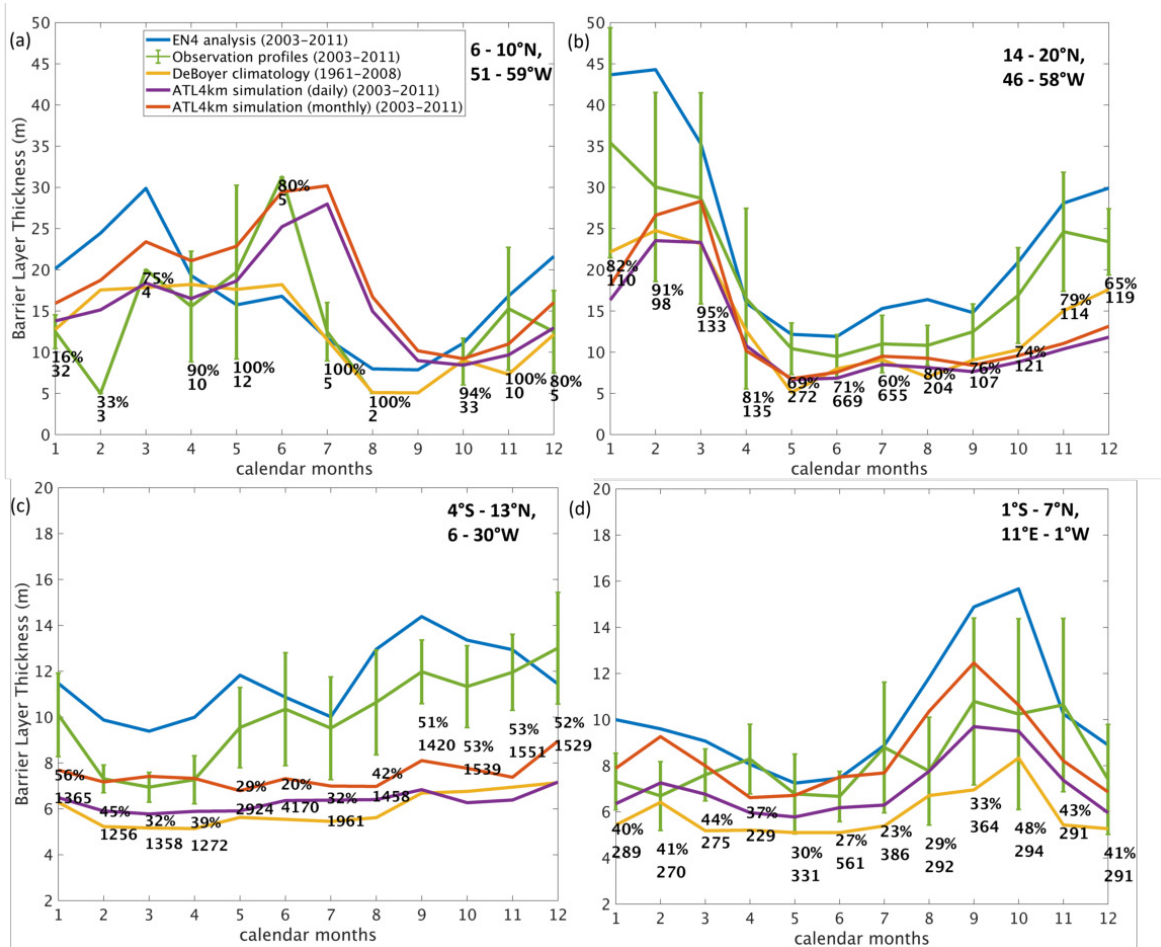


Figure 3.4: Monthly variability of area-averaged BLT in the (a) NBC-box (6-10°N, 51-59°W), (b) NEC-box (14-20°N, 46-58°W), (c) ITCZ-box (4°S-13°N, 6-30°W) and (d) ETA-box (1°S-7°N, 11°E-1°W) from EN4 objective analyzed data (2003-2011, blue), observational profiles (2003-2011, green), DeBoyer climatology (1961-2008, yellow), ATL4km daily output (2003-2011, violet) and ATL4km monthly output (2003-2011, red). The values at the bottom of the error bars represent the percentage of the number of profiles with barrier layers (top value) with respect to the total number of profiles present (bottom value) for that month in the period 2003-2011.

the simulation and in the profiles, while the BLT peaks in October in the EN4 analysis and DeBoyer climatology. The second, but smaller peak in BLT occurs in February in the simulation and DeBoyer climatology and in January in EN4 analysis. As also seen in the spatial comparisons, the BLT values in the ITCZ-box and the ETA-box are smaller compared to the two regions in the western tropical Atlantic.

In summary, BLT daily fields from ATL4km for the period 2003 to 2011 showed four distinct localized regions with barrier layers having different seasonal cycles: 1) the NBC rings area with BLT maxima in June-August, 2) the NEC region with BLT peaking during January-March, 3) the ITCZ region with BLT peaking in December and September, and 4) the Niger river plume region with BLT peaking in September-

October and February. An explanation for the seen seasonality of BLT is given in the following Chapter 4 with details on the mechanisms responsible for the growth and decay of the seasonal and short-term barrier layers at the above locations.

Chapter 4

Barrier layer growth and decay mechanisms in the tropical Atlantic Ocean

4.1 Introduction

The objective of this chapter is to detect and demarcate the growth and decay mechanisms of the localized barrier layers in four regions of the tropical Atlantic Ocean and discuss them in relation to ocean circulation features, like the regional current systems (the NBC/NECC and the NEC), and certain other local small-scale processes like eddies and fronts. The following are the four regions, each having a different seasonal cycle of barrier layers, as identified in Chapter 3:

- The region of the North Brazil Current rings (NBC-box, 6-10°N, 51-59°W)
- The region south of the subtropical gyre along the North Equatorial Current (NEC-box, 14-20°N, 46-58°W)
- The region in the central tropical Atlantic under the Intertropical Convergence Zone (ITCZ-box, 4°S-13°N, 6-30°W)
- The region encompassing the Niger river plume at the eastern tropical Atlantic (ETA-box, 1°S-7°N, 11°E-1°W)

Four sections of this chapter focus on the above four identified regions respectively, each section addressing the following specific question:

- Q. What are the mechanisms responsible for the growth and decay of the seasonal and short-term barrier layers?

The answers from each section collectively address the first primary question posed in this thesis (section 1.3 of Chapter 1): What are the mechanisms responsible for the growth and decay of barrier layers and their variabilities in the tropical Atlantic Ocean?

The histograms in Figure 4.1 show the number of occurrences in space and time, of a BLT value in the years 2003-2011 at the four identified regions in ATL4km simulation. As we see, for all the regions, it is not a standard Gaussian distribution. The minimum BLT values ranging from 5-10 m occur the maximum, the number of occurrences being $\sim 1.2 \times 10^7$ for the NBC rings region, $\sim 3.5 \times 10^7$ for the NEC-box, more than 5×10^7 for the ITCZ-box and $\sim 3 \times 10^7$ in the ETA-box. The occurrences of the small values of BLT is the maximum in the ITCZ region. The number of occurrences reduces as the BLT increases for all the regions. The large BLT of around 80 m has the least occurrence in space and time for the NBC and NEC regions. The same is observed in the ITCZ and ETA regions, but the largest values of BLT there are smaller than in NBC rings and NEC regions in the western tropical Atlantic. Therefore, in all four regions that have barrier layers in the tropical Atlantic, the large BLT amplitudes do not sustain for long periods or in large spatial extents, but they occur occasionally, as localized events. This was also visible from the spatial maps of BLT and its occurrence, seen in Figure 3.3 in Chapter 3. Thus these histograms reaffirm the fact that barrier layers have an acute nature, as they occur for a short time with large intensity and are localized. The high temporal and spatial resolution data used in this analysis thus enables a detailed study of these acute barrier layers.

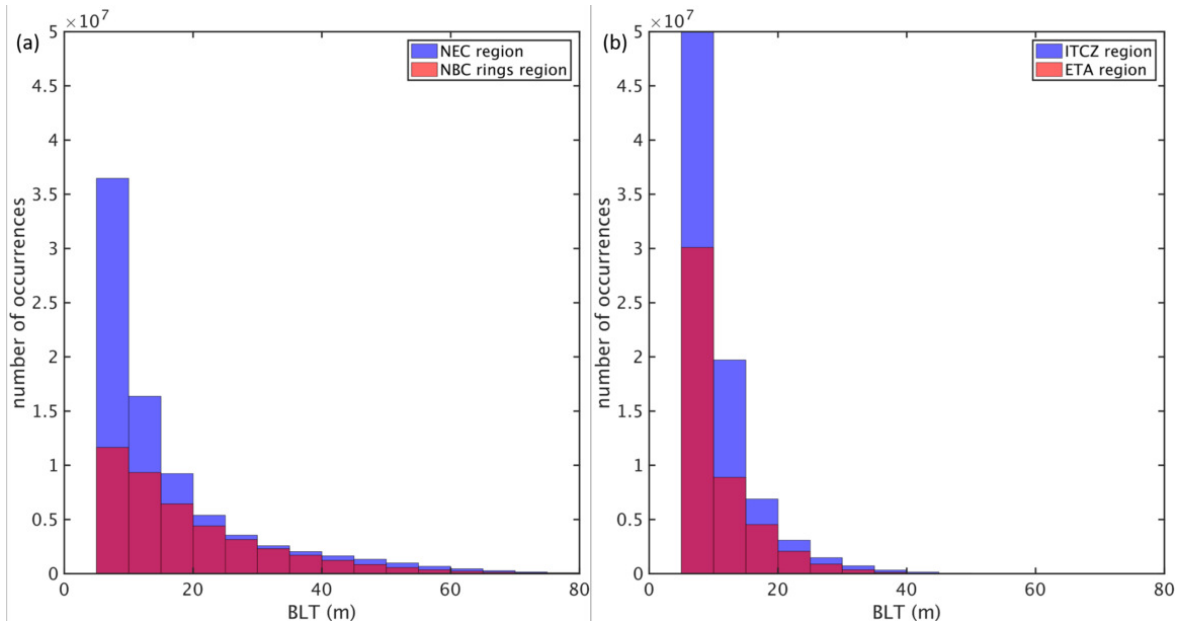


Figure 4.1: Histogram of the number of occurrences (in terms of model grid points) of BLT values (in meters) during the years 2003-2011 for (a) NBC rings and NEC regions, (b) ITCZ and ETA regions.

In order to quantify the physical mechanisms of barrier layer growth and decay, the terms of the vertical gradient of salinity and temperature balance equations (Cronin

and McPhaden, 2002) were computed with the daily outputs for the 9 year period 2003-2011 using the 4 km resolution simulation of the Atlantic Ocean (ATL4km, described in Chapter 2). The next section introduces these physical mechanisms that can be in play during the entire lifetime of a barrier layer. This chapter ends with a discussion of the similarities and differences between the results from the four regions.

4.2 Balance equations and governing mechanisms

To understand how upper-ocean salinity/temperature stratification can develop in the tropical Atlantic, I computed the terms from the balance equations derived by Cronin and McPhaden (2002), using salinity, temperature, and the zonal, meridional and vertical components of velocity from daily-averaged ATL4km model output. To study the growth and decay processes of upper ocean stratification and therefore of BLT, it is essential to have the four-dimensional fields of the above variables. Following Cronin and McPhaden (2002), the vertical derivative of the salinity balance equation is:

$$\frac{\partial}{\partial z} \left(\frac{\partial S}{\partial t} \right) = \underbrace{-U \cdot \frac{\partial}{\partial z} (\nabla S)}_1 - \underbrace{w \frac{\partial^2 S}{\partial z^2}}_2 - \underbrace{\frac{\partial U}{\partial z} \cdot \nabla S}_3 - \underbrace{\frac{\partial w}{\partial z} \frac{\partial S}{\partial z}}_4 - \underbrace{\frac{\partial^2 (\overline{w'S'})}{\partial z^2}}_5. \quad (4.1)$$

The vertical derivative of the temperature balance equation is:

$$\frac{\partial}{\partial z} \left(\frac{\partial T}{\partial t} \right) = \underbrace{-U \cdot \frac{\partial}{\partial z} (\nabla T)}_1 - \underbrace{w \frac{\partial^2 T}{\partial z^2}}_2 - \underbrace{\frac{\partial U}{\partial z} \cdot \nabla T}_3 - \underbrace{\frac{\partial w}{\partial z} \frac{\partial T}{\partial z}}_4 - \underbrace{\frac{\partial^2 (\overline{w'T'})}{\partial z^2}}_5 + \underbrace{\frac{1}{\rho c_p} \frac{\partial^2 Q_{rad}}{\partial z^2}}_6. \quad (4.2)$$

In the above equations, S is salinity, T is temperature, $U = (u, v)$ is the horizontal velocity, w is the vertical velocity, z is depth and $\overline{w'S'}$ and $\overline{w'T'}$ are the vertical turbulent fluxes of salinity and temperature, respectively. At the air-sea interface ($z = 0$) the turbulent salinity flux depends on the surface freshwater forcing by precipitation (P), evaporation (E) and river runoff (R):

$$\overline{w'S'} \big|_{z=0} = S_0(P - E + R) \quad (4.3)$$

where S_0 is the surface salinity. The surface forcing is thus contained in the turbulent mixing component (term 5 in the right hand side (RHS) of Eq. 4.1). In Eq. 4.2, ρc_p is the volumetric heat capacity, Q_{rad} is the penetrative solar radiation, and $\overline{w'T'}$ at $z = 0$ is proportional to the net surface heat flux reduced by the solar radiation at the surface.

Each term in the RHS of each balance equation corresponds to a physical mechanism.

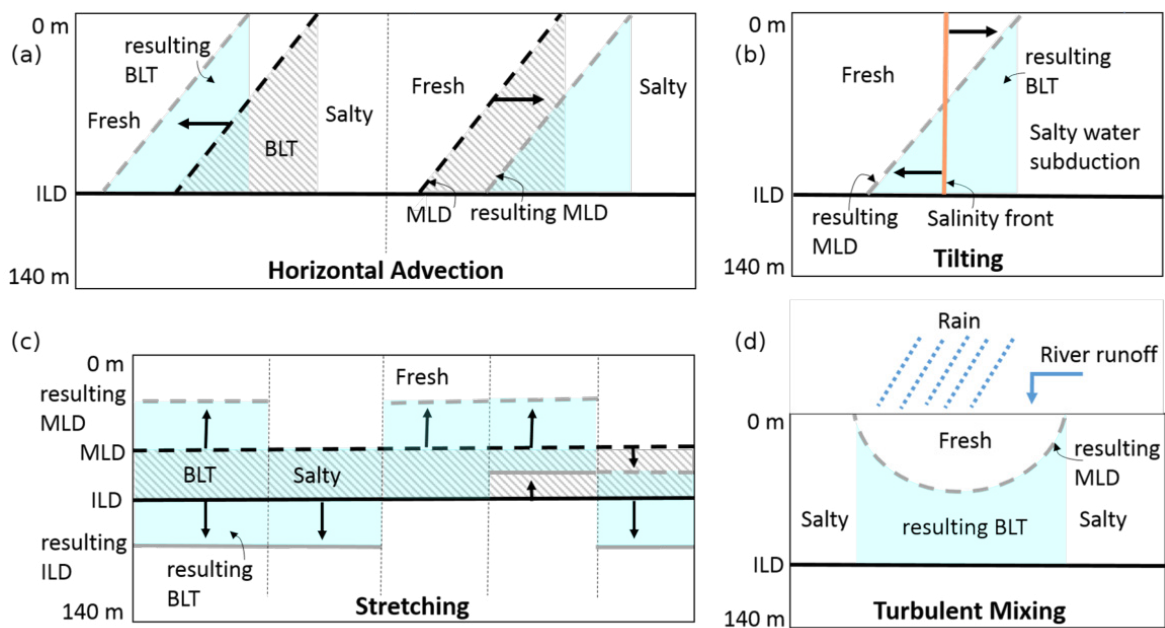


Figure 4.2: Schematics of (a) horizontal advection, (b) tilting, (c) stretching and (d) turbulent mixing, the mechanisms responsible for barrier layer formation and growth. The black and grey dashed lines are, respectively, the initial and the resulting mixed layer depth (MLD). The black and grey solid lines depict, respectively, the initial and the resulting isothermal layer depth (ILD). Hatched regions are the initial barrier layers and the blue shaded regions depict the resulting barrier layers. Adapted and expanded from Cronin and McPhaden (2002).

Term 1 - Horizontal Advection: Term 1 is the contribution to the tendency (either of salinity or temperature stratification) from horizontal advection. If favorable T/S conditions are advected leading to a "translation" of the MLD with constant ILD, a local change will be noticed by a thickening of the barrier layer in the flow direction (Figure 4.2a).

Term 2 - Vertical Advection: This occurs when the vertical velocity is uniform in the upper ocean. Vertical velocity acting uniformly on both the MLD and ILD will cause the barrier layer to shift vertically, with no change in BLT. Thus this term is not implicated in the formation/evolution of barrier layers.

Term 3 - Tilting: A barrier layer can form and grow when a vertically sheared horizontal flow advects a horizontal salinity gradient within the isothermal surface layer. This causes near-vertical isohalines to tilt into the horizontal, thus forming a shallow mixed layer on top of the ILD (Figure 4.2b).

Term 4 - Stretching: If the vertical velocity acts non-uniformly on the MLD and ILD surfaces, then the barrier layer can grow through vertical stretching. There could be five possibilities for a barrier layer to grow due to stretching as shown in Figure 4.2c. Stretching could happen when there are two opposite vertical velocities pulling MLD and ILD apart, when the vertical velocity acts downward only on ILD or upward only

on MLD while the other surface stays stable with no change, and when there is vertical velocity in one direction but weaker on one surface and larger on the other.

Term 5 - Turbulent Mixing: Rainfall (and/or river discharge) in the absence of strong turbulent mixing and surface heating, can cause a barrier layer to form between the base of the rainwater puddle (fresh lens) and top of the ILD (Figure 4.2d).

The above four mechanisms lead to the formation and growth of barrier layers. These barrier layers decay when the same above mechanisms act in an opposite manner. Therefore, the T/S conditions forming a barrier layer can be advected away from a location and the T/S conditions unfavorable for the existence of barrier layers can be advected to that place. The tilting of a strong vertical salinity gradient (a horizontal front) that exists in presence of barrier layer can get tilted to form a horizontal salinity gradient (i.e. tilted into a vertical front) thus decaying the barrier layer. The vertical velocities shown in the five cases of stretching in Figure 4.2c act in opposite directions (in all five cases) and magnitudes (in the cases when the different magnitudes of velocities act on both the surfaces, two right-most cases in Figure 4.2c) in order to decay the BLT. A strong turbulent mixing of saline and cold water from greater depths can destroy the BLT and turbulent mixing of warm water on the surface can also destroy the BLT. Thus these are the ways in which the mechanisms act when the barrier layer decays or is destroyed.

Area-averages of simulated BLT were computed in the four regions identified before: 1) the area where NBC rings form and propagate (NBC-box, 6-10°N, 51-59°W), 2) the region south of the subtropical gyre along the NEC (NEC-box, 14-20°N, 46-58°W), 3) the region under the ITCZ (ITCZ-box, 4°S-13°N, 6-30°W), and finally 4) the region encompassing the Niger river plume at the eastern tropical Atlantic (ETA-box, 1°S-7°N, 11°E-1°W). The events showing a strong peak in the resulting daily time series were chosen and the mechanisms contributing to the growth and decay of each of those barrier layers were examined in detail. To study the relation between barrier layers and NBC rings, the NBC rings were identified in the daily model output with the help of the Okubo-Weiss parameter (Isern-Fontanet et al., 2004; Chelton et al., 2011).

For every region and for each event, an average of T/S properties and of the balance terms were taken over a period of a few days before the event and compared with those at the time of peak BLT to understand the formation/thickening of the barrier layers. Conversely, averages over a few days after the peak BLT were used to understand the barrier layer destruction/thinning. In the region of NBC rings and for each event, an average of T/S properties and of the balance terms over a period of 3 days before and after the day of peak BLT was performed. For the events in the other regions, the same procedure was conducted, averaging over periods of 3 to 5 days before and after the day showing the peak BLT. The number of days averaged over, were chosen depending on the evolution of the daily BLT in each of the events.

The salinity and temperature vertical gradients ($\frac{\partial S}{\partial z}$, $\frac{\partial T}{\partial z}$) were examined along with the behavior of the isohalines and isotherms. The relative contribution of salinity and temperature to stratification was found by decomposing the squared Brunt-Väisälä frequency (N^2) as a sum of haline (N_S^2) and thermal (N_T^2) contributions, i.e., $N^2 = N_S^2 + N_T^2 \equiv -\frac{g}{\rho} \frac{\partial \rho}{\partial z} = -g\beta \frac{\partial S}{\partial z} + g\alpha \frac{\partial T}{\partial z}$, where β is the haline contraction coefficient, α is the thermal expansion coefficient, g is acceleration due to gravity and ρ is density (Maes and O’Kane, 2014).

In the following sections we look into each of the four identified regions having barrier layers in the tropical Atlantic individually.

4.3 Barrier layer in the NBC rings region

The regional circulation in the western tropical Atlantic is dominated by the NBC, an intense western boundary current. The maximum Amazon discharge during May-June and Orinoco discharge during July-August (Masson and Delecluse, 2001; Silva et al., 2005; Fournier et al., 2017; Varona et al., 2019) cause a surface plume of freshwater which spreads northwestward due to the NBC and associated rings, not just during the months of maximum river discharge, but all year round. Previous studies have shed some light on the advection of the Amazon/Orinoco freshwater and their interaction with the seasonally varying NBC and NBC rings (Fratantoni and Glickson, 2002; Ffield, 2007; Fournier et al., 2017). This interplay between river runoff and surface ocean dynamics cause the emergence of variability in barrier layer formation associated with the NBC rings, which is the topic explored in this section. The relation between BLT and NBC rings has never been, to my knowledge, studied in detail, though barrier layers have been observed in a Caribbean Sea eddy in September 2014, suspected to originate from the NBC (Rudzin et al., 2017) and in another eddy in February 2018 also in the Caribbean Sea (van der Boog et al., 2019). In the latter case, the surface water in the eddy is suggested to originate from the Orinoco River.

Figure 4.3, is a Hovmöller diagram at 51°W longitude, of the Okubo-Weiss parameter. NBC eddies can be identified as for them the Okubo-Weiss parameter is negative. All the NBC rings pass through this section at a given time in their lifespan. The NBC rings were tracked, with the daily fields of the Okubo-Weiss parameter and relative vorticity, according to a negative Okubo-Weiss parameter and positive relative vorticity criteria. An instantaneous view of the existing rings on 17th June 2005 is presented in Figure 4.4a, which shows a mask defining the eddies computed based on the values of the Okubo-Weiss parameter and of the relative vorticity. North of 5°N the NBC breaks down into NBC rings, mainly forming around 6-9°N. Table 4.1 shows the number of eddies generated every month in these 9 years and the total number of eddies every year. It was seen that an average of six large NBC rings (out of which 3-4 are largest) plus a few smaller rings in a total of 7-9 eddies form every year in the model

in the period 2003-2011, a total of 75 rings in 9 simulated years (Table 4.1 and noticeable also in Figure 4.3). NBC rings have been characterized earlier with observations (Fratantoni and Glickson, 2002; Fratantoni and Richardson, 2006; Schiller and Smith, 2018) and simulations (Jochum and Malanotte-Rizzoli, 2003). They have a diameter ranging from 100-500 km and form throughout the year. Most of the rings last for 2-4 months and travel along a "corridor" offshore the south American coast, reaching up to 13-15°N, with some surviving up to 18°N (Figure 4.4). In the simulated 9 years, the studied box encloses the region where the passage of NBC rings is more frequent, namely over one third of the time, as can be seen by the "heat" map in Figure 4.4b.

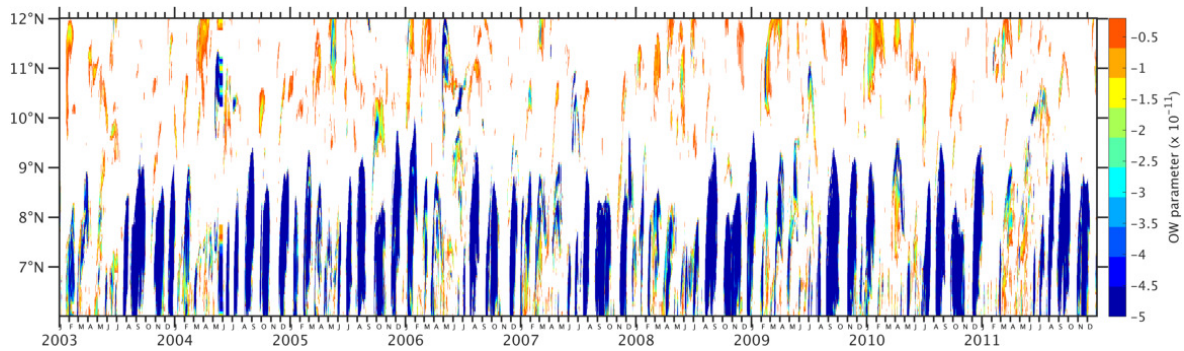


Figure 4.3: Hovmöller diagram of Okubo-Weiss parameter (s^{-2}) showing the NBC rings passing through $51^{\circ}W$ in the years 2003-2011.

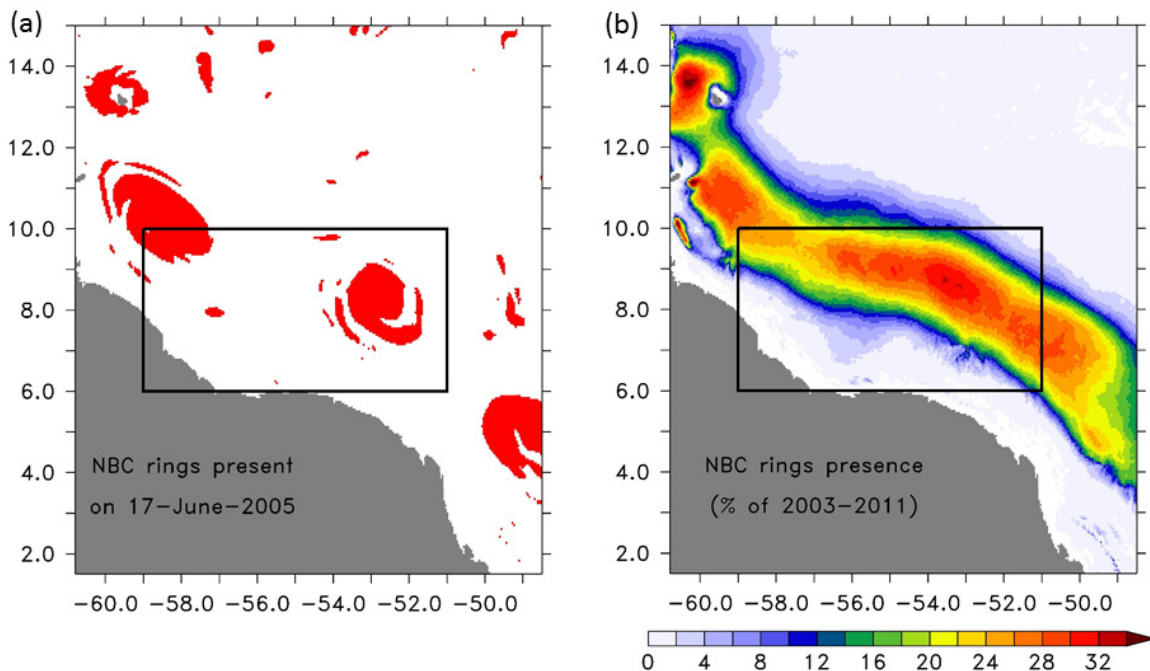


Figure 4.4: (a) Simulated NBC rings shown as an instantaneous mask, defined using a criteria which uses the Okubo-Weiss parameter and relative vorticity. (b) Percentage of the nine years (2003-2011) when NBC rings are present. The black box encloses the studied NBC rings region ($6-10^{\circ}N$, $51-59^{\circ}W$).

Months	2003	2004	2005	2006	2007	2008	2009	2010	2011
Jan	1				1	1			
Feb		1	1	1		1			1
Mar	1		1	1	1		2	1	
Apr		1	1			1		1	2
May	1	1	1	1	1	1	1		
Jun	2	2	1	2	1	1		1	1
Jul	1	1	1	1	1	1	2	2	2
Aug	1		1	1	1	1	1		1
Sep		1				1		1	
Oct	1	1			1		1		1
Nov			1	1		1		1	
Dec	1	1	1				1		1
Total	9	9	9	8	7	9	8	7	9

Table 4.1: Monthly generation of NBC rings in 2003-2011

Daily area-averaged ILD, MLD and BLT for the NBC-box ($6-10^{\circ}\text{N}$, $51-59^{\circ}\text{W}$) are shown in Figure 4.5. Large BLT is found from May to August, being thickest in late June-July (blue curve in Figure 4.5). All the events enclosed in circles are cases when there is a barrier layer present in NBC rings. The green circles depict rings formed in winter or spring, when the NBC retroflection is further to the northwest, and the red circles correspond to rings generated in summer, when the retroflection into the NECC is more pronounced. A total of 22 NBC rings had the thickest barrier layers in summer and 10 NBC rings had large BLT in late winter-spring.

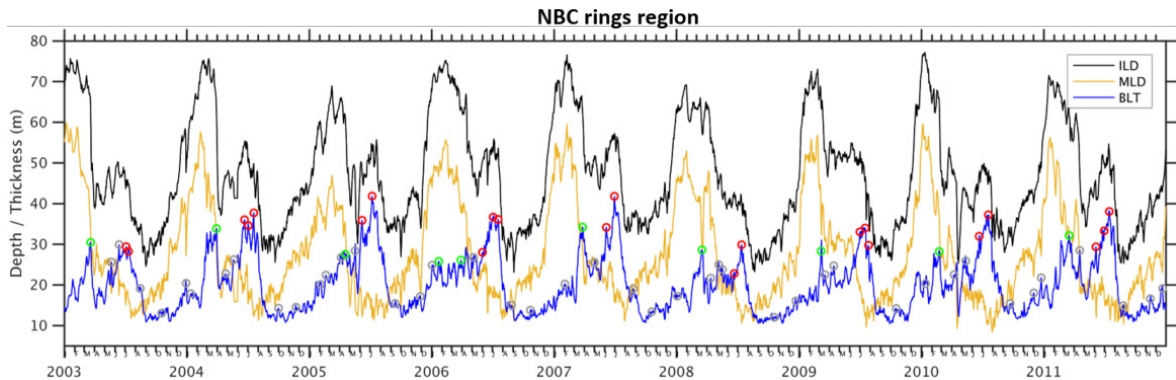


Figure 4.5: Daily time series of area-averaged ILD (black), MLD (yellow) and BLT (blue) (in meters) in the region of NBC rings ($6-10^{\circ}\text{N}$, $51-59^{\circ}\text{W}$). Red circles depict events when the eddies have large summer BLT; green circles show events when the eddies have large winter BLT; grey circles correspond to the remaining eddies which have significant BLT.

Investigation of the mechanisms behind the growth and decay of barrier layers in this NBC rings region will be conducted separately for the seasonal cycle and for the

extreme isolated events, since they have different reasons for growth and decay. So, before we take a look at those events marked with circles in Figure 4.5, we will first focus on the seasonal evolution, over which the events are superimposed.

4.3.1 Seasonal evolution

Figure 4.5 shows that the ILD and MLD have a maximum every winter. The ILD and MLD are largest during this time due to the well known winter convective mixing in the upper ocean, when the cool, saline and dense water on the surface sinks and when there is mixing in the upper layer due to intense wind stirring caused by strong Trade Winds, as shown by Foltz et al. (2004) and Foltz and McPhaden (2008).

Typical in summer are shallow mixed and isothermal layers due to higher surface temperatures than in winter. The MLD is shallow in summer also because of the large freshwater outflow from the rivers in May-July and the high transport and spreading of this freshwater by the NBC and its rings in July. The MLD remains shallow until October, as the surface water still remains fresher due to the plume water, and MLD starts increasing only after November. But the deepening of the ILD from May to August in spite of the warm water at the surface is a peculiarity seen in this region (black line in Figure 4.5). A deeper ILD and a shallow MLD are both responsible for the BLT being large during that period of the year, but to a certain extent the magnitude of BLT is determined by the deepening of ILD from May to August. In winter the BLT is small in this NBC-box, having a few peaks every year in winter (total 10 peaks encircled in green in Figure 4.5).

Since this box is populated by NBC rings, the first question to answer is if the seasonal behavior in the box seen in Figure 4.5 is imposed by what is happening in the core of the rings, or if on the other hand, the rings are acquiring the seasonal evolution of ILD and MLD from their periphery, i.e., from the large-scale seasonal evolution of temperature and salinity. To that end, the eddies were tracked according to a negative Okubo-Weiss parameter and positive relative vorticity criteria. With those quantities, a mask was produced isolating the core of the eddies, as previously shown in Figure 4.4. On the basis of the mask, the eddies were tracked. Averaging now over only the cores of the NBC rings, the same behavior as in Figure 4.5 was seen (not shown).

Most of the times a barrier layer is created near the Amazon/Orinoco shelf break due to tilting of the strong salinity fronts created at the plume edge, as the freshwater immediately comes in contact with the saline ocean water (Silva et al., 2005), also shown by the daily fields of the budget terms. Daily distributions of BLT from 2003-2011 in the ATL4km simulation show that the NBC rings transport the conditions for barrier layer maintenance, which are formed near the Amazon/Orinoco shelf break. But the barrier layers can also newly form within NBC rings themselves, when the ring starts to generate, as we will see next. The barrier layers in the NBC rings erode

away as the rings dissipate, sometimes in the Caribbean Sea, and sometimes east of the Lesser Antilles after interacting with the chain of islands.

The time series of ILD, MLD and BLT (obtained by taking area-average of ILD, MLD and BLT in the core) of the tracked NBC rings were detrended. There is a positive linear relation between MLD and ILD within the cores of NBC rings generated throughout the year except for summer (Figure 4.6b). All the eddies generated in June and July (marked with red circles in Figure 4.5) do not show any significant linear relation (Figure 4.6a). This is because during that time, there is an increase in ILD inside the eddy (as also seen in Figure 4.5, reason for which we see ahead), while the MLD remains nearly constant.

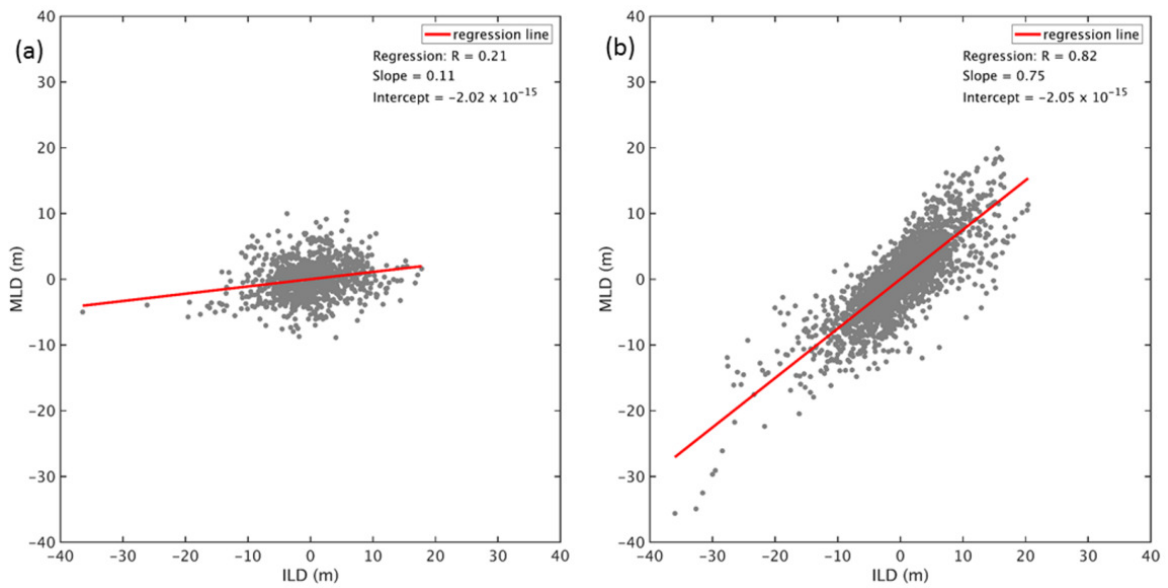


Figure 4.6: Relation of ILD and MLD in NBC eddy cores: (a) eddies generated in June-July (marked with red circles in Figure 4.5) and (b) all other eddies except those in (a) (marked with grey and green circles in Figure 4.5).

There is a good positive linear relation between BLT and ILD (Figure 4.7a) within the cores of NBC rings generated from April (when the ILD reduces and BLT also is small in those eddies) to July when the ILD and BLT both are large. In August and September there tends to be a slight positive linear relation between BLT and ILD, but with a very small positive slope, as the BLT is small all the time in those months (Figure 4.7b). Thus, a positive linear relation is seen in late-spring to summer and for the 6 months in autumn-winter no linear relation exists between BLT and ILD. Subsequently, in the eddies marked in red in Figure 4.5 there is a positive linear relation, and in the eddies marked in green no relation exists between BLT and ILD.

There is a good inverse linear relation between BLT and MLD in winter in the NBC rings in January, February and early March (Figure 4.7c). These are the eddies marked in green in Figure 4.5. The barrier layers in the winter NBC rings are therefore

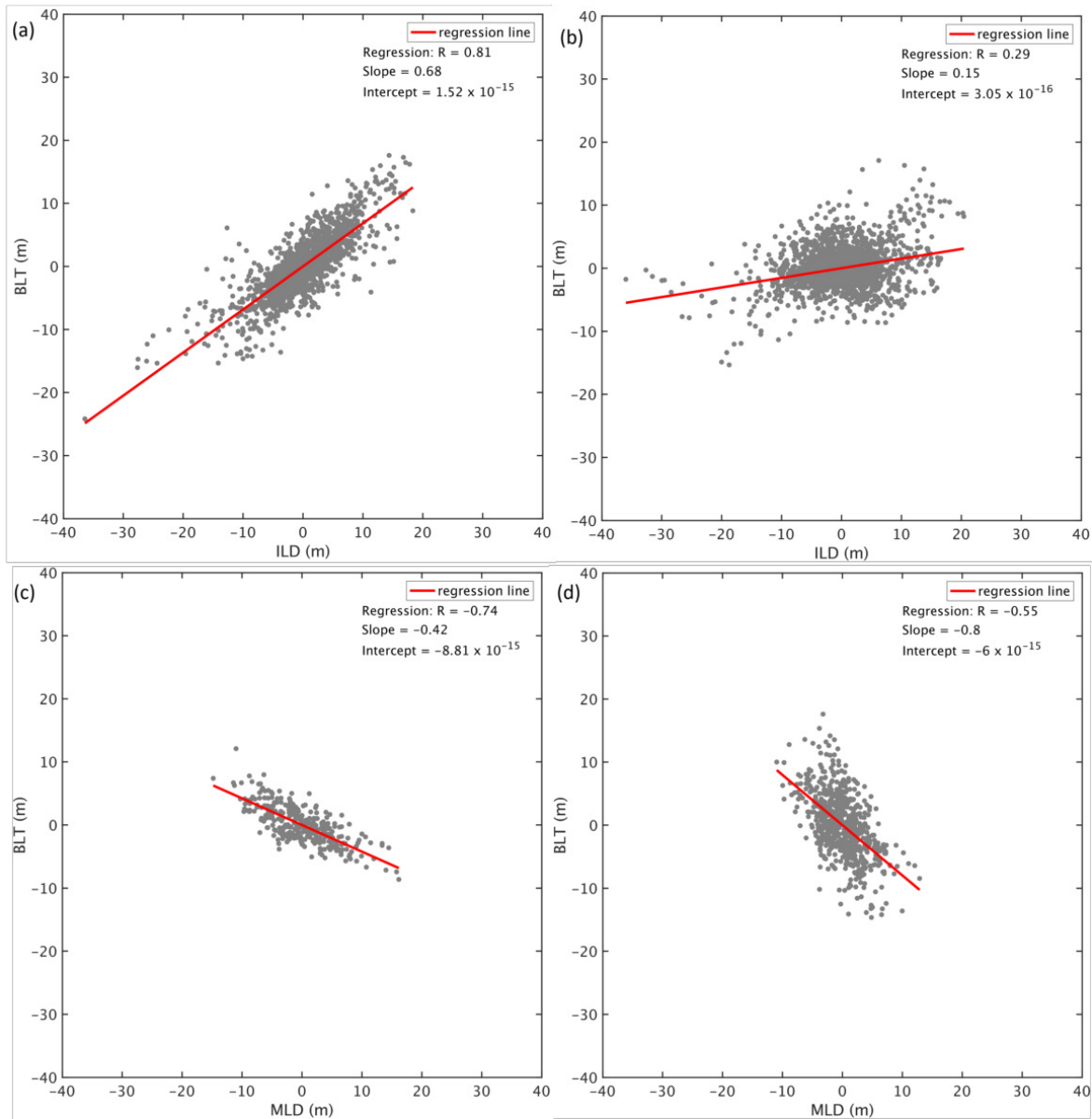


Figure 4.7: Relation of BLT and ILD in cores of NBC rings generated in: (a) April-July, (b) August-March. Relation of BLT and MLD in cores of NBC rings generated in: (c) January-early March and (d) May-July.

dependent more on the MLD than ILD. There is an inverse relation between BLT and MLD also in a few eddies during summer during May-July (Figure 4.7d, red circles in Figure 4.5) when there is a large change in BLT, but very small change in MLD, thus suggesting that the summer barrier layers in the NBC rings are more dependent on ILD. In the rest of the year the BLT changes are small, and MLD changes comparatively larger, giving a negative linear relation with a very small slope.

In conclusion, we see that in the NBC rings the BLT is more determined by ILD in summer (red circles), and more determined by MLD in winter (green in Figure 4.5). In the rest of the year the BLT and its variations are small, since both MLD and ILD

have a positive linear relation.

In order to check if the seasonal evolution in ILD, MLD and BLT between the core of the NBC rings and their periphery differs, a climatology of the area-average of these quantities over the core and only over the periphery were computed separately. Again no significant difference in the seasonal evolution was seen, meaning that the cores of the eddies mainly acquire the seasonal conditions for the development of the barrier layers from the background where they are embedded. Figure 4.8 shows the seasonal evolution of the ILD, MLD and BLT at the eddy cores, i.e., in regions following the eddy translation. Two regions are shown, one more to the east, closer to the generation region ($51\text{-}56^\circ\text{W}$, $7\text{-}13^\circ\text{N}$, Figure 4.8b) and one in the west, the region where the eddies are matured and dissipate ($56\text{-}61^\circ\text{W}$, $7\text{-}13^\circ\text{N}$, Figure 4.8a).

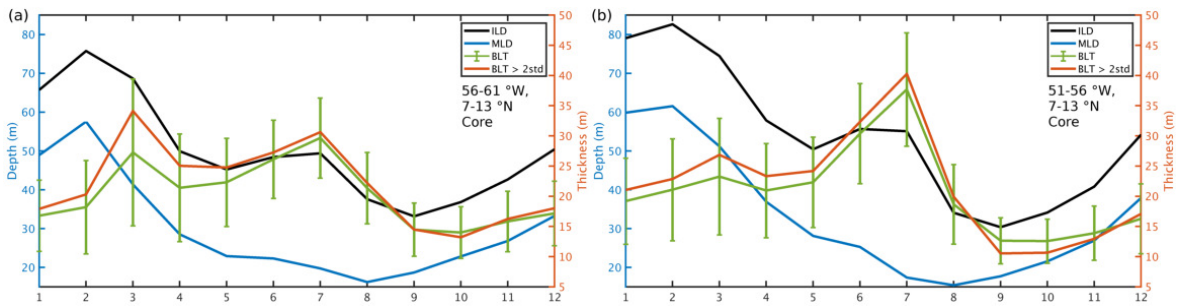


Figure 4.8: Monthly variability of area-averaged ILD, MLD and BLT (meters) for eddy cores in the two regions (a) $56\text{-}61^\circ\text{W}$, $7\text{-}13^\circ\text{N}$ and (b) $51\text{-}56^\circ\text{W}$, $7\text{-}13^\circ\text{N}$, respectively.

The eddy cores in the east box have the deepest winter MLD and ILD in February, however the BLT curve in March is much smaller than that further downstream in the west. In May-June the MLD remains almost constant and the ILD increases, causing a second peak BLT in July. In the east, the July peak is more pronounced than the March relative maximum. In the west, instead, the late winter peak is larger or comparable to the summer one. This reveals that the eddies experience different conditions as they travel downstream to the northwest. The difference seems to be attributable to the March MLD, which in the west decreases faster than in the east. The ILD and MLD get shallow in August-September and start increasing again from October onwards. The BLT remains small in the core during those autumn and early winter months. This also explains the above scatter plots. In the periphery of the eddies (not shown), the ILD, MLD and BLT seasonality is the same as for the core but the magnitude of all the quantities is smaller.

Through inspection of daily fields of the zero line of meridional velocity at every model depth level, the east and west limits of the NBC were determined, with the NBC seen to extend up to about 150 m depth, beyond which depth the current becomes very faint and the NBUC emerges. Daily fields of temperature and salinity in the NBC show that the NBC carries cool ($17\text{-}25^\circ\text{C}$) and saline (> 36 psu) water from 5°S to around 6°N and northwards at depths of 50-180 m. Warmer ($> 26^\circ\text{C}$) and fresher

(34-35.5 psu) water is transported by this current starting from the Amazon mouth at 0°N , 50°W towards the northwest, at depths from surface up to 50-80 m. The time series of meridional non-recirculated freshwater transport by the NBC (Figure 4.9b) presents how much of this freshwater discharged from the Amazon and Orinoco rivers is transported northward. The non-recirculated volume (Figure 4.9a) and freshwater (Figure 4.9b) transports were estimated as $\int_{-152.5}^0 \int_{west}^{east} v dx dz$ and $\int_{-152.5}^0 \int_{west}^{east} v(1 - \frac{S}{34.5}) dx dz$ respectively, where $v > 0$ (northward) and 34.5 psu is the reference salinity. The simulation for years 2003-2011 shows a high seasonality in the NBC transports. The freshwater transport signals start from the equator and propagate to 10°N in a span of 2-3 months, with a maximum transport being in the months of May-August, peaking in July. From Figure 4.9a and on studying the individual transport fields it is observed that during the end of June the NBC starts becoming strong. The non-recirculated transport for July 2007 being 24.45 Sv at 2.3°N . According to Hellweger and Gordon (2002), the Amazon plume water takes around 2-3 months to reach the Barbados Island at 13°N , after the maximum Amazon discharge in May. My results corroborate this observation. The Amazon discharge is the lowest from October to February (Masson and Delecluse, 2001; Silva et al., 2005; Fournier et al., 2017; Varona et al., 2019), also seen in the individual daily SSS model fields.

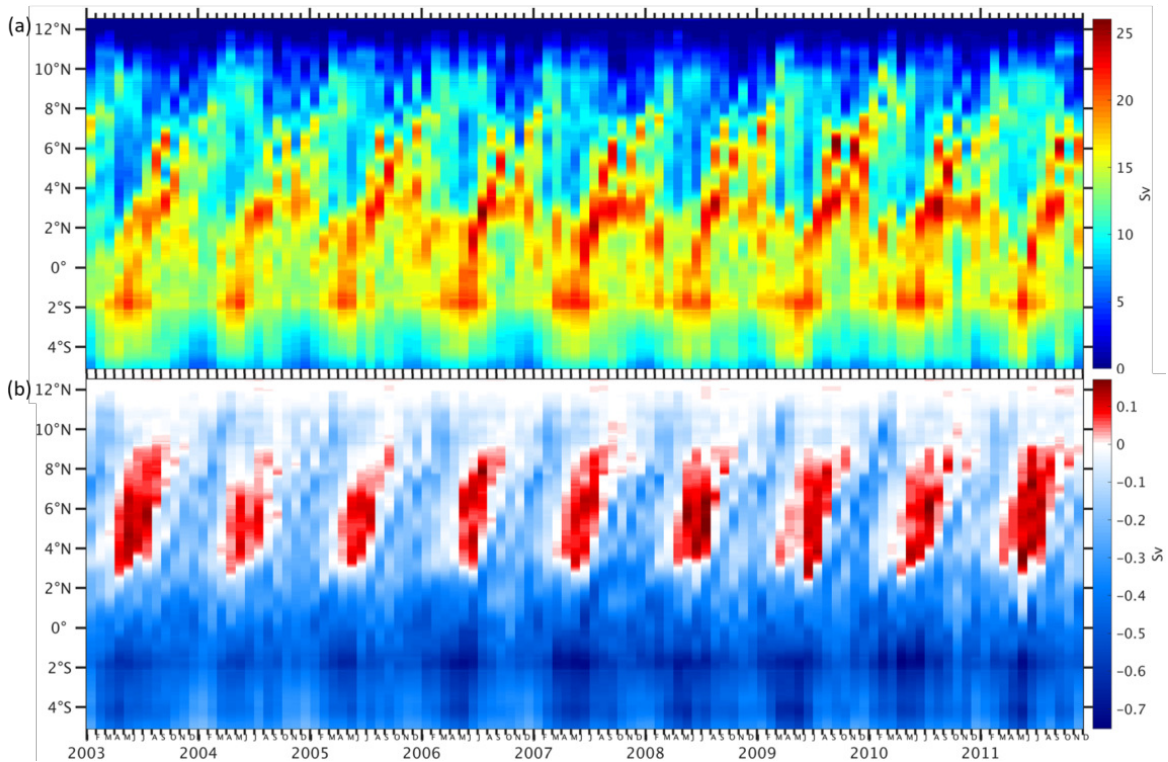


Figure 4.9: (a) NBC meridional non-recirculated transport (Sv); (b) NBC meridional non-recirculated freshwater transport (Sv), both monthly for 2003-2011 from ATL4km simulation.

In order to more easily correlate the ILD, MLD and BLT seasonal evolution of the NBC-box with surface fields of temperature and of atmospheric forcing, the time

series in Figure 4.5 were low-pass filtered with a cut-off period of 60 days. Results are presented in Figure 4.10, where the circles still correspond to the times of NBC eddies being present in the box. As can be immediately seen, the summer maximum of BLT is always associated to a second deepening of the ILD in June-July, with the MLD shallowing progressively towards the height of summer.

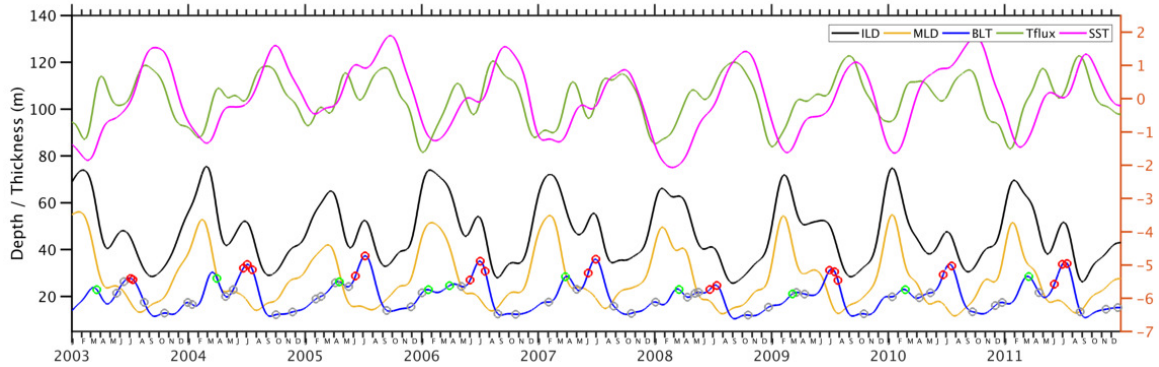


Figure 4.10: Time series of ILD, MLD, BLT, net surface heat flux and SST low-pass filtered with a 60 days cut-off filter. Red circles depict events when the eddies have large summer BLT; green circles show events when the eddies have large winter BLT; grey circles correspond to the remaining eddies which have significant BLT.

The reasons behind this behavior are various. On the one hand, there is freshwater carried in the periphery of the NBC rings, what causes mostly the MLD to shallow due to salinity stratification being strong. On the other hand, and more importantly, during the second maximum in ILD magnitude, one can observe a plateau in the warming trend towards summer, as seen in the SST seasonal evolution. This small plateau (or even in some years an actual reduction in SST) is associated to a pronounced reduction in the net heat flux forcing the upper ocean. In conclusion, the semi-annual cycle in net heat fluxes in the region imparts a tendency for a reduction in the warming speed in June-July of the surface and subsurface. In consequence, the layers below the surface remain more homogeneous (and sometimes develop a temperature inversion, when the surface is colder than the subsurface) and the ILD criterion ($SST - 0.2^{\circ}\text{C}$) is met at deeper depths. If the heat fluxes would only show an increase towards summer, the continuous warming of the surface and subsurface would lead to a fast development of a strong seasonal thermocline, resulting in a small ILD, which together with an also small MLD would lead to a vanishing barrier layer. That is seen to happen during September.

In conclusion, in this region of NBC rings, the seasonal BLT time series match that of the seasonal ILD more than that of the seasonal MLD. The reason seems to be the behavior of the net heat fluxes, which show a relative minimum during late spring-early summer.

When removing the low-pass filtered version of ILD, MLD and BLT from the original time series, the remaining high-frequency variations have an overall amplitude

of about 10 m with strong amplitude events occurring in spring reaching 15 m (Figure 4.11). Nearly all events correspond to the time when a NBC ring was present in the box, as seen by the grey, green and red circles superimposed in the high-pass filtered time series. It is therefore concluded that in this region, the passage/presence of eddies is responsible for the emergence of large amplitude BLT variations. In the following section I will focus on those events and search for the mechanisms responsible for the large BLT associated with NBC rings.

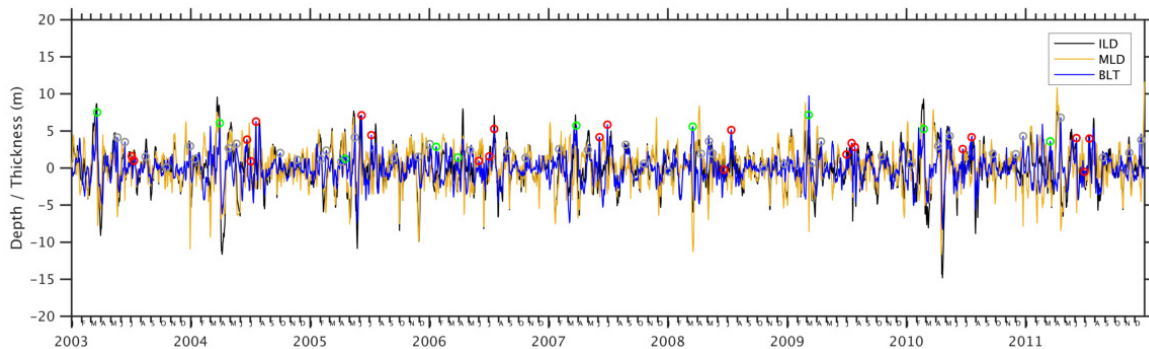


Figure 4.11: Daily anomalies of ILD, MLD and BLT (meters) after high-pass filtering (cut-off 60 days). Red circles depict events when the eddies have large summer BLT resulting in a peak in the BLT time series, green circles depict events when the eddies have large winter BLT and grey circles depict events when the remaining eddies have BLT resulting in a peak in the years 2003-2011.

4.3.2 Short timescale events

Barrier layer growth

The summer cases of high-frequency barrier layer growth/decay in NBC rings are more numerous (22 events) than those present in winter (10 events) (Figure 4.5). In the NBC rings area, the evolution of the summer BLT, the period of the seasonally largest barrier layers, is caused mainly by changes in ILD (Figure 4.6, 4.7, 4.8 and 4.10). In this section I focus on the high-frequency events that are superimposed on the seasonal behavior. Figure 4.12 shows snapshots of the evolution of BLT and ILD in one of the NBC rings having maximum BLT on 30-06-2007. Figure 4.13 shows a snapshot of variables affecting the BLT for that day (this episode corresponds to one of the red circles in Figures 4.5, 4.10 and 4.11).

The largest BLT in the box, of about 85 m is concentrated in the anticyclonic eddy, depicted by the clockwise rotation (Figure 4.12). Like most of the NBC rings, this ring forms around 6°N from the NBC retroflection. At its periphery it transports fresh Amazon water to the northwest after the maximum Amazon discharge in May-June. The NBC ring itself encloses a mass of comparatively higher salinity water inside its

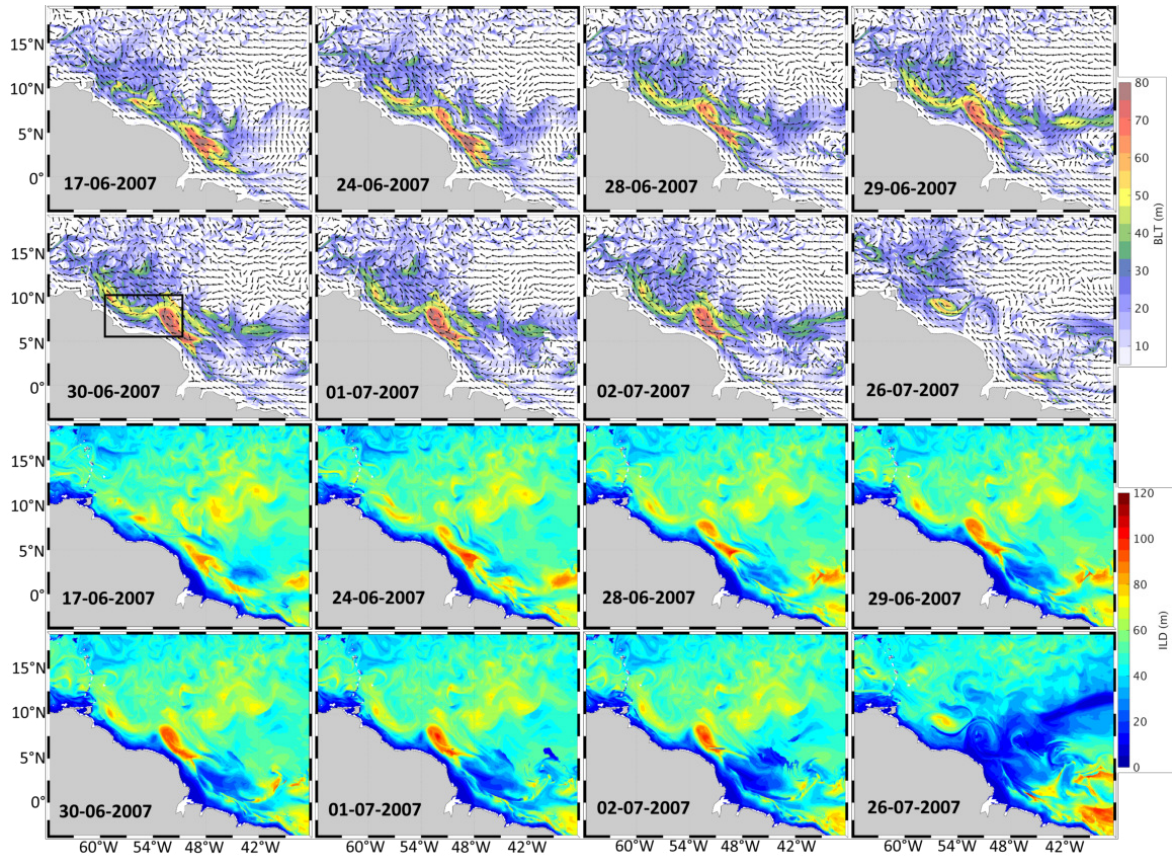


Figure 4.12: Snapshots from 17-06-2007 to 26-07-2007 showing the growth and decay of the maximum BLT on 30-06-2007 (summer) (black box delineates the NBC region): (row 1 and 2) BLT (meters) with vectors showing surface currents and (row 3 and 4) ILD (meters).

core (SSS around 34 psu) than at the periphery (SSS around 33 psu) (Figure 4.13b), with the large BLT not coinciding with the locations of fresher surface water. The ILD, with a maximum at the core of the eddy of about 95 m, causes the BLT to be maximum at the eddy core (Figure 4.12). The MLD in the ring (Figure 4.13a), in turn, is small and does not have as high a difference from its surrounding as in the case of ILD. Figure 4.12 shows the evolution of the large BLT on 30-06-2007. The surrounding deep ILD from near the mouth is carried and isolated within the NBC ring. This BLT grows corresponding to the deepening ILD in the ring and it decays corresponding to the shoaling ILD, until the ILD is same as the surrounding and the BLT in the core of the ring vanishes, as the eddy passes northwestward.

As discussed earlier, the NBC transport is maximum in June-August and the magnitude of the top 152.5 m transport is large at the NBC in Figure 4.13c on this day, transporting the fresher water from the river mouth, and freshwater from rainfall under ITCZ, to the northwest. Moreover, the ITCZ is reaching its northernmost location at this time of the year, shown by Foltz et al. (2004) and Foltz and McPhaden (2008) (their Figure 1) (also in Chapter 2, Figure 2.2). The E-P-R is therefore negative up to 15°N on this day in the region of low SSS (Figure 4.13b). SST is high in regions of large BLT

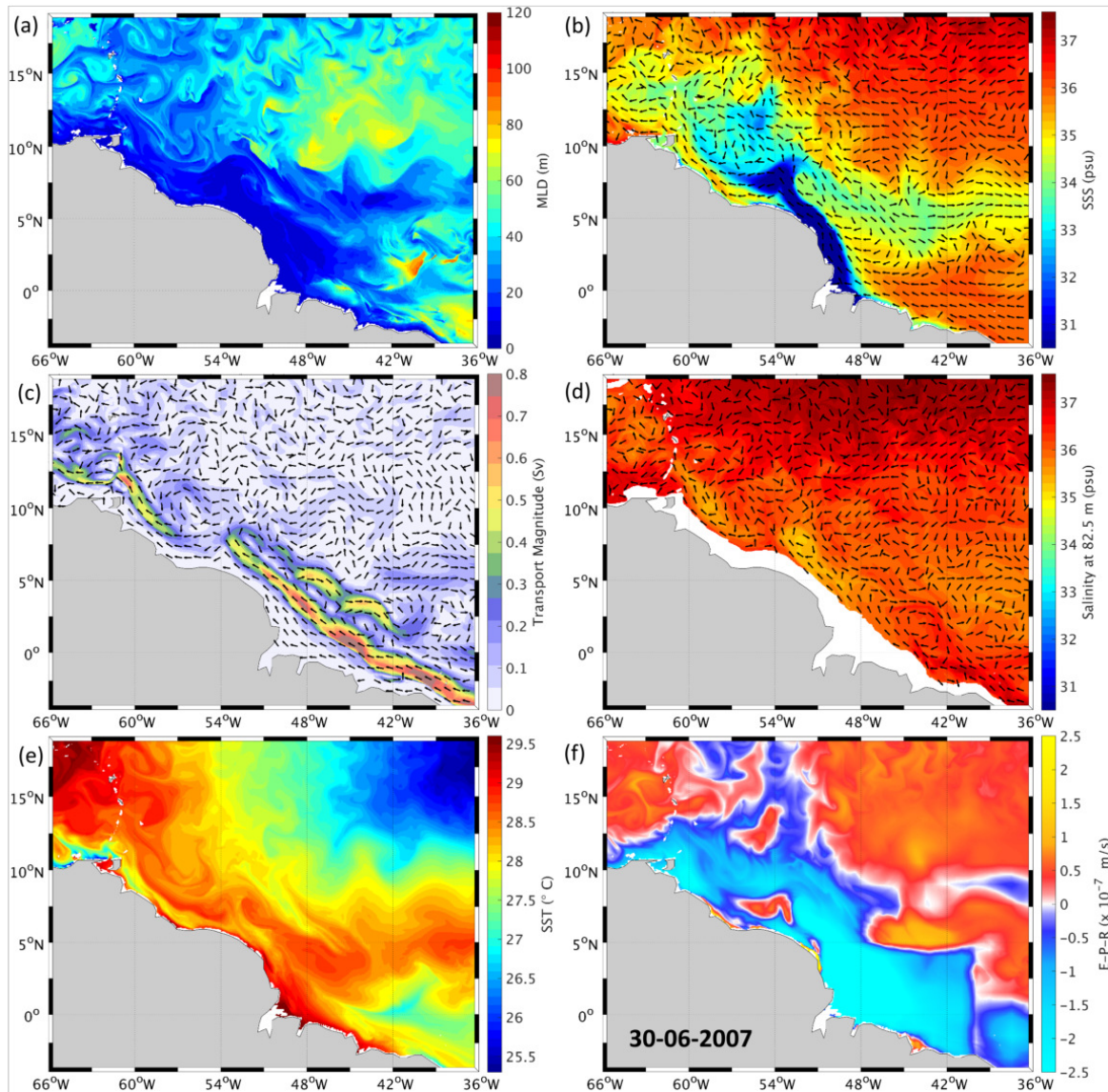


Figure 4.13: Snapshots for 30-06-2007 (summer) of (a) MLD (meters), (b) SSS (psu) with vectors showing surface currents, (c) top 152.5 m horizontal transport magnitude (Sv) and direction, (d) salinity (psu) at 82.5 m with corresponding currents, (e) SST ($^{\circ}\text{C}$) and (f) E-P-R ($\times 10^{-7}$ m/s).

(Figure 4.13e), as summer conditions prevail during the shown snapshot. In summer the SST is larger in the AWP (Wang and Enfield, 2003; Enfield and Lee, 2005; Wang et al., 2007; Liu et al., 2012) encompassing this region, and presence of river discharge also increases the SST (explored in Chapter 5). All in all, the spatial distribution of barrier layers resemble the spatial distribution of SSS and surface currents. However, the localization of the maximum BLT in the core of the NBC eddy is unexpected and will be seen in detail next.

In order to study the mechanisms that are responsible for the growth of the barrier layers, the terms of the temperature and salinity vertical gradient balance equations

(Eqs. 4.1 and 4.2 in section 4.2) were computed on a daily basis and averaged over the day of the event of maximum BLT in the ring (30-6-2007) and 2 days before this date (i.e., a 3-day average). With the balance terms I am able to quantify the contribution of each term in bringing about the change in ILD and MLD between two days before the event and the event day, which is needed to explain the observed BLT distribution. Since the focus is to explain the high-frequency event, the averaging period is small.

Typical event with predominantly ILD change

I focus on the changes at a section across which the NBC ring passes. This section is taken at 52.32°W (from 5.5-10°N) through the core of the NBC ring seen on 30-06-2007 having the maximum BLT of around 85 m inside the core (Figure 4.14). From this figure it is clear that, from the 28-06-2007 to the 30-06-2007, what changed was a deepening of the ILD, as seen by the change in position of the solid green to solid black curves. When looking at the tendency term (Figure 4.14a), it is clear that co-located with this change there is a positive temperature gradient tendency from the 28-06-2007 to the 30-06-2007 at those particular depths. Please note that stronger changes are seen elsewhere outside the barrier layer, namely in the eddy peripheries, where strong dynamical or thermodynamic changes occur. They are not of relevance for explaining the signal at hand, which lies in between the green and black curves.

From Figure 4.14g,h we see that the temperature gradient drastically increased in the southern part of the ring in the region where the ILD resides during 30-06-2007. Furthermore, from visual inspection, we see a moving apart and a downward shift of the isotherms in the region between the green and black curves from 28-06-2007 to the 30-06-2007. This corroborates the computed positive temperature gradient tendency seen in the tendency term. Looking at the terms in the RHS of the balance equations, the summation of which give the LHS term, one sees a large amount of compensation in the patterns. In the region between the green and black curves, the dominant mechanisms causing the isotherms to move apart in the south and to shift downward in general, in the process growing the ILD, are horizontal advection and to a minor extent vertical advection, tilting and stretching (Figure 4.14b,c,d,e). Turbulent mixing (Figure 4.14f) balances only partly the above terms, so that a residual positive tendency results.

In the presented event, at the lateral edges of the barrier layer, the processes acting are mainly horizontal advection (depths of 40-80 m), stretching and tilting. At the bottom of the barrier layer, horizontal advection and stretching sum up, with mixing partially canceling them. The salinity vertical gradient balance equation terms are not discussed in this case since 1) we see negligible changes in MLD and 2) the ILD is solely dependent on temperature.

From an inspection of every summer event showing a peak in the BLT time series (all red circles in Figure 4.5), it was inferred that when the ILD grows, the temperature vertical gradient tendency between the days before and the resulting ILD is mostly positive. From all analyzed summer events, the ILD grows 1) when the isotherms

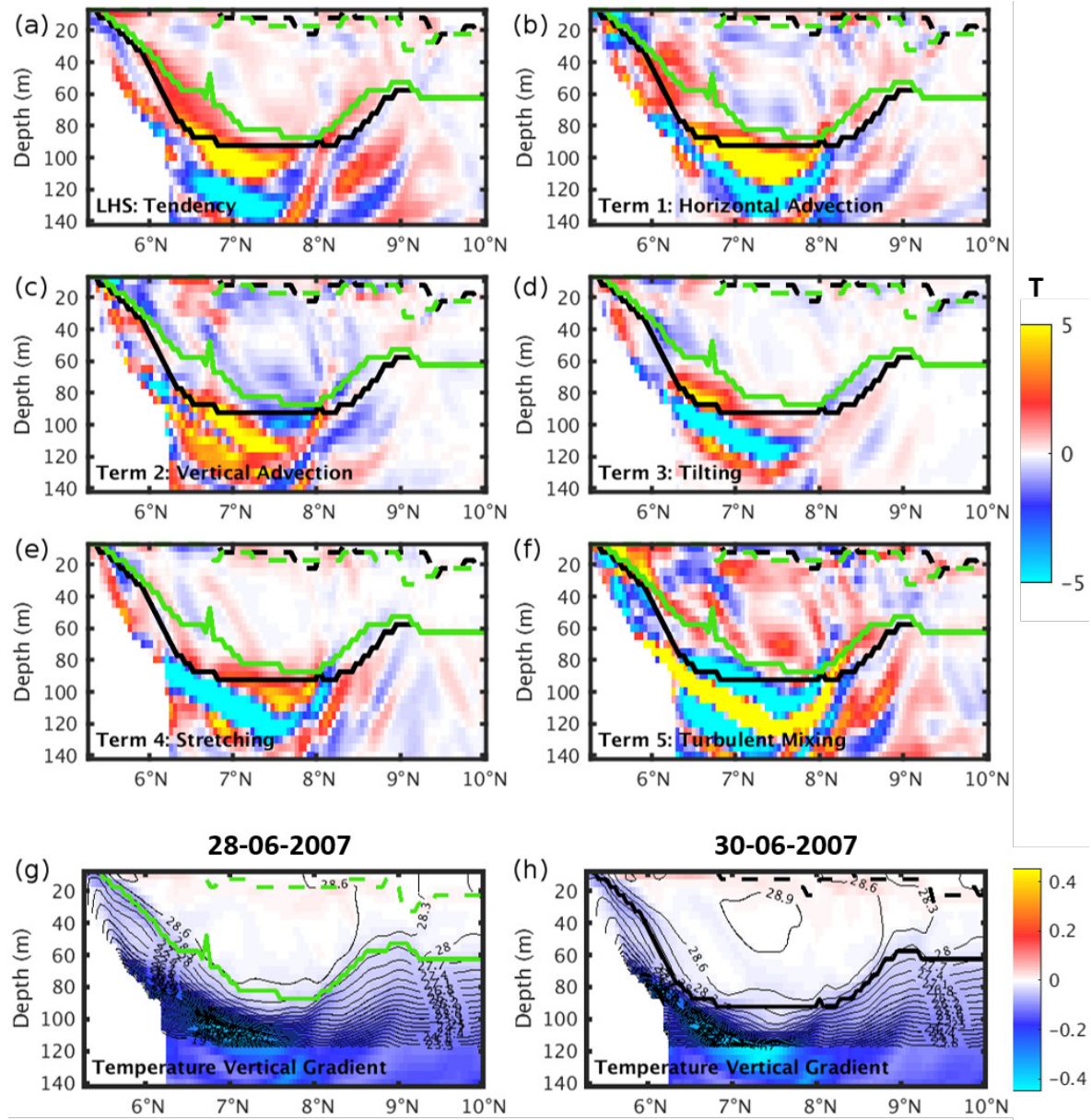


Figure 4.14: Vertical section at 52.32°W through the core of the NBC ring present on 30-06-2007 in the NBC-box. Temperature gradient balance terms (a) LHS; (b) Term 1: horizontal advection; (c) Term 2: vertical advection; (d) Term 3: tilting; (e) Term 4: stretching; (f) Term 5: turbulent mixing, averaged from 28-06-2007 to 30-06-2007, units ($\times 10^{-7} \text{ }^\circ\text{C}/\text{m.s}$). Temperature vertical gradient ($^\circ\text{C}/\text{m}$) with contours being isotherms ($^\circ\text{C}$) are shown for (g) 28-06-2007 and (h) 30-06-2007. Black (green) solid line correspond to the ILD, black (green) dashed line corresponds to the MLD for 30-06-2007 (28-06-2007).

move apart (16/22 cases, 72.73%), or 2) when the isotherms move together (compress) (6/22 cases) (notice ILD change in Figure 4.15 and Figure 4.16c,d).

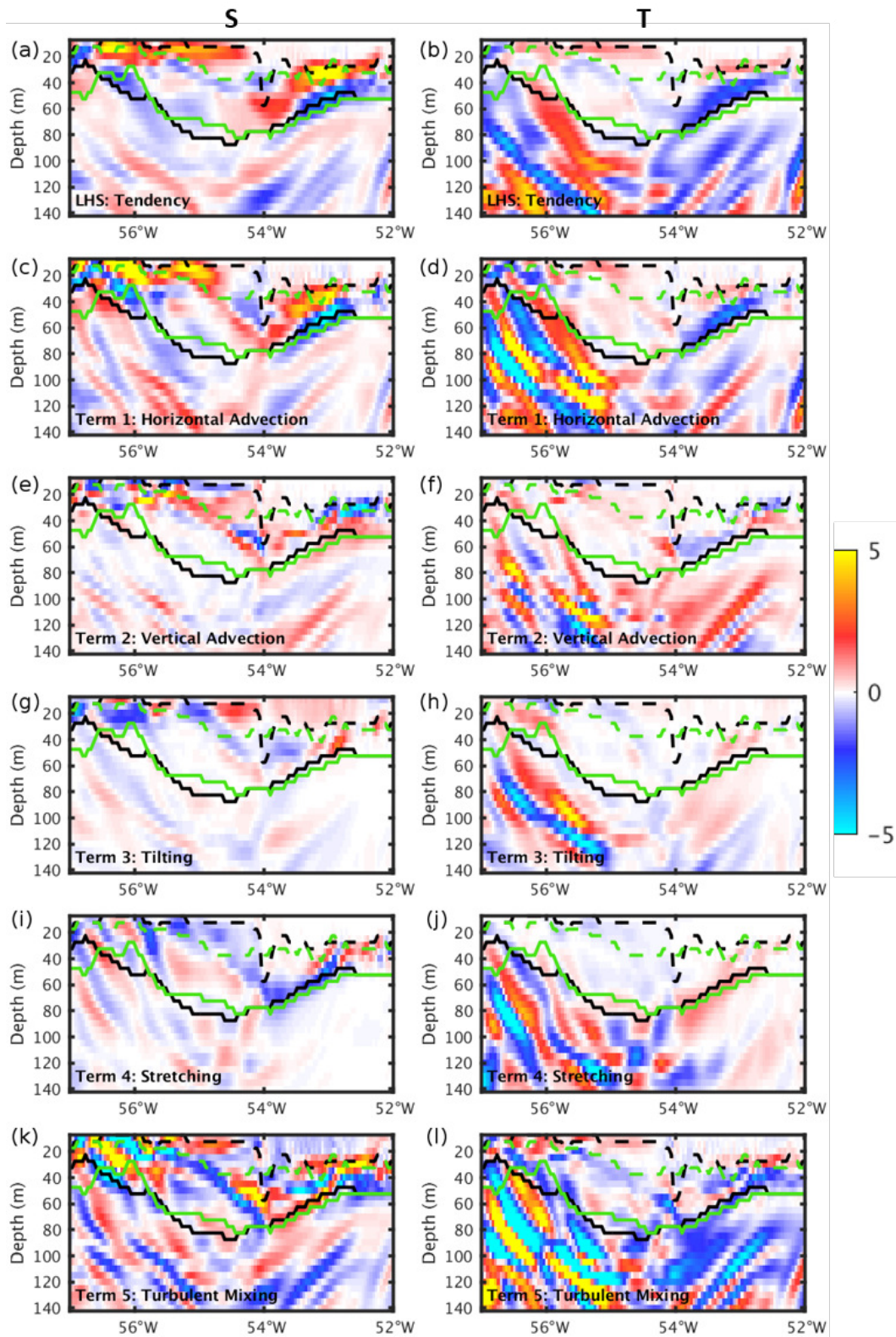


Figure 4.15: Vertical section at 8.95°N through the core of a NBC ring on 30-06-2011 of salinity and temperature gradient balance terms: (a,b) LHS, (c,d) Term 1: horizontal advection, (e,f) Term 2: vertical advection, (g,h) Term 3: Tilting, (i,j) Term 4: stretching; (k,l) Term 5: turbulent mixing, averaged from 28-06-2011 to 30-06-2011 (units are $\times 10^{-7}$ psu/m.s and $\times 10^{-7}$ $^{\circ}\text{C}/\text{m.s}$, respectively). Black (green) solid lines correspond to ILD and black (green) dashed lines to MLD for 30-06-2011 (28-06-2011).

Exception case with predominantly MLD change

In the region of NBC rings there are in the majority of cases negligible changes in MLD which would cause a change in BLT, but there are a few exceptions. Illustrated in Figures 4.15 and 4.16 is one of the few exceptions, with a significant shallowing of the mixed layer resulting in the growth of the barrier layer in the eddy. The barrier layer growth event takes place from 28-6-2011 to 30-6-2011 and the vertical section is now taken at 8.95°N through the core of the NBC ring as it stands on 30-6-2011.

The first row in Figure 4.15 shows the average salinity and temperature vertical gradient tendencies between two days before 30-6-2011 and that date. From the dashed green and black curves, showing the MLD on 28-6-2011 and on 30-6-2011, respectively, one sees that the MLD has shoaled considerably in the core of the eddy. One notices also a strong positive tendency in the salinity gradient close to the surface, accompanied by a more moderate positive tendency in the temperature gradient at those locations.

Since the MLD definition is based on density, both temperature and salinity can be determinant. In order to see which variable plays a more important role, the salinity and temperature stratification fields were computed. They reveal how much of the density stratification can be attributed solely to salinity stratification or solely to temperature stratification. Figure 4.16e,f,g,h,i,j show that in this event, the density stratification is almost completely determined by salinity and one can see how the surface halocline strengthens and shallows from 28-6-2011 to 30-6-2011 in the western part of the eddy. This compression of isohalines takes place as a result of fresher water appearing at the surface (see contours in Figure 4.16a,b). In 11/22 cases there is some change in MLD along with the typical change in ILD in the NBC ring during summer.

The RHS term contributing to the increase in salinity vertical gradient tendency at the surface is almost exclusively horizontal advection of the salinity gradient (Figure 4.15c). The second most important term is turbulent mixing followed by tilting, which partly compensate the horizontal advection (Figure 4.15k,g). When looking at the region where the MLD changed during the 3 days, one sees that a positive tendency due to vertical advection and a negative tendency due to stretching are also present, but they are weak.

Tilting of the salinity fronts occurs due to the shear created by the seasonal maximum northwestward transport of freshwater from the Amazon discharge and ITCZ precipitation, by the NBC rings (Ffield, 2007; Da-Allada et al., 2013; Fournier et al., 2017) in June-August (Figure 4.13b,c) and the equatorward transport of the SMW in general southwestward (Figure 4.13d). The SMW is also carried southward by the recirculating NEC that supplies SMW to the seasonal maximum transport of the retroflection and NECC at depths around 60-150 m in June-August (19.6 Sv) (Schott et al., 1998; Bourlès et al., 1999a). The Guiana Undercurrent is the equatorward branch of the northern-shallow tropical-sub-tropical cell (STC), which carries the SMW from the north at around 100 m during August (Wilson et al., 1994). Both the above, being well inside the ILD, shoal the MLD in relation to the ILD.

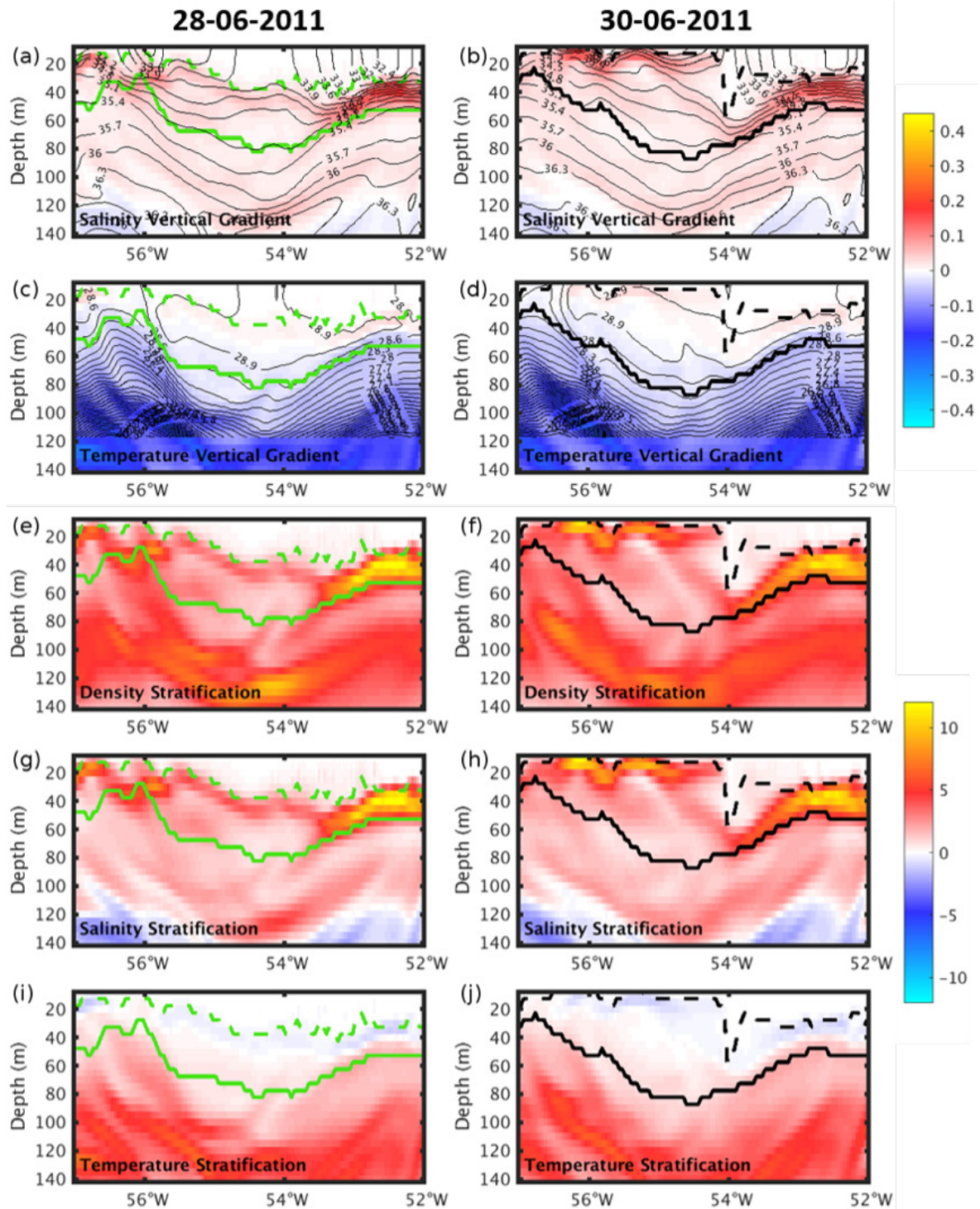


Figure 4.16: Vertical section at 8.95°N through the core of a NBC ring on 30-06-2011: (a,b) salinity vertical gradient (psu/m), with isohalines (psu) superimposed; (c,d) temperature vertical gradient ($^{\circ}\text{C}/\text{m}$) with isotherms ($^{\circ}\text{C}$) superimposed, (e,f) density, (g,h) salinity and (i,j) temperature stratification ($\times 10^{-4}/\text{s}^2$) for 28-06-2011 and 30-06-2011, respectively. Black (green) solid lines are ILD, black (green) dashed lines are MLD for 30-06-2011 (28-06-2011).

In Figure 4.16a,b we see that there is fresher and warmer water at the periphery than in the core of the ring. The NBC carries the saline warm water from the south Atlantic, the South Atlantic Central Water (Blanke et al., 2002; Kirchner et al., 2009) or the "dead" midocean water (Fratantoni and Glickson, 2002), immediately below the cap of freshwater from the Amazon. The ring encloses the higher salinity south Atlantic water inside and transports it (Field, 2007), giving rise to conditions such that the MLD shoals and a barrier layer grows.

In conclusion, northwestward horizontal advection of freshwater by the NBC rings is a dominant mechanism in many of the events, increasing the salinity vertical gradient at the immediate subsurface, thus shoaling the MLD and giving conditions leading to BLT growth in the rings. Also, tilting of salinity fronts due to the flow of freshwater at the surface (or periphery) of the eddy and salty water at the subsurface (or core) of the eddy, raises the MLD in a deeper ILLD.

During August-November there are thicker and more frequent barrier layers forming in the peripheries of the rings or as elongated filaments and less than 30 m in the core of the rings. In these instances, the ILLD is around 35-40 m, much lesser than in the cases seen above when there is BLT > 80 m in the core of the ring (due to ILLD > 100 m). From December-April thick BLT is seen in the periphery, and sometimes in the core of the ring, thicker than in autumn. The peaks encircled in green in Figure 4.5 correspond to these winter NBC rings which have larger BLT in their periphery, rather than in the core. The shallowing of MLD is more responsible for growing the BLT rather than an increase in ILLD. The MLD reduces when the isohalines compress in 9/10 cases (90%) due to freshwater on surface at the periphery of the rings. This is demonstrated from 05-03-2009 to 07-03-2009 for a NBC ring having the peak BLT on 07-03-2009 (Figure 4.17g,h). Horizontal advection, followed by turbulent mixing and tilting are dominant in forming the barrier layer in the periphery of the ring in winter (Figure 4.17a,b,f,d).

Barrier layer decay

To investigate the mechanisms responsible for the decay of the high-frequency barrier layer events in NBC rings, I averaged the terms from the day when the BLT is at its peak (red circles in Figure 4.5) to 2 days later when a significant change in ILLD/MLD is seen, i.e., when an increase in MLD and/or a decrease in ILLD occurs in the NBC ring.

The barrier layers in NBC rings get usually thinner when the ILLD gets smaller. After examining the decay of the barrier layers in all the 22 events it was observed that the temperature vertical gradient tendency is mostly negative. Associated to the reduction in ILLD, in most cases (17/22 cases, 77.3%) the isotherms are moving vertically apart. One of these decay events is shown in Figure 4.18, occurring from

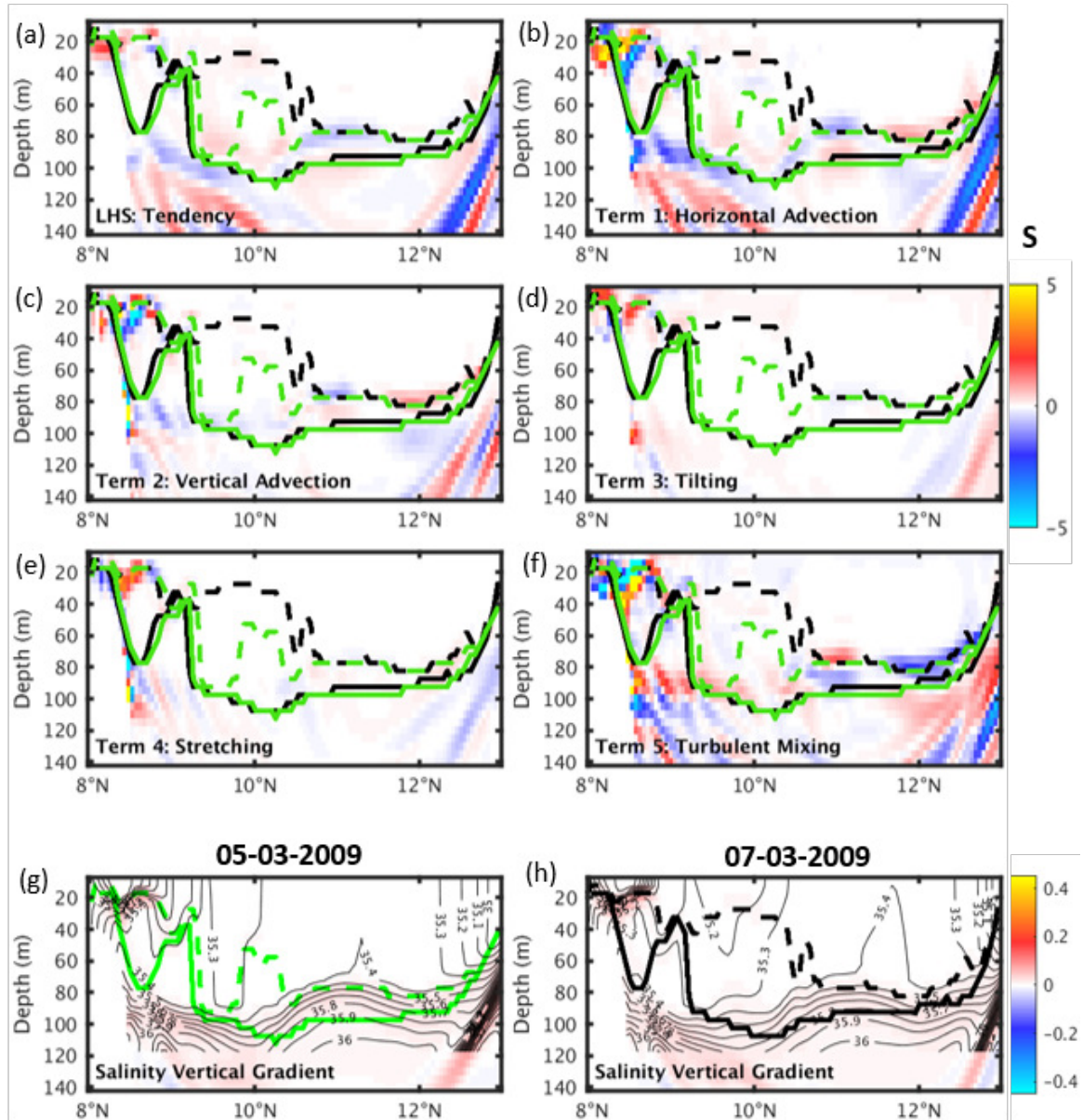


Figure 4.17: Same as Figure 4.14, but for a vertical section at 58.31°W through the core of the NBC ring present on 07-03-2009 and here salinity gradient balance terms are averaged from 05-03-2009 to 07-03-2009 (units are $\times 10^{-7}$ psu/m.s) and (g,h) are salinity vertical gradient (psu/m), with isohalines (psu) superimposed. Black (green) solid lines correspond to the ILD, black (green) dashed lines to the MLD for 07-03-2009 (05-03-2009).

11-7-2003 to 13-7-2003. The vertical section is now taken at 56.12°W through the core of the eddy on 11-7-2003 and the change in BLT two days after is studied.

From the temperature vertical gradients superimposed with isotherms in Figure 4.18g,h, it is noticeable that the ILD shoaled, as the isotherms around the ILD moved vertically apart. In the tendency term (LHS) in Figure 4.18a one sees a negative tendency between the solid black and solid green curves, which led to the ILD criterion being met at a shallower depth. The dominating term contributing to the negative

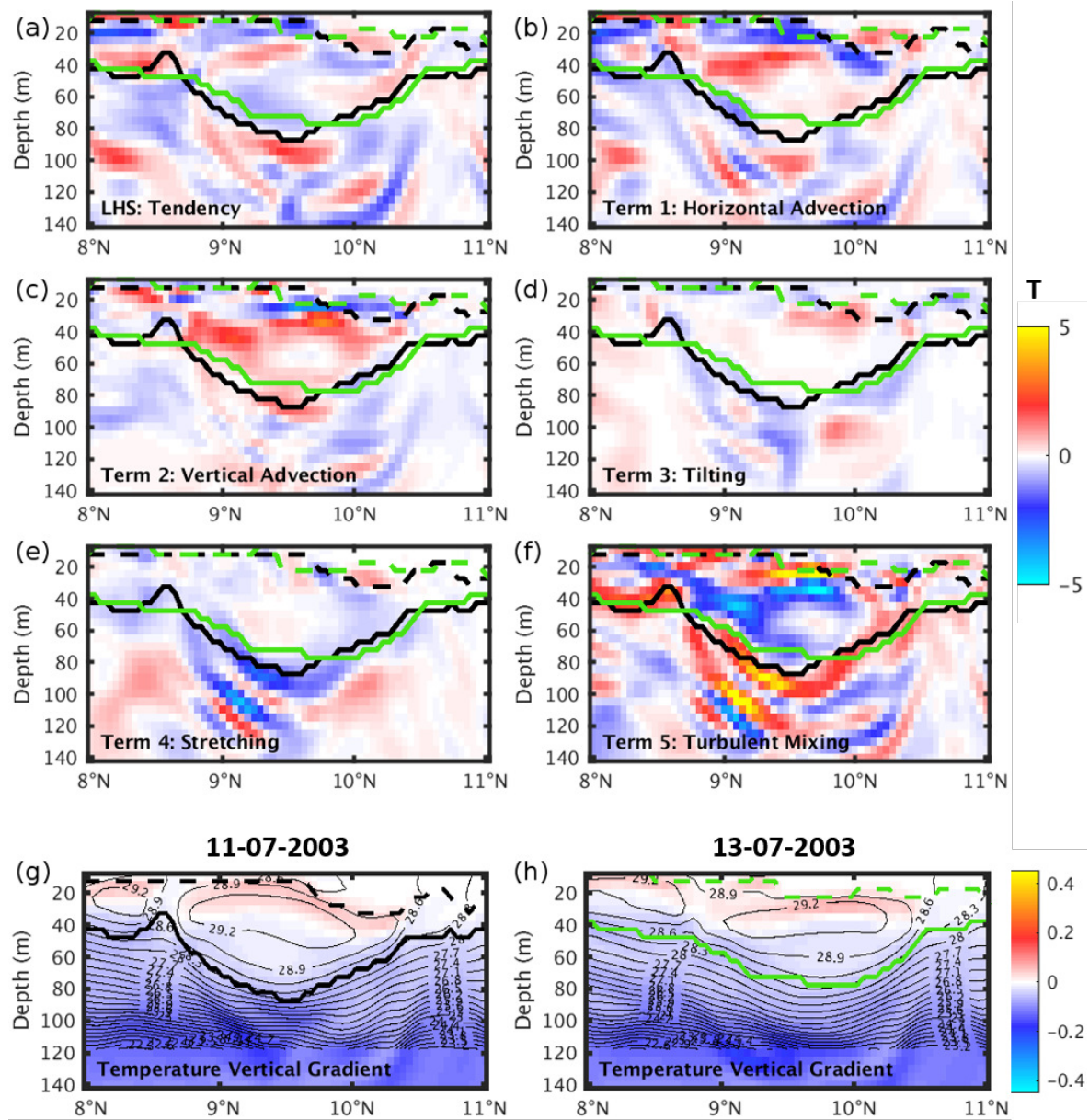


Figure 4.18: Same as Figure 4.14, but for a vertical section at 56.12°W through the core of the NBC ring present on 11-07-2003. Temperature gradient balance terms are averaged from 11-07-2003 to 13-07-2003 ($\times 10^{-7} \text{ } ^\circ\text{C}/\text{m}\cdot\text{s}$) and (g,h) are temperature vertical gradient ($^\circ\text{C}/\text{m}$) with isotherms ($^\circ\text{C}$) superimposed. Black (green) solid lines correspond to the ILLD, black (green) dashed lines to the MLD for 11-07-2003 (13-07-2003).

temperature gradient tendency is again horizontal advection in the southern part of the eddy and stretching in the base of the isothermal layer (Figure 4.18e). Turbulent mixing once again opposes the horizontal advection to the south but contributes slightly to the LHS tendency at the isothermal layer base, as seen in Figure 4.18b,f. In this event, like in the majority of the other events, there is negligible change in MLD compared to ILLD.

The decay of the barrier layer happens also due to the deepening of the mixed layer in certain cases (10/22 cases, not shown). The deepening of the mixed layer is associated with a negative salinity vertical gradient tendency which indicates a reduction in salinity vertical gradient between the MLD of the day of peak BLT in the ring and the MLD 2 days after. It occurs due to the stretching of isohalines, with, in this case, horizontal advection, stretching and tilting being dominant for deepening the MLD.

In conclusion, we saw in this section that the BLT is at its maximum in the region of NBC rings during the summer months of June-August and has a seasonal minimum in autumn. The high-frequency, event-like growth of the ILD and consequent growth of the barrier layer is associated with a stretching of isotherms most of the times. Horizontal advection, tilting and stretching are dominant processes in generating a barrier layer in the NBC rings. ILD shallows and reduces the barrier layer again by stretching of isotherms. The evolution of barrier layers here is controlled more by the changes in ILD than in MLD.

In winter there are fewer rings with barrier layers in them (green circles in Figure 4.5). In those winter cases, as we saw, the MLD is more responsible in forming the barrier layer, but both the MLD and ILD play equally important roles in the thinning of the barrier layer.

4.4 Barrier layer in the NEC region

The NEC area studied here resides in the southern part of the subtropical gyre, where barrier layers persist almost throughout the year. Figure 4.19 shows the simulated daily variability of ILD, MLD and BLT for 2003-2011 in the NEC box. During December-March there are thick barrier layers, with the largest extent being in February-March.

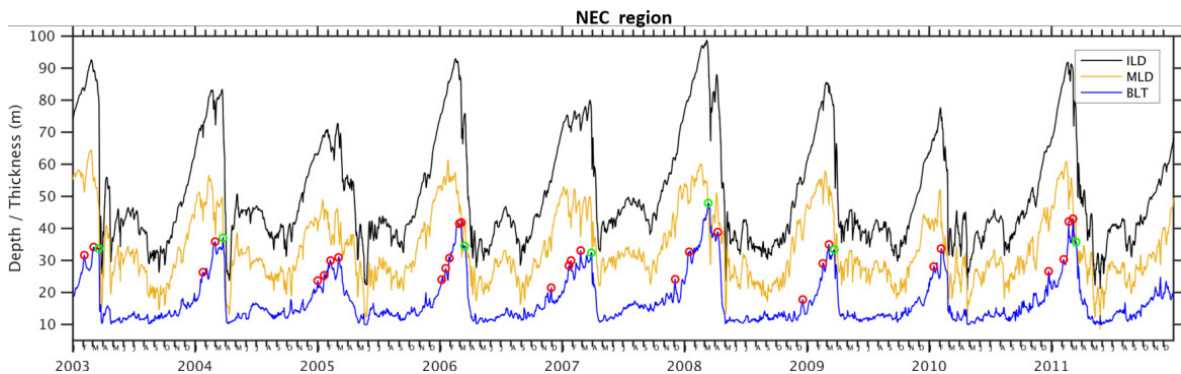


Figure 4.19: Daily time series of area-averaged ILD (black), MLD (yellow) and BLT (blue) in the NEC region (14-20°N, 46-58°W). Red circles denote the large peak events of BLT. Green circles indicate the events when the winter barrier layer peaks before getting eroded in spring.

From April-May onwards, the BLT has small amplitudes, increasing slightly in July-August, and thinning again in September-November (Figure 3.4b and 4.19). Just like

for the NBC area, beside this dominant seasonal signal in BLT, there is high-frequency variability superimposed, although of much smaller amplitude than in previous section. Those short events are marked in red circles (29 events) and in green circles (7 events), the latter corresponding to events after which the winter BLT is completely eroded. The growth and decay of the seasonal barrier layer and of the individual peak events were investigated and results are presented next.

4.4.1 Seasonal evolution

The ILD and MLD have similar seasonality, being large in winter due to wind- and buoyancy-induced mixing and presenting a secondary maximum in May-July. The MLD in winter overlies, however, a relatively deep isothermal layer, giving rise to the large barrier layers in winter (Figure 4.19, blue curve). During the secondary maximum, ILD and MLD roughly have the same behavior, leading to reduced or almost vanishing barrier layers.

The mechanisms responsible for the seasonal cycle of barrier layers in the NEC region are identified here. As seen so far in Figure 3.1, Figure 3.4b and Figure 4.19, the maximum seasonal BLT is in winter. Figure 4.20 presents a vertical section at 53.72°W (between 15°N and 20°N) of the balance terms. They are averaged from November to February in order to retain the main contribution at the seasonal scale (with the contribution from all small scale events being averaged out). The black and green curves in the figure show how the MLD and ILD change from November, when the barrier layer just starts to form, to February, when there is a maximum BLT.

From November onwards the saline and cold (dense) water at the surface sinks down, giving rise to convective mixing, along with mixing due to strong winds in the surface layer, which deepens the mixed and the isothermal layers until February. Consequently, there is very thin BLT in November, which grows until February. The isothermal layer deepens because of turbulent mixing as this term contributes most to the positive temperature vertical gradient tendency between the ILD in November and February, as can be seen in Figure 4.20b,l). The decrease in the salinity gradient tendency between the mixed layers in November and February is sustained by horizontal/vertical advection and turbulent mixing (Figure 4.20a,c,e,k). The tilting and stretching mechanisms oppose the advection term (Figure 4.20c,g,i).

In conclusion, the mixed layer deepens from November to February but less than the ILD, as we see the magnitude of decrease in salinity vertical gradient tendency between the two MLDs being smaller than the magnitude of the positive temperature vertical gradient tendency between the two ILDs from November to February.

In Figure 4.21 the somehow abrupt seasonal decay of the barrier layers from March to April is presented. We see that the barrier layer is destroyed due to a shallowing of the ILD and MLD, i.e, the opposite situation compared to the slow growth during

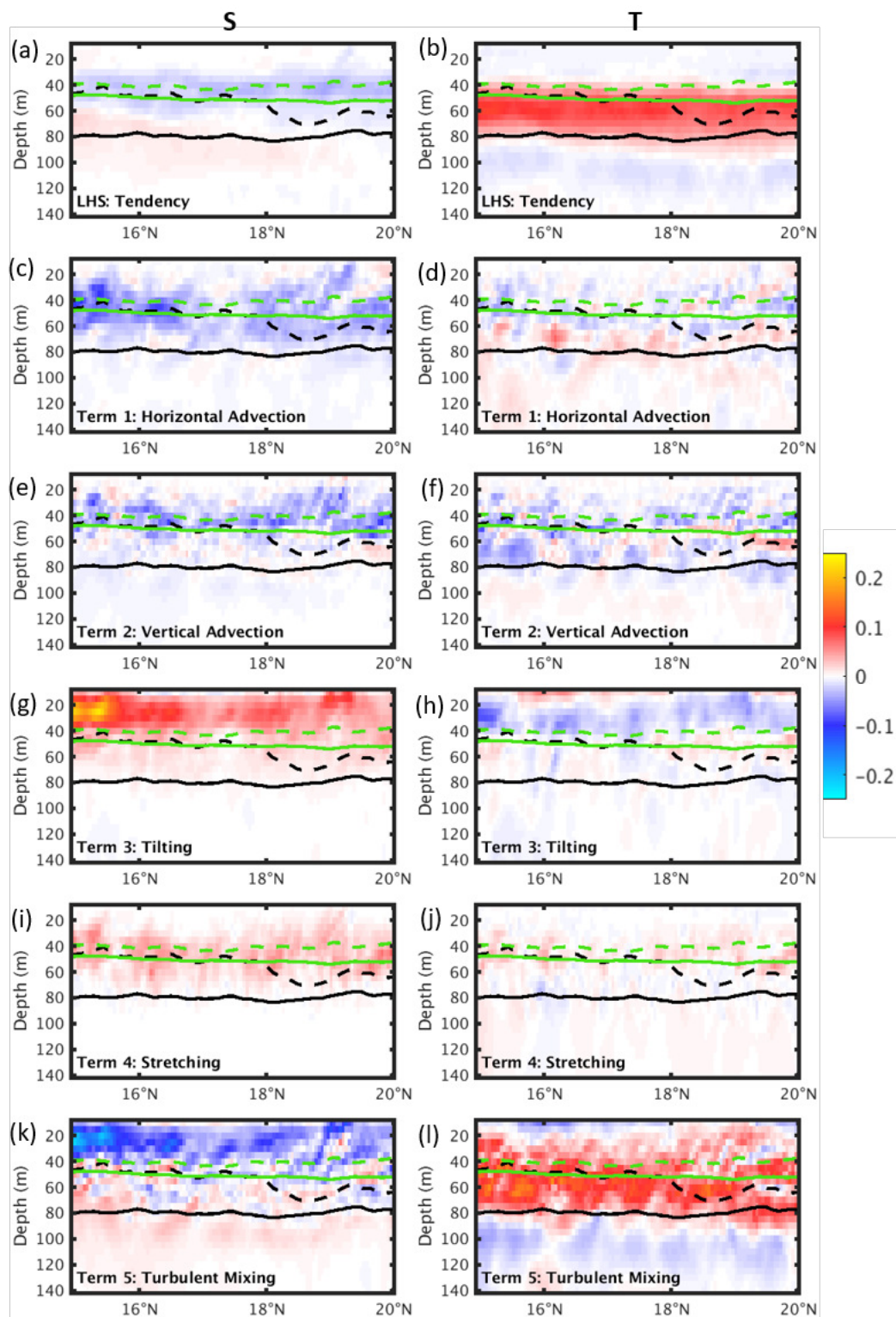


Figure 4.20: Same as Figure 4.15, but vertical section at 53.72°W through the maximum climatological BLT in February. Salinity and temperature gradient balance terms are averaged from November to February (units are $\times 10^{-7}$ psu/m.s and $\times 10^{-7}$ $^{\circ}\text{C}/\text{m.s}$, respectively). Black (green) solid line is ILD, black (green) dashed line is MLD for February (November).

autumn and winter. The negative temperature vertical gradient tendency between the ILD in March and April is again due to a contribution of turbulent mixing of the warmer water on top in spring, which destroys the barrier layer during that season (Figure 4.21b,l). The MLD reduces due to tilting and stretching and moderately due to turbulent mixing (Figure 4.21g,i,k).

After the erosion of the winter maximum BLT in spring, we see in the Figure 4.19 that there is a comparatively thinner BLT rising from May to July which gets thinner in September. During this time in summer, compared to winter, increased surface heating stratifies the upper layer, thus reducing the ILD. Like in the NBC area, a semi-annual behavior of net heat flux, SST and wind stress magnitude exists in this region. There is a reduction in SST due to the forcing from the reduction in net heat flux and a second peak in wind stress magnitude in July. Convective and wind mixing therefore cause the small increase in ILD and MLD. Turbulent mixing of temperature mainly deepens the ILD from May to July (not shown). Additionally, during summer the maximum spatial extent of spread of the freshwater from the Amazon and Orinoco rivers occurs and the ITCZ reaches its northernmost position. The seasonal maximum transport of NBC in July, carrying the above fresher water northwards, and the seasonal maximum NEC in late-summer getting salty water from the open ocean to the west, cause tilting of salinity fronts and shoal the MLD. The shoaling MLD over the slightly deepened ILD gives rise to this thin summer BLT. Alternatively, the increase in ILD due to penetrating solar radiation, with MLD maintained at constant depth in summer, could also cause this thin barrier layer to occur (Mignot et al., 2012). Turbulent mixing and tilting shoal the ILD from July to September, causing the thin summer BLT to decay.

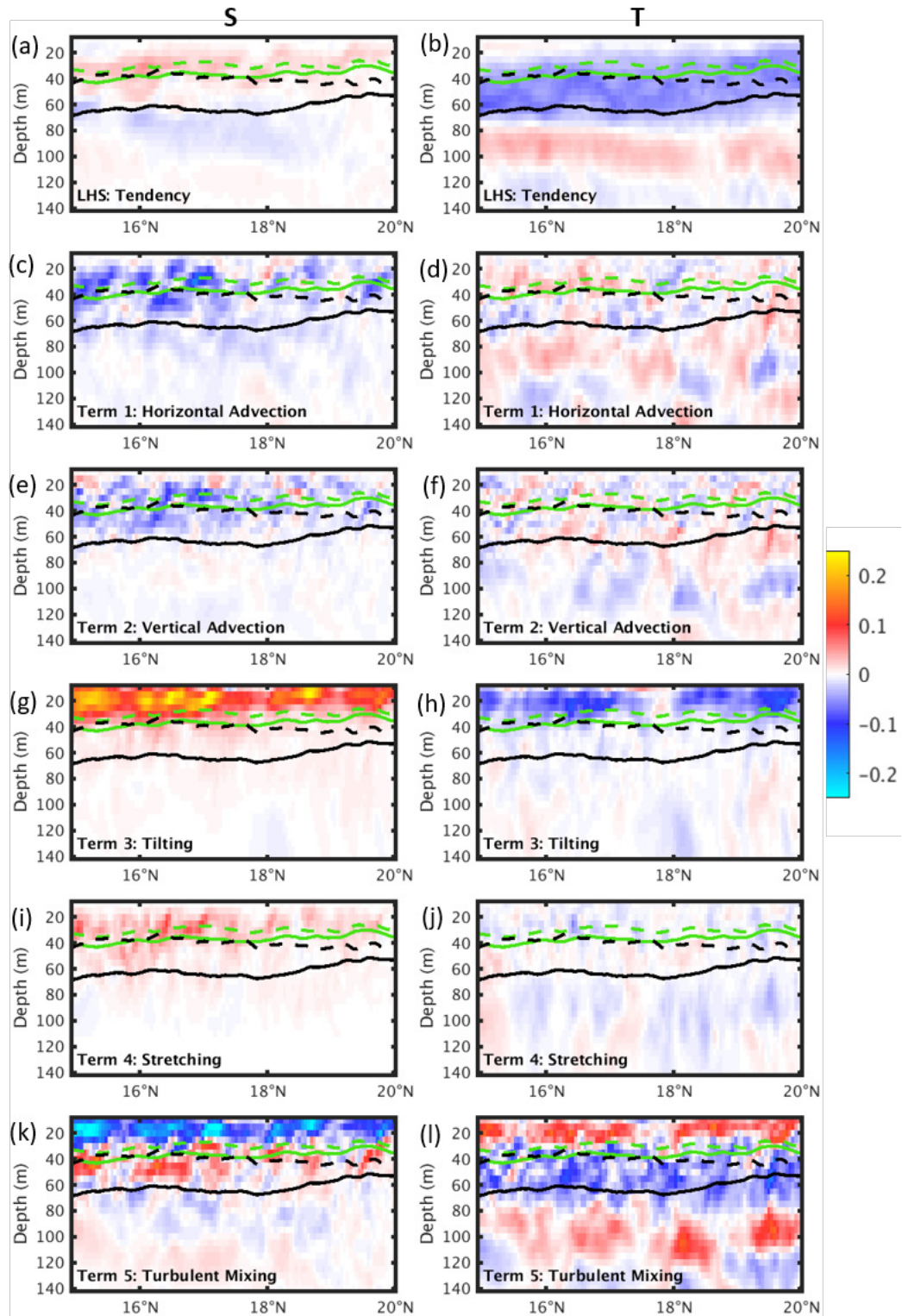


Figure 4.21: Same as Figure 4.15, but vertical section at 53.72°W through the maximum climatological BLT. Salinity and temperature gradient balance terms are averaged from March to April (units are $\times 10^{-7}$ psu/m.s and $\times 10^{-7}$ $^{\circ}\text{C}/\text{m.s}$, respectively). Black (green) solid line is ILD, black (green) dashed line is MLD for March (April).

4.4.2 Short timescale events

Barrier layer growth

By closely inspecting the daily evolution in the simulation, it was seen that during September-November, the horizontal advection of the existing runoff and precipitation freshwater takes place up to 23°N . As seen in the seasonal evolution, the ILD and MLD start both to become deep in late autumn, but with the MLD change, in comparison to ILD, staying small. In October-January, the formation of barrier layers at the fresher side of the large-scale salinity front in the form of faint filaments occurs. The resulting BLT becomes maximum in February-March at $15\text{-}18^{\circ}\text{N}$. I now focus on those small-scale and highly-frequent events superimposed over the seasonal evolution.

Figure 4.22 (row 1) presents the evolution of the BLT from one of the peak events (red circles in Figure 4.19) occurring on 17-02-2009. The figure shows the BLT distribution in the middle of the winter season, when it is growing to reach its maximum extent. It can be seen that barrier layers occur on the lower SSS side of the large-scale salinity front (compare Figure 4.22, row 1 and row 4). From December-February, E-P-R is strongly positive from 5°N northwards (Figure 4.23d), meaning more evaporation in the place of this barrier layer than freshwater flux by precipitation. In fact, the ITCZ is located south of this region during this time of the year.

Also, there are prevailing easterly Trade Winds (Foltz et al. (2004) and Figure 1 of Foltz and McPhaden (2008)), which cause the large evaporation in this region of barrier layers. From November-March around 15°N , the salinity in the upper ocean is higher (Figure 4.22 row 4) and water is colder (Figure 4.23c) as compared to summer (Figure 4.13b,e). Therefore, the cool, saline, dense surface water sinks in convective mixing processes. This, along with the wind stirring, causes the larger ILD and MLD in winter than in summer.

BLT of up to 40-80 m is present from $13\text{-}22^{\circ}\text{N}$, with a maximum being located at $15\text{-}18^{\circ}\text{N}$. These barrier layers align in an interesting pattern of very localized variability, in general terms, confined to the salinity frontal region. The ILD is deep (90-120 m) in this region and time of the year (Figure 4.22 row 2). The MLD is shallow, around 20-40 m, in exactly the locations where there are barrier layers present (Figure 4.22 row 3), therefore also presenting the highly spatially variable pattern. This BLT is seen to decay as the MLD deepens.

The event of barrier layer growth from 14-02-2009 to 17-02-2009 is illustrated in Figures 4.24 and 4.25. The 40 m thick barrier layer present on 14-02-2009 extending from $55\text{-}53^{\circ}\text{W}$ in this section along 17.69°N , grows to 60 m until 17-02-2009 due to a shallowing of the MLD during those 4 days (see dashed curves in Figure 4.24a and Figure 4.25a,b). The shoaling of the mixed layer causes the BLT to be larger and is associated with a positive salinity vertical gradient tendency, meaning an increase in the salinity vertical gradient from 3 days before until the day of the peak BLT (Figure 4.24a). A similar, but weaker, pattern is seen in the temperature gradient tendency.

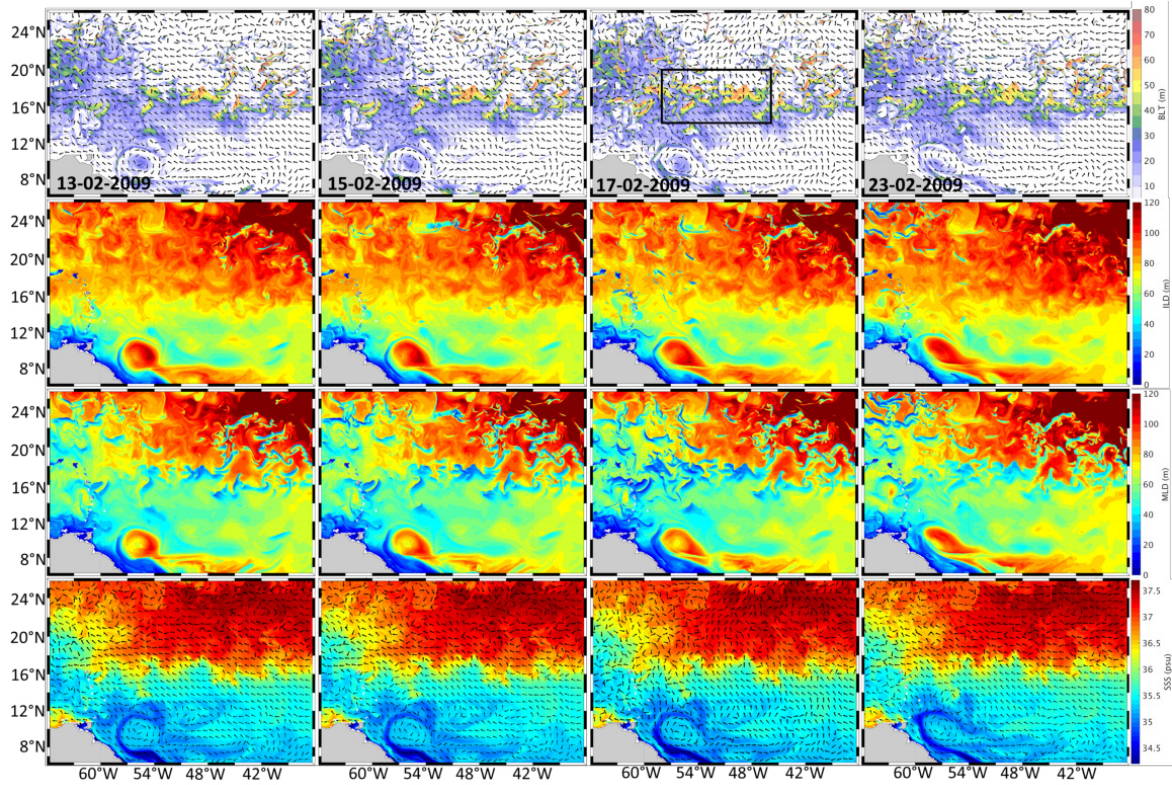


Figure 4.22: Snapshots from 13-02-2009 to 23-02-2009 showing the growth and decay of the maximum BLT on 17-02-2009 (winter) (black box delineates the NEC region): (row 1) BLT (meters) with vectors showing surface currents, (row 2) ILD (meters), (row 3) MLD (meters) and (row 4) SSS (psu) with vectors showing surface currents.

Looking at the individual contribution of salinity and temperature for the density stratification (Figure 4.25c,d,e), it can be noticed, that once again the MLD is mainly controlled by salinity, as the salinity stratification almost entirely matches that of density. It can be also seen that the isohalines mostly move apart (stretch) and shift upwards during those 4 days (Figure 4.25a,b), which is the general case in 18/29 cases (62.1%).

Analyzing now the terms of the balance equations, the shifting upwards of the salinity gradient, seen in the tendency as a dipolar structure surrounding the MLD from 14-02-2009 (Figure 4.24a), can almost entirely be explained by horizontal advection (Figure 4.24c) and tilting (Figure 4.24g). Vertical advection and stretching are small and turbulent mixing of salinity acts to reduce the tilting and horizontal advection mechanisms. On the other hand, the temperature gradient tendency is entirely determined by horizontal advection, demonstrating that the tilting mechanism indeed is changing mostly salinity, since that is the variable possessing strong fronts in the region. So, despite the fact that evaporation exceeds river runoff and precipitation in this region (Figure 4.23d), there are thick barrier layers dominantly formed in this NEC region due to the tilting mechanism.

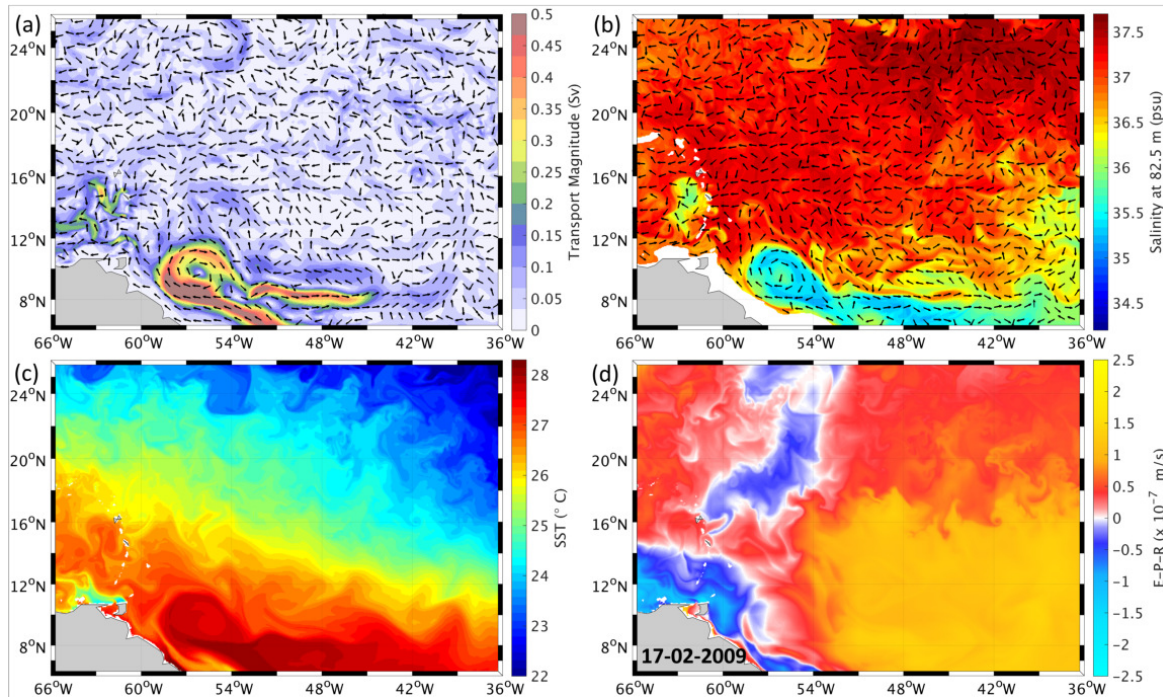


Figure 4.23: Snapshots for 17-02-2009 (winter) of (a) top 152.5 m horizontal transport magnitude (Sv) and direction, (b) salinity (psu) at 82.5 m with corresponding currents, (c) SST ($^{\circ}$ C) and (d) E-P-R ($\times 10^{-7}$ m/s).

At the surface, there is northward horizontal advection of fresh waters from the Amazon river outflow and ITCZ precipitation by NBC and associated rings which are prevalent throughout the year and by equatorial divergence in autumn and winter (Mignot et al., 2007). Indeed, Figure 4.22 (row 4) shows the SSS and the currents at the surface pointing to a northwestward movement in the location of maximum BLT (Figure 4.22 row 1). The SMW also exhibits a strong seasonality, with maximum subduction and export of the "salt river" towards the Caribbean occurring in winter-spring (Blanke et al. (2002), Schmitt and Blair (2015), Figure 4 in Qu et al. (2011)). Blanke et al. (2002) pointed out that most of the flow from the center of the gyre enters the Caribbean Sea (8.2 Sv, 73%) and the peripheral salty water (1.1 Sv, 10%) reach 10° N. So, the high salinity water is transported equatorward by the westward and equatorward oriented NEC out of the formation domain in the subtropical gyre.

In Figure 4.23b we see the large-scale southwestward flow and SMW spreading southwestward at 82.5 m which is a depth inside the ILD on this day. The saline water >37 psu is seen to penetrate the ILD depth range and in the process raise the MLD (Figure 4.25a,b). This explains the horizontal advection negative contribution to the salinity gradient tendency (Figure 4.24a,c). But a vertical shear is created when the southwestward moving SMW subducts and penetrates into the isothermal layer, and, above that, a fresher northward flow is present. The shear in turn promotes a tilting of the vertical salinity front, leading to the positive signal in the tendency term (Figure 4.24a,g).

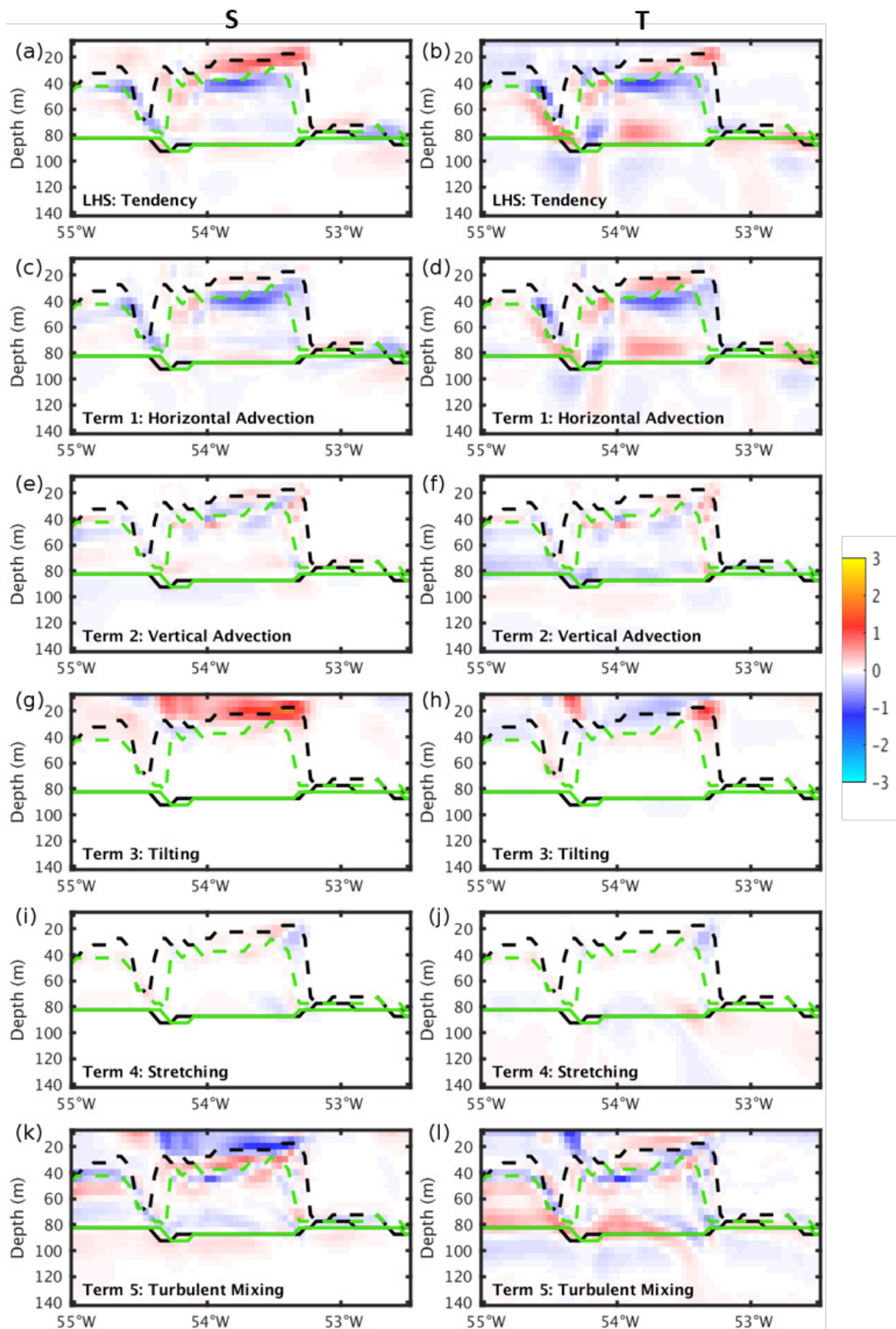


Figure 4.24: Same as Figure 4.15, but in a vertical section at 17.69°N through the maximum BLT present on 17-02-2009. Black (green) solid lines correspond to the ILLD, black (green) dashed lines correspond to the MLD for 17-02-2009 (14-02-2009).

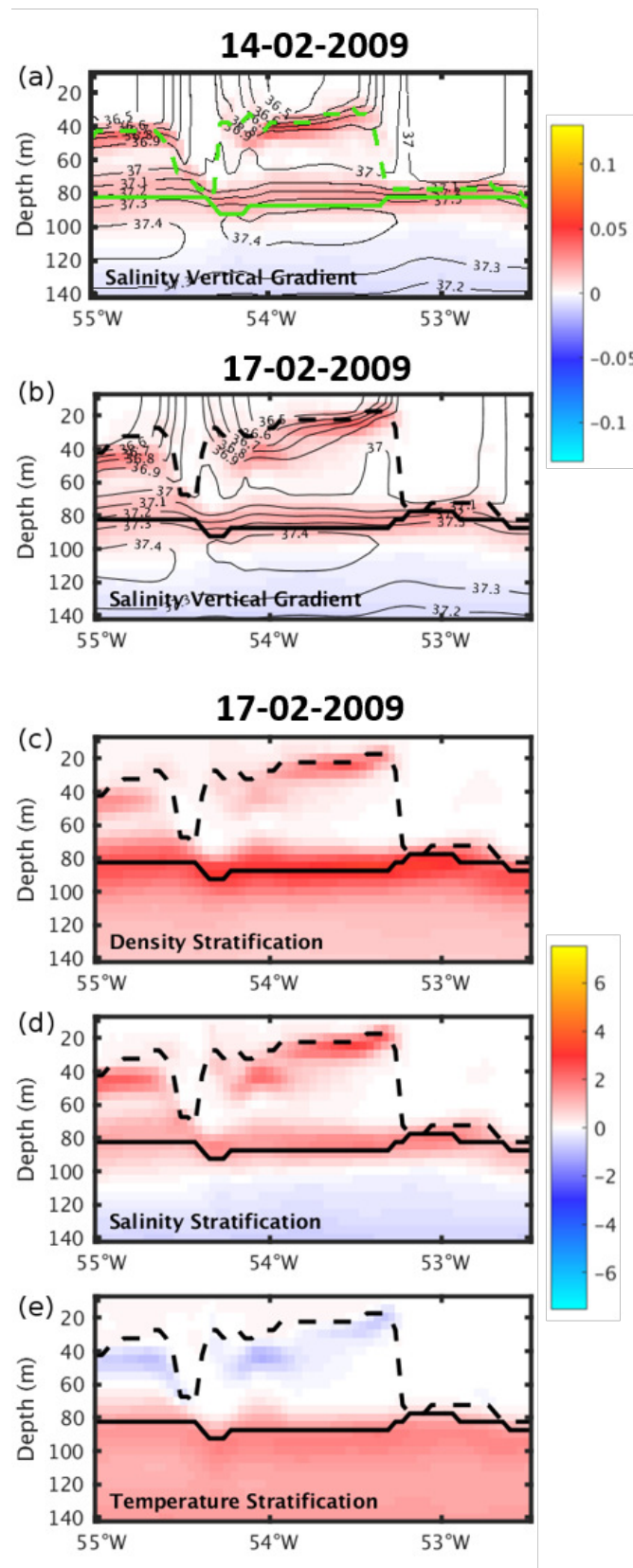


Figure 4.25: Vertical section at 17.69°N through the maximum BLT on 17-02-2009. Salinity vertical gradient (psu/m) with isohalines (psu) superimposed for (a) 14-02-2009 and (b) 17-02-2009. (c) Density, (d) salinity and (e) temperature stratification ($\times 10^{-4}/s^2$) for 17-02-2009 are shown. Black (green) solid lines correspond to the ILLD, black (green) dashed lines to the MLD for 17-02-2009 (14-02-2009).

Turbulent mixing of fresher water homogenizes the water column near the surface above MLD thus decreasing the salinity vertical gradient (Figure 4.24k), but below and at the MLD the turbulent mixing of the salinity increases the salinity gradient as the saltier water from below the MLD is entrained into the MLD, also reducing the MLD and contributing to the growth of BLT.

In conclusion, barrier layers in the NEC region are formed in an area of relatively uniform temperature, due to mainly tilting of salinity fronts. Barrier layers exist on the lower SSS side where the MLD is around 20 m adjacent to the higher SSS side where the MLD is around 90 m (Figure 4.22 row 1, row 3 and row 4). This is consistent with the results of Katsura et al. (2015) for the subtropical Pacific and Veneziani et al. (2014) for subtropical south Atlantic. If a strong shear does not exist above the ILD base due to a weaker northward flow in some areas, simply the convergence of the two water masses may also cause the salinity gradient to intensify. The heavy dense salty water could subduct into the isothermal layer at this region of convergence, thus also shoaling the MLD and forming a barrier layer. This process is explained by Vialard and Delecluse (1998) for barrier layers in the Pacific. In the total 36 events analyzed, I found that the NEC BLT grew due to a shoaling of MLD with negligible or no change in ILD.

Barrier layer decay

In order to study the decay of the above described barrier layers, the average of the salinity and temperature gradient balance terms are now taken for the day of the peak BLT in each of the events encircled in the BLT time series and few days after the peak, when we see the barrier layer getting thinner.

In the shown case of 06-01-2006 (Figure 4.26), the mixed layer deepens during the course of the averaged 4 days (see depth change of black to green dashed curves). The pattern of salinity gradient tendency is now the opposite of the one seen before when analysing the growth of BLT in the region. The deepening of the MLD is associated with a negative salinity vertical gradient tendency (blue in Figure 4.26a) above the resulting MLD (green curve) and with a positive tendency below it. This reveals a downward shift of the salinity gradient (see change from Figure 4.26g to Figure 4.26h) and an increase in its magnitude, brought about by compression and the downward shift of isohalines. In fact this is happening in the majority of the cases identified (18/29 times, 62.1%).

Like for the barrier layer growth, the dominant terms contributing to the tendency are still horizontal advection and tilting (Figure 4.26b,d), but in the decay phase, turbulent mixing (Figure 4.26f) is fundamental. Tilting is now being completely counteracted by turbulent mixing, so that in the end the tendency above the MLD is negative.

The events marked in green in Figure 4.19 are the short-term episodes of large BLT after which the BLT is completely eroded in end-March-April (seen in the seasonal

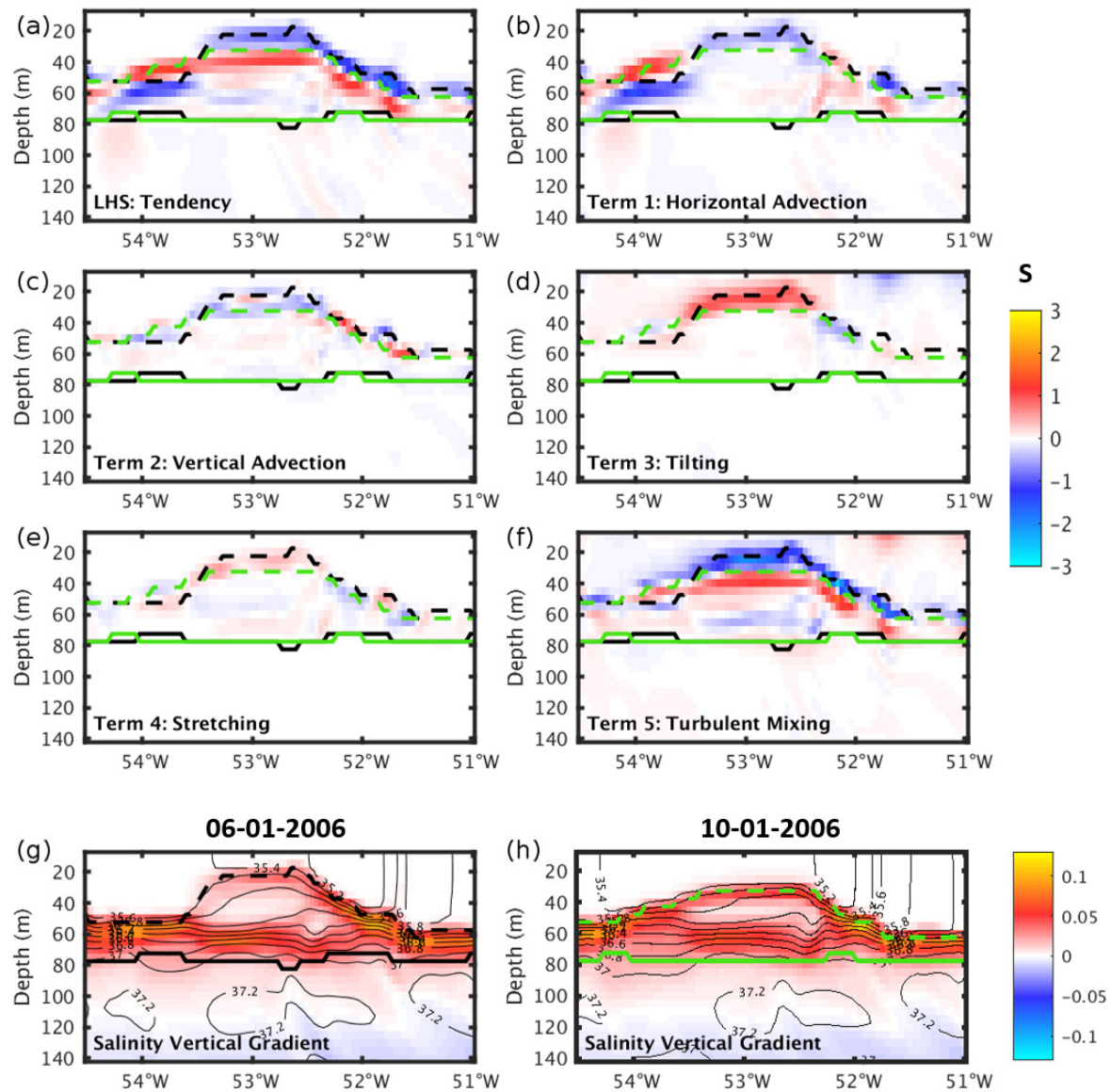


Figure 4.26: Same as Figure 4.14, but vertical section at 14.23°N through the maximum BLT of 06-01-2006, and salinity gradient balance terms are averaged from 06-01-2006 to 10-01-2006 (units are $\times 10^{-7}$ psu/m.s). The salinity vertical gradient (psu/m) with isohalines (psu) superimposed are shown for (g) 06-01-2006 and (h) 10-01-2006. Black (green) solid lines correspond to the ILD, black (green) dashed lines to the MLD for 06-01-2006 (10-01-2006).

evolution). These green events represent the abrupt erosion of these localized barrier layers at the end of the season. Figures 4.27 and 4.28 illustrate one of these events. Figure 4.28e,g,i show that the shallowing of MLD and therefore the peak BLT on 19-03-2003 is due to salinity stratification as explained in the above subsection, but four days later this barrier layer erodes completely. MLD and ILD both shoal from 19-03-2003 to 23-3-2003.

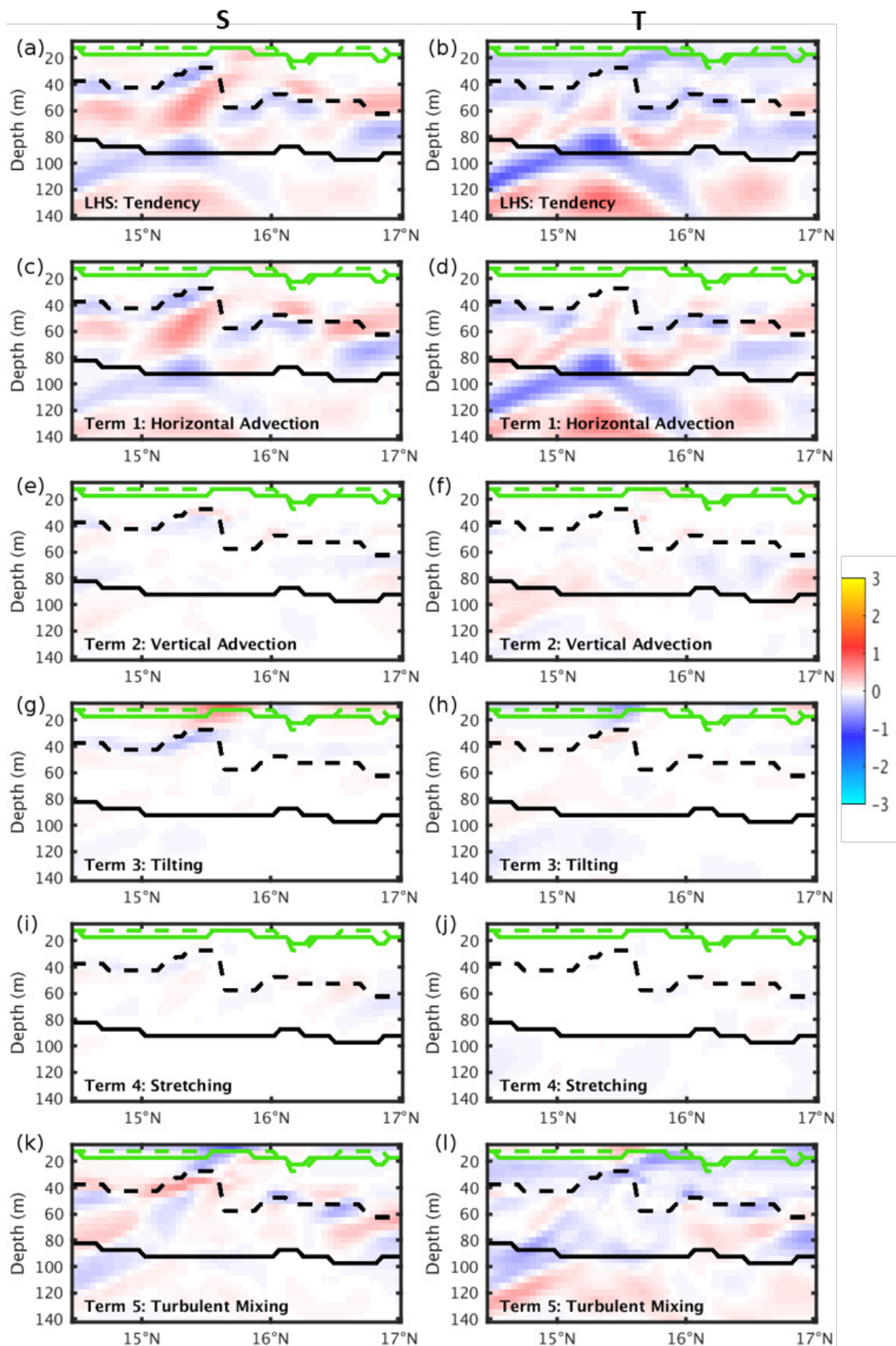


Figure 4.27: Same as Figure 4.15, but vertical section at 54.87°W through the maximum BLT on 19-03-2003, and the gradient balance terms are averaged from 19-03-2003 to 23-03-2003. Black (green) solid line is ILD, black (green) dashed line is MLD for 19-03-2003 (23-03-2003).

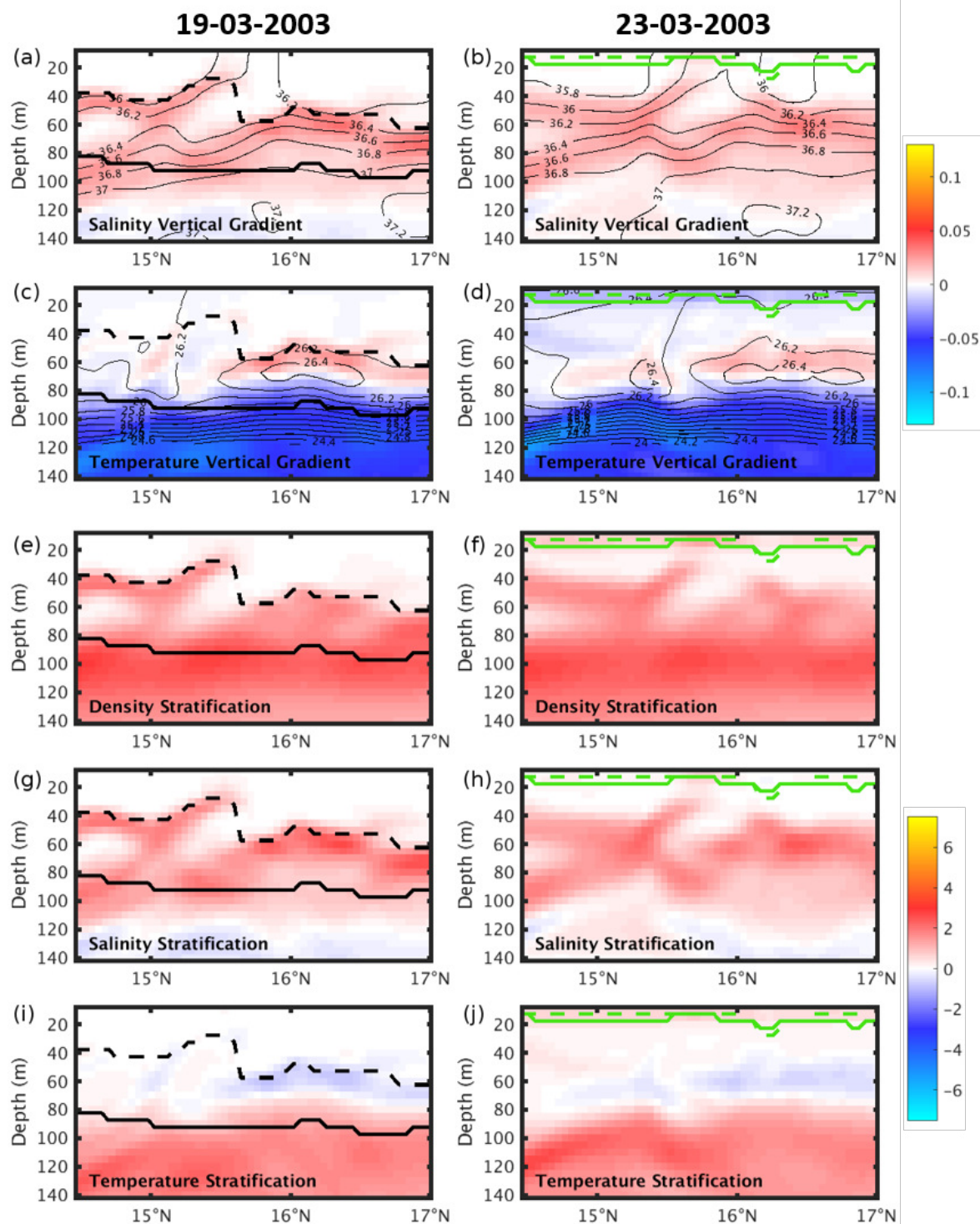


Figure 4.28: Same as Figure 4.16, but vertical section at 54.87°W through the maximum BLT on 19-03-2003. (a,b) salinity vertical gradient (psu/m), with isohalines (psu) superimposed; (c,d) temperature vertical gradient ($^{\circ}\text{C}/\text{m}$) with isotherms ($^{\circ}\text{C}$) superimposed, (e,f) density, (g,h) salinity and (i,j) temperature stratification ($\times 10^{-4}/\text{s}^2$) for 19-03-2003 and 23-03-2003, respectively. Black (green) solid line is ILD, black (green) dashed line is MLD for 19-03-2003 (23-03-2003).

So far in this region there were almost no changes in ILD in the evolution of the short-term barrier layers, except now in spring, as on 23-3-2003 (Figure 4.28 right column), when there is decay of BLT by shallowing of ILD. Due to increasing net heat flux in spring, the temperature at the surface above MLD increases from 19-03-2003 to 23-03-2003 by 0.2°C , producing a negative temperature vertical gradient (Figure 4.28c,d) at the surface as the isotherms compress, which occurs in all the 7 cases (100%).

Turbulent mixing and tilting dominantly contribute to the negative temperature vertical gradient tendency (Figure 4.27l,h), while for salinity tilting and horizontal advection seem to be dominant in reducing the MLD (Figure 4.27g,c). The temperature stratification (Figure 4.28j) is more dominant than salinity stratification (Figure 4.28h) in determining the density stratification (Figure 4.28f) and reducing the ILD as well as MLD in this case, eroding the barrier layer.

In conclusion, we saw in this section that the BLT is maximum in the NEC region during the winter months of February-March and has a seasonal minimum in April-May. Tilting followed by stretching, horizontal advection and turbulent mixing are the dominant mechanisms that mostly stretch the isohalines to reduce the MLD, generating a barrier layer in this region. The barrier layers here decay mostly due to the compression and a downward shift of isohalines brought about by turbulent mixing and horizontal advection. On a seasonal perspective, the barrier layer grows due to slower deepening of MLD and comparatively faster deepening of ILD in winter and is completely eroded in spring by shoaling of ILD due to temperature stratification change. The formation and evolution of the high-frequency events of barrier layer growth/decay are controlled more by the changes in MLD than ILD.

4.5 Barrier layer in the ITCZ region

The seasonal migration of the ITCZ was highlighted in Chapter 2. In this section I investigate the barrier layers formed in the central tropical Atlantic, in the chosen region of 4°S - 13°N , 6 - 30°W . This region was identified to have BLT of small magnitudes (Figure 3.4c and Figure 4.1). Away from any fresh river water being advected, the freshwater source that could possibly cause barrier layers in the open ocean is rainfall.

The daily time series of ILD, MLD and BLT area-averaged in the ITCZ region over the period 2003-2011 are presented in Figure 4.29. There is only a weak tendency for the BLT to show a seasonal cycle, being largest in December-January, August-October and June-July. The peak BLT events, corresponding to short daily episodes of barrier layers (denoted in red circles in Figure 4.29, 123 events), have large amplitudes compared to the small seasonal cycle in this region.

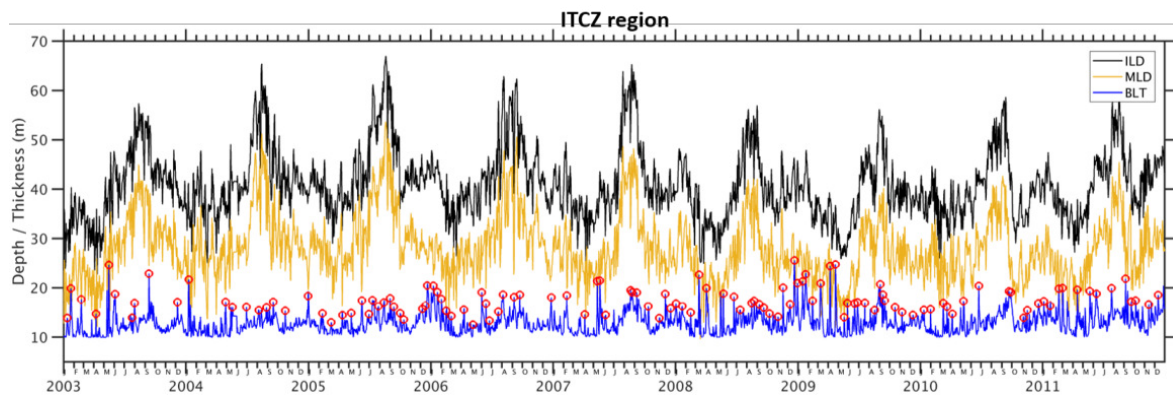


Figure 4.29: Daily time series of area-averaged ILD (meters, black), MLD (meters, yellow) and BLT (meters, blue) in the central tropical Atlantic in the ITCZ region (4°S - 13°N , 6 - 30°W). Red circles are the events of large BLT.

4.5.1 Seasonal evolution

The ILD and MLD both start rising in June-July, are largest in August-September (~ 67 m for ILD and ~ 55 m for MLD), and start decreasing from October onwards. The wind stress magnitude (Figure 4.30) is largest in this region in July-September, which is one of the factors causing the wind-mixing to take place in the upper ocean, deepening the MLD and ILD. The surface net heat flux, and consequently the SST, are smallest in August-September (Figure 4.30). In this box, the Evaporation-minus-Precipitation time series (not shown) drops from June onwards, until it is the smallest in September and rises thereafter peaking in February and later again in May. The seasonal SSS is also largest in May-June. Therefore, the cold and saline water causes convective mixing which also contributes to the deepening of ILD and MLD. The SSS weakens and starts getting small when the ILD is at its peak, thus causing the MLD to be smaller than ILD and giving rise to the barrier layers in September.

There is a second peak in ILD from December-February, when there is usually a drop in MLD. In most of the years we also see a second peak in wind stress magnitude in December-January, which contributes to this second deepening of MLD and ILD. There is a larger decrease in net heat flux, and a comparatively smaller decrease in SST every year, also in December-January after the largest decrease seen previously in August-September. This causes the second deepening of ILD. The SSS continues to decrease and is the smallest in December-January, causing the shoaling of MLD over the deep ILD, giving rise to the large seasonal BLT in these months.

On examining the daily fields of BLT I found that in this region the barrier layers do not last for an entire season in one particular location, like in the case of the NEC region. Rather, the brisk and brief episodes of rainfall due to the migrating ITCZ cause barrier layers to be of the same nature, lasting thus for brief periods of a few days.

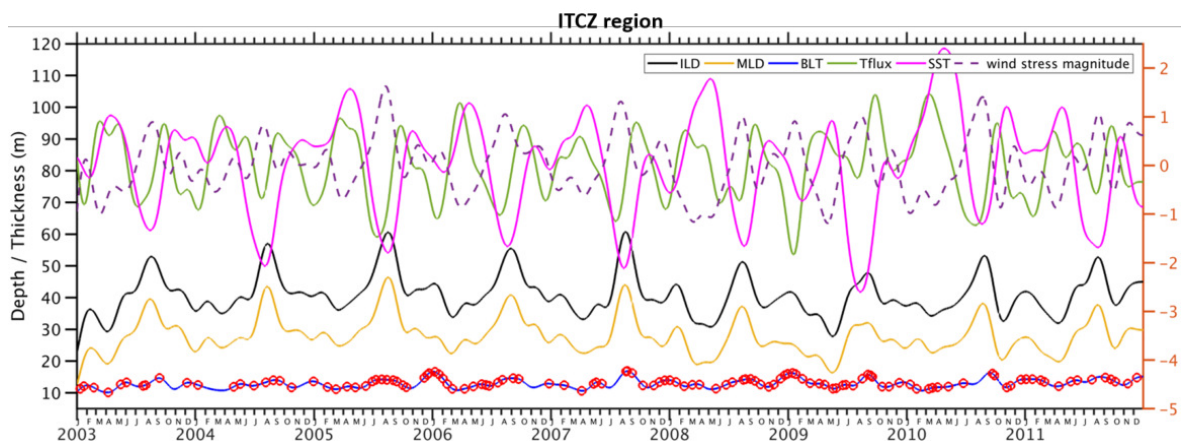


Figure 4.30: Time series of ILD, MLD, BLT, net surface heat flux, SST and wind stress magnitude low-pass filtered with a 60 days cut-off filter. Red circles depict events with large BLT.

4.5.2 Short timescale events

Next I will shed light on the formation mechanisms of the high frequency daily events of large barrier layers in this ITCZ region. As stated, in the central tropical Atlantic, the barrier layers change their position over the year, according to the migration of the ITCZ. So to examine the growth and decay mechanisms of the BLT, vertical sections are taken over different locations in the ITCZ-box depending on where the localized BLT signal exists.

Barrier layer growth

The largest BLT peaks in this region are found every year during December-February. Figure 4.31 presents the BLT from one of the peak events (red circles in Figure 4.29) during 30-12-2004. The figure shows the progression of the growth and decay of this BLT from 29-12-2004 to 01-01-2005. It is clearly noticeable that the large BLT at 20.72°W , 2.51°N occurs due to the ITCZ rainfall passing over it. The E-P-R magnitude is largely negative in that area, meaning large precipitation (Figure 4.31 row 1, row 5). The SSS is seen to decrease at that location, with a freshwater lens forming on top of the saline water (Figure 4.31 row 4). The MLD and ILD are deep in the background in that region, but as soon as the rainfall takes place, the MLD shoals due to salinity changes, while the ILD still remains unaffected (Figure 4.31 row 2, row 3). This gives rise to the thick BLT on 30-12-2004 and 31-12-2004.

The event of barrier layer growth from 28-12-2004 to 30-12-2004 is illustrated in Figures 4.32. The 60 m thick barrier layer present on 30-12-2004 extending from $1-4^{\circ}\text{N}$ in this section along 20.72°W , forms since 28-12-2004 due to a drastic shallowing of the MLD (see also dashed curves in Figure 4.32a,g,h). The shallowing of the mixed layer causes the BLT to increase and is associated with a positive salinity vertical gradient

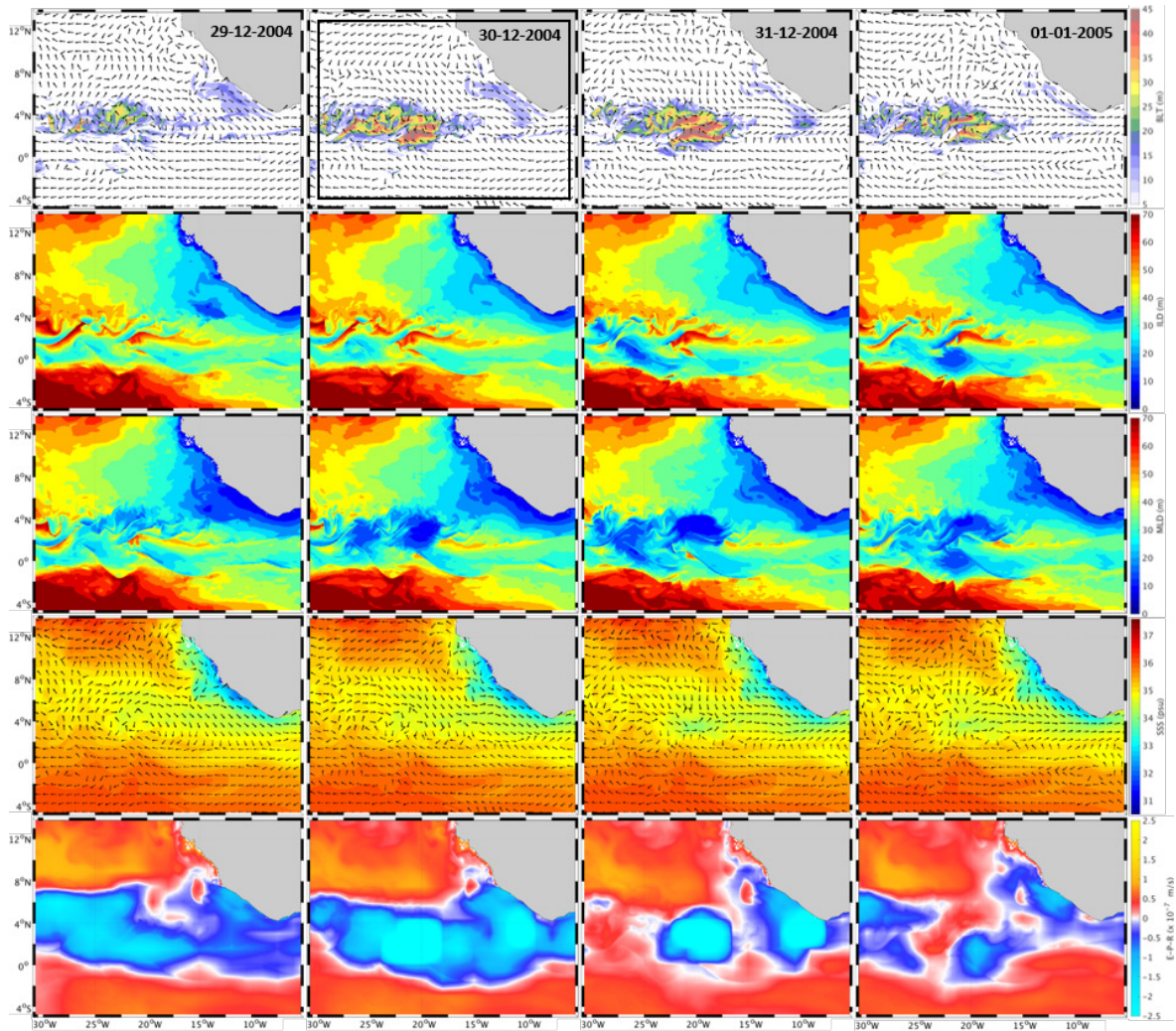


Figure 4.31: Snapshots from 29-12-2004 to 01-01-2005 showing the growth and decay of the maximum BLT on 30-12-2004 (black box delineates the ITCZ region): (row 1) BLT (meters), with vectors showing surface currents, (row 2) ILD (meters), (row 3) MLD (meters), (row 4) SSS (psu), with vectors showing surface currents and (row 5) E-P-R ($\times 10^{-7}$ m/s).

tendency, meaning an increase in the salinity vertical gradient from 2 days before until the day of the peak BLT (Figure 4.32a). A similar, but weaker, pattern is seen in the temperature gradient tendency (not shown).

Looking at the individual contributions of salinity and temperature for the density stratification (Figure 4.32i,j,k), it can be noticed that once again the MLD is mainly controlled by salinity, as the salinity stratification almost entirely match that of density, and almost no temperature stratification exists in the upper 30 m. It can be also seen that the isohalines mostly move together or compress at the surface during those 3 days (Figure 4.32g,h), due to fresher water on the surface. This is the general case in 100% of the peak BLT cases.

Analyzing now the terms of the balance equations, it is clear that co-located with

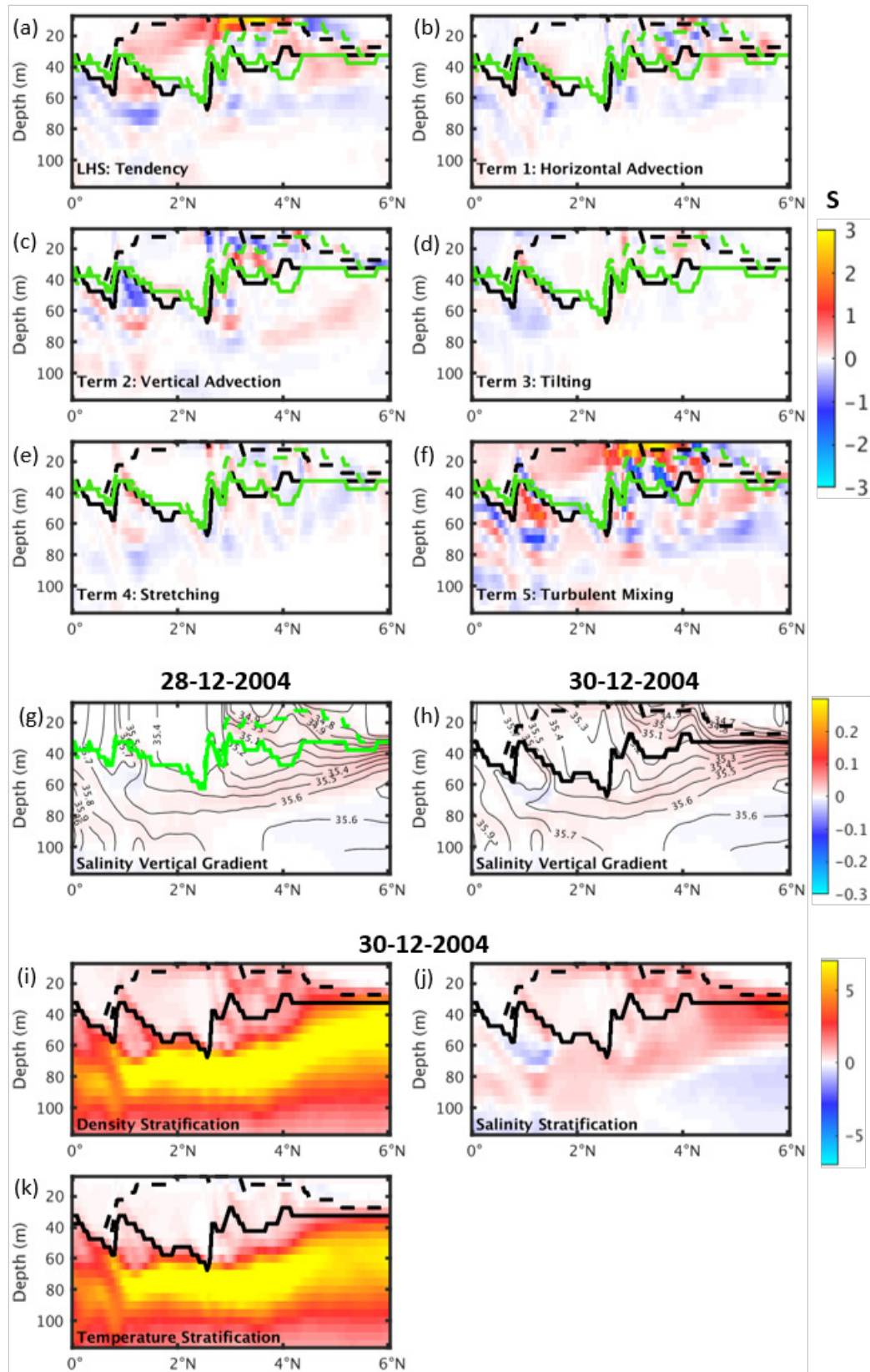


Figure 4.32: Vertical section at 20.72°W of the salinity gradient balance terms averaged from 28-12-2004 to 30-12-2004 (units are $\times 10^{-7}$ psu/m.s). Black (green) solid lines correspond to the ILLD, black (green) dashed lines to the MLD for 30-12-2004 (28-12-2004). Salinity vertical gradient (psu/m) with isohalines (psu) superimposed for (g,h) both days. Corresponding (i) density, (j) salinity and (k) temperature stratification ($\times 10^{-4}/\text{s}^2$) on 30-12-2004.

this change in MLD, there is a positive salinity gradient tendency, meaning that the salinity gradient increased from the 28-12-2004 to the 30-12-2004 at those particular depths. This can almost entirely be explained by the turbulent mixing term which contains the surface forcing (Eq. 4.1 and Eq. 4.3 in section 4.2). At the air-sea interface, turbulent salinity flux depends on precipitation and evaporation. The other terms of the salinity balance do not contribute much; horizontal advection and tilting negligibly contribute to the positive tendency. Vertical advection and stretching are also small and oppose the affect of turbulent mixing, horizontal advection and tilting.

Figure 4.33 illustrates an event of the peak BLT in September, which was also seen to be one of the months with peak BLT in this region. The snapshots present the growth and decay of barrier layers present on 05-09-2011, one of the many large BLT peaks circled in red in Figure 4.29. In this event, we see that the intense localized precipitation is responsible for the MLD to shoal over a nearly constant ILD, giving rise to 50 m BLT on 05-09-2011. The emergence of the freshwater signal at that spot is seen in the SSS field of 05-09-2011 which is accompanied by a drastic localized shoaling of MLD.

The 50 m thick barrier layer present on 05-09-2011 extending from 5-9°N in the section along 25.56°W, forms since 03-09-2011 due to dominantly a shallowing of the MLD during those 3 days (see dashed curves in Figure 4.34a,g,h). In September the salinity gradient is high at the surface due to vertical compression of isohalines and shallowing of the MLD due to fresh water at the surface. At the MLD on 05-09-2011, the density stratification is completely explained by the salinity stratification (Figure 4.34i,j,k). The term dominantly contributing to the formation of this BLT is the turbulent mixing of this surface forcing of freshwater (Figure 4.34a,f).

The same behavior of the isohalines is seen for all the events marked in red thus giving a 100% occurrence over the entire year, mostly with largest BLT magnitudes in December, September and April-June. The compression of isohalines at the surface due to turbulent mixing of freshwater on the surface is the main reason for the shoaling of the MLD and the formation of these barrier layers under the ITCZ. On examining all the events with peak BLT, along with the shoaling of MLD there was generally no deepening of ILD. Only rarely a negligible deepening of ILD occurred.

Barrier layer decay

In order to study the decay of the above described barrier layers, the averages of the salinity and temperature gradient balance terms are now taken between the day of the peak BLT and a few days after the peak, when we see the barrier layer getting thinner.

Along with the formation, Figure 4.31 and Figure 4.33 show the decay of the large barrier layers on 30-12-2004 and 05-09-2011, respectively. We see that the decay of these barrier layers on both days is due to dominantly the mixed layer deepening soon after the episode of the intense ITCZ rainfall is past.

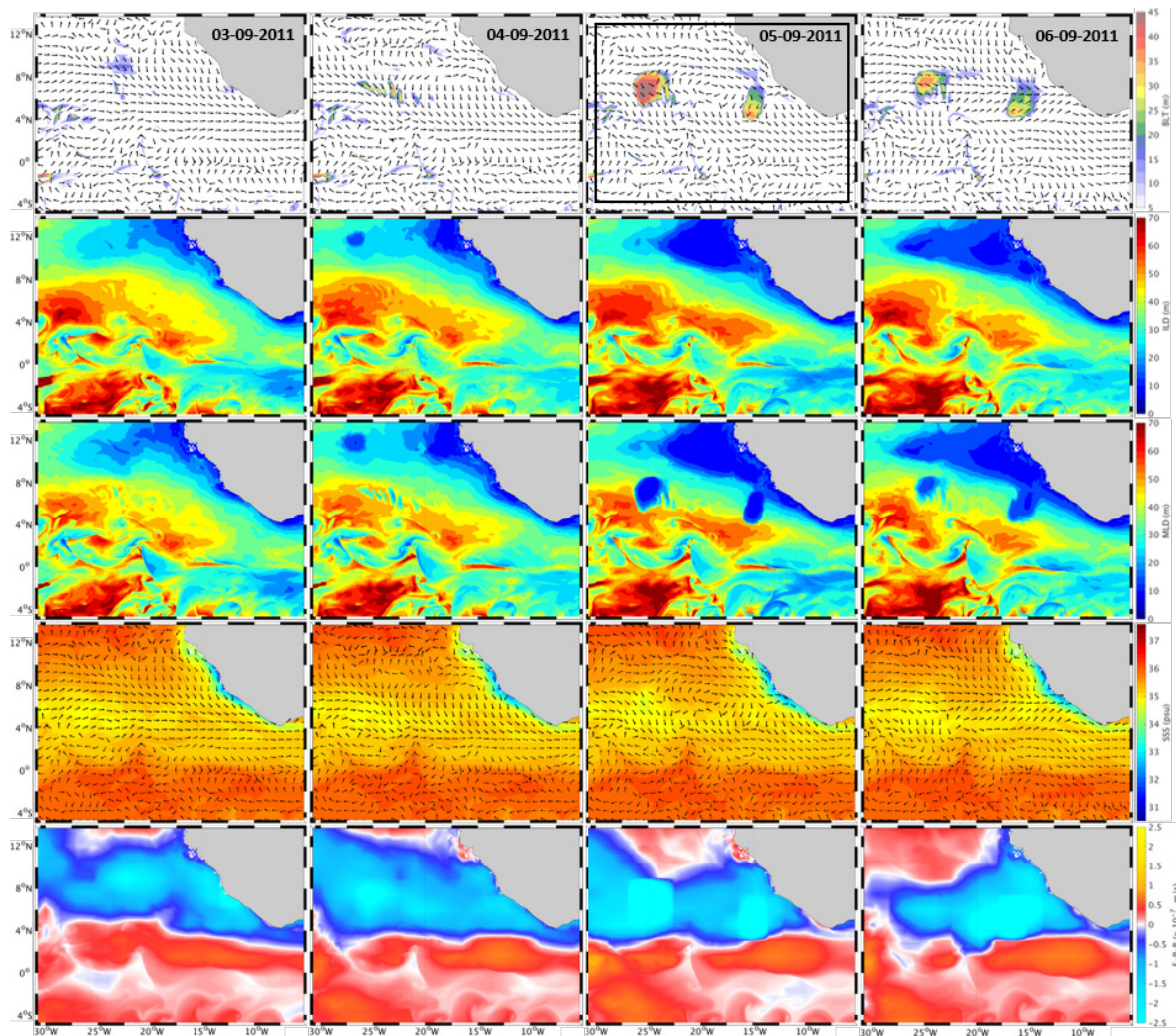


Figure 4.33: Same as Figure 4.31 for an event with maximum BLT on 05-09-2011

In the shown case of 05-09-2011 (Figure 4.35), the mixed layer deepens during the course of the averaged 3 days (see depth change between dashed black and dashed green curves). The pattern of salinity gradient tendency is now the opposite of the one seen before when analysing the growth of BLT in the region. The deepening of the MLD is associated with a negative salinity vertical gradient tendency (blue in Figure 4.35a) above the resulting MLD (green curve) and to a positive tendency below it. This reveals a downward shift of the salinity gradient (see change from Figure 4.35g to Figure 4.35h) and an increase in its magnitude due to moving apart of isohalines at the surface. In fact this is happening in the majority of the cases identified (95/123 times, 77%).

The dominant terms contributing to the tendency are turbulent mixing, tilting and horizontal advection. Stretching is negligible, while vertical advection counteracts the above processes. In the minority of cases, MLD deepens in 24/123 cases (19.31%) by the compression of isohalines. Apart from the deepening of MLD, a minor shoaling of ILD contributes to the thinning of the barrier layer in 48/123 times (39.02%). This

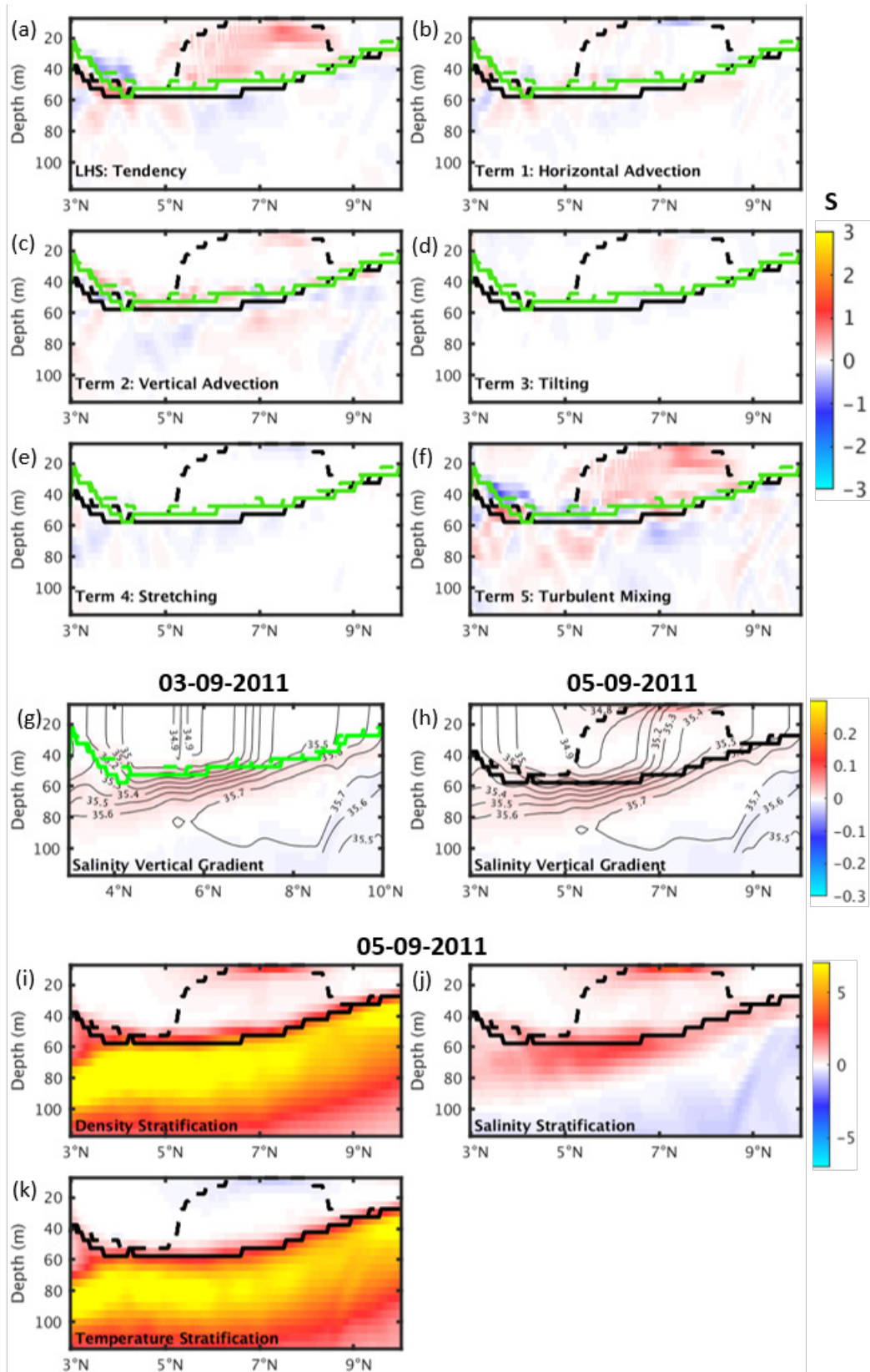


Figure 4.34: Same as Figure 4.32, but vertical section at 25.56°W of the salinity gradient balance terms averaged from 03-09-2011 to 05-09-2011. Black (green) solid lines correspond to the ILLD, black (green) dashed lines to the MLD for 05-09-2011 (03-09-2011). Corresponding (i) density, (j) salinity and (k) temperature stratification on 05-09-2011.

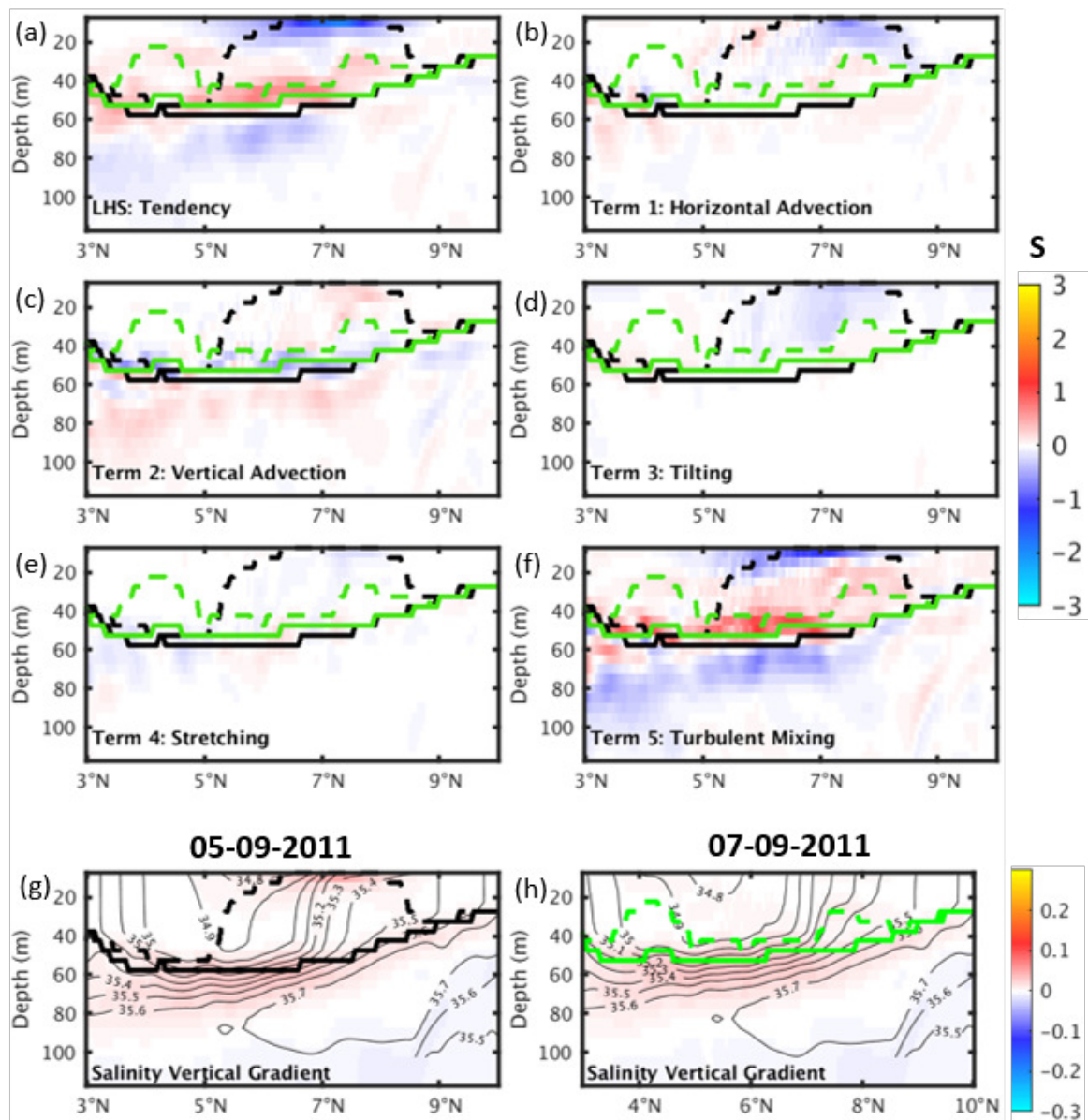


Figure 4.35: Vertical section at 25.56°W of the salinity gradient balance terms averaged from 05-09-2011 to 07-09-2011 (units are $\times 10^{-7}$ psu/m.s). Salinity vertical gradient (psu/m) with isohalines (psu) superimposed for (g,h) both days. Black (green) solid lines correspond to the ILD, black (green) dashed lines to the MLD for 07-09-2011 (05-09-2011).

happens mostly when the isotherms are compressed vertically due to turbulent mixing.

Thus we see in the ITCZ region that the BLT forms and decays generally because of a change in MLD. Turbulent mixing of the freshwater on the surface plays a major role in the formation, while turbulent mixing along with a tilting of the salinity front into vertical, locally destroys the BLT. In most of the cases there is no ILD change in the formation or decay of the BLT here.

4.6 Barrier layer in the ETA region

The last of the four identified regions having significant BLT in the tropical Atlantic is the region in the eastern tropical Atlantic (ETA) in the Niger river plume (1°S - 7°N , 11°E - 1°W). The magnitude of the BLT is in general smaller than the ones seen earlier at the Amazon plume (in sections 4.3 and 4.4, as well as in Figure 4.1 in section 4.1, and in Figure 3.4 of Chapter 3). The Niger River also discharges a smaller amount of freshwater than the Amazon. Further south, thin barrier layers are formed by the Congo River's freshwater discharge. They are not accounted in this analysis, since those barrier layers are much smaller and sparse than the ones addressed here.

Figure 4.36 shows the simulated daily variability of ILD, MLD and BLT for the years 2003-2011 in the ETA box. During August-October there are thick barrier layers, with the thickest occurring in September-October. Every year there is a second season of large BLT occurrences in February-March. Just like for the NBC and NEC areas, beside the dominant seasonal signal in BLT, there is high-frequency variability superimposed. Those short events are marked in red circles (69 events). The growth and decay of the seasonal barrier layer and of the individual peak events were investigated and results are presented next.

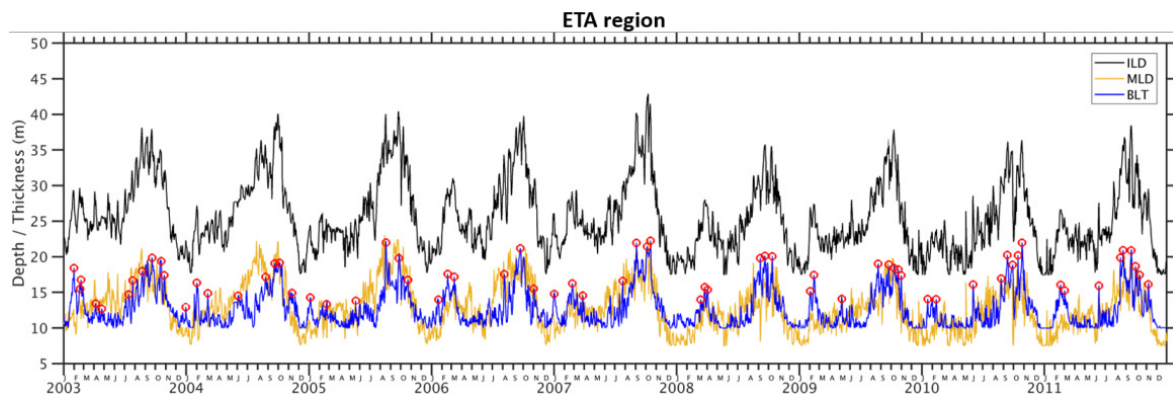


Figure 4.36: Daily time series of area-averaged ILD (meters, black), MLD (meters, yellow) and BLT (meters, blue) in the Niger river plume in the eastern tropical Atlantic (1°S - 7°N , 11°E - 1°W). Red circles are the events of large BLT.

4.6.1 Seasonal evolution

In Figures 4.36 and 4.37 the ILD and MLD curves rise in August, have their seasonal maximum in September-October and a seasonal minimum in December-January. There is a second peak in ILD and sometimes a very small peak in MLD in February-April.

The wind stress has largest magnitude in July-September, which stirs the upper ocean and thus deepens the ILD and MLD. There is also, in most years, a second peak in wind magnitude in February which contributes to deepen the ILD and MLD

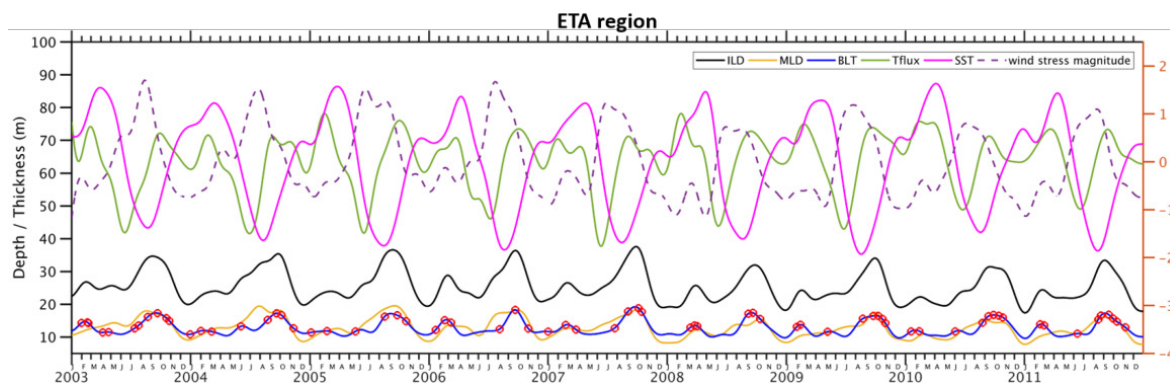


Figure 4.37: Time series of ILD, MLD, BLT, net surface heat flux, SST and wind stress magnitude low-pass filtered with a 60 days cut-off filter. Red circles depict events with large BLT.

in that time. The net heat flux is minimum around June in this box, and has a second minimum in December. Following the drops in net heat flux, the SST is minimum around September (Figure 4.37) and has a plateau or a reduction again in January-February. Thus the convective mixing caused by the cold dense water along with the strong wind stirring results in the deepest isothermal and mixed layer in September-October and again in February.

Even though the ILD and MLD both have their seasonal peaks in September-October, the difference between them is the largest in those months, the largest ILD being ~ 44 m in October 2007, with MLD amounting to ~ 21 m. This gives rise to the largest BLT of ~ 23 m, also seen in certain other years in the time series. The Niger river runoff rises from June, peaks in September-October and reduces thereafter (Dossa et al., 2019). Additionally, precipitation here is also high during September-October. Both factors lead to more freshwater and thus small values of SSS from September-April. This shoals the MLD during this period.

The mechanisms responsible for the seasonal cycle of barrier layers in the ETA region are identified next. As seen so far in Figure 3.4d, Figure 4.36 and Figure 4.37, the maximum seasonal BLT is in September-October. Figure 4.38 presents a vertical section at 1.7°N (between 9°E and 4°E) of the temperature and salinity gradient balance terms. They are averaged from July to September in order to retain the main contributions at the seasonal scale (with the contribution from all small-scale events being averaged out). The black and green curves in the figure show how the MLD and ILD change from July, when the barrier layer just starts to form, to September, when there is a maximum BLT.

The MLD shoals slightly from July to September with a positive salinity gradient tendency due to primarily tilting and partially by stretching, as these terms increase the salinity gradient tendency between the two MLDs (Figure 4.38a,g,i). The rest of the terms compensate the above. The ILD deepens from July to September with a positive

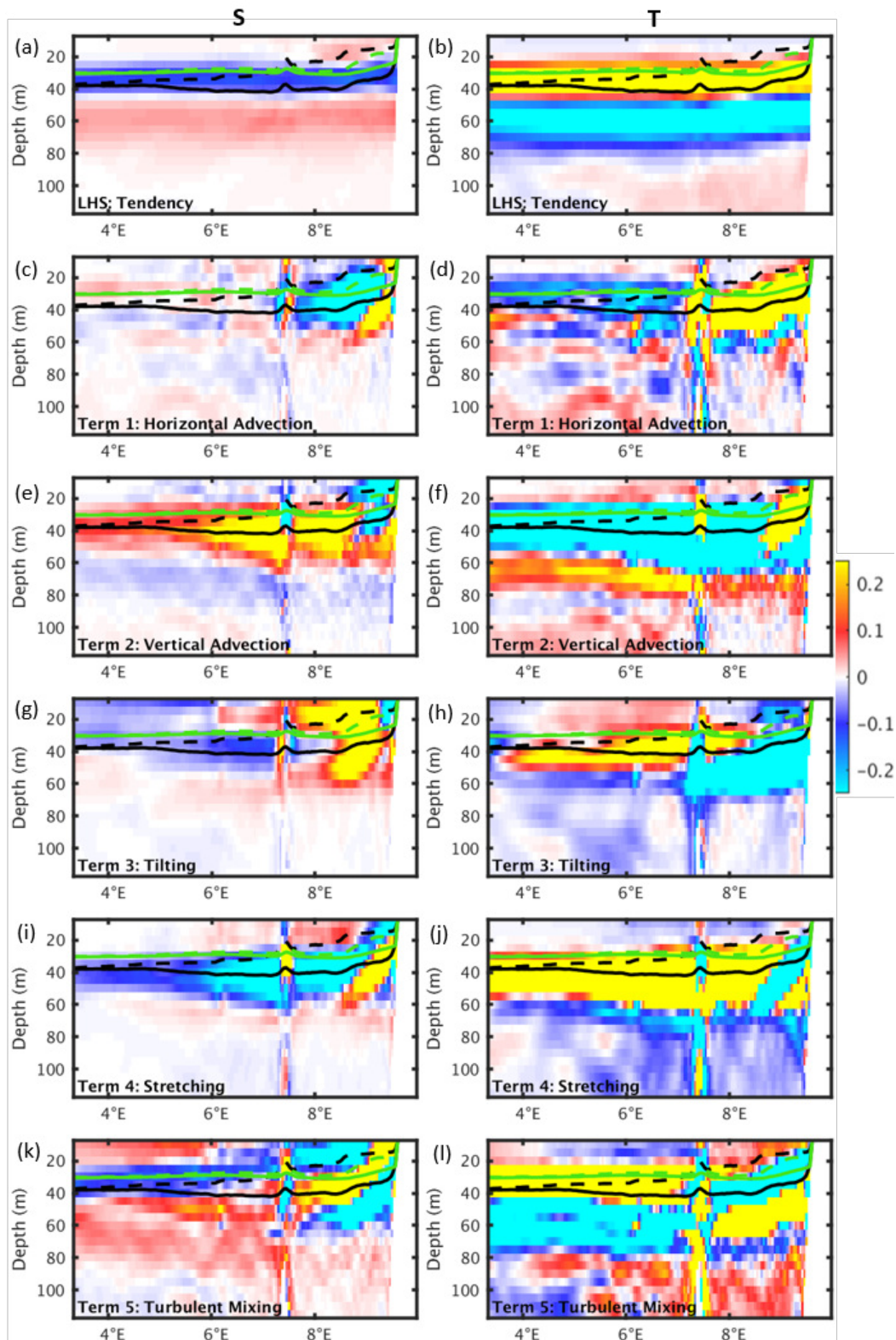


Figure 4.38: Vertical section at 1.7°N through the maximum climatological BLT in September, of salinity and temperature gradient balance terms averaged from July to September (units are $\times 10^{-7}$ psu/m.s and $\times 10^{-7}$ $^\circ\text{C}/\text{m.s}$, respectively). Black (green) solid line is ILD, black (green) dashed line is MLD for September (July).

temperature vertical gradient tendency between the two ILDs (Figure 4.38b). Stretching, horizontal advection, turbulent mixing and tilting contribute to this increase in ILD (Figure 4.38b,d,h,j,l).

This seasonal peak of barrier layers in September gets smaller in November-December. MLD and ILD both shoal from September to November-December, as also seen in Figure 4.36 and Figure 4.37. In Figure 4.39 it is noticed that the ILD shoals with a negative temperature vertical gradient tendency due to turbulent mixing of warmer water (net heat flux and SST curves in Figure 4.37), tilting and vertical advection. The temperature stratification due to heating of the ocean surface causes this shoaling of ILD and MLD in November-December.

In Figure 4.40 a vertical section at the same location (1.7°N) of balance terms averaged from December, when there is almost no BLT, to February, when there is the second peak in the seasonal cycle of BLT, with the climatological MLD and ILD for those months superimposed, shows that the ILD deepens from December to February, but the MLD does not undergo much change. The deepening of the ILD is seen to be caused by stretching and temperature gradient horizontal advection. This peak BLT in February is thin again in April (Figure 4.41) due to shoaling of ILD and deepening of MLD. Shoaling of the ILD is due to turbulent mixing, tilting and vertical advection. Deepening of the MLD is due to horizontal advection, stretching and turbulent mixing.

In summary, tilting is the dominant mechanism in the shoaling of the seasonal MLD followed by turbulent mixing and stretching. Stretching, turbulent mixing and horizontal advection are the mechanisms contributing to the increase in ILD. The decay of BLT here is due to both the shoaling of ILD due to turbulent mixing, tilting and vertical advection, and the deepening of MLD due to horizontal advection, stretching and turbulent mixing, with the shoaling of ILD being dominant in the decay of BLT in December.

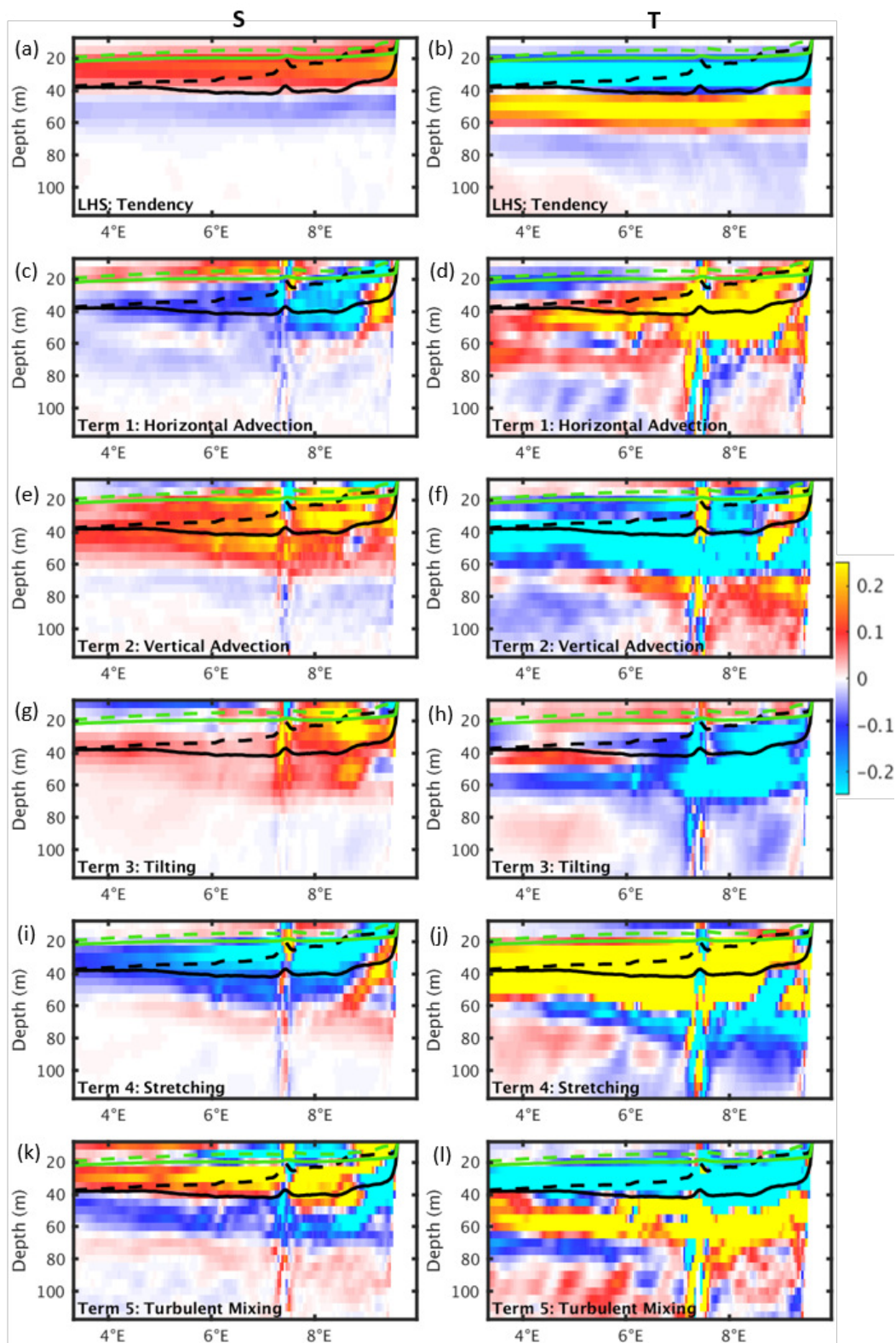


Figure 4.39: Same as 4.38 but salinity and temperature gradient balance terms averaged from September to December (units are $\times 10^{-7}$ psu/m.s and $\times 10^{-7}$ $^{\circ}\text{C}/\text{m.s}$, respectively). Black (green) solid line is ILLD, black (green) dashed line is MLD for September (December).

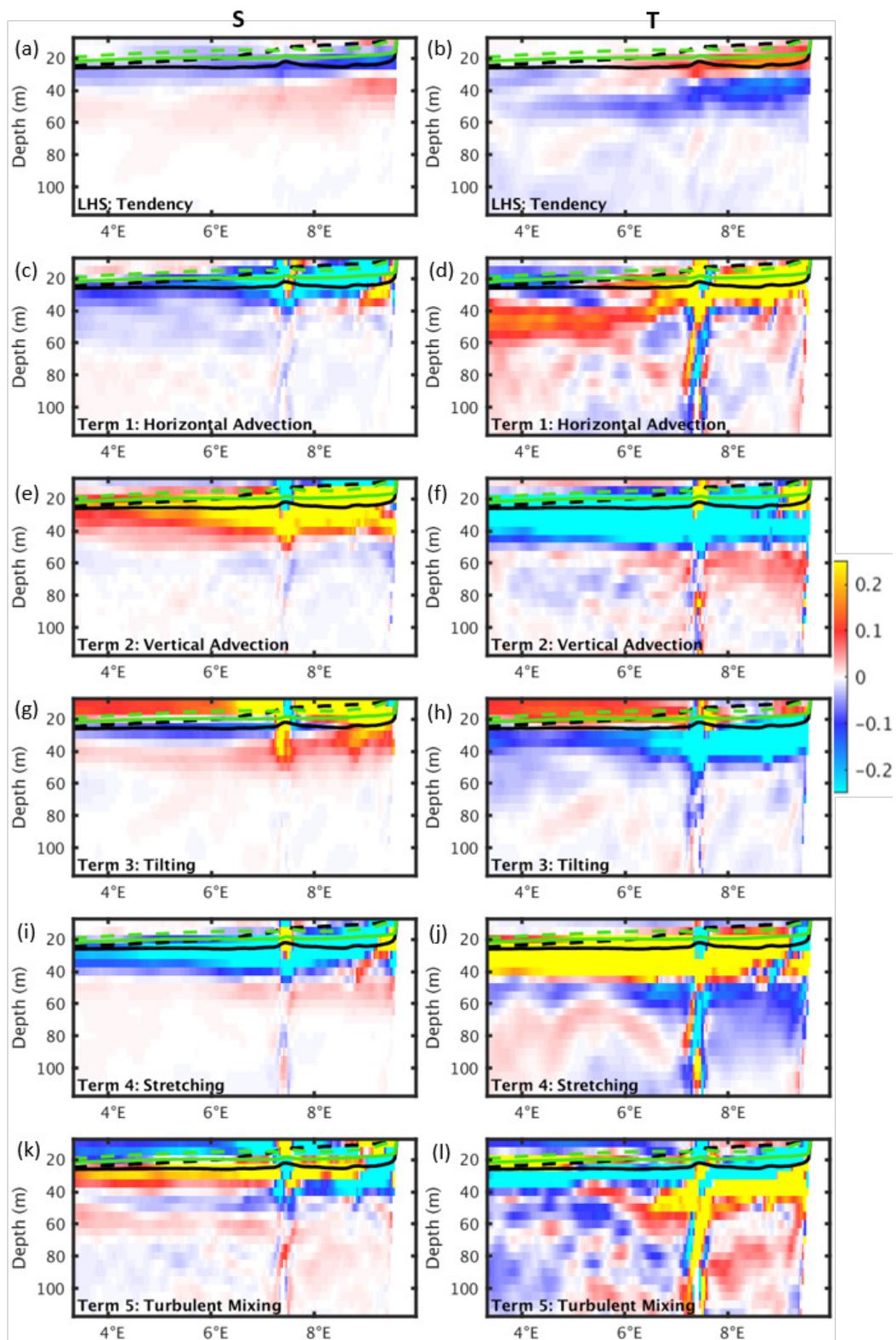


Figure 4.40: Same as 4.38 but salinity and temperature gradient balance terms averaged from December to February (units are $\times 10^{-7}$ psu/m.s and $\times 10^{-7}$ $^{\circ}C$ /m.s, respectively). Black (green) solid line is ILLD, black (green) dashed line is MLD February (December).

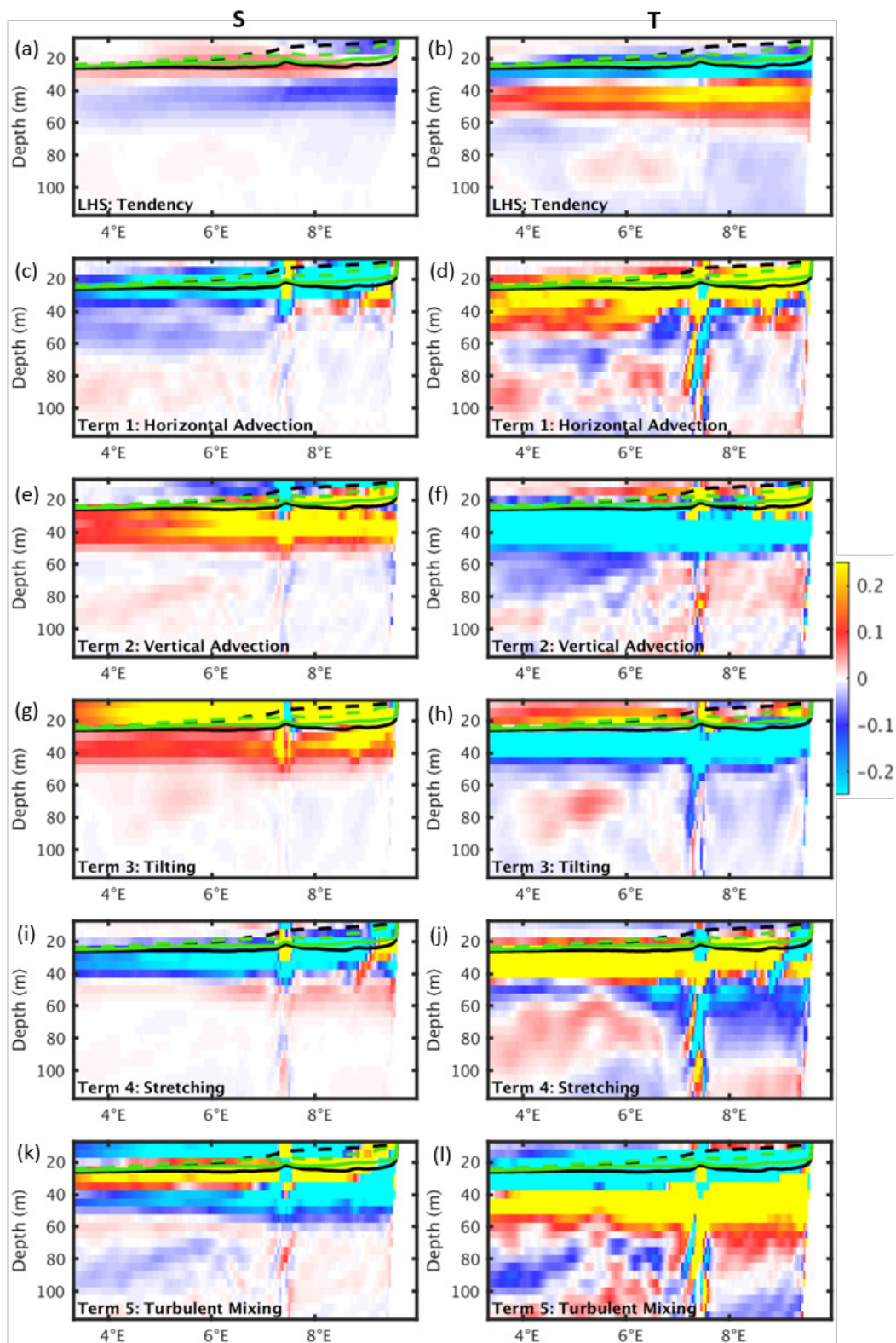


Figure 4.41: Same as 4.38 but salinity and temperature gradient balance terms averaged from February to April (units are $\times 10^{-7}$ psu/m.s and $\times 10^{-7}$ $^{\circ}\text{C}/\text{m.s}$, respectively). Black (green) solid line is ILD, black (green) dashed line is MLD February (April).

4.6.2 Short timescale events

Barrier layer growth

Figure 4.42 presents the growth and decay of the BLT from one of the peak events in October, (red circles in Figure 4.36) occurring on 18-10-2003. A 60 m BLT is seen around 1.8°N, 7°E on that day. The E-P-R is negative, both large runoff and heavy precipitation are acting on these days in this region (Figure 4.42 row 5). We see the signal of freshwater spreading from the coast towards the open ocean, against the direction of the surface currents (Figure 4.42 row 4). Away from the coast, the ILD and MLD are both large (Figure 4.42 row 2, row 3). The ILD keeps getting large in the region of the large BLT formation until 18-10-2003 and the MLD shoals, helping the barrier layer to grow. The MLD reduces on the side of smaller SSS where there is fresher water. On the west of the salinity front the SSS is large and so is the MLD. We see that the saline water from west is being pushed towards the coast, while the freshwater moves in the opposite direction. These barrier layers align in an interesting pattern, that is localized and small in spatial extent variability, confined to the salinity frontal region. On 18-10-2003 the ILD is deep (around 60 m) in this region and time of the year (Figure 4.42 row 2). The MLD is shallow, around 5-20 m, in exactly the locations where there are barrier layers present (Figure 4.42 row 3, row 1), therefore also presenting the highly spatially variable pattern.

The event of barrier layer growth from 14-10-2003 to 18-10-2003 is illustrated in Figures 4.43 and 4.44. The 0-20 m BLT present on 14-10-2003 extending from 2-10°E in this section along 1.8°N, grows to 60 m until 18-10-2003 due to dominantly a shoaling of the MLD during those 5 days (see dashed curves in Figure 4.43a,b). The shoaling of the MLD causes the BLT to be larger and is associated with a positive salinity vertical gradient tendency, meaning an increase in the salinity vertical gradient from 5 days before until the day of the peak BLT (Figure 4.43a). A similar, but weaker, pattern is seen in the temperature gradient tendency between the two MLDs.

Looking at the individual contribution of salinity and temperature for the density stratification (Figure 4.44e-j), it is noticed, that once again the MLD is mainly controlled by salinity, as the salinity stratification almost entirely match that of density. The isohalines mostly come together at the surface during those 5 days (Figure 4.44a,b), which is the general case in 58/69 cases (84%).

Analyzing now the terms of the balance equations, the vertical compression of the isohalines, seen in the tendency as a positive salinity tendency between the MLDs from 14-10-2003 to 18-10-2003, can be explained by tilting, turbulent mixing and partly stretching mechanisms (Figure 4.43a,g,i,k). This reveals that turbulent mixing of the surface freshwater flux due to rainfall is an important contributing factor in the BLT here, along with the Niger river runoff peaking in September. The temperature gradient tendency is very faintly positive between the MLDs, also true for the terms in

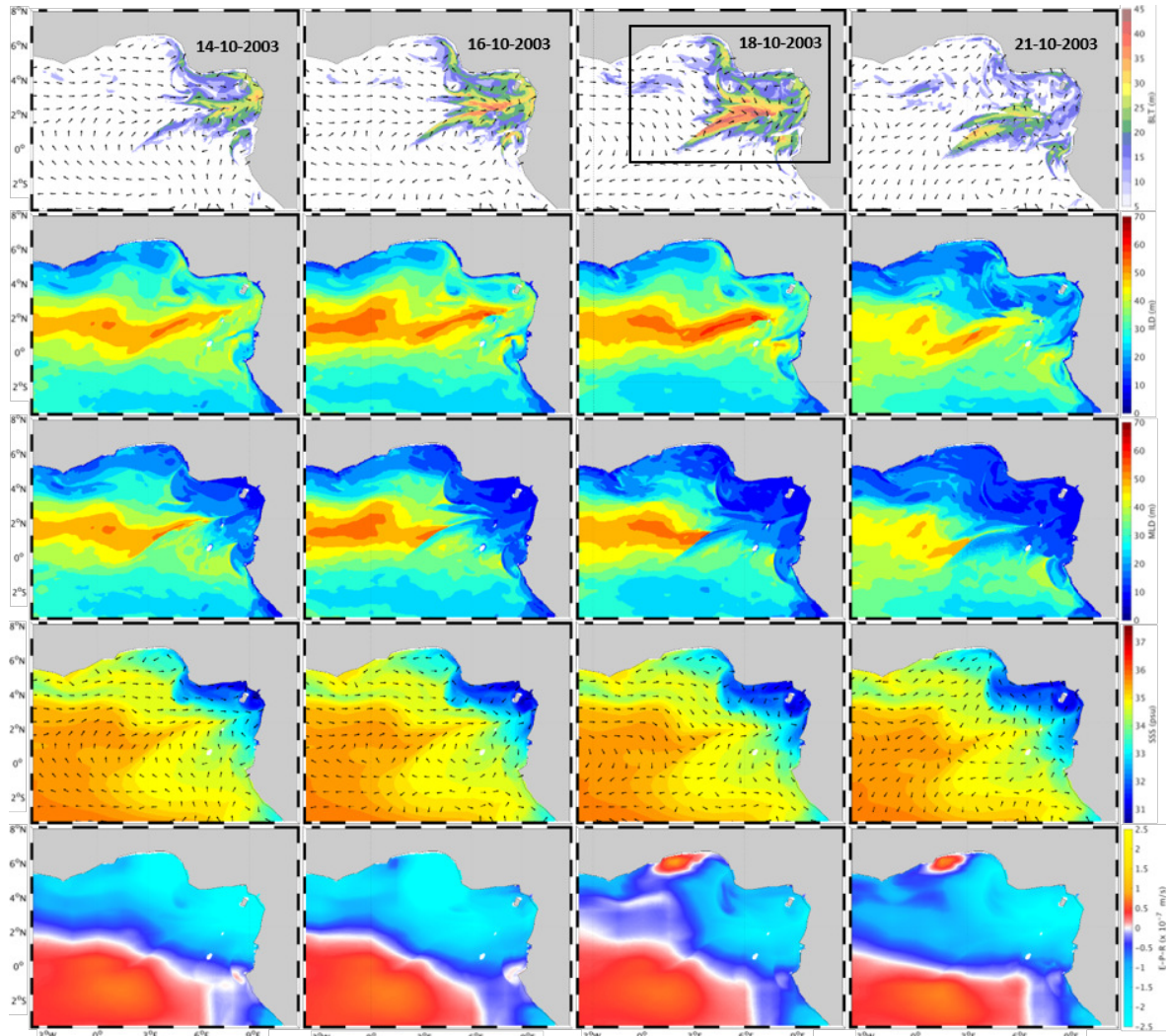


Figure 4.42: Snapshots from 14-10-2003 to 21-10-2003 showing the growth and decay of the maximum BLT on 18-10-2003 (black box delineates the ETA region) of (row 1) BLT (meters) with vectors showing surface currents, (row 2) ILD (meters), (row 3) MLD (meters), (row 4) SSS (psu) with vectors showing surface currents and (row 5) E-P-R ($\times 10^{-7}$ m/s).

the temperature balance, thus also pointing to the fact that salinity plays a dominant role in the shoaling of MLD.

There is also a small increase in ILD until the peak day, accompanied with a positive temperature gradient tendency between the ILD of the two days (Figures 4.43b). Though not seen in all the cases, and seen less often than the shoaling of MLD, the BLT also grows due to the deepening of ILD, in turn due to the compression and a downward shift of isotherms (Figure 4.44c,d), what occurs in 38/69 cases (55%). The terms dominant in causing this are turbulent mixing, stretching and horizontal advection (Figures 4.43b,l,j,d,h). Vertical advection clearly counteracts all the other mechanisms.

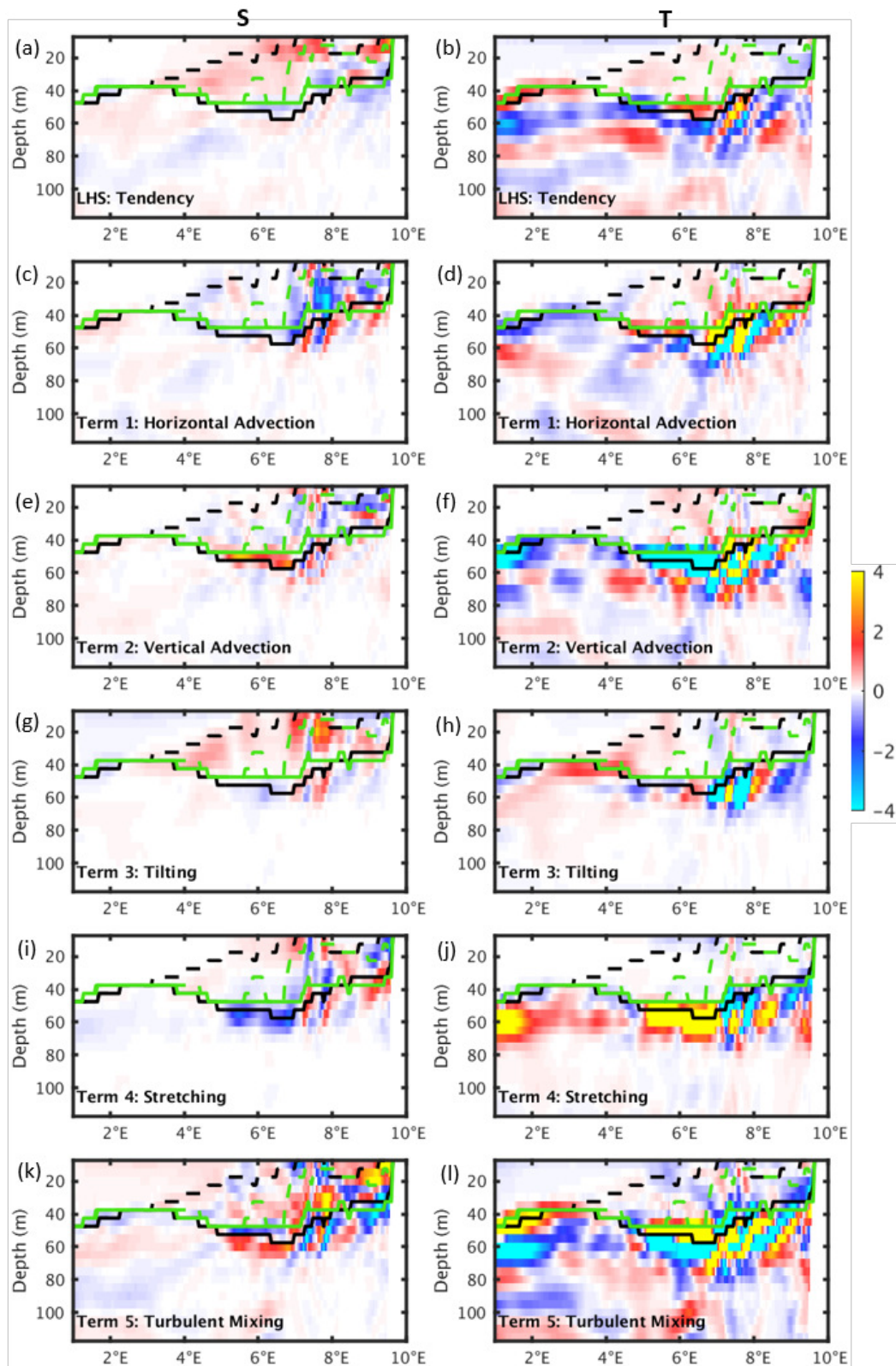


Figure 4.43: Same as Figure 4.15, but in a vertical section at 1.8°N through the maximum BLT present on 18-10-2003. Salinity and temperature gradient balance terms are averaged from 14-10-2003 to 18-10-2003 (units are $\times 10^{-7}$ psu/m.s and $\times 10^{-7}$ $^{\circ}\text{C}/\text{m.s}$, respectively). Black (green) solid lines correspond to the ILLD, black (green) dashed lines correspond to the MLD for 18-10-2003 (14-10-2003).

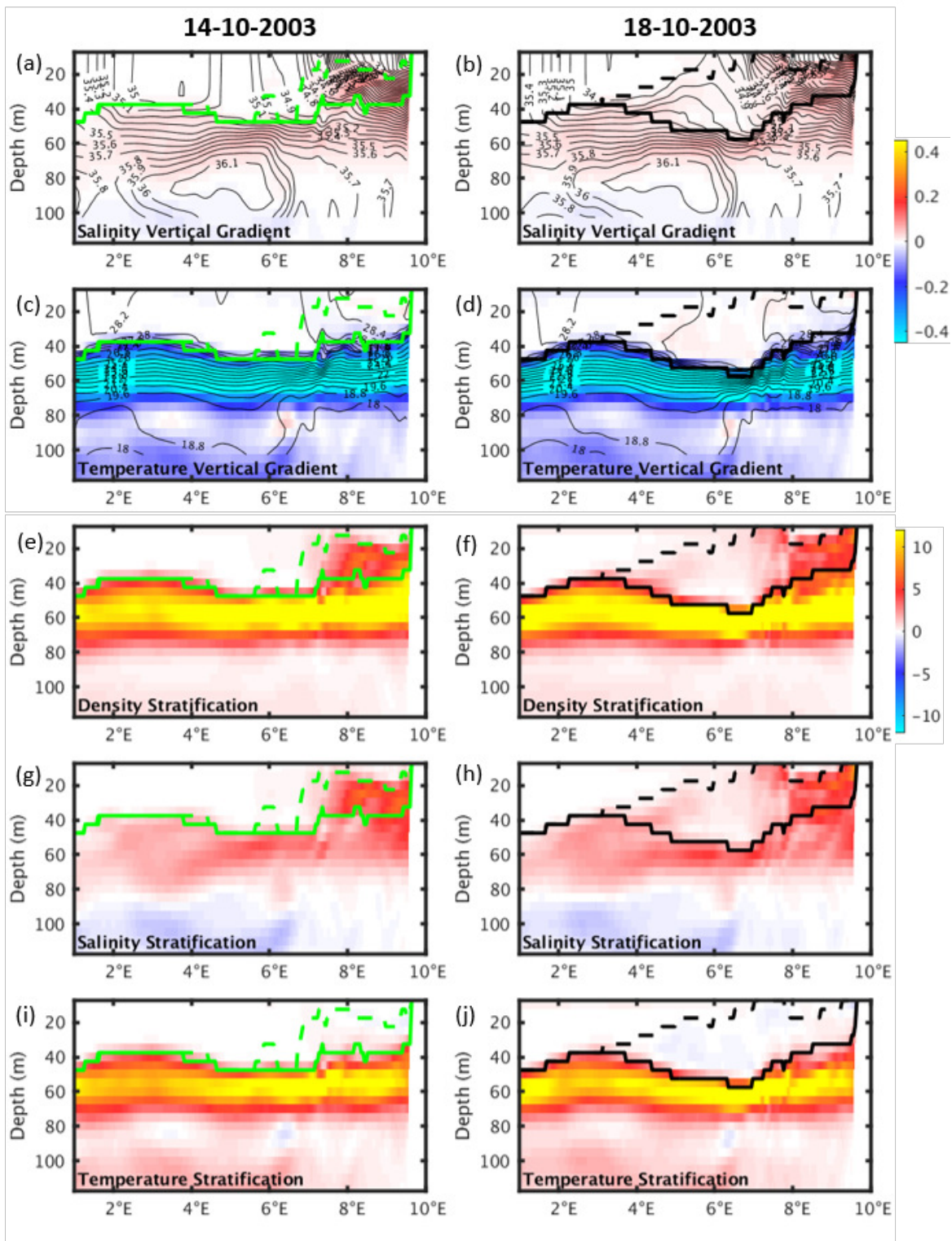


Figure 4.44: Vertical section at 1.8°N through the maximum BLT on 18-10-2003. Salinity vertical gradient (psu/m) with isohalines (psu) superimposed and Temperature vertical gradient ($^{\circ}\text{C}/\text{m}$) with isotherms ($^{\circ}\text{C}$) superimposed for (a,c) 14-10-2003 and (b,d) 18-10-2003. (e,f) Density, (g,h) salinity and (i,j) temperature stratification ($\times 10^{-4}/\text{s}^2$) for 14-10-2003 and 18-10-2003 are also shown. Black (green) solid lines correspond to the ILLD, black (green) dashed lines to the MLD for 18-10-2003 (14-10-2003).

Figure 4.45 presents the growth of the BLT in one of the peak events in February (red circles in Figure 4.36), namely on 12-02-2010. The 30 m thick barrier layer extending from 4-8°E in this section along 2°N, forms from 9-2-2010 to 12-2-2010 due to predominantly a shallowing of the MLD during those 3 days (see dashed curves in Figure 4.45a,b) and a small deepening of the ILD.

This event of large BLT occurring in February has smaller MLD and ILD compared to ones occurring in September-October as seen before, and the BLT is smaller as well. In February we see the similar behavior of the isotherms and isohalines as in September. The isohalines compress (Figure 4.46a,b) to shoal the MLD and the isotherms also compress and shift down, deepening the ILD, both giving rise to this barrier layer in February.

The deepening of the ILD is due to turbulent mixing, stretching, horizontal advection and tilting, again agreeing with the majority of events and the previous event (Figure 4.45). The difference lies in the terms contributing to the positive salinity vertical gradient tendency between the two MLDs. In the present event, tilting followed by stretching contribute to the shoaling of MLD. Unlike in the previous event in October, in this case the turbulent mixing of surface freshwater flux, i.e. rainfall, does not play a role in the positive salinity vertical gradient tendency and rather completely counteracts the tilting term. Thus the barrier layers in events occurring in February mainly grow due to the tilting of salinity fronts formed at the edge of the Niger river freshwater plume as it meets the open ocean saline water flowing eastward in latitudes 1-4°N in February.

Barrier layer decay

Figure 4.42 shows the spatial variations during the decay of the BLT after the peak on 18-10-2003. The E-P-R field shows that the precipitation remains the same or rather increases and the SSS field shows the spreading of freshwater towards the open ocean. The MLD follows the SSS and is shallower covering larger areas, but the ILD is seen to shoal. This is because of heating up of surface water, which shoals the ILD and MLD towards November in this region (Figure 4.37) and during this event (Figure 4.47).

It is found that the ILD shoals and decreases the BLT in 53/69 cases (76.8%) by upward shifting of the isotherms and negative temperature gradient at the surface (Figure 4.47g,h). The temperature vertical gradient balance terms corroborate this, as turbulent mixing almost entirely causes the negative tendency in the temperature gradient between the ILD on 18-10-2003 and 21-10-2003 (Figure 4.47a,f).

In February, also the shoaling of ILD (though not too large) occurs by an upward shift of the isotherms due to the above mechanism of turbulent mixing and partially tilting.

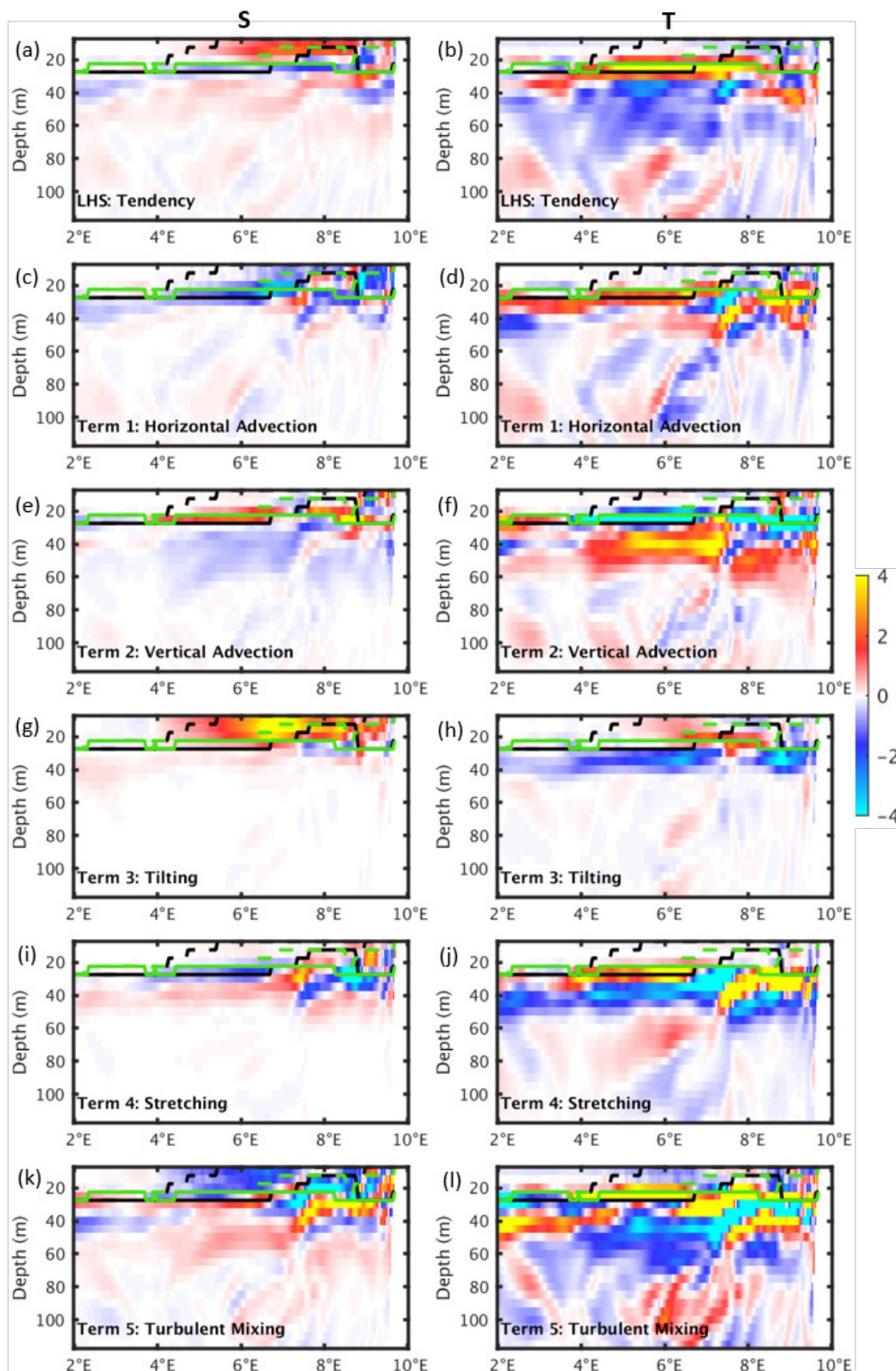


Figure 4.45: Same as Figure 4.15, but in a vertical section at 2°N through the maximum BLT present on 12-02-2010. Salinity and temperature gradient balance terms are averaged from 09-02-2010 to 12-02-2010 (units are $\times 10^{-7}$ psu/m.s and $\times 10^{-7}$ $^{\circ}\text{C}$ /m.s, respectively). Black (green) solid lines correspond to the ILLD, black (green) dashed lines correspond to the MLD for 12-02-2010 (09-02-2010).

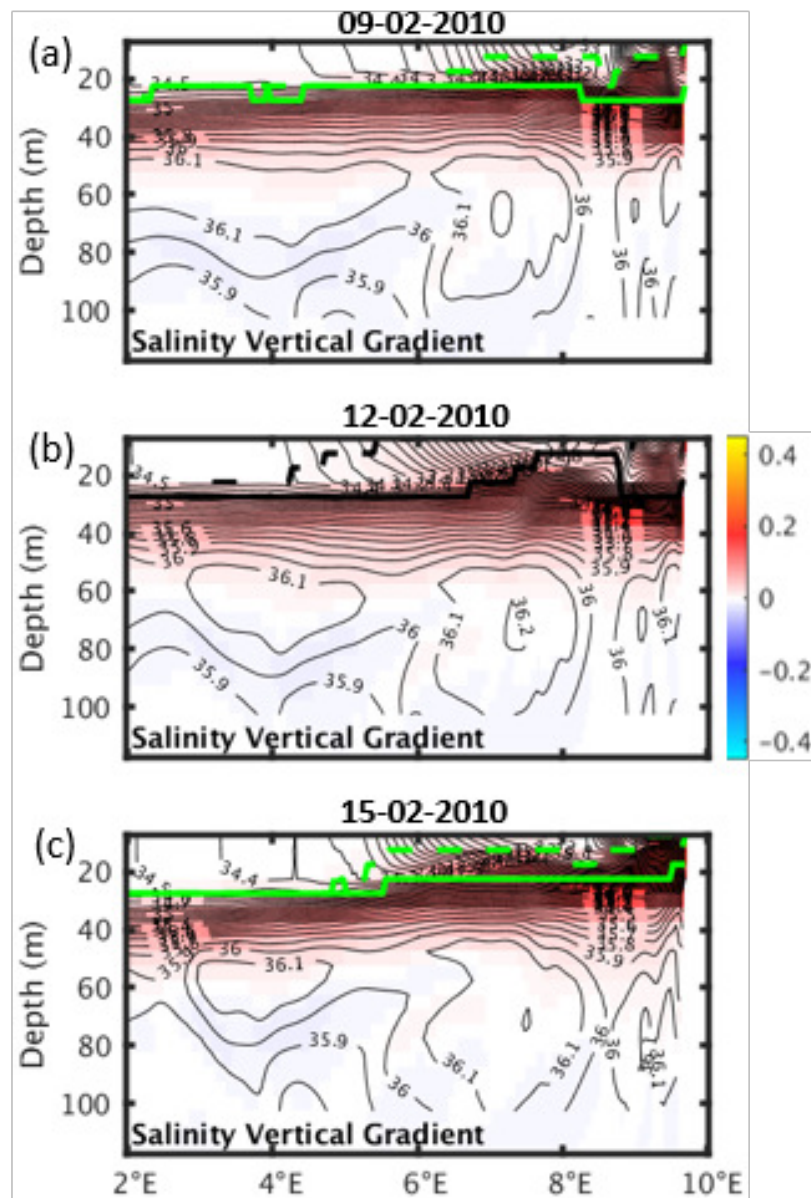


Figure 4.46: Salinity vertical gradient (psu/m) at 2°N with isohalines (psu) superimposed for (a) 09-02-2010, (b) 12-02-2010 (day of the largest BLT) and (c) 15-02-2010. Black (green) solid lines correspond to the ILLD, black (green) dashed lines correspond to the MLD.

In conclusion, from the analysis of the events in the BLT daily time series it was found that the largest BLT grows in September-October due to shoaling of MLD. The MLD shoals with a vertical compression of the isohalines due to tilting of salinity fronts and turbulent mixing of surface freshwater. This shows the influence of tilting of vertical salinity fronts around the Niger river plume, and the influence of ITCZ rainfall (Figure 4.42). The comparatively smaller BLT in February grows due to only tilting and partly stretching mechanisms, thus indicating no prominent influence of rainfall. In February the ITCZ intensifies over the southwestern tropical Atlantic.

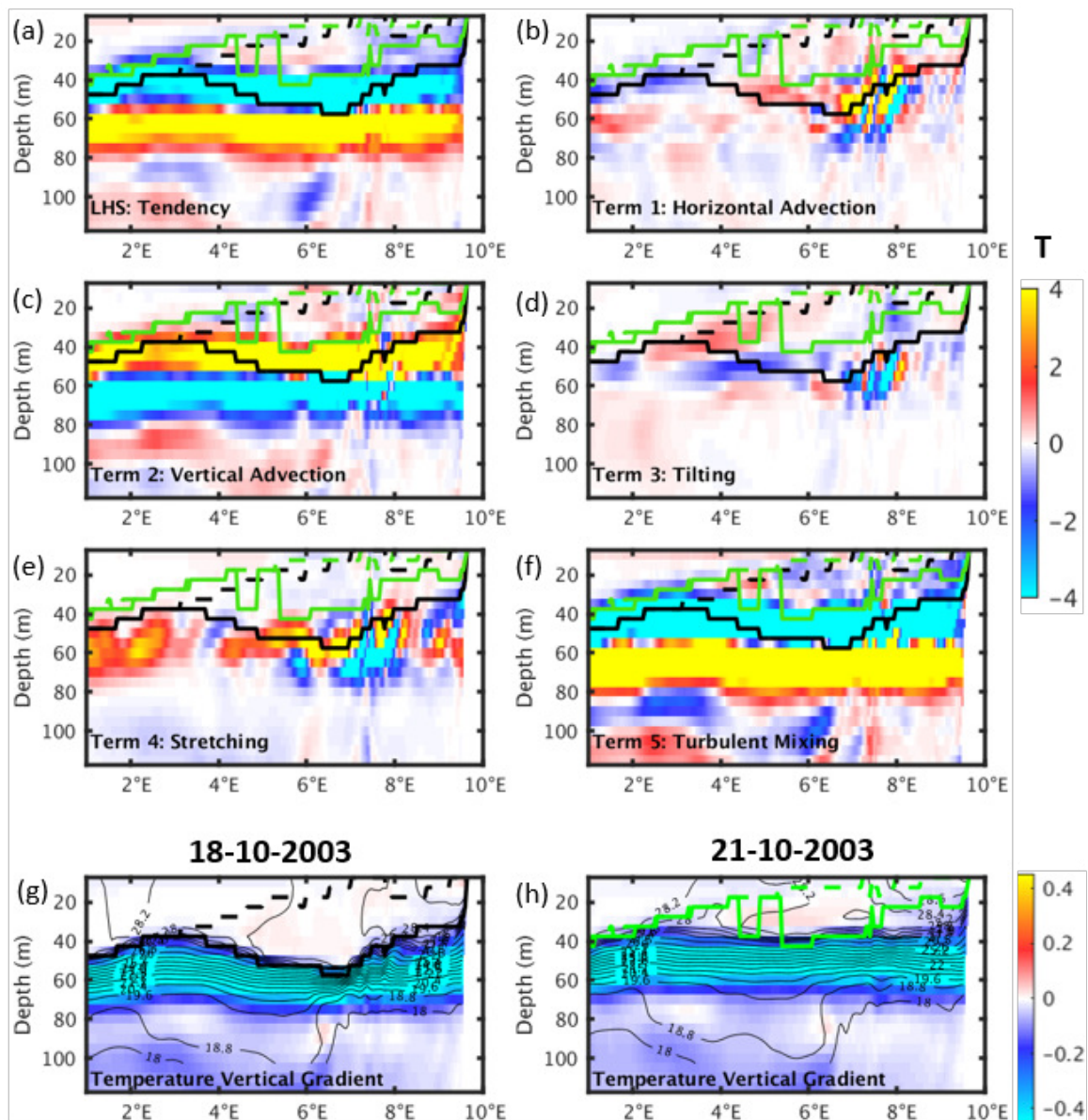


Figure 4.47: Same as Figure 4.43, but only the temperature gradient balance terms are averaged from 18-10-2003 to 21-10-2003 (units are $\times 10^{-7} \text{ }^\circ\text{C}/\text{m}\cdot\text{s}$). Black (green) solid lines correspond to the ILLD, black (green) dashed lines to the MLD for 18-10-2003 (21-10-2003). The temperature vertical gradient ($^\circ\text{C}/\text{m}$) with isotherms ($^\circ\text{C}$) superimposed for both dates are shown in (g,h).

The BLT, be it peaking in September or February, also grows in some events when the ILLD deepens due to turbulent mixing, stretching and horizontal advection mechanisms. Throughout the year the decay of BLT in most of the events in this region is dominantly due to shoaling of ILLD brought about by the upward shifting of isotherms caused by turbulent mixing.

4.7 Summary and discussion

The objective of this chapter was to answer the question: What are the mechanisms responsible for the growth and decay of barrier layers and their variabilities in the tropical Atlantic Ocean? Specifically, the objective was to identify the mechanisms behind both the seasonal behavior and the short-term events of barrier layers.

Results indicate that the northwestern tropical Atlantic has quasi-permanent barrier layers present in two localized regions: the NBC rings area and the region along the NEC, both formed mainly under the influence of the Amazon river plume. In the rest of the northern tropical Atlantic, significant barrier layers are present in the central and eastern tropical Atlantic due to precipitation related to the ITCZ and in the Niger river plume. The physical mechanisms represented by the different terms of the salinity and temperature vertical gradient balance equations have been studied to understand the growth and decay of those barrier layers.

In this study the NBC rings have been identified to play a major role in advecting the conditions supporting barrier layers towards the northwest. This happens as the NBC rings transport freshwater from the Amazon and Orinoco rivers and from ITCZ precipitation to the northwest. The dynamics intrinsic to the NBC rings and intrinsic to their formation, also are per se capable of growing barrier layers within the rings. All the NBC rings generated in the analyzed simulation have barrier layers either in their core or in their periphery during some period of their lifetime. According to my findings, the BLT is maximum in the ring's core and periphery in summer. There are thin barrier layers in the core and periphery of the rings in autumn. There are also barrier layers observed in winter, in the NBC rings, at the periphery and sometimes in the core. The instances of the occurrence of significant winter barrier layers in NBC rings are much less compared to the barrier layers found in summer (Figure 4.5). Amazon freshwater advected by NBC rings have been referred to before in Ffield (2007) but the barrier layers were not studied.

Localized barrier layers larger than 80 m inside NBC rings in summer are due to deep ILD in the rings caused mainly by stretching (Figure 4.14) of isotherms. The horizontal advection mechanism is the most dominant one in deepening the ILD in the ring, followed by tilting, stretching and turbulent mixing. Results suggest that the barrier layers in NBC rings in summer are destroyed mainly by stretching of isotherms (Figure 4.18).

My results also shed light on the non-typical cases of growth/decay of BLT in NBC rings. The shallowing of the mixed layer can cause BLT to grow in the rings in summer due to compression and upward shifting of isohalines (Figure 4.15 and Figure 4.16), where the dominating terms are horizontal advection, turbulent mixing and tilting of salinity fronts. In the case of winter barrier layers in NBC rings, the shallowing of MLD is more responsible for growing the BLT rather than an increase in ILD, but in the decay phase, increase of MLD and decrease of ILD both are equally responsible.

Horizontal advection, followed by turbulent mixing and tilting is dominant in forming the barrier layers in the peripheries of the rings in winter (Figure 4.17).

The seasonal maximum in barrier layer presence in the NEC region further to the north is in winter and the minimum in spring (Figure 3.4b and Figure 4.19), a result that is consistent with previous studies (Sprintall and Tomczak, 1992; Breugem et al., 2008; Mignot et al., 2012; Balaguru et al., 2012a). The winter BLT growth is mainly due to a reduction in MLD caused by stretching apart of the isohalines (Figure 4.25), over a deeper seasonal ILD. Tilting of salinity fronts by northwestward transport of freshwater at the surface by NBC and Ekman currents and equatorward subsurface transport of SMW, has been identified to be dominant in the growth of barrier layers there (Figure 4.24). This corroborates recent studies by Katsura et al. (2015) and Katsura and Sprintall (2020), in which tilting of salinity front is suggested to be the main mechanism acting in the subtropical Pacific and eastern tropical north Pacific in forming the barrier layers there. In the subtropical Atlantic it was hypothesized by Sprintall and Tomczak (1992) and Sato et al. (2006). Apart from tilting I found that stretching, horizontal advection and turbulent mixing also contribute to the formation of the barrier layers in the NEC region.

It was found that the barrier layers there get thin mainly because of compression and downward shifting of isohalines (Figure 4.26), due to turbulent mixing and horizontal advection, which cause the mixed layer to deepen. The seasonal maximum BLT erodes in spring due to temperature stratification, a finding which corroborates results from Mignot et al. (2012). Turbulent mixing of temperature and tilting are the mechanisms dominant in compressing the isotherms to shoal the isothermal layer, along with shoaling the mixed layer to erode the seasonal barrier layer.

In the ITCZ region, comparing the daily time series and the 60-days filtered time series of BLT, ILD and MLD (Figure 4.29 and Figure 4.30), the short timescale episodes of BLT have large amplitudes, dominating over the seasonal cycle. The barrier layers here form and grow due to the turbulent mixing of rainwater from ITCZ at the surface during the entire year in different places in the central tropical Atlantic, depending on the position of the ITCZ. Turbulent mixing along with a tilting of the salinity front into the vertical, deepens the MLD and locally destroys the barrier layer. A change in ILD is very rare and very negligible in the growth and decay of BLT here.

On the seasonal timescale, it was seen that the BLT is large in December-January, September-October and around June. This was attributable to the seasonal changes of ILD and MLD. ILD is influenced by the surface net heat flux (forcing the SST), while ILD and MLD both are influenced by wind stress over this region (Figure 4.30). MLD additionally is affected by the ITCZ rainfall falling over a deep seasonal ILD, giving rise to a significant BLT.

In earlier studies, the mechanisms of formation and decay of these barrier layers in the central and equatorial tropical Atlantic region were not studied in detail to my knowledge. The mixed layer salinity in the central tropical Atlantic was found earlier

to be dominantly influenced by precipitation (Camara et al., 2015). Barrier layers have been hypothesized in previous studies to be formed due to ITCZ precipitation in the tropics of the World Ocean including the tropical Atlantic (Sprintall and Tomczak, 1992; Foltz et al., 2004; Sato et al., 2006; Mignot et al., 2007; de Boyer Montégut et al., 2007; Breugem et al., 2008). Some of the above studies mention the small contribution of ITCZ rainfall along with the larger influence of the Amazon discharge on the BLT growth in the earlier discussed western tropical Atlantic. My results discussed here identified the formation and decay mechanisms and described the nature of the barrier layers which are fairly away from the influence of river runoff in the central tropical Atlantic.

The ETA region has the largest barrier layers in autumn during September-October when the MLD shoals by vertical compression of the isohalines due to tilting of salinity fronts and turbulent mixing of surface freshwater (Figures 4.43 and 4.44). The smaller BLT in February grows by shoaling of MLD due to tilting and partly stretching mechanisms (Figure 4.45). This indicates that rainfall under ITCZ does not play a role in the BLT formation here in February, but only in autumn. The influence of tilting of salinity fronts along the Niger river plume happens during both the seasonal peaks of BLT. BLT grows in some events when the ILD deepens by compression and downward shifting of isotherms due to dominantly turbulent mixing and stretching mechanisms, while the BLT decays in most of the events by shoaling of ILD due to turbulent mixing.

The ILD was seen to be driven by net heat flux (forcing the SST) and wind stress. The seasonal ILD deepens both in September and February due to stretching, temperature gradient horizontal advection and turbulent mixing mechanisms, along with a shallow MLD, giving rise to the seasonal maxima in September-October and February in the ETA region. The decay of the BLT here is due to both the shoaling of ILD due to turbulent mixing, tilting, and the deepening of MLD due to horizontal advection, stretching and turbulent mixing.

In September the Niger river discharge and rainfall due to ITCZ both contribute to the freshwater forcing (Camara et al., 2015; Dossa et al., 2019). Dossa et al. (2019) describe the seasonality of this barrier layer at the Niger river mouth. My results corroborate their findings regarding the seasonal cycle of BLT. They suggest that in February the BLT could be because of horizontal advection of barrier layers and freshwater due to the GC2 and the SEC (currents demarcated in Figure 2.1c). A seasonal decrease in the salinity of the mixed layer in the northeastern Gulf of Guinea was a consequence of both freshwater flux (precipitation and runoff) and horizontal advection (Da-Allada et al., 2014). Therefore they hypothesize that the horizontal advection of fresh water might be the mechanism inducing high BLT values in February.

My results additionally show that in February the seasonal large BLT is also due to the second peak in ILD caused by the reduction of surface heat flux (and SST) and strengthening of wind stress magnitude. While these atmospheric forcings also affect the MLD, freshwater forcing of Niger river discharge being advected westward

and coming in contact with the saline open-ocean water being carried eastward, causes the tilting of salinity front and shoals the MLD dominantly here. On inspection of daily fields of top 150 m horizontal transport and salinity and currents in the top 100 m, it was seen that the dominant current is the westward flowing nSEC from 0° - 2° N, but from 2 - 6° N there is the GC2 (currents demarcated in Figure 2.1c) carrying the accumulated fresh water from precipitation (in north latitudes) and saline open-ocean water (around 2° N) to the east. The latter is true for the depth range 22-45 m which is just above the ILD here. This helps explain the high salinity water entering the ILD, that shoals the MLD due to the tilting process and ultimately gives rise to the barrier layer.

In general, some similarities exist between the four studied regions. Firstly, there is large occurrence of the small amplitude BLT (5-15 m) in all the regions. The occurrence of large amplitudes in BLT (>50 m) is smaller in all the regions (Figure 4.1). Secondly, though the seasonal cycles of the ILD and MLD are different in the different regions, it was seen that the reduction in net heat flux forcing the SST played an important role in cooling the surface and thus giving rise to convective mixing at the surface. This along with mixing due to strong winds caused the ILD and MLD to deepen. The freshwater influx or advection caused the MLD to remain shallower at certain times. The combination of the seasonalities of MLD and ILD gave rise to BLT. Thus the semi-annual behavior of net heat flux was an important factor in determining the ILD variability which affected the BLT in all the regions in the tropical Atlantic.

Lastly, though analyzing temperature inversions inside barrier layers is not one of the aims of this thesis, it is worth a mention that a temperature inversion was noticed to exist in the simulated barrier layers in most of the events in all the four regions (Figure 4.14h, Figure 4.16, Figure 4.18, Figure 4.25e, Figure 4.28, Figure 4.34k, Figure 4.44, Figure 4.47), but the largest inversions being in the thick barrier layers of the western tropical Atlantic, in the NEC region and in the NBC rings. Figure 4.28c represents an example of the characteristic temperature inversion inside the northwestern tropical Atlantic winter barrier layers (NEC-box) which is proposed to be caused by the maximum penetration of solar radiation under the mixed layer, also due to the persistence of warm water from summer below the cold surface waters in winter; as the presence of barrier layer does not allow the winter wind mixing to penetrate below the mixed layer (Vialard and Delecluse, 1998; Masson and Delecluse, 2001; Mignot et al., 2007; Balaguru et al., 2012a; Balaguru et al., 2012b; Mignot et al., 2012). The above region, and those warm NBC rings having temperature inversions have potential to influence air-sea processes during tropical cyclone passage over the western tropical Atlantic, and intensify the cyclones. Two eddies with temperature inversions were spotted earlier by Rudzin et al. (2017) and van der Boog et al. (2019) in only the Caribbean Sea. Thus the simulation captures well the temperature inversions associated with the northwestern tropical Atlantic barrier layers.

All the four localized regions of the tropical Atlantic have different seasonality of barrier layers and different main mechanisms behind their growth and decay. The BLT in NBC rings is more determined by changes in ILD rather than of MLD. The formation and evolution of BLT in the NEC and ITCZ area are dominantly depending on changes in the MLD. The BLT at Niger plume in the ETA region are determined equally by both the MLD and ILD. There are few events with exceptions in all the regions, but they form the minority. For instance, changes in MLD are more important for the winter BLT formation in the NBC rings and in some non-typical cases small changes in MLD also contribute to the growth and decay of the summer barrier layers in the NBC rings.

Tilting of salinity fronts was seen to be a dominant mechanism in shoaling the MLD at NEC, NBC and ETA regions, due to the spread of the fresh river water plumes mixed with the freshwater from rainfall in all the regions. Tilting of temperature fronts in the NBC rings played a role in increasing the ILD. Horizontal advection was an important mechanism in all regions, but dominantly in NBC region, in shoaling MLD, and for changes in ILD. Turbulent mixing of rainwater on the surface was dominant in shoaling the MLD in ITCZ region and also in the ETA region in September. Deepening of ILD due to turbulent mixing is important in the formation of the seasonal BLT in the NEC region and of the seasonal and short-term BLTs in the ETA region. Shoaling of ILD is important in the decay of barrier layers in the NBC rings, of the seasonal barrier layers in the NEC region, and also in the decay of the seasonal and short-term barrier layers in the ETA region, dominantly by the turbulent mixing of temperature.

There are some differences between the regions as well. The largest amplitudes of BLT in the tropical Atlantic are found in the first two regions, NBC and NEC in the western sector. A maximum of around 80-100 m is seen in the western tropical Atlantic while a maximum of around 60 m is found in the rest of the tropical Atlantic in the daily events.

Amazon river water is a freshwater source for the formation of the barrier layers near the Amazon mouth. But that freshwater along with freshwater from ITCZ rainfall and the conditions for a BLT growth are being transported northwestward by the NBC rings. The freshwater reaches the northernmost latitudes in the northwestern tropical Atlantic (NEC region) and contributes to the conditions for BLT growth.

The Amazon plume spreads to the east in autumn, which was seen to have large barrier layers in September-November as well. They exist therefore mainly due to the horizontal advection of the Amazon freshwater to the east by the NECC and to a lesser extent also because of the freshwater from ITCZ precipitation. Tilting of salinity fronts caused by the freshwater advected eastward at the surface by the NECC and the movement of high salinity waters in opposite direction at deeper depths by the subduction of SMW carried by the NEC and the saline open-ocean water carried by the northern branch of SEC is also a mechanism here. This region of the eastern limb of the Amazon plume was not chosen to be studied individually, as the reasons for BLT

growth and decay here can be translated from the previous two regions in the western tropical Atlantic. These above inferences were seen in the daily fields of the balance terms and oceanic variables which we saw for the four presented regions.

The Amazon runoff is not a relevant contributor of freshwater in the other two chosen regions in the tropical Atlantic analyzed in this chapter. In the ITCZ region, the ITCZ precipitation was the only freshwater influx, and in the ETA region, the Niger river discharge and the ITCZ precipitation both were the freshwater influxes, which caused the conditions for the formation and maintenance of barrier layers in those two regions.

The seasonal cycle was pronounced in the NEC and ETA regions, while in the ITCZ region it was not pronounced. The short-term barrier layers occurring as events in NBC rings and ITCZ regions had higher frequency and amplitudes compared to the seasonal cycle. In the case of NBC rings, the significant barrier layers near the Amazon mouth and its surroundings are enclosed inside the NBC rings and pass along with it, apart from the growth of the barrier layers in the rings due to the internal eddy dynamics. BLT is very isolated inside the high frequency rings here. These two regions were regions of high frequency occurrence of BLT. Averaging the daily BLT smooths out those signals and results in non-significant BLT. The quantification of the mechanisms behind the seasonal barrier layer is therefore possible for the NEC and ETA regions and not for the other two regions.

Finally, the magnitude of the terms in all the regions were not the same. Overall, the magnitude of all the mechanisms responsible for the growth and evolution of barrier layers are the largest in NBC rings compared to other regions. This may be because the region south of 13°N close to the western boundary has higher magnitude of temperature and freshwater forcing and stronger western boundary currents and eddy dynamics, which would lead to stronger physical processes. The second largest magnitudes of the governing mechanisms are seen in the ETA region for the Niger river plume, which is also due to the stronger dynamics at the plume region near the coast. Smaller and similar magnitudes of the terms are in the NEC and ITCZ regions, which are comparatively away from the river plumes.

Chapter 5

Impact of Amazon river runoff on the western tropical Atlantic Ocean

5.1 Introduction

The western tropical Atlantic has the largest barrier layers in the tropical Atlantic. In the previous chapter, one of the reasons for the existence of these prominent and perennial barrier layers in the western tropical Atlantic was seen to be the presence of freshwater that is discharged by Amazon River directly into the western tropical Atlantic. The Amazon River has the world's largest discharge with an average of about 0.2 Sv. This chapter discusses the possible impacts that a change in the Amazon river runoff can have on the physics and dynamics of the western tropical Atlantic. In order to investigate this, a series of idealized numerical experiments were performed by changing the Amazon river runoff, details of which are described in the next section. The following specific scientific questions are addressed in three individual sections of this chapter:

- Q.1. What is the impact of increasing/decreasing the mean Amazon river runoff and its seasonal amplitude on the upper ocean salinity and temperature and consequently on the ILD, MLD and BLT variability?
- Q.2. How do increasing/decreasing the mean Amazon river runoff and its seasonal amplitude (thus modifying the resulting barrier layers) impact the NBC/NECC current systems and associated eddy activity in the western tropical Atlantic?
- Q.3. Do the changes in the physical quantities and dynamics due to the variations of Amazon runoff further influence the large-scale Atlantic circulation and have a climatic impact? Moreover, is there a relation between barrier layers and the large-scale circulation?

This chapter ends with a summary and discussion of the answers to the above questions which collectively answer the second primary question of this thesis (section 1.3 of Chapter 1): What is the impact of changing the Amazon river runoff on the tropical Atlantic barrier layers and on the local and large-scale Atlantic circulations?

5.2 Description of experiments

Since a constant river runoff was employed in the simulations analyzed in previous sections, dedicated experiments using the 8 km version of the model were performed (see Table 5.1) by modifying the Amazon river discharge to complete the study of possible forcing mechanisms of barrier layer variability in the western tropical Atlantic.

Experiment 0 (exp0, "no runoff") is a simulation with zero Amazon river runoff. Experiment 1 (exp1, "constant") has a constant mean river runoff of 0.2 Sv for all months. Experiment 2 (exp2, "control run") has the same overall mean runoff as exp1 but incorporates a seasonal cycle of the Amazon outflow. This one is the most realistic from all experiments. Experiment 2b (exp2b, "+10⁻⁴% mean") is as exp2 but has 10⁻⁴% increased mean runoff. Exp2b was conducted to test the significance and robustness of the obtained results. Experiment 3 (exp3, "+10% mean") is as exp2 but has 10% increased mean runoff. Experiment 3b (exp3b, "+20% mean") has 20% increased mean runoff compared to exp2 and Experiment 3c (exp3c, "+100% mean") has 100% increased mean runoff. Experiment 4 (exp4, "+40% amplitude") is the simulation where the seasonal runoff cycle of the Amazon River is amplified by 40%, but featuring the same mean runoff as in exp1 and exp2.

In order to test the linearity of the ocean response, experiments were performed with reduced mean runoff and reduced amplitude. Experiment 5 (exp5, "-10% mean") is as exp2 but has 10% decreased mean runoff and experiment 5b (exp5b, "-20% mean") has 20% decreased mean runoff. Finally, experiment 6 (exp6, "-40% amplitude") is the simulation where the seasonal runoff amplitude is attenuated by 40%, still having the same mean as in exp1 and exp2.

All the experiments start from an initial condition in January 2008 extracted from the previously described 1948-present ATL8km run. All the experiments were integrated for 10 years, with a monthly temporal resolution output (120 months in total), and were forced by fluxes computed with bulk formula and the 6-hourly NCEP reanalysis from 2008-2017. In this analysis I focus on the 8 years period 2008-2015.

The experiments were designed based on the inspection of the actual time series of the Amazon river discharge over the past 90 years from Dai (2017), described in detail in Dai (2016) and presented in Figure 5.1a. It can be noticed how the discharge varies in amplitude at interannual timescales, with periods of decreased and increased mean runoff. In order to distinguish between the separate effects of mean and amplitude change, the runoff applied to the model was idealized. The idealized runoff cycle was

exp. no.	label	description
exp0	"no runoff"	zero runoff
exp1	"constant"	mean runoff; constant for all months
exp2	"control run"	runoff seasonal cycle; same mean as exp1
exp2b	" $+10^{-4}\%$ mean"	exp2 + $10^{-4}\%$ mean
exp3	" $+10\%$ mean"	exp2 + 10% mean
exp3b	" $+20\%$ mean"	exp2 + 20% mean
exp3c	" $+100\%$ mean"	exp2 + 100% mean
exp4	" $+40\%$ amplitude"	40% larger amplitude seasonal cycle than exp2; same mean as exp2
exp5	" -10% mean"	exp2 - 10% mean
exp5b	" -20% mean"	exp2 - 20% mean
exp6	" -40% amplitude"	40% smaller amplitude seasonal cycle than exp2; same mean as exp2

Table 5.1: Summary of experiments performed at 8 km resolution including different idealized Amazon river discharge time series.

simulated with a sine wave multiplied by a constant mean runoff value. The vertical offset of the sine wave was changed in the "mean" experiments, which is equivalent to increasing/decreasing the constant mean runoff. On the other hand, the amplitude of the sine wave was changed to attain the forcing for the "amplitude" experiments (see Figure 5.1b,c). All experiments except exp0 and exp3c remain within the observed values of Amazon discharge. The experiments differ solely by the imposed river runoff, specified as a salt flux added to Evaporation-minus-Precipitation forcing at the grid cells constituting the Amazon mouth (Box A in Figure 5.2a), with the magnitudes being as stated in Table 5.1.

The observed monthly Amazon discharge (Figure 5.1a) for the period 1928-2013 ranges from 0.076 to 0.287 Sv. The amplitude of the seasonal cycle for some years is large and for some other years it is small. Also, the annual mean runoff is not the same for every year, as seen in the vertical shift in the observed wave for some years. The above experiments, excluding exp0 and exp3c, designed with varying means and amplitudes, are made with respect to this observed data of Amazon river discharge. So these experiment cases have been actually observed in the past, and therefore are realistic. While exp3c with a 100% increase in mean runoff and exp0 with zero runoff have not been seen in the past, these experiments representing the two extreme conditions, which could occur in future climate scenarios, have been additionally conducted for comparison of their impacts on the tropical Atlantic with the other experiments. By examining the climatological mean runoff of exp2 (control run) and the observations, I saw that the model reproduces the seasonal cycle and magnitude of the runoff similar to the observations, both having the seasonal peak in May and the seasonal low in November, with a ~ 0.2 Sv mean (Figure 5.1).

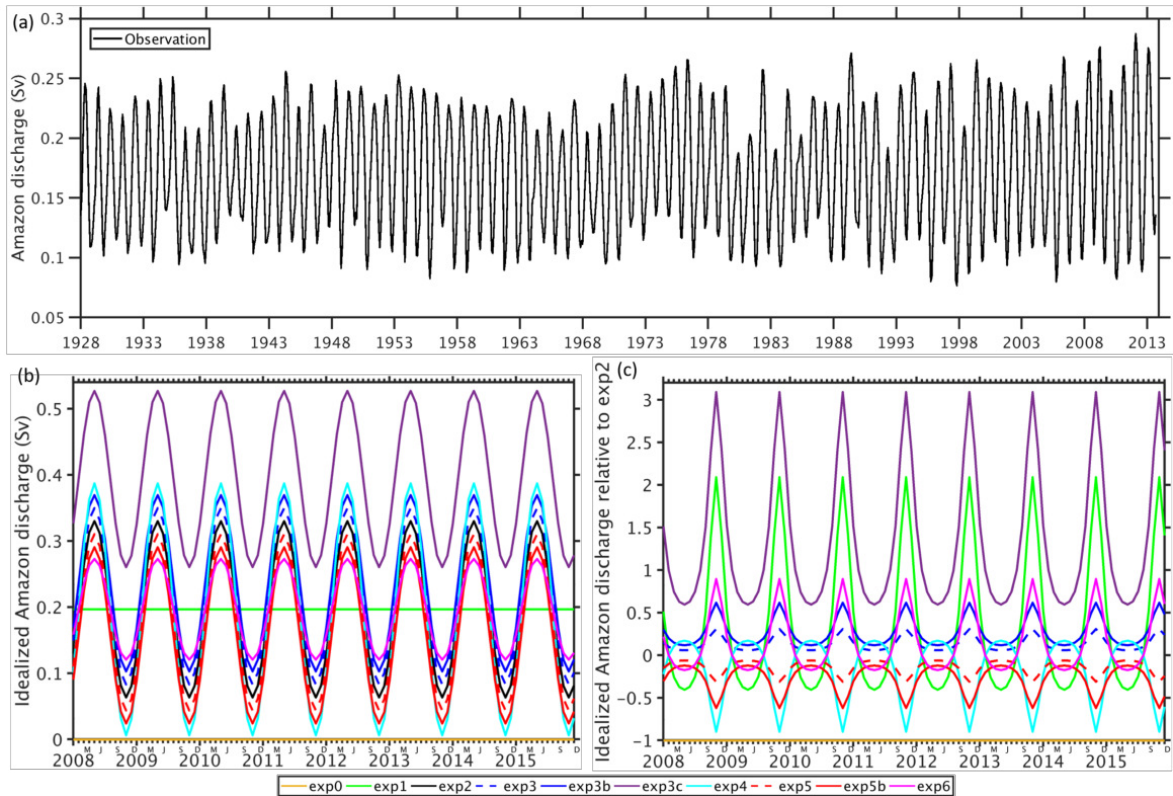


Figure 5.1: (a) Observed Amazon river discharge from Dai (2017). (b) Idealized Amazon discharge imposed in the model for different experiments. (c) Idealized model discharges of different experiments shown relative to that of exp2.

Figure 5.2a and 5.2b present the time mean over the study period 2008-2015 of the SSS in the EN4 observations and in exp2, respectively, in the tropical Atlantic. The model reproduces the river plumes fairly well. The Amazon plume spreads to the northwest until 20°N and west of the Lesser Antilles, and the eastward spread in the north equatorial Atlantic is well simulated. Comparing with exp2, the salinity maximum north of 24°N is higher in the observations. Salinity in the top 50 m was also looked at and, in both, the model and the observations, shows similar behavior as the SSS, but with a smaller magnitude. In Figures 5.2c and 5.2d we see a good agreement between the 2008-2015 time mean BLT in the observations and model. There is a time mean maximum BLT of ~ 35 m in the Amazon plume in both observations and model. With the simulation, it is noticed that the barrier layers are very localized. The solid and dashed black boxes show the areas having persistently high BLT, which are also the areas affected by the Amazon plume. In the next section, the changes in ILD, MLD, BLT and other physical variables and dynamics are examined in detail for these areas.

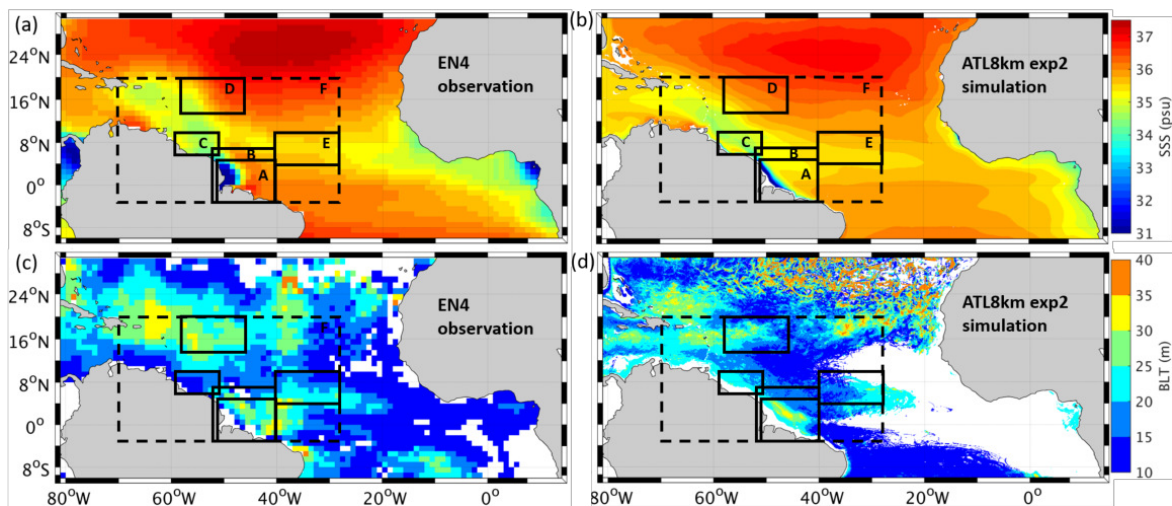


Figure 5.2: 2008-2015 time mean (a,b) SSS (psu) and (c,d) BLT (meters) from (a,c) EN4 observations and (b,d) exp2 simulation. Black solid boxes: Box A (3°S - 5.5°N , 40 - 51°W) represents the Amazon river mouth, Box B (3°S - 7°N , 40 - 52°W), Box C (6 - 10°N , 51 - 59°W), Box D (14 - 20°N , 46 - 58°W) and Box E (4 - 10°N , 28 - 40°W) are the four areas having localized large BLT and are under the influence of the Amazon plume. The black dashed Box F (3°S - 20°N , 28 - 80°W) delineates the entire area in the western tropical Atlantic featuring barrier layers.

5.3 Relation between Amazon runoff and upper ocean salinity, ILD, MLD and BLT

In order to understand the impact of the changes in the Amazon runoff on physical variables of the tropical Atlantic, we will first look into the changes in SSS directly at the river mouth and then into the changes in upper ocean salinity and temperature, ILD, MLD and BLT at localized areas of the tropical Atlantic (boxes in Figure 5.2) which have large barrier layers and lie within the Amazon plume spread, i.e., the region of freshwater influence (ROFI).

The area-averages of SSS and Amazon runoff over a small region covering the Amazon river mouth (3°S - 5.5°N , 40 - 51°W - Box A in Figure 5.2a) over the period 2008-2015 were computed for the 10 experiments to test the sensitivity of SSS to the varying runoff imposed as a virtual salt flux over Box A. This relation is analyzed in the experiments for the time mean and climatology (12 monthly means), in order to obtain the overall and the seasonal behavior of the impact, respectively.

The time mean SSS and runoff (Figure 5.3a) show a clear inverse linear relation with a slope of -4.54 . Exp0 with no runoff has a maximum SSS of 35.8 psu at the Amazon mouth. Exp3c having 100% increase in mean runoff, has the weakest SSS, smaller than 34.1 psu. Exp1 with a constant runoff has 35 psu. Exp2 having a seasonal cycle of runoff with mean equal to exp1, exp4 having a 40% amplified seasonal cycle compared to exp2 and exp6 with a 40% attenuated seasonal cycle, also have a time

mean SSS similar to exp1. Exp3/exp5 and exp3b/exp5b having respectively 10% and 20% larger/smaller mean runoff than exp2, with no change in seasonal amplitude, have consequently smaller/larger SSS. The SSS differences between exp2 and exp3b/exp5b amount to 0.2 psu, and there is a difference of around 1 psu between exp2 and exp3c or exp0. The experiments confirm well that the model is responding to the forcing as expected, with a higher mean runoff leading to low SSS and with lower mean runoff resulting in larger SSS at the river mouth. The change in the amplitude of the seasonal cycle does not seem to impart a major change to the time mean SSS at the river mouth.

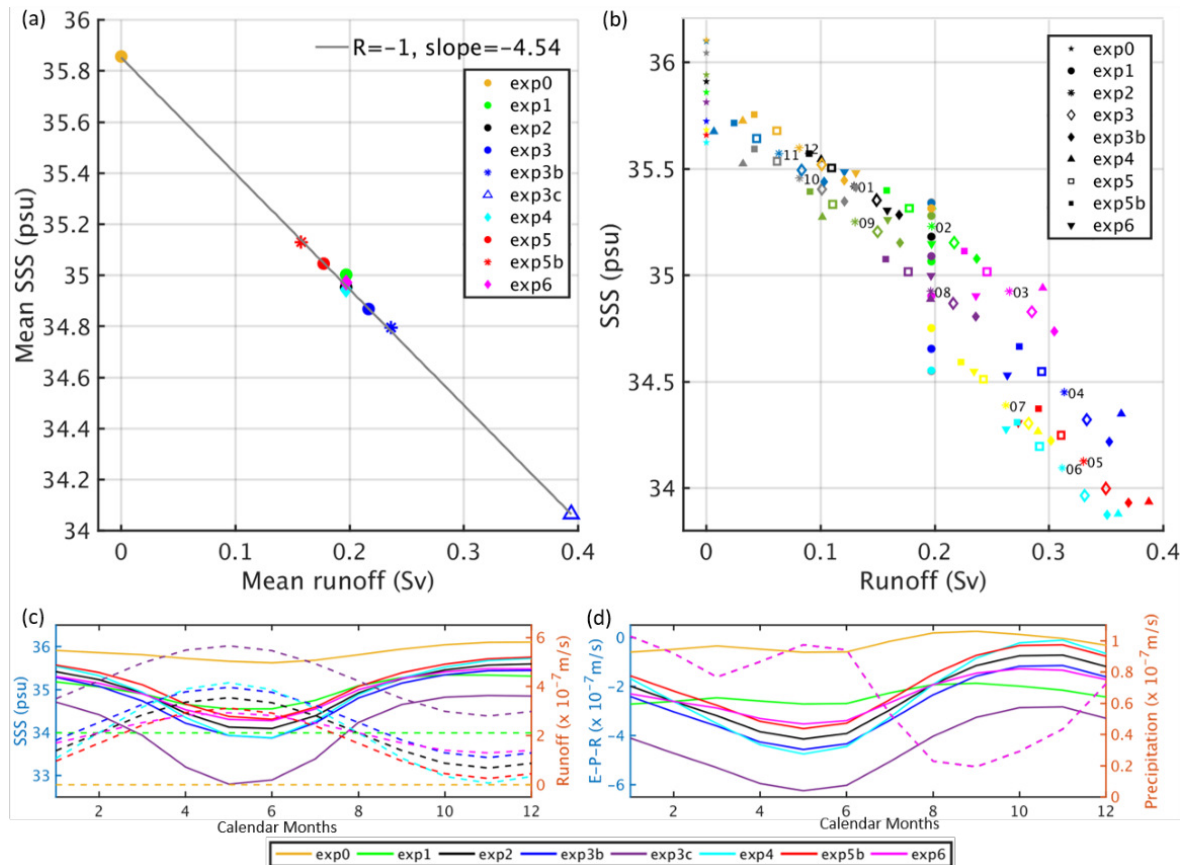


Figure 5.3: (a) Time mean and (b) monthly mean (the number of the calendar month is shown next to the exp2 symbol) relationship between SSS (psu) and runoff (Sv). Exp0 and exp1 both are forced with constant runoff. Monthly mean (c) SSS (solid) and runoff (dashed) and (d) E-P-R (solid) and precipitation (dashed) ($\times 10^{-7}$ m/s), area-averaged at the Amazon mouth (3°S - 5.5°N , 40 - 51°W - Box A in Figure 5.2a) over the period 2008-2015.

For the monthly climatology, the relation of SSS and runoff is shown in Figure 5.3b, where each month is denoted by a colour and the different symbols represent the 9 experiments. In Figures 5.3c and 5.3d, 8-year climatologies of the Amazon mouth SSS, runoff, E-P-R and precipitation are presented for all experiments. Exp3c is not shown in Figure 5.3b because invariably for every month it has the largest runoff and the smallest SSS. Exp3c shows the same seasonal cycle as the other experiments (excluding exp0 and exp1) but the highest magnitude of runoff amongst all experiments and the

smallest SSS and E-P-R compared to other experiments (Figures 5.3c, 5.3d).

All twelve months together show once again an inverse linear relation between SSS and runoff (Figure 5.3b). The runoff and SSS have a clear linear negative relation in July and January (see the colors). From April-June and October-December, when the runoff is larger in exp4/exp6 than in exp3b/exp5b, 20% change in just the mean runoff (keeping the seasonal amplitude the same, exp3b/exp5b) result in greater differences in SSS than 40% change in just the seasonal amplitude (exp4/exp6). Amongst all the experiments, exp0 has the largest SSS in all months. Despite no runoff, SSS still varies in this experiment, being smaller in June and larger in December, reflecting the seasonality of Evaporation-minus-Precipitation alone and/or salinity advection or mixing processes. Since the runoff is constant in exp1 without any seasonal cycle (Figure 5.3b and 5.3c), exp1 has larger SSS compared to the other experiments in the months of high discharge and has lower SSS in the months of low discharge. It is very interesting to notice how the seasonal amplitude varies between exp0 (0.5 psu) and exp1 (1 psu), despite the fact that both are forced with constant runoff. The seasonality difference has thus to be attributed to circulation changes imposed in exp1 by the runoff.

The precipitation is the same in all experiments. The seasonal cycle of precipitation in this region (dashed curve in Figure 5.3d) is because of the seasonal migration of the ITCZ in this region. Maximum rainfall at the river mouth is in May-June when the ITCZ migrates northward and again in winter when it travels south. The E-P-R cycles of exp0 and exp1 have a phase opposite to the precipitation cycle, meaning that precipitation is only slightly larger than evaporation and its amplitude is largely balanced by the latter.

For all experiments other than exp0 and exp1, E-P-R (Figure 5.3d) reaches the largest (negative) value in May and the smallest (negative) value in November, because of the runoff cycle. Overall we can see in Figure 5.3b and 5.3c that exp4, having the highest seasonal amplitude of runoff, has the largest climatological range of SSS, forming the outermost spread (see triangles in Figure 5.3b), exp6 forced with the smallest seasonal runoff amplitude has the least spread and exp2, the control run, has an SSS spread between the above two experiments. Among the experiments with a difference in mean runoff, the seasonal cycle of SSS is similar in exp2, exp3, exp3b, exp3c, exp5 and exp5b, but there is a shift in their positions for all months due to the different mean runoff. This is also seen in the case of E-P-R where exp3c, exp3b, exp3, exp2, exp5 and exp5b have in that order high (negative) to low (negative) E-P-R for all months. Thus, the experiments having a seasonal runoff have an E-P-R and SSS cycle influenced more by the runoff than by precipitation and currents. In Figure 5.3c,d we see the magnitude of E-P-R is similar to the runoff magnitude, while precipitation magnitude is comparatively much smaller. Interestingly, the range of SSS across all experiments combined, excluding exp0, is larger for March-June than in winter, largest being in May-June (Figure 5.3c). This is because during this time the seasonal runoff

risers and there is higher precipitation, leading to an accumulation of the freshwater at the Amazon mouth.

The upper ocean salinity, temperature, ILD, MLD, BLT, and precipitation over the 8 years, were then analyzed at four localized areas affected by the Amazon runoff (boxes in Figure 5.2b). The four regions, Box B (3°S - 7°N , 40 - 52°W) covering the Amazon mouth and near periphery (termed mouth-Box B), Box C (6 - 10°N , 51 - 59°W) covering the NBC rings (termed NBC-Box C, same as the NBC-box in Chapter 3 and section 4.3 of Chapter 4), Box D (14 - 20°N , 46 - 58°W) situated at the subtropics where the NEC is dominant (termed NEC-Box D, same as the NEC-box in Chapter 3 and section 4.4 of Chapter 4) and Box E (4 - 10°N , 28 - 40°W) covering the eastern spread of the Amazon plume (termed east-Box E) in Figure 5.2b, are chosen because they show different seasonal cycles of the physical variables but are all in the ROFI. The relations between the area-average of runoff over the box at the Amazon river mouth (Box A in Figure 5.2b) and the area-averaged BLT at each of the above four mentioned boxes are shown in Figure 5.4.

The strongest positive linear relation between the time mean (not shown) and monthly mean runoff and BLT, compared to the other boxes, is in the area covering the Amazon mouth and its near periphery (mouth-Box B). As one gets closer to the river mouth there is larger BLT (21 m for exp3b) and larger range of BLT (10-21 m) for the same runoff values (Figure 5.4a), resulting in a steeper slope of the regression line in the time mean. Being close to the river mouth, there is maximum freshwater throughout the year. The BLT standard deviation and runoff also showed a positive linear relation, meaning more variability in BLT with more runoff. Seasonal variability of SSS here is similar to that in Box A seen in Figure 5.3c,d. The precipitation is largest from April-June, which also causes the SSS to be small in June. The SST has almost similar values in all the experiments, with a high in April-June and a low in the rest of the months (not shown). ILD and MLD both have similar seasonality in mouth-Box B, having the maximum in February, least in July, then rising again, with maximum difference between them (BLT) being in June (Figure 5.4a).

The time mean BLT of the NBC-Box C and the runoff at the mouth have a positive linear relation with a smaller slope, as the NBC-Box C is further away from the Amazon mouth and therefore the freshwater gets further mixed with saline water. Exp4 with amplified seasonal cycle of runoff creates a larger BLT (~ 11.75 m) than all other experiments apart from exp3c with the largest BLT (12.48 m). The NBC and its rings transport the freshwater anomaly northwestward into the NBC-Box C, most dominantly in June-August (as seen in section 4.3 of Chapter 4). The impact on the seasonality of the physical variables in this region is much similar to the mouth-Box B. SSS (Figure 5.5a) is smallest in this region in June-July; precipitation is highest in June, also contributing to the decrease in SSS in all experiments. In Figure 5.5b the ILD has a seasonal maximum in February-March and a second maximum in June. The seasonal high of MLD is in February-March, it then drops in July-August. The

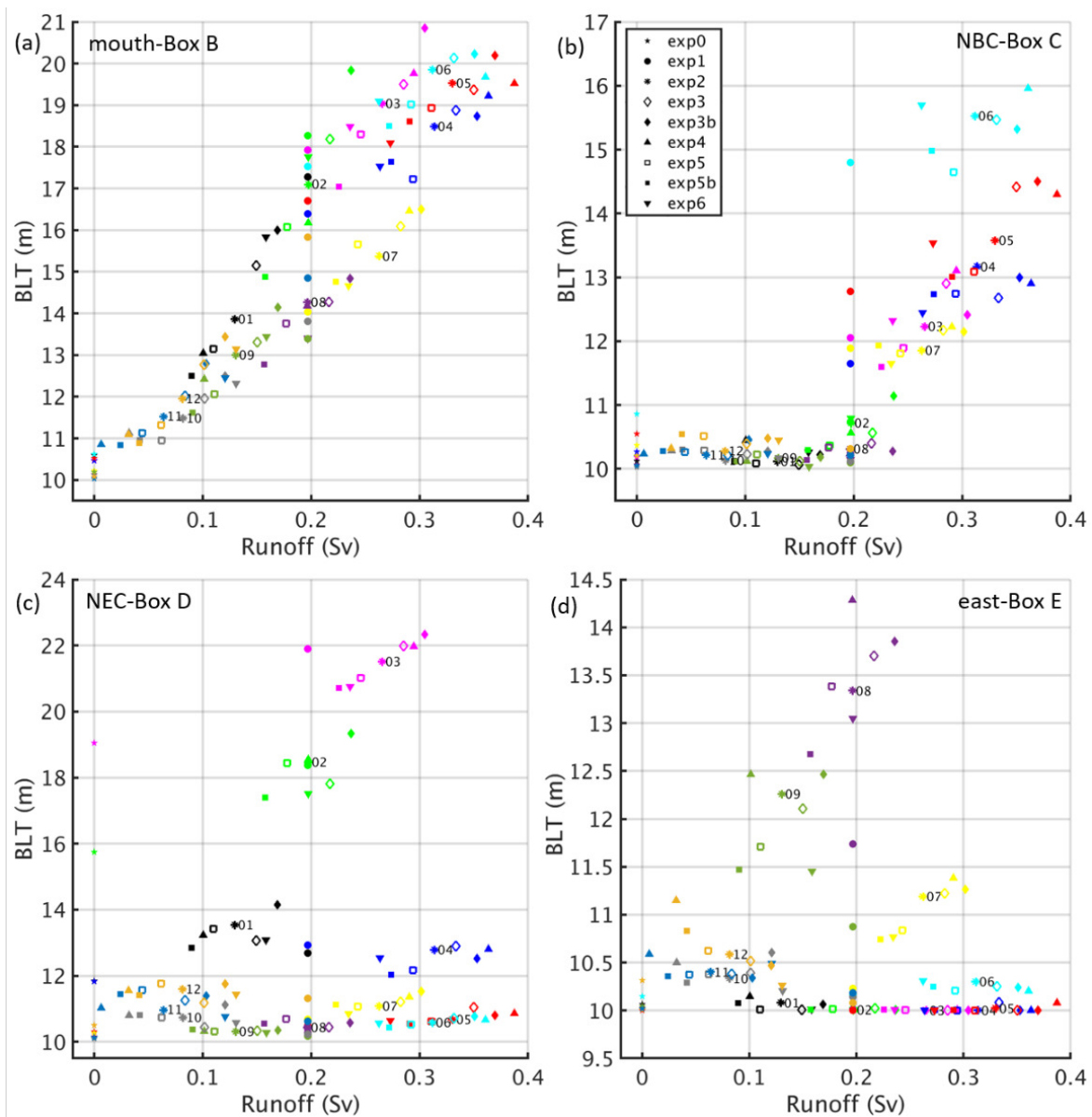


Figure 5.4: Relationship over the period 2008-2015 between monthly-mean runoff (Sv) (area-averaged in Box A directly at the Amazon mouth) and monthly means of BLT (meters) area-averaged in (a) mouth-Box B, (b) NBC-Box C, (c) NEC-Box D and (d) east-Box E.

maximum difference in ILD and MLD is in June, when there is the seasonal largest BLT in this region (Figure 5.4b). Compared to exp4, we see that the BLT is the largest in certain months for exp3b and exp3 like in May, April, November and February. The BLT is higher in exp6 than in exp5 and exp5b for June and May, though the runoff is larger in the experiments with smaller BLT. Thus, sometimes the BLT corresponds to the runoff among the experiments for a month, but some other times the BLT does not correspond to the order of the runoff among the experiments for a month. Like for the time mean, here as well we see that in June exp4 has the largest BLT (16 m) and runoff, after the extreme case of exp3c (16.5 m, not shown). The linear relation is

mainly present from March to July.

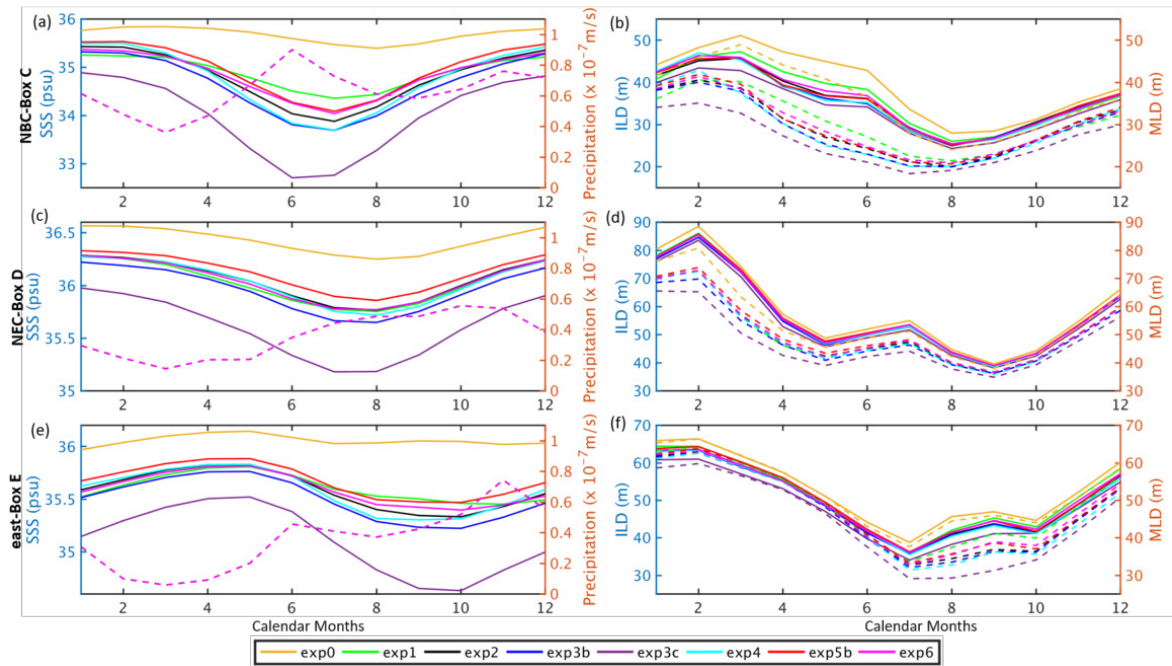


Figure 5.5: Monthly means over the period 2008-2015 of area-averaged (a,c,e) SSS (psu, solid) and precipitation ($\times 10^{-7}$ m/s, dashed), and (b,d,f) ILD (meters, solid) and MLD (meters, dashed) over (a,b) NBC-Box C, (c,d) NEC-Box D, (e,f) east-Box E, for different experiments.

On the other hand, in the NEC region (Box D in Figure 5.2b), the linear relation is present in the winter months of January-March, the time of the year with persistent barrier layers in the NEC region (Figure 5.4c and section 4.4 of Chapter 4). In NEC-Box D the SSS is highest in the months December to March and is small during July-September (Figure 5.5c). The SSS is small 3 to 4 months after the highest Amazon discharge in May, since it takes 3 to 4 months for the signal to travel to this region. Exp0 has again the largest SSS, followed in all months by exp5b and exp5. Exp3c, exp3b and exp3 have the smallest SSS. Precipitation is high during June-November, which also influences the SSS in all experiments, especially seen in exp0. The seasonal ILD and MLD (Figure 5.5d) are large for all experiments in February and small in September, as seen in section 4.4 of Chapter 4, with an intermediate maximum in July. In the NEC-Box D the BLT is the largest (20-22.5 m) in March and the smallest in September (Figure 5.4c). This feature is almost the same for exp0, which has no runoff. Thus, the BLT variability in this region is not mainly influenced by the runoff discharge, but more by the mechanisms I addressed in the previous chapter, which are the subduction of SMW towards the tropics along with the northward Ekman transport of fresher water, causing the tilting of salinity fronts. The runoff is the highest in May but it does not reach this region in the north at the same time (as seen in the SSS variation in Figure 5.5c), one of the reasons apart from the above explained mechanism, because of which we do not see a correlation between the runoff and the largest BLT here. During March, the order of experiments for the largest to the smallest BLT is

exp3c (~ 23.7 m, not shown), exp3b, exp4, exp3, exp1, exp2, exp5, exp6, exp5b, exp0 and is mostly proportional to runoff (Figure 5.4c).

In the region covering the eastern extent of the Amazon plume (Box E in Figure 5.2b) the linear relation between BLT and runoff is present in the summer months of July-September and like in NBC-box C, in this region as well the exp4 dominates over the experiments with a change in just the mean. SSS (Figure 5.5e) is low in September-October, the other months being higher. This is because after the bifurcation of the NBC due to its retroreflection, the resulting NECC has maximum strength during August-October, transporting the freshwater from the Amazon eastward. From August-October the SSS is largest in exp0, exp1, exp5b, and smallest in exp3c, exp3b. The precipitation in east-Box E rises from June and is highest in November, which reflects more the SSS in exp0 and exp1. The ILD and MLD (Figure 5.5f) both are largest in February and smallest in July, rising in August with the second peak in September, dropping in October, then rising again from November to February. The experiments have similar values for ILD and MLD, respectively, from January to June, but from July-October there is a greater difference between the ILD and MLD. In Figure 5.4d the largest BLT of 16 m (exp3c) and 14.3 m (exp4) occur in August. The BLT has a seasonal high in July-September and is around 10-10.5 m for other months, except for a slight rise in December (probably because of the precipitation, as it has a seasonal high in November-December in east-Box E). Exp4 has the largest BLT in July-September and October-December. Thus in this region the exp4 is dominating, as seen also in the time mean. Therefore, currents like the NECC play an important role in east-Box E region, spreading the freshwater to the east after the maximum discharge in May, which gives rise to a large BLT in summer-autumn.

From the monthly patterns in each box it is inferred that in all the boxes the SSS decreases with larger runoff and precipitation, but is influenced more by the runoff in the regions closer to the mouth. The freshwater causes the SSS to be small in different months in each box, depending on the time it takes for the currents to transport the freshwater to the respective location. MLD has more differences amongst experiments than ILD in all the regions studied (Figure 5.5b,d,f). Compared to the other experiments, exp3c with 100% increased mean discharge has the largest runoff and BLT in every month, while having the same seasonal cycle of BLT as seen for every individual box, therefore not shown in Figure 5.4. Thus, the overall pattern seen in all regions from the time mean, monthly mean and standard deviation relations between runoff and BLT is that exp3b (exp5b) have largest (smallest) mean BLT, except in NBC-boxC and east-boxE where exp4 and exp6 dominate.

5.3.1 Time mean differences

The time mean difference between each of the experiments and the control run (exp2) is examined in the western tropical Atlantic (Figure 5.6 and Figure 5.7). Exp3 and exp5

with 10% increase and decrease in mean runoff showed similar patterns and signals as exp3b and exp5b respectively, but with a smaller magnitude of the differences. On comparison of the difference between exp2b (where the mean runoff is increased by just $10^{-4}\%$) and exp2 (control run) and the differences between exp3/exp5 and exp2, nearly similar magnitudes of differences were found. Hence, exp3 and exp5 results are not presented.

In Figure 5.6a exp0 has a larger SSS than exp2 with a difference of 6 psu at the Amazon shelf and around 1 psu in the periphery and plume. Exp1 has still a larger SSS than exp2 (Figure 5.6c) in most of the regions under the Amazon plume. Exp3 and exp3b have a smaller SSS than exp2 overall (Figure 5.6e). Exp3c has the smallest SSS (Figure 5.6g), the difference being as large in magnitude as in the case exp0m2. Exp5 and exp5b have a larger SSS than exp2 and exp5b (Figure 5.6k) has the maximum SSS of all the experiments in all the regions, especially at the Amazon shelf. Compared to exp2, in all the regions, the SSS is only very weakly different in exp4 (Figure 5.6i). The salinity in the top 50 m shows the same pattern in all experiments as the SSS, though the magnitude of the differences is a little smaller than for SSS. Density in the top 50 m follows the same patterns as salinity.

SST (Figure 5.6, right column) differences between experiments and exp2 are overall very weak, except for the extreme cases of no runoff (exp0) and 100% more runoff (exp3c). In the former case, a saltier surface layer is associated to colder conditions along the NBC and its retroreflection region, i.e., a denser surface layer. In the latter case, a large discharge makes exp3c fresher and warmer at the surface (i.e., lighter) in the same region. All other experiments have patchy and non-significant differences to exp2 (Figure 5.6d,f,j,l,n). The temperature in the top 50 m was also examined and showed similar results as the SST. There is not a very clear signal seen in SST and temperature in the top 50 m since the changes in the runoff forcing translate directly in SSS changes near the Amazon mouth. The temperature forcing associated with the discharge is not modeled. Therefore, salinity changes currents, which in turn change the SST distribution in the simulations.

In the time mean of exp0m2 the ILD is overall smaller in exp2 than in exp0, with a maximum difference of -15 m at the mouth-Box B (Figure 5.7a). ILD is also larger in exp1 than in exp2 (Figure 5.7d). Exp4m2 (Figure 5.7m) has smaller ILD differences and a patchy undefined (mostly not significant) pattern, the same applying to exp6 but with a reversed sign (Figure 5.7s). The ILD is smaller in exp3b compared to exp2 (Figure 5.7g), but again not significantly different. Exp5b (Figure 5.7p) has the largest ILD in all the regions amongst all the realistic experiments and its difference to exp2 is positive in a localized area offshore the Amazon mouth.

The MLD (Figure 5.7b,e,h,k,n,q,t) has the same differences like in ILD between the experiments and exp2, but the magnitude and the spatial extent of the differences are much larger in MLD than in the ILD. This means that MLD is impacted stronger than ILD.

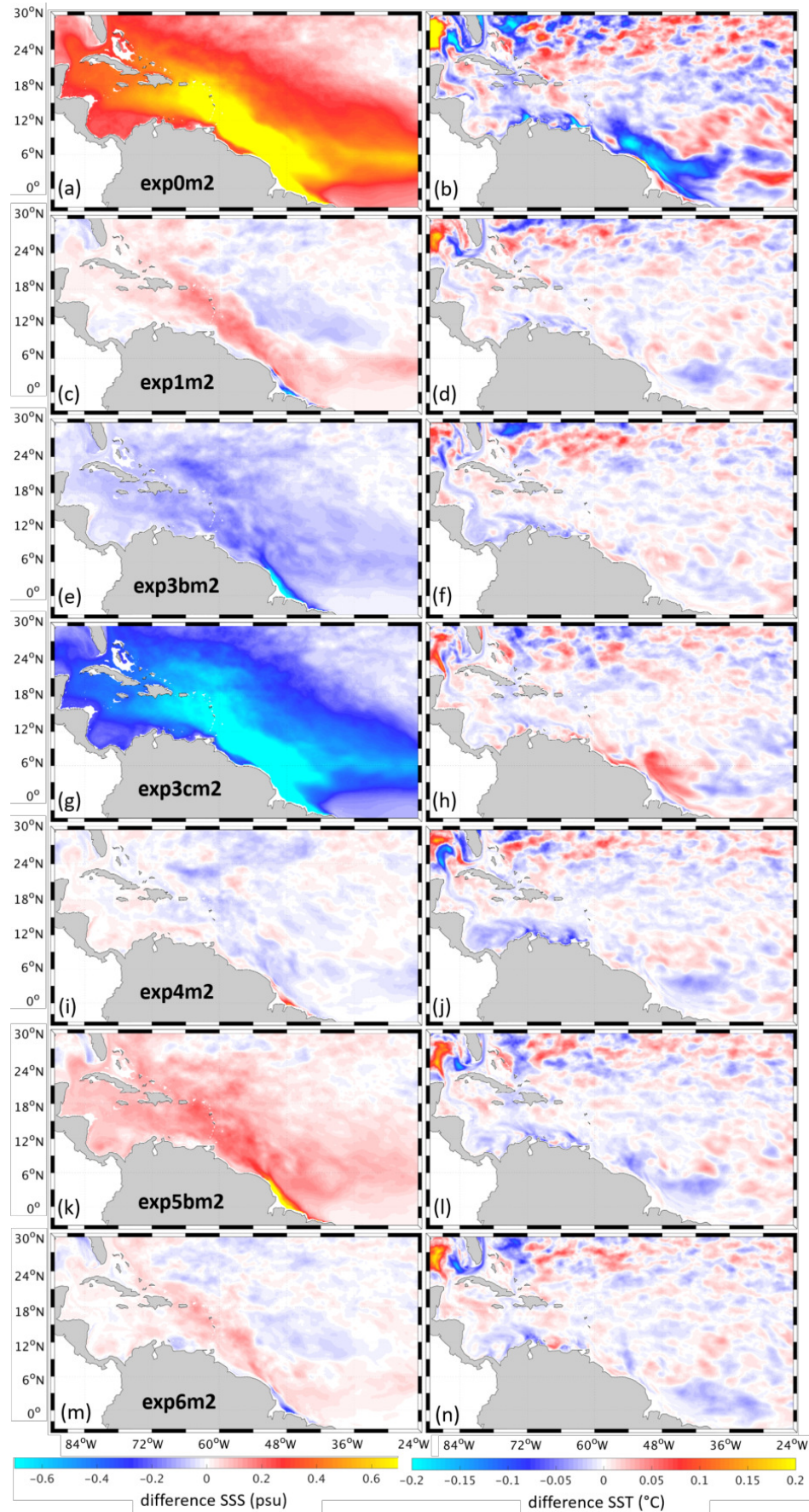


Figure 5.6: Time mean over the period 2008-2015 of (a,c,e,g,i,k,m) SSS (psu) and (b,d,f,h,j,l,n) SST (°C) differences (a,b) exp0-exp2 (exp0m2), (c,d) exp1m2, (e,f) exp3bm2, (g,h) exp3cm2, (i,j) exp4m2, (k,l) exp5bm2, (m,n) exp6m2.

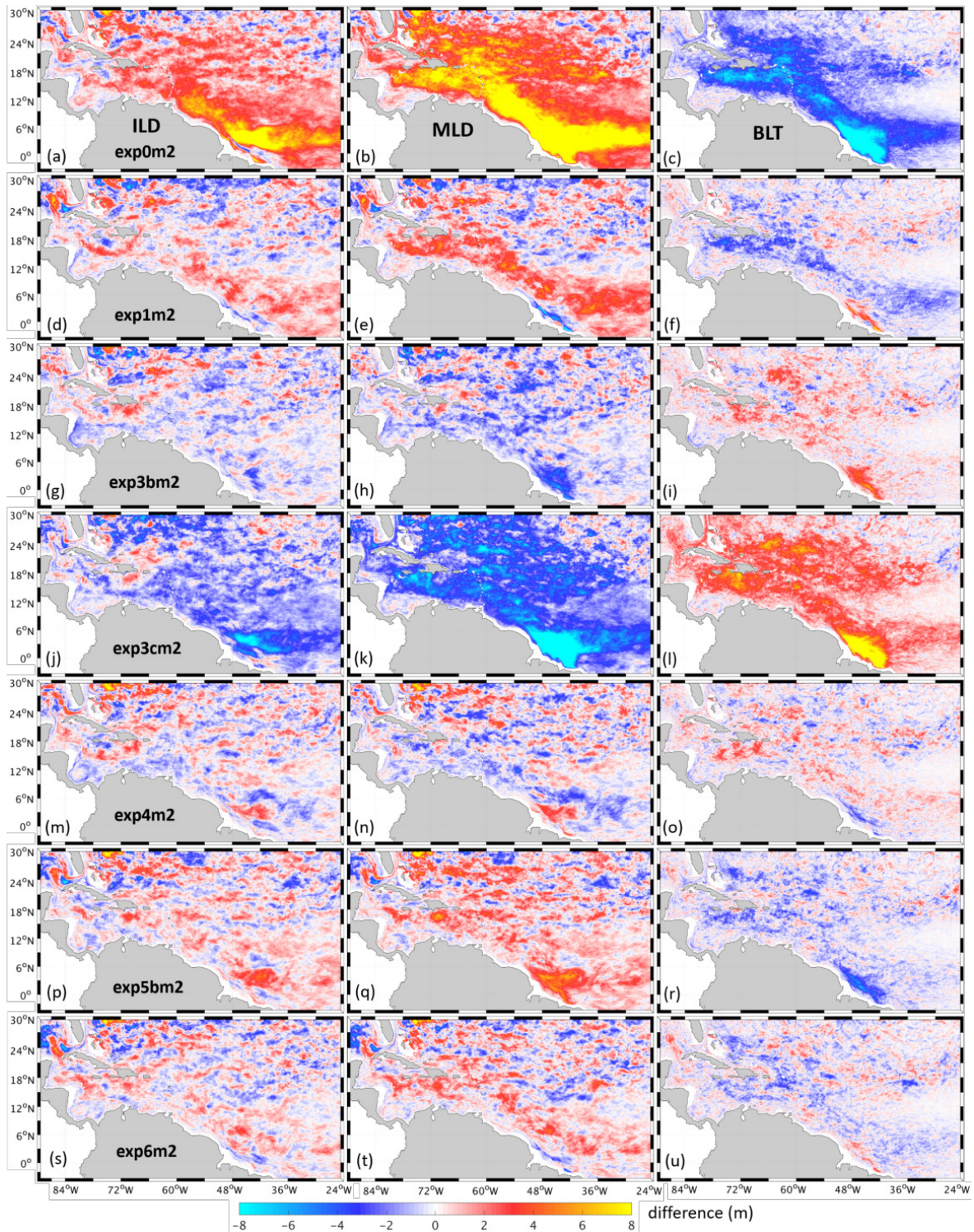


Figure 5.7: Time mean over the period 2008-2015 of the differences (a,b,c) exp0-exp2 (exp0m2), (d,e,f) exp1m2, (g,h,i) exp3bm2, (j,k,l) exp3cm2, (m,n,o) exp4m2, (p,q,r) exp5bm2, (s,t,u) exp6m2 in (a,d,g,j,m,p,s) ILD, (b,e,h,k,n,q,t) MLD, and (c,f,i,l,o,r,u) BLT (meters).

In the time mean of exp0m2 the BLT (Figure 5.7c) is 25 m larger in exp2 (with seasonal runoff) than in exp0 (with no runoff) in the mouth-Box B, while around 8 m larger in the rest of the Amazon plume. Exp1 has smaller BLT than exp2 overall (Figure 5.7f). Exp4 (Figure 5.7o) (with amplified seasonal amplitude) has larger BLT and exp6 (Figure 5.7u) (with attenuated seasonal runoff) has mostly smaller BLT than exp2 in the plume. However, BLT mean differences in the two amplitude change experiments are very low, with differences appearing in the seasonal cycle but are averaged out in the time mean. Exp3b and exp3c have larger BLT than exp2 (Figure 5.7i,l). Exp3b has the largest BLT at the mouth-Box B. Exp3c and exp0 have the largest, but opposite differences in BLT. Exp5b (Figure 5.7r) has smaller BLT than exp2.

From the time mean of the differences between the experiments and exp2, the largest differences are seen in the cases of no river runoff (exp0) and 100% increase in mean runoff (exp3c). It seems that in general the experiments with 20% change in the mean Amazon discharge have a larger impact on the tropical Atlantic compared to the experiments with changes in the runoff seasonal amplitude.

5.3.2 Seasonal variability of differences

The objective here is to investigate the changes in the monthly variabilities of the physical variables in response to the changes in Amazon runoff. The spatial maps of the differences between the experiments and exp2 for SSS, MLD and BLT in the month of June (Figure 5.8), one of the months with largest differences, reveal that the largest differences occur in the case exp0m2. The SSS is larger in exp0 than in exp2 by 10 psu at the shelf (Figure 5.8a), MLD is smaller in exp2 than exp0 by 40-50 m (Figure 5.8b) and BLT (Figure 5.8c) is larger in exp2 than exp0 by a maximum of 42 m at the mouth-Box B and sometimes NBC-Box C. SST has a maximum difference of $\sim 1^\circ\text{C}$ in June and the ILD maximum difference ranges from 26 m (in May) to 42 m (in September) at mouth-Box B (not shown).

The next largest differences are seen between exp3c and exp2 for all the variables (Figure 5.8j,k,l). Exp1 and exp6 have smaller runoff than exp2 in June, while the exp4 has larger runoff than exp2. We see the corresponding impacts in exp1m2 (Figure 5.8d,e,f), exp6m2 (Figure 5.8s,t,u), and exp4m2 (Figure 5.8m,n,o), exp1 and exp6 showing opposite behaviors from exp4. Exp3b (Figure 5.8g,h,i) with the larger mean runoff and exp5b (Figure 5.8p,q,r) with the smaller mean runoff also show the opposite behavior.

The differences of the above physical variables were area-averaged over all the boxes defined above along the plume. The results for SSS, MLD and BLT are presented in Figure 5.9. The maximum difference in SSS is seen in the NBC-Box C (Figure 5.9d): 1.6 psu for exp0m2 in July, followed by exp3cm2 in June. The mouth-Box B (Figure 5.9a) has the second largest difference magnitude: 1.5 psu for exp0m2 in June, 1.3 psu for exp3cm2 in May. The maximum difference in MLD is in mouth-Box B (Figure

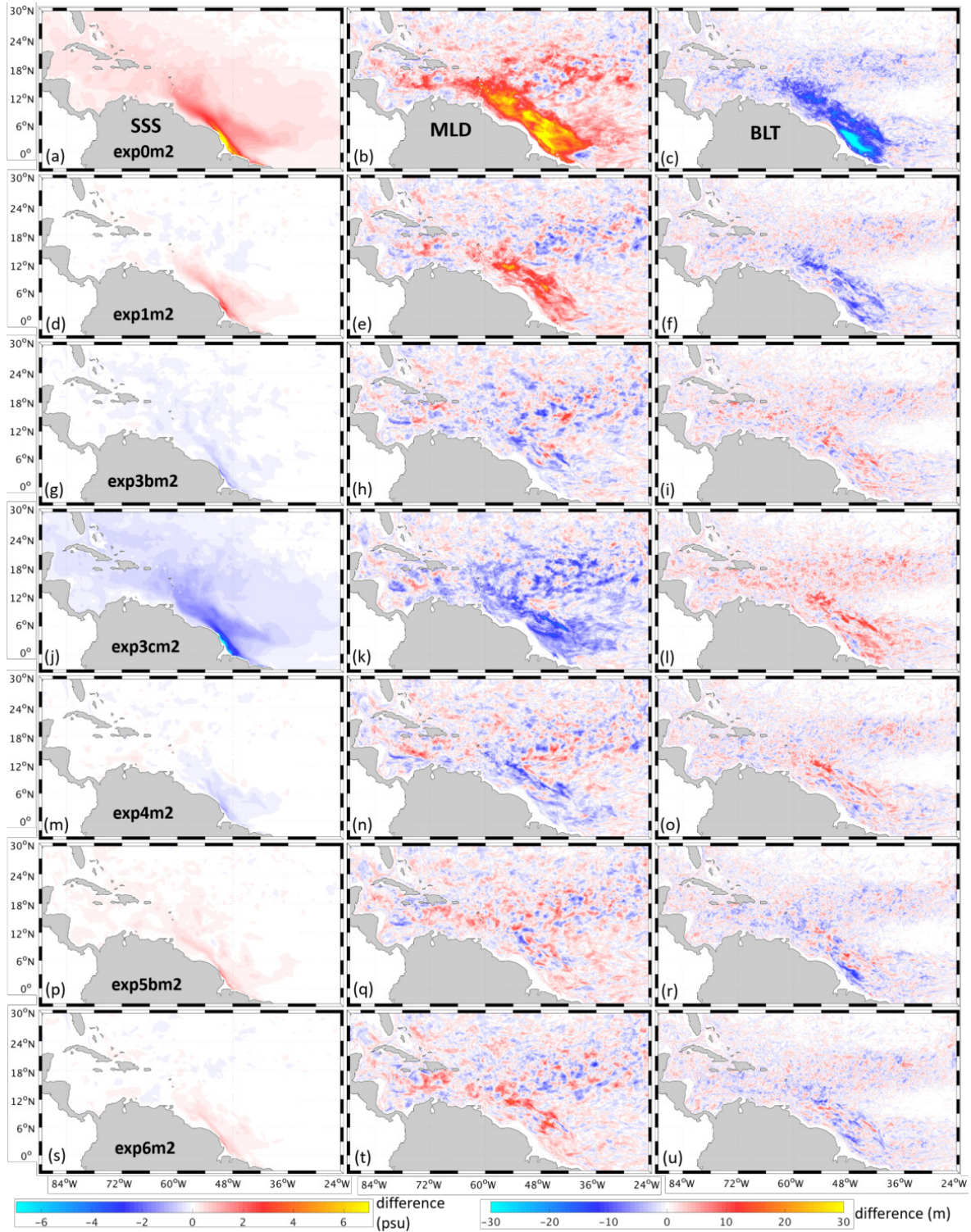


Figure 5.8: Mean over the period 2008-2015 for June of the differences (a,b,c) exp0-exp2 (exp0m2), (d,e,f) exp1m2, (g,h,i) exp3bm2, (j,k,l) exp3cm2, (m,n,o) exp4m2, (p,q,r) exp5bm2, (s,t,u) exp6m2 in (a,d,g,j,m,p,s) SSS (psu), (b,e,h,k,n,q,t) MLD and (c,f,i,l,o,r,u) BLT (meters).

5.9b): 15 m for exp0m2 in June, 11 m for exp3cm2 in December. NBC-Box C (Figure 5.9e) follows with a MLD difference of 14 m for exp0m2 in May and 6 m for exp3cm2 in March. The BLT difference is maximum in mouth-Box B (Figure 5.9c), with 12 m for exp0m2 in June and 9 m for exp3cm2 in January. NBC-Box C (Figure 5.9f) follows with a BLT difference of 6 m for exp0m2 in April-June, and 4 m for exp3cm2 in February. East-Box E (Figure 5.9l) also has 6 m BLT difference for exp0m2 in September followed by exp3cm2 with 2.5 m difference also in September. The minimum difference in all the above variables is seen in NEC-Box D (Figure 5.9g,h,i).

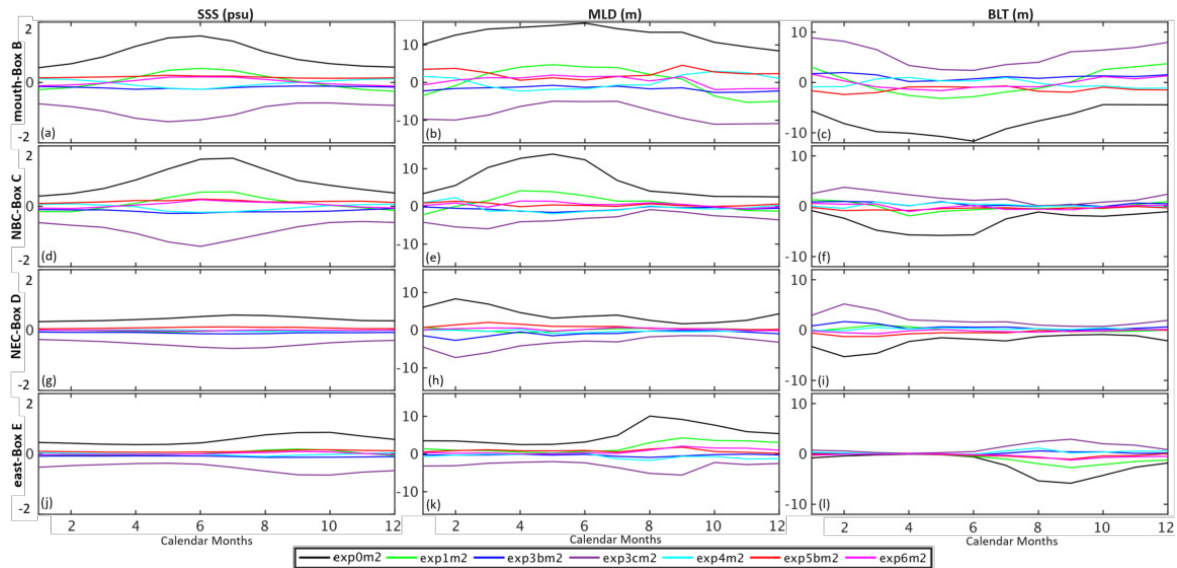


Figure 5.9: Monthly means over 2008-2015 of the area-averaged differences: exp0-exp2 (exp0m2), exp1m2, exp3bm2, exp3cm2, exp4m2, exp5bm2, exp6m2 for (a,d,g,j) SSS (psu), (b,e,h,k) MLD and (c,f,i,l) BLT (meters) over (a,b,c) mouth-Box B, (d,e,f) NBC-Box C, (g,h,i) NEC-Box D and (j,k,l) east-Box E.

ILD shows similar behavior in the climatology as MLD (Figure 5.5, also seen in the time mean in Figure 5.7), therefore is not shown. Though the seasonal cycle of SST has a range of around 5°C , the differences between the experiments are very small (of the order 10^{-2}) and SST has a behavior that is the opposite of SSS (also seen in time mean Figure 5.6).

For salinity and density in the top 50 m, the differences to exp2 are like those of SSS and for some months stronger than SSS at the farthest reaches of the plume, since the signal of the previous months stay in the depths below the immediate surface. Exp3cm2 and exp0m2 have the largest differences in all the variables and areas, but exp3cm2 has opposite phase of the seasonal cycle of the differences compared to exp0m2. They are nevertheless of the same sign/phase in the boxes close to the mouth, as in mouth-Box B and NBC-Box C (Figure 5.9b,c,e,f), because exp0 has no runoff and thus no seasonal cycle, while in exp3cm2 both exp3c and exp2 have the same seasonal cycle. Therefore in exp0m2 a high in the seasonal cycle during summer is captured unlike in exp3cm2.

From the spatial maps of differences for each month (shown for June in Figure 5.8 and January in Figure 5.10) I infer the following. The sign of the differences between the experiments with a change in just the mean runoff remain the same throughout the year in the entire plume and have the same signs of differences as seen in the time mean (Figure 5.6, Figure 5.7 and Figure 5.9). The signs of differences change throughout the year in experiments with a change in seasonal amplitude. In January exp1 has more runoff than other experiments (Figure 5.3b,c), therefore SST and BLT are larger in exp1, while MLD, ILD and SSS are smaller. The behavior of exp6 is the same as exp1, while the opposite is true for exp4, as exp6 has slightly more runoff than exp2 in January, and exp4 a smaller runoff (Figure 5.10).

We saw in Figure 5.3c that the period September-January has less runoff. The difference between exp4 and exp6 is maximum in November, and minimum in September and January, while the opposite is true from March-July, with maximum difference between exp4 and exp6 being in May, and least in July and March. The runoff values are the same in exp1, exp2, exp4 and exp6 in February and August. So in February exp1, exp4 and exp6 do not show much differences with respect to exp2, but they show similar signs of differences as in January. The differences exp3cm2, exp3bm2 and exp5bm2, especially for MLD and BLT, are larger in the mouth-box B in December-February, seen in Figure 5.9b,c and Figure 5.10. In March the results are the opposite as for in January for exp1 only at the Amazon shelf (as it now has smaller runoff than other experiments), and exp4 and exp6 have almost no differences with exp2. April and May successively have larger magnitude of differences than March. For instance SSS, in exp4 is smaller than in exp2, and SSS in exp1 and exp6 are now larger than exp2 overall (starting more intensely from river mouth). In June (Figure 5.9 NBC-Box C (d,e,f), mouth-Box B (a,b,c)) and July (Figure 5.9 NBC-Box C (d,e,f)), these differences spread more to the northwest (Figure 5.8). August and February have the same runoff, but the differences spread more east now in August and September (Figure 5.9 east-Box E (j,k,l)), and the differences between exp4m2, exp6m2 and exp1m2 start getting smaller in the rest of the plume. In October-November the experiments with changes in mean are spread in the entire plume in the tropical Atlantic, but the exp1 and exp6, as they have larger runoff now than exp2 the SSS, MLD, ILD are smaller than in exp2, and SST, BLT larger; the opposite is true for exp4. All variables show similar behavior as November in December-January. This is clearly evident in mouth-Box B (Figure 5.9 mouth-Box B (a,b,c)), and occurs with a few months lag in the other boxes depending on how far they are from the mouth.

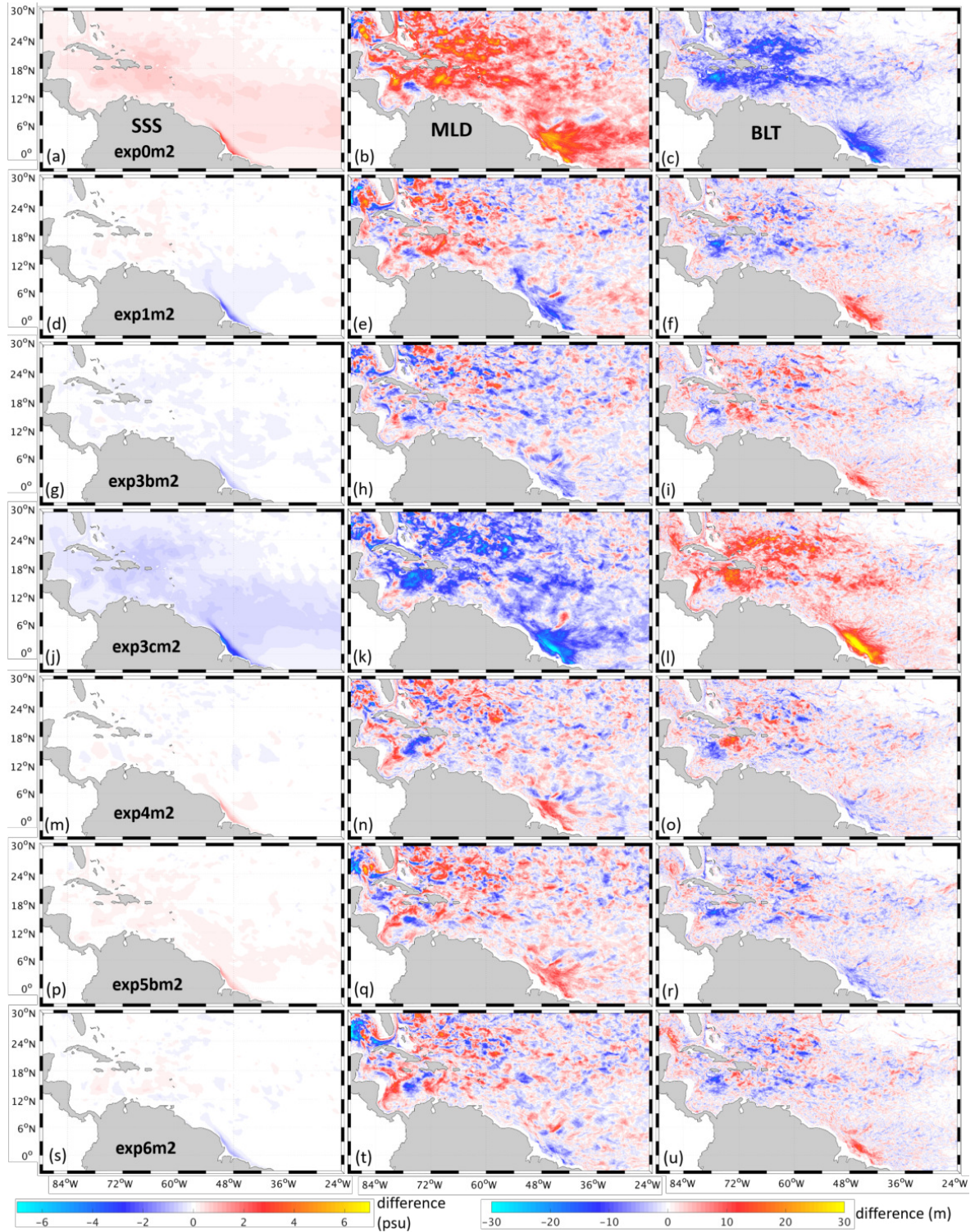


Figure 5.10: Mean over the period 2008-2015 for January of the differences (a,b,c) exp0-exp2 (exp0m2), (d,e,f) exp1m2, (g,h,i) exp3bm2, (j,k,l) exp3cm2, (m,n,o) exp4m2, (p,q,r) exp5bm2, (s,t,u) exp6m2 in (a,d,g,j,m,p,s) SSS (psu), (b,e,h,k,n,q,t) MLD and (c,f,i,l,o,r,u) BLT (meters).

5.4 Relation between Amazon runoff and the NBC/NECC and related eddy activity

In this section I focus on dynamical changes imparted by the modification in Amazon discharge. More specifically, I investigate how the total kinetic energy (KE) and its decomposition into mean kinetic energy (MKE) and eddy kinetic energy (EKE) changes in the different experiments due to the modifications in the Amazon runoff. The KE, MKE and EKE are computed for the period 2008-2015 and averaged over the top 50 m of the water column. The KE is computed as $0.5 (u^2 + v^2)$ and MKE is computed as $0.5 (\bar{u}^2 + \bar{v}^2)$, where \bar{u} and \bar{v} are the time mean over the 8 years of the zonal (u) and meridional (v) components of the velocity. EKE is computed as $0.5 (u'^2 + v'^2)$, where $u' = u - \bar{u}$ and $v' = v - \bar{v}$ are the deviations from the time mean.

5.4.1 Time mean differences

The KE difference between exp0 and exp2 in Figure 5.11a shows that exp2 has more energetic northwestward currents along the NBC and NBC rings region, all along the Caribbean Sea and Gulf of Mexico and in the FC (current demarcated in Figure 2.1c). So all of the western boundary currents in the tropical Atlantic seem to be affected by the suppression of Amazon runoff in exp0. Around 6°N an interesting pattern emerges along the axis of the NBC retroflexion and NECC, with exp2 having larger KE inshore of the NBC axis and north of the NECC axis and smaller KE offshore of the NBC axis and south of the NECC axis. This means that the presence of Amazon freshwater inshore of the NBC tends to intensify the NBC and tends to decrease the retroflexion and the emerging NECC. The same patterns are observed for the difference in MKE between the two experiments (Figure 5.11b). The MKE differences seem to explain the KE differences in general, in particular downstream of the Lesser Antilles, with a signal in the EKE difference only being present there in the highly non-linear areas of the LC (current demarcated in Figure 2.1c and Figure 5.11c).

In the NBC/NECC region, the EKE differences are substantial and translate mostly in interannual differences of the meandering associated with the retroflexion into the NECC. So, the clear emerging picture when introducing freshwater is a general intensification of the boundary current system and a weakening of the NECC. Therefore, the westward, north-westward surface currents in the western tropical Atlantic get stronger in magnitude with river runoff while the eastward moving currents remain the same or are smaller in magnitude, without significant changes in the position of the time mean currents.

We turn now attention to exp3b and exp3c, both with increased freshwater discharge relative to exp2. The patterns of KE differences are essentially the same as in exp0m2 but now with reversed sign, since exp2 has less freshwater than exp3b and

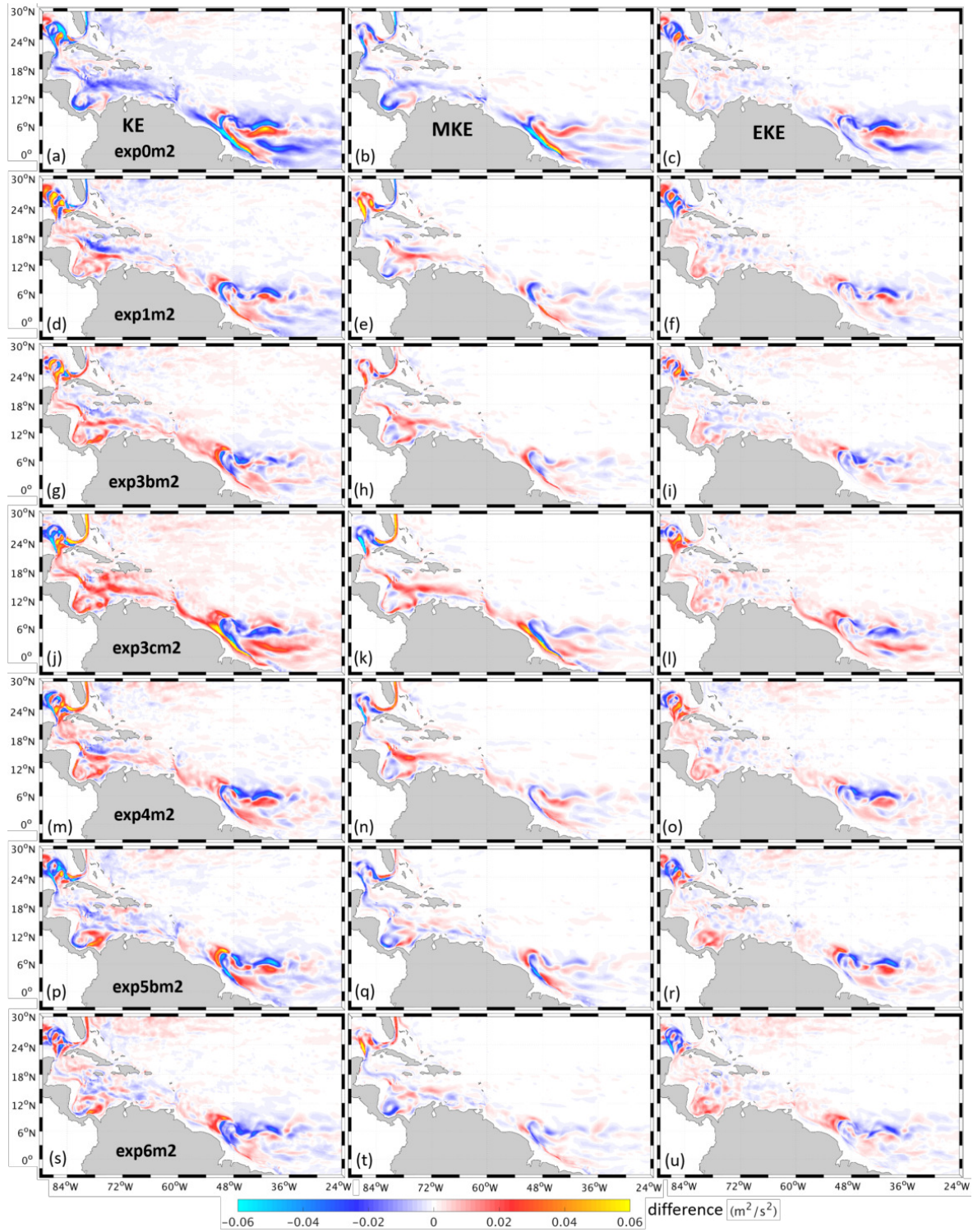


Figure 5.11: Time mean over the period 2008-2015 of the differences (a,b,c) exp0-exp2 (exp0m2), (d,e,f) exp1m2, (g,h,i) exp3bm2, (j,k,l) exp3cm2, (m,n,o) exp4m2, (p,q,r) exp5bm2, (s,t,u) exp6m2 of (a,d,g,j,m,p,s) KE (m^2/s^2), (b,e,h,k,n,q,t) MKE (m^2/s^2) and (c,f,i,l,o,r,u) EKE (m^2/s^2).

exp3c. We see still a general increase in the energy of the boundary currents (Figure 5.11g,j), specially when the freshwater forcing is stronger (like in exp3c). In these two cases, one notices that also the area where NBC rings propagate is affected, showing stronger transient energy (EKE) for stronger freshwater forcing (Figure 5.11i,l).

In exp5b the Amazon discharge has a smaller mean than it has in exp2. Strong KE differences are still present in the same places as for the experiments described above, with a tendency for a general decrease of the energy along the boundary. However, the coherence of the signal is weak; in particular there is no connection between the changes in the retroreflection area and the area downstream of 72°W. On the other hand, in the experiment with the same magnitude of forcing but opposite sign (i.e., exp3b), a coherent signal of intensification connects both regions. This means that the current system is not completely responding linearly to the increase/decrease of freshwater. It seems that the increase of freshwater results in a strong response and that the ocean is more insensitive when freshwater is decreased. However, in the extreme case of no runoff, a clear response is retained.

The experiments with change in runoff amplitude (exp4 and exp6) are also not symmetric in their response (Figure 5.11m,s). Exp4, including a large amplitude runoff, shows a coherent increase in energy all along the boundary, just like exp3b and exp3c. Exp6 on the other hand, shows only a coherent response in the NECC. Furthermore, in exp4 the total KE can partly be explained by changes in MKE and partly by changes in EKE whereas in exp6 it is mainly due to changes in EKE (Figure 5.11n,o,t,u). Exp1, the extreme case of zero amplitude seasonal cycle shows a pattern of differences to exp2, similar to that of exp6. This means that the seasonal cycle gives a surplus of freshwater, thus acting like exp3, exp3b and exp3c.

Finally, an interesting additional fact is that the response in the NECC area is similar across all experiments. Only in exp0 and exp3c, when the discharge modification is large, does the NECC shift slightly meridionally in their mean position and/or presents different meandering (Figure 5.11a,j). Moreover, exp4m2 and exp5bm2 show similar patterns at the retroreflection and NECC as exp0m2.

5.4.2 Seasonal variability of differences

The objective of this section is to identify the impacts of changes in Amazon runoff on the seasonal variations in the dynamics. For this, the differences of all the experiments to exp2 were area-averaged over the boxes defined along the plume in the previous section and are presented as a climatology in Figure 5.12.

The KE (Figure 5.12c) difference is maximum in the NBC-Box C, with $0.024 \text{ m}^2/\text{s}^2$ for exp3bm2 in August, and exp0m2 in September. Mouth-Box B (Figure 5.12a) follows with a KE difference of $0.016 \text{ m}^2/\text{s}^2$ for exp1m2 in October and $0.01 \text{ m}^2/\text{s}^2$ for exp3cm2 in July. The minimum difference in KE, EKE and surface current magnitude (not

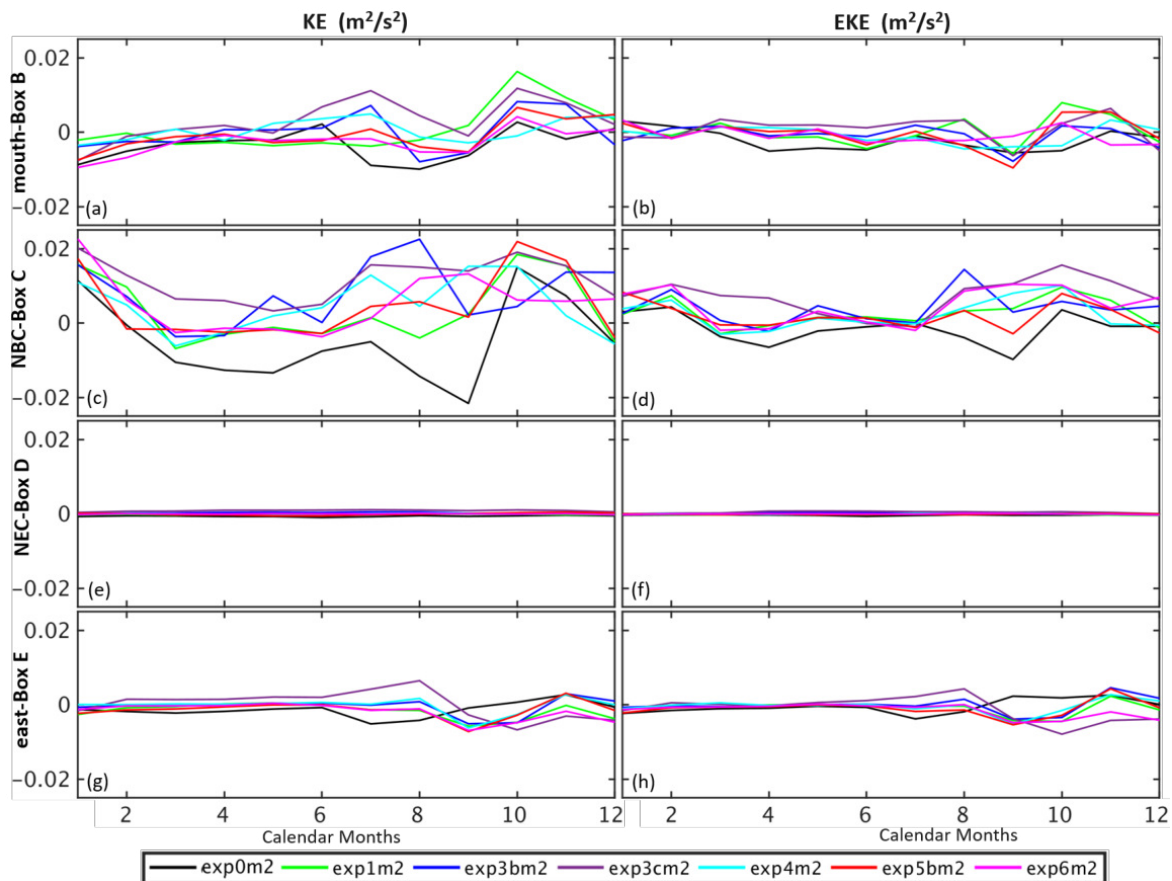


Figure 5.12: Monthly mean over the period 2008-2015 of the area-average of the differences $\text{exp0}-\text{exp2}$ (exp0m2), exp1m2 , exp3bm2 , exp3cm2 , exp4m2 , exp5bm2 , exp6m2 for (a,c,e,g) KE and (b,d,f,h) EKE (m^2/s^2) over (a,b) mouth-Box B, (c,d) NBC-Box C, (e,f) NEC-Box D, and (g,h) east-Box E.

shown) is seen in the NEC-Box D (Figure 5.12e,f). The maximum difference in EKE is also in the NBC-Box C (Figure 5.12d) with $0.016 m^2/s^2$ for exp3cm2 in October, and $0.015 m^2/s^2$ for exp3bm2 in August. Mouth-Box B (Figure 5.12b) follows with an EKE difference of $0.007 m^2/s^2$ for exp1m2 in October and $0.005 m^2/s^2$ for exp0m2 in April-June. The surface current magnitude differences show similar behavior as KE differences.

In Figure 5.12 it can also be seen that the energy changes in the NEC-Box D are very small throughout the year and therefore, they are not significant compared to the other boxes, and the changes in east-Box E occur during the second half of the year, when the freshwater from the Amazon carried by the NECC arrives.

By observing the spatial maps of the differences in KE, EKE and surface current speed (shown only for KE and exp0m2 from July-November in Figure 5.13) and the area-averages of those differences (Figure 5.12), the following can be inferred. In January the surface current magnitude, KE and EKE show similar results as the time mean for all experiments. The exception being exp1 , as it has more runoff than exp2

in that month. Therefore, the western boundary currents are stronger in exp1 (as in mouth-Box B and NBC-Box C in Figure 5.12a,c). The retroreflection and NECC are stronger in exp2 (east-Box E in Figure 5.12g,h). Same is true for exp6, while opposite is true for exp4, since exp6 has slightly more runoff than exp2 in January, and exp4 smaller.

In February, the experiments with changes in mean discharge show the usual trend and exp1, exp4 and exp6 do not show significant differences with respect to exp2. At the NBC-Box C all these experiments have larger magnitude than exp2 for all quantities. In March the results are the opposite of January for exp1, exp4 and exp6. Same behavior as in January is seen for the experiments with change in mean runoff. April shows similar patterns as March. May in most areas in the plume shows a similar tendency as well with slightly higher magnitude of differences, and the differences get larger in June-July, especially at the NBC. The largest KE difference ($\sim -0.6 \text{ m}^2/\text{s}^2$) is found between exp0 and exp2 in the NBC in May-June. Experiments in August show similar pattern as in July but exp4 and exp6 have similar runoff values in August and similar values of differences in mouth-Box B, NBC-Box C and NEC-Box D (Figure 5.12a-d). Same holds for September, but exp1, exp4 and exp6 start to have the opposite behavior gradually in mouth-Box B and NBC-Box C (Figure 5.12a-d) where the western boundary currents dominate, since exp1 and exp6 have larger runoff than exp2, and exp4 has smaller runoff than exp2 from this month onwards. In the east-Box E, exp4 is larger than exp2 in the later quarter of the year as well, and exp1 and exp6 have negative differences (Figure 5.12g,h), the reason for which we will see next.

Figure 5.12g,h (east-Box E) presents the behavior in the NECC when it is further east, and Figure 5.13 shows the evolution of the KE at the retroreflection and NECC in exp0 and the KE difference between exp0 and exp2. From February-May negligible differences exist in the retroreflection and the NECC, as they are not developed in those months. In June the retroreflection is in the early stage of development. In July the differences are stronger, the retroreflection being larger in exp0 than exp2 (Figure 5.13a,b). August has the same runoff in the experiments as February, but now the retroreflection is developed. During this month the retroreflection and NECC are stronger in magnitude in exp0 than exp2 (Figure 5.13c,d), and the position seems to have changed a little. The NECC moves a little northward in exp2 than in exp0. Indeed, the area between the retroreflection and NECC is more curved/bent in exp2, thus making the NECC shift further northward in exp2, but the magnitude is larger in exp0. Same is true in September (Figure 5.13e,f). The differences in KE (exp0-exp2) have a maximum magnitude of $\sim 0.6 \text{ m}^2/\text{s}^2$ in the monthly mean for October at the retroreflection of NBC into the NECC. From end October-November the retroreflection in exp0 gets weaker and the NECC is shifted more to the east than in exp2 (Figure 5.13g-j).

In the retroreflection and the NECC areas, exp5, exp5b and exp4 behave like exp0, i.e., the smaller the runoff in the experiments, the larger the magnitude of the retroreflection/NECC (east-Box E in Figure 5.12g,h). On the other hand, exp3, exp3b, exp3c

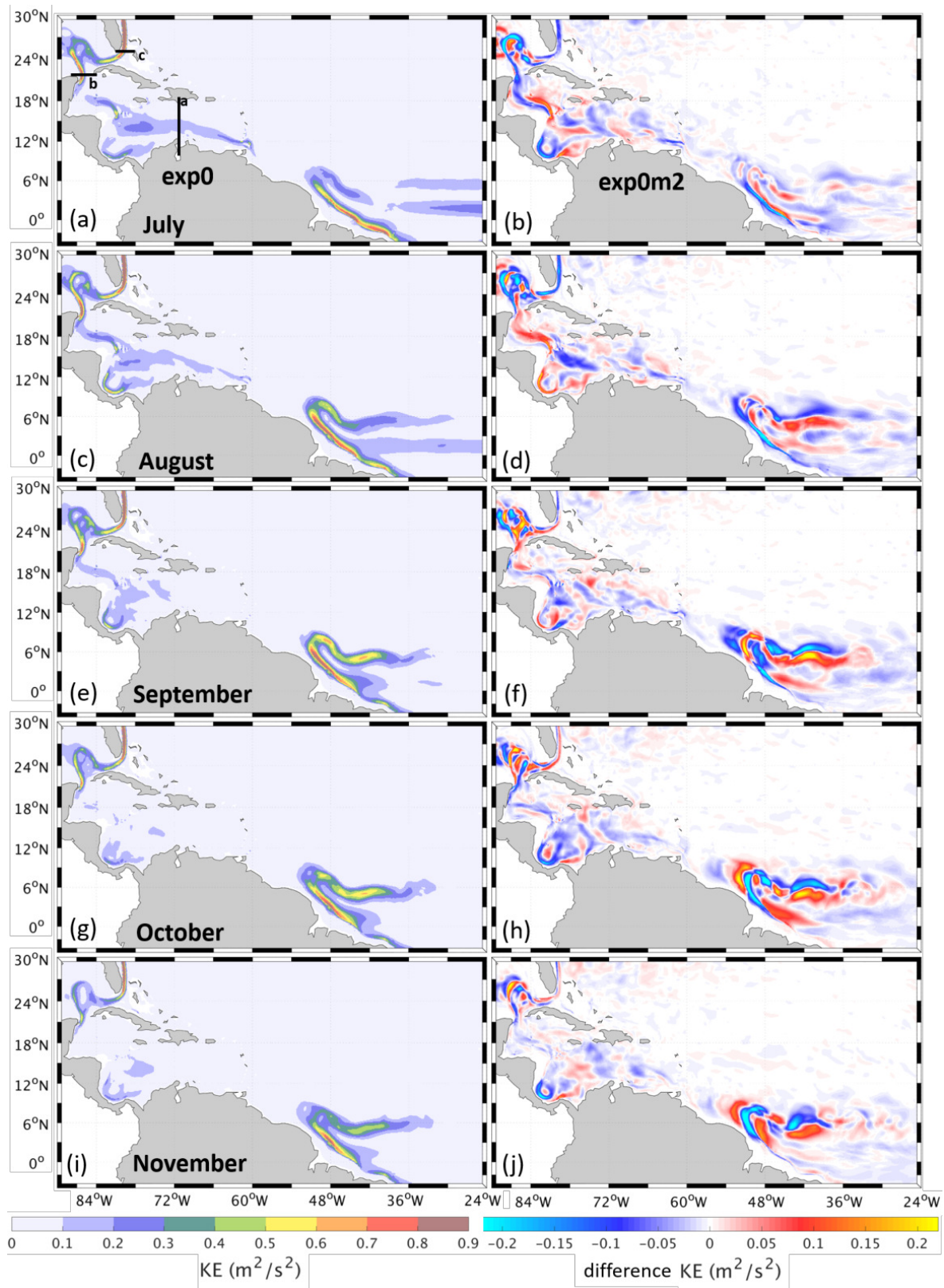


Figure 5.13: Monthly mean KE (m^2/s^2) for (a,c,e,g,i) exp0 from July-November and (b,d,f,h,j) differences exp0-exp2 (exp0m2) of KE. Black lines show sections studied later: (a) Caribbean Sea section, (b) Yucatan Channel section, (c) Florida Strait section.

and exp6 are more like exp2, i.e., the larger the runoff, the smaller the magnitude of the retroflection/NECC. Exp6 compared to exp4 has a little more meandering between the retroflection and the NECC, which is justified since exp4 has smaller runoff than exp6 during August-December (the months of the presence of strong retroflection and NECC) and therefore behaves more like exp0.

5.5 Relation between Amazon runoff and the large-scale north Atlantic circulation

In the previous sections, we saw that an increase in the mean runoff by 10%, 20% and 100% causes an increase in BLT, SST, temperature in top 50 m, surface current magnitude, KE, MKE and EKE for the western boundary currents in the tropical Atlantic (especially the NBC). Increasing the mean runoff also decreases the SSS, salinity and density in top 50 m, MLD and ILD. On the other hand, we saw that a decrease in mean runoff causes the opposite of the above. An increase or decrease in the seasonal amplitude cause mainly the similar impacts in time mean of the physical variables and dynamics that the increase or decrease in the mean runoff forcings have, respectively. In this section we will find out if the modifications in the Amazon river runoff also have an influence on the western boundary current transports, which in turn take the water further north into the Gulf Stream, as they are a part of the upper limb of the AMOC. Finally, we will find if there is a link between the changes in Amazon river runoff, the BLT formed due to it in the tropical Atlantic, and the large-scale AMOC.

5.5.1 Amazon runoff/BLT and the western boundary current transports

The volume transport (T) through three sections (black lines a, b, c in Figure 5.13a) taken across the western boundary flow along the eastern coast of America is computed for the meridional flow as:

$$T(y, t) = \int_{-H}^0 \int_{west}^{east} v(x, y, z, t) dx dz \quad (5.1)$$

where x is longitude, y is latitude, z is depth, t is time, $v(x, y, z, t)$ is the velocity component which is perpendicular to the Yucatan Channel and Florida Strait sections (black lines (b) and (c) in Figure 5.13a) (i.e. the meridional velocity), *west* and *east* limits are the respective land boundaries of the section, H is the depth of the ocean upto which the integration is performed. This results in a time series of the transport through the Yucatan Channel (or Florida Strait) section at the latitude (y) where the

section lies. In the case of transport through the Caribbean Sea section (vertical black line (a) in Figure 5.13a) the equation for volume transport remains the same as Eq. 5.1 just that now the integration is over latitudes covered by the section having the land limits to the south and north, and of the velocity component perpendicular to this section (zonal velocity u). This results in a time series of the transport through the Caribbean Sea section at the longitude (x) where the section lies.

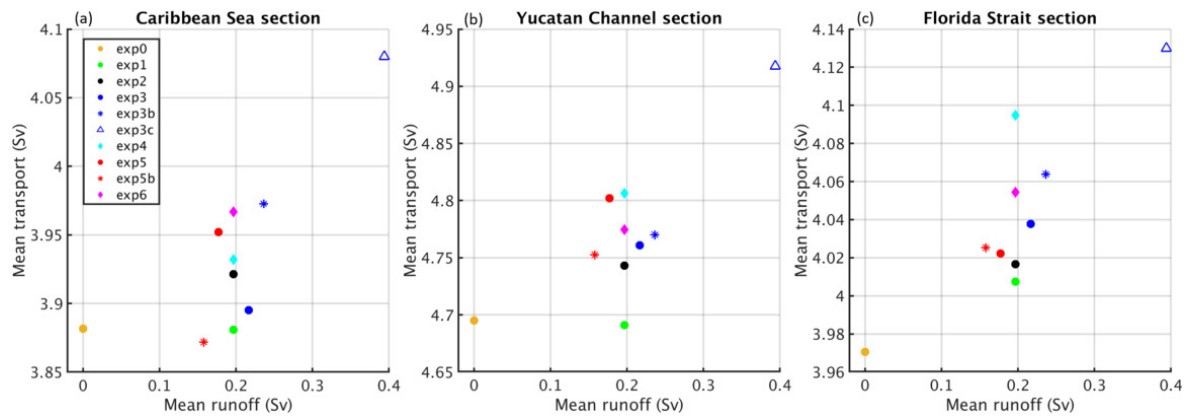


Figure 5.14: Relation between time mean runoff (Sv) area-averaged in Box A and time mean top 50 m transport (Sv) through (a) Caribbean Sea section, (b) Yucatan Channel section and (c) Florida Strait section for all experiments.

The relation of the time mean of the top 50 m transports through each section and the runoff at the Amazon mouth (Box A in Figure 5.2a) is presented in Figure 5.14. The top 50 m transport at the Caribbean Sea section running north-south (black line (a) in Figure 5.13a) is dominantly westward by the CC1 (current demarcated in Figure 2.1 of Chapter 2). The relation of Amazon runoff and this transport in time mean shows (Figure 5.14a) that the transport is high for large runoff and small for smaller runoff as seen by exp0, exp5b, exp3c, exp3b and exp2; but the experiments with 10% changes in runoff (exp3, exp5) show a slight negative linear relation. The relation of Amazon runoff and top 50 m transport computed across the Yucatan Channel section (black line (b) in Figure 5.13a, Figure 5.14b) shows that the experiments with 10% and 20% decrease in mean runoff are non-linear but the other experiments show a linear relation. Exp1 has a constant mean and no seasonal amplitude, while exp6 has 40% attenuated, and exp4 has 40% amplified seasonal amplitude of runoff, though the time mean runoff is the same, they show that with increased seasonal amplitude of runoff, the magnitude of the western boundary transport increases. In case of the top 50 m transport through the Florida Strait section (black line (c) in Figure 5.13a, Figure 5.14c), which has the FC passing northward through it (current demarcated in Figure 2.1c of Chapter 2), a linear tendency between runoff and transport is seen for the extreme changes, and for the changes when the mean runoff is increased. Also, exp4 has stronger transport than exp6, exp2 and exp1. The transports through the sections across Yucatan Channel and Florida Strait are northward (black lines (b) and (c) in Figure 5.13a, respectively). All three transports, seem to be a little insensitive to a

realistic decrease in mean and amplitude of runoff (exp5, exp5b, exp6), but follow the linear relation when there is no runoff in exp0.

Power spectral density (PSD) curves obtained using Welch's method for spectral density estimation were analyzed for these three top 50 m transport time series (Figure 5.15) through each of the above three western boundary sections. The clear and interesting change among experiments is on the energy contained at interannual frequencies. Looking at Figure 5.15a,c,e, for all three sections, the transports in exp3c and exp3b have larger amplitude than exp0 and exp5b, respectively. The amplitude is therefore distinctly larger in the experiments with more runoff than the experiments with less runoff at the interannual frequencies. This distinction between exp3c and exp0, and exp3b and exp5b are wider at the transports further downstream through the Yucatan Channel section (Figure 5.15c) and the Florida Strait section (Figure 5.15e) than in the transport upstream through the Caribbean Sea section (Figure 5.15a). In case of the experiments with changes in the seasonal amplitude of runoff, exp4 with 40% larger amplitude of runoff has larger amplitude of PSD than exp6 with 40% smaller amplitude of runoff, in all the three sections. The distinction is prominent for transport through the Caribbean Sea section (Figure 5.15b) and the Yucatan Channel section (Figure 5.15d), almost at all frequencies, being more prominent at interannual frequencies. At the more downstream Florida Strait section (Figure 5.15f) it is prominent for smaller interannual frequencies. In Caribbean Sea section (Figure 5.15b) exp1 which has just a constant mean runoff and no seasonal cycle has smaller PSD amplitude than exp4 and exp6 for larger interannual frequencies, and larger than the other two for smaller interannual frequencies. For Yucatan Channel section (Figure 5.15d) the exp4 has larger amplitude than exp1 in general but both the amplitudes are quite similar. For the transport through the Florida Strait section (Figure 5.15f) exp1 has a smaller amplitude than the other two experiments, the distinction widening at smallest frequencies. Thus in general, from all the experiments, if more freshwater is present, the interannual fluctuations in the western boundary transports have a larger amplitude. This is best seen in the spectra of the top 50 m volume transport time series.

In section 5.4, in the time mean spatial maps of the differences of the top 50 m KE, the FC (current demarcated in Figure 2.1c of Chapter 2) tended to be marginally larger in all the experiments compared to exp2, but smaller only in exp0 and exp1 compared to exp2. Figure 5.14c indicates the same. The linear relation is maintained by the extreme changes in runoff in exp0, exp1 and exp3c, and for increases in the mean and the amplitude of runoff.

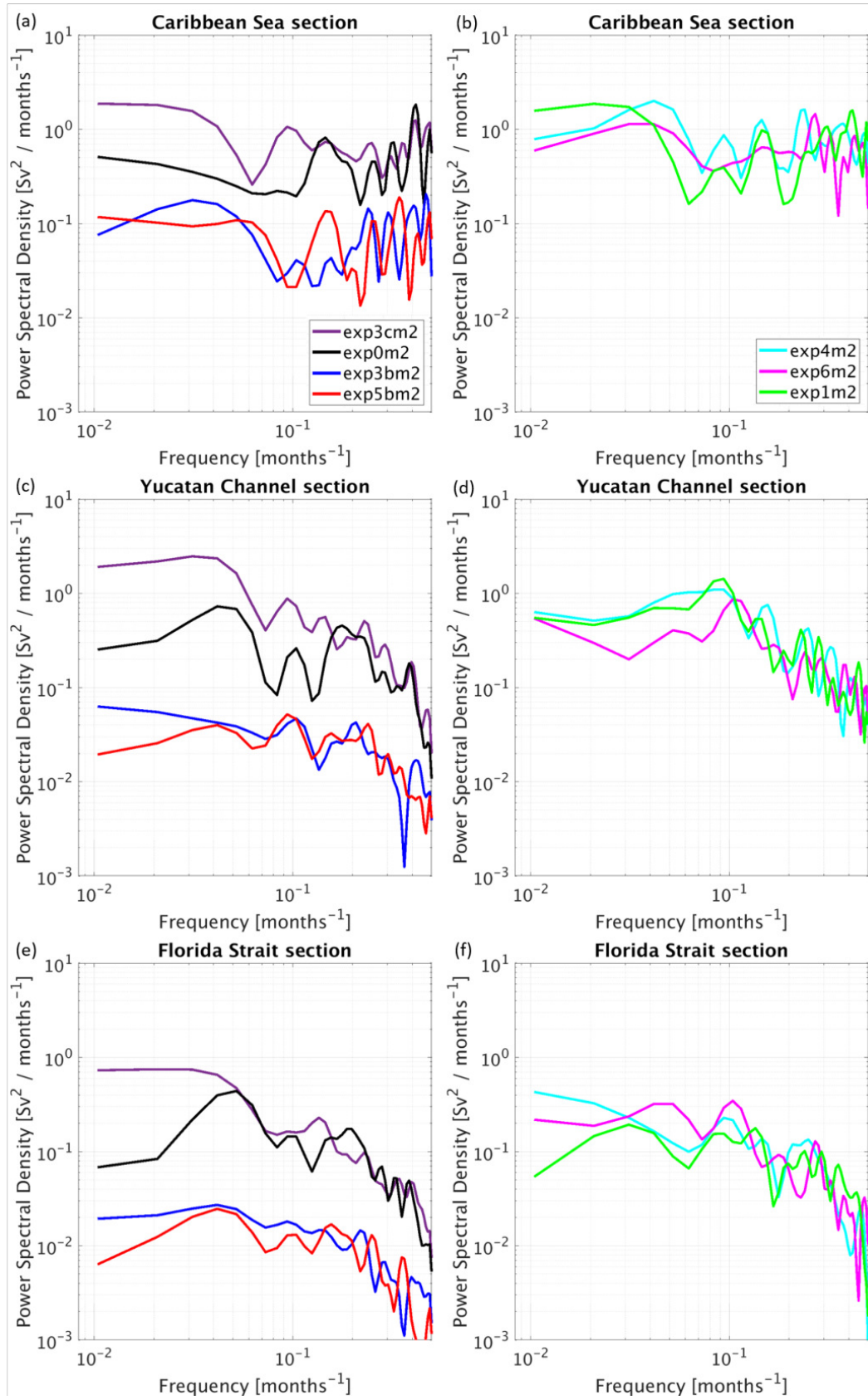


Figure 5.15: Power Spectral Density (PSD) (Sv²/months⁻¹) estimation for top 50 m transports through the (a,b) Caribbean Sea section, (c,d) Yucatan Channel section and (e,f) Florida Strait section for all experiments. PSD for exp3b and exp5b are divided by a factor of 10.

The top-to-bottom Florida Current transport (FCT) also computed with Eq. 5.1 is now analyzed. The time series of the top-to-bottom FCT is represented by the transport at the latitude 26.8°N . At this latitude FCT has the highest correlation with the runoff and BLT, compared to the other latitudes covered by the FC passing through the Florida Strait.

Figure 5.16a shows that the mean FCT is inversely related with the mean runoff for the experiments with a realistic increase/decrease in mean runoff (exp2, exp3, exp3b, exp5, exp5b). Exp0 and exp3c are not included, as these experiments have the extreme changes. Exp0 and exp3c had similar mean FCT values though they have extreme mean runoff values, which suggests that extreme runoff forcings could cause a change in other processes in the interior of the Atlantic that impact the top-to-bottom transport. The mean FCT is highest for exp5b (30.62 Sv) and smallest for exp3b (29.98 Sv). Therefore, the larger the mean runoff, the smaller is the FCT and vice versa. A similar negative linear relation is seen between the mean FCT and mean BLT area-averaged over the Box F (3°S - 20°N , 28 - 80°W), which includes all the barrier layers in the western tropical Atlantic. All the localized boxes explored before having BLT also show a similar inverse linear relation with the FCT, but this box represents all areas the best and has the best correlation. The mean BLT increases with an increase in mean runoff as seen before, and the mean FCT decreases with an increase in BLT and runoff. Exp4 with a 40% larger seasonal amplitude of runoff has the same mean runoff as the exp6 with a 40% smaller seasonal amplitude. The mean FCT is larger in exp6 (30.55 Sv) than in exp4 (30.36 Sv). The BLT is larger in exp4 than in exp6. Thus, here as well we see that larger mean BLT corresponds to smaller mean FCT.

There is an interesting relation seen between the time series of the FCT and the area-averaged BLT. Both the time series were detrended and deseasoned with a moving average of 15 months. The BLT leads the FCT by 9 months and they are anti-correlated. It was found that the lagged BLT has high correlation with FCT in exp6 (-0.74) (Figure 5.16d), exp2 (-0.7) (Figure 5.16c), exp1 (-0.7), exp3c (-0.63), exp3b (-0.6) and exp5 (-0.6). The highest correlation is seen in exp6 followed by exp2 and exp1. In conclusion, an increase in BLT leads to a decrease in FCT 9 months later. Hence, BLT is here suggested to be a potential predictor of FCT.

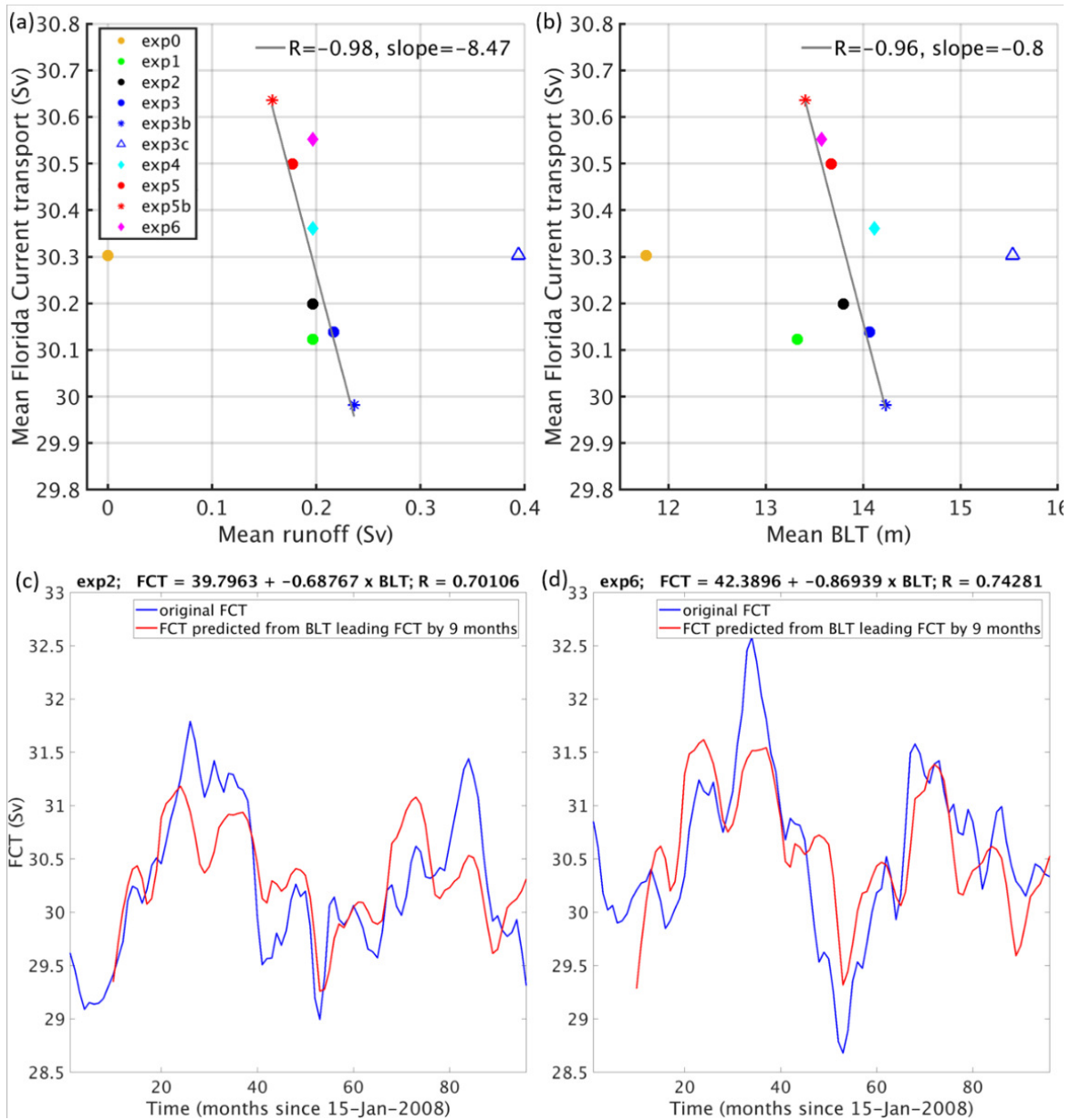


Figure 5.16: Relation between time mean FCT (Sv) and (a) time mean runoff (Sv) area-averaged in Box A, and (b) time mean BLT (m) area-averaged in Box F. Exp0, exp3c, exp4 and exp6 are not included in the regression line. Monthly time series (2008-2015) of FCT and FCT predicted from BLT (leading the FCT by 9 months) are shown for (c) exp2 and (d) exp6.

5.5.2 Amazon runoff/BLT and the AMOC

In the subsection above we saw that there is an anti-correlation between FCT and BLT variations and that BLT could be used to predict FCT with a lead time of 9 months. In what follows, I will explore the hypothesis of a relation between runoff, BLT and the AMOC.

The meridional overturning circulation is derived from the overturning streamfunction in the latitude-depth plane, computed for each experiment as:

$$\psi(y, z, t) = \int_z \int_{west}^{east} v(x, y, z, t) dx dz \quad (5.2)$$

where $v(x, y, z, t)$ is the meridional velocity component, z is the depth, and the *west* and *east* limits represent the western and eastern land boundaries of the Atlantic Ocean. The overturning streamfunction at 38.7°N and 910 m depth was chosen to represent the AMOC time series, since at this point in the latitude-depth plane the overturning circulation shows the best correlation and signal with the runoff and BLT.

Figure 5.17a shows the relation between mean AMOC and mean runoff, and between mean AMOC and mean BLT area-averaged over the Box F (3°S-20°N, 28-80°W). As seen before in this chapter, the BLT has a positive linear relation with the runoff. The AMOC is larger for experiments with smaller mean runoff, like for exp5, exp5b (around 11.5 Sv), and is smaller for exp3, exp3b (11.1 Sv) and exp3c, which have larger mean runoffs. The goodness of the fit is high with a slope of -5.08, taken for the experiments with realistic modifications in the mean runoff (exp2, exp3, exp3b, exp5 and exp5b). The relation between the mean BLT and mean AMOC (Figure 5.17b) also has a good fit with a slope of -0.49. The experiment with smaller mean runoff has smaller BLT, but larger AMOC, and vice versa. Exp3c with the largest runoff has the weakest AMOC amongst all experiments. Exp0 has a stronger AMOC than the experiments with runoff, except experiments with decrease in mean runoff (exp5, exp5b), and experiments with a change in the amplitude of runoff (exp4 and exp6 that do not show negative linear relation). Thus overall, we see that there is a negative linear relation between the BLT and the AMOC, and between runoff and the AMOC.

The time series of the AMOC and of the area-averaged BLT were detrended and deseasoned (again with a moving average of 15 months). It is seen in Figure 5.17c,d,e,f that the BLT leads the AMOC by 23 months and that they are anti-correlated. It was seen that the 23-months lagged BLT and AMOC have correlation (R) of -0.85 in exp3b (Figure 5.17d), -0.79 in exp5b (Figure 5.17e), -0.79 in exp2 (Figure 5.17c), -0.77 in exp6 (Figure 5.17f), -0.78 in exp3, -0.79 in exp3c, -0.73 in exp5, -0.72 in exp0, -0.68 in exp1 and -0.64 in exp4. The highest correlation is seen in exp3b, followed by exp5b. In conclusion, my analysis suggests that an increase in BLT has a decrease in the AMOC, with the BLT leading the AMOC by 23 months. Hence, BLT could also potentially be a predictor of the AMOC.

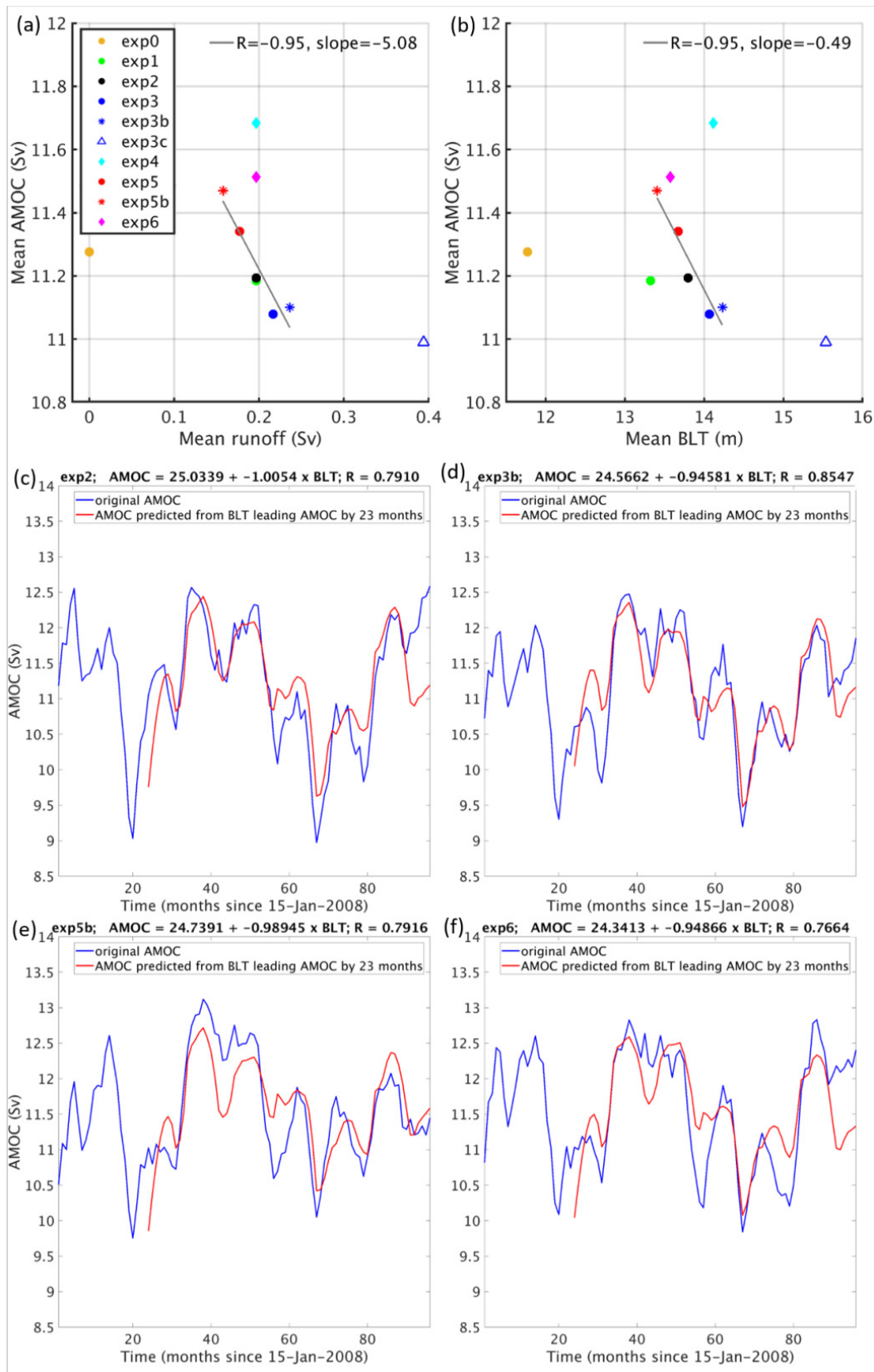


Figure 5.17: Relation between time mean AMOC (Sv) and (a) time mean runoff (Sv) area-averaged in Box A, and (b) time mean BLT (meters) area-averaged in Box F (dashed in Figure 5.2a). Exp0, exp3c, exp4 and exp6 are not included in the regression line. Monthly time series (2008-2015) of the AMOC and of the AMOC predicted from BLT (leading the AMOC by 23 months) are shown for (c) exp2, (d) exp3b, (e) exp5b and (f) exp6.

5.6 Summary and discussion

In order to study the sensitivity of the tropical Atlantic to the Amazon river discharge, a series of idealized numerical experiments were performed. In the first experiment, exp0, I examined the effect of having zero Amazon runoff. The next experiment, exp1, has a constant mean river runoff of 0.2 Sv for all months. Exp2 is the control experiment and has the same mean runoff as exp1 but with a seasonal cycle. An experiment just like exp2 but with 10⁻⁴% increase in mean runoff was conducted to test the significance and robustness of the results. To check the impact of an increase in just the mean runoff, there is exp3, having 10% increased mean, exp3b having 20% increased mean, and exp3c having 100% increased mean. To check the impact of increasing just the seasonal amplitude of the runoff with no change in the mean, exp4 was conducted, the simulation where the seasonal runoff cycle is amplified by 40% with the same mean as exp1 and exp2. On the other hand, exp5, which has 10% decreased mean runoff, exp5b having 20% decreased mean runoff and exp6 where the seasonal runoff of the Amazon River is attenuated by 40%, are the experiments to check the effect of decreasing the mean and the seasonal amplitude of the Amazon runoff. Exp2, exp3, exp3b, exp4, exp5, exp5b and exp6 are based on actual observations of the Amazon river runoff (Dai, 2016; Dai, 2017). So these situations are realistic and have occurred in the past and could occur in the future. Exp0 and exp3c are extreme cases, and exp1 has the realistic mean runoff from observations but is kept constant over all months.

First, the experiments confirmed and reproduced well, that with a higher mean runoff the SSS is smaller and with a lower mean runoff the SSS is larger at the river mouth. Exp3c has the same seasonal cycle but the highest magnitude of runoff, the smallest SSS and the smallest E-P-R compared to other experiments. For months with largest runoff (May-June), and smallest runoff (October-December) a 20% change in the mean runoff (exp3b/exp5b), results in greater differences in the SSS than 40% change in the seasonal amplitude (exp4/exp6). The seasonal cycle of the SSS in exp0 and exp1 was seen to be largely attributable to the seasonal cycles of precipitation and currents, potentially leading to the accumulation of the freshwater.

After determining the effects directly at the Amazon mouth, the impacts of the runoff in the rest of the Amazon plume was studied. The vast plume was divided into four localized regions since the seasonal cycles of the BLT and other physical variables along the plume are different. In the time mean and monthly mean relation between runoff and BLT, exp3b/exp5b has the largest/smallest mean BLT for all the regions, apart from the NBC-Box C and the east-Box E where exp4/exp6 dominate. The monthly mean time series revealed that the SSS decreases in each box depending on the time it takes for the currents to transport the fresh runoff water from the mouth into that box. With larger runoff the SST increases and the ILD and MLD decrease. The BLT gets larger since the decrease in MLD is much stronger than the ILD decrease. In the mouth-Box B and the NBC-Box C, the peak BLT is in June. The largest BLT in mouth-Box B is in exp3b, while in the NBC-box it is in exp4. In NEC-Box D the BLT

peaks in March and exp3b has the largest BLT, while in the east-Box E the BLT peaks in August, being the largest in exp4. The best positive linear correlation between the runoff and the BLT is in the mouth-Box B.

With two numerical experiments using ROMS, one with a seasonal river discharge and another without river discharge, Varona et al. (2019) suggested that in the presence of river discharge both the MLD and ILD are 20-50 m shallower over the entire extension of the Amazon plume, ILD differences being smaller than MLD differences, while the BLT is larger by 70 m at the Amazon river mouth during summer-winter in the western tropical Atlantic. Their SST is larger by less than 2°C, whereas the SSS decreased by ~8 psu in the plume area close to the coast from March-December. Firstly, their inferences and analyses are based on simulation data for just one year. Secondly, the model resolution is 0.25° (approximately 27.8 km) with a sigma vertical coordinate (Varona, 2018). The sigma coordinate discretization is problematic and causes an overestimation of the difference in the BLT between both experiments at the river mouth. In fact, the total depth of the ocean is smaller than 70 m at the shelf region, which implies that a BLT of more than 70 m (as reported) cannot exist there in reality (verified with ETOPO2 and Figure 3 and Figure 5 of Silva et al. (2005)).

The analysis in this chapter is conducted over a period of 8 years, with a simulation at 8 km horizontal resolution. The model utilized in my study uses a depth discretization, which does not have the need to smooth the topography (like in the sigma model) to stabilize the computations (with no smoothing, the pressure gradient error intrinsic to those type of models would be too large). In this way a realistic topography is attained that results in more realistic differences between the experiments with and without runoff. The BLT difference between exp2 and exp0 has a maximum of 42 m in June in my results. The higher horizontal resolution employed here reveals that the differences in SST, SSS, ILD, MLD and BLT between the experiments are not so spatially homogeneous and differ in magnitudes and time of the year in different regions in the plume. The analysis in this chapter takes the study of Varona et al. (2019) forward by showing the impacts of having a change in the mean Amazon discharge or its seasonal amplitude on the tropical Atlantic, localized regions and the entire Amazon plume. These changes in the discharge are based on the observed past discharge variability.

The time mean of the differences between each experiment and the control run regarding SSS, SST, ILD, MLD, BLT, top 50 m salinity, temperature and density reveal that the experiments with 20% (exp3b, exp5b) and 100% (exp3c) change in only the mean Amazon discharge have a larger impact on the tropical Atlantic compared to the experiments with changes in the seasonal amplitude of the runoff (exp4, exp6). The monthly means of the differences showed that an increase in SST and BLT and a decrease in SSS, ILD and MLD remains the same throughout the year in the experiments with a larger mean runoff (exp3, exp3b, exp3c), the opposite taking place all year round for experiments with a smaller mean runoff (exp5, exp5b, exp0). However,

the signs of the increase/decrease in the variables change in exp1, exp4 and exp6, as they have a smaller runoff than exp2 in one half of the year and a larger runoff than exp2 in the other half. Also in every experiment the largest impacts are found at the mouth-Box B, the largest amongst them being in the extreme cases of exp0 and exp3c. Exp4 and exp6 dominate in the changes in MLD and BLT at the NBC-Box C and the east-Box E. Finally, the top 50 m salinity and density show similar patterns as the SSS, while the top 50 m temperature shows similar behavior as the SST in the plume.

Thereafter, the impacts on the surface currents, the top 50 m KE, MKE and EKE in the tropical Atlantic brought by modifications in the Amazon runoff in the ten numerical experiments were analyzed. The MKE explains a large part of the KE differences, with EKE changes being present only in the highly nonlinear areas of the NBC rings, the retroflexion into the NECC and the LC (currents demarcated in Figure 2.1 of Chapter 2). I found that larger runoff leads to stronger western boundary currents. Furthermore, the smaller the runoff, the more intense are the retroflexion and the NECC. The KE (or speed) of the western boundary NBC is the greatest in exp3c (followed by exp3b), while exp0 (followed by exp5b) has the smallest magnitude. Exp4 dominated the NBC-Box C and east-Box E for the changes in EKE and KE in the time mean and in certain monthly differences. Currents in general are weaker in exp1 than in exp2, so a seasonal cycle in runoff is important for the currents to be stronger. The largest differences in all the quantities are seen in the NBC-Box C and the smallest differences for all the quantities are seen in the NEC-Box D.

An interesting observation was revealed at the retroflexion and the NECC through the time mean and the climatology of the surface currents, KE and EKE. Exp5, exp5b and exp4 were more similar to exp0, i.e., the smaller the runoff, the larger the magnitude of the retroflexion/NECC. Exp3, exp3b, exp3c and exp6 were more like exp2, i.e., for increased runoff, there is smaller magnitude of retroflexion/NECC and a slight northward shift with more meandering between the retroflexion and the NECC. In conclusion, large runoff leads to a smaller magnitude of the retroflexion and a slightly more meandering between the retroflexion and the NECC, thus shifting the NECC a little to the north; small runoff leads to a larger magnitude of the retroflexion and the NECC and a straighter curving from one into the other.

In the time mean (Figure 5.11) we saw that exp4 exhibits a behavior closer to exp0, while exp6 has more of a retroflexion bend like in exp2. This is because exp4 has lesser runoff than exp6 during the autumn months of peak retroflexion and NECC, and therefore behaves more like exp0 having a stronger and straighter retroflexion and NECC. Exp4 has the largest BLT in the east-Box E, as seen in the time mean and the monthly means. Exp4, having 40% amplified seasonal runoff cycle, has a smaller runoff in the autumn-winter months than exp2. The retroflexion and NECC are thus stronger in exp4 than in exp2. Moreover, the retroflexion and the NECC take place and peak during August-December. Also, the excess freshwater accumulated from previous months in exp4 is transported more to the east in these months, and gives rise to the

largest BLT in exp4 in the east-Box E. The other experiments, like exp5b, exp5 and exp0, which also have a stronger retroreflection than exp2, have a retroreflection at the same time (August-December), but they transport less freshwater than exp4. Therefore exp3b is the one having the next largest runoff and thus it has the next largest BLT in the east-Box E in August-September (Figure 5.4d). Exp3c has the least NECC and retroreflection magnitude, followed by exp3b, while exp0, exp4, exp5b and exp2 (in that order) have the maximum magnitudes. Therefore, increasing the seasonal amplitude seems to increase the retroreflection and NECC magnitude more than attenuating it.

Masson and Delecluse (2001) showed that there is a possibility to change the amplitude of the NBC retroreflection only by introducing Amazon runoff. In their experiment, which has a seasonal cycle of Amazon runoff, the surface current at the NBC retroreflection and NECC is smaller than in their experiment with no runoff for August (Figure 5 of Masson and Delecluse (2001)). Thus the differences (seen in this chapter) in the time mean and monthly means for the KE between exp2 and exp0 corroborate the findings of Masson and Delecluse (2001). Although the NBC and other surface western boundary currents are intensified with a larger runoff, the retroreflection and NECC show a different result.

The monthly variability of the longitudinally-averaged zonal component of surface velocity (u) from 45°W - 48°W (in the retroreflection-NECC region) for exp0 (Figures 5.18a) and the difference between exp0 and exp2 (Figure 5.18b) are presented. The retroreflection starts in May around 4.5°N in exp0, intensifies and becomes broader until it reaches its maximum magnitude of 0.55 m/s in October. Like in exp0, in exp2 the retroreflection starts in May. It is however shifted a little northward. The 0.55 m/s in October in exp0 is reached only later in November in exp2. In exp0 the 0.55 m/s stay only in October, and intensify again a little in December, but in exp2 the zonal velocity remains unchanged for November and December. As seen in Figure 5.18, in exp2 the retroreflection has a smaller magnitude than exp0 and moves a little northward while attaining its maximum intensity in November-December. Exp0 reaches its maximum intensity one month earlier than exp2 (Figures 5.18b). Comparing the result from Figure 5.18a,b with Figure 11 of Varona et al. (2019), one cannot say that exp2 intensifies or makes the retroreflection have a two months phase shift, as suggested in Varona et al. (2019). They conclude that the currents are stronger in the experiment with river discharge in the NECC area from September-December and that the river discharge causes a phase shift in the zonal currents, anticipating the retroreflection of the NBC by two months and enhancing eastward NECC transport. Therefore, the results in this chapter agree more with Masson and Delecluse (2001).

Experiment exp2b, which has the seasonal amplitude same as exp2, but only a $10^{-4}\%$ larger mean runoff, still has some differences with exp2, though the difference in forcing is tiny. These differences serve as a basis to determine the significance of the differences between the other experiments and the control run. The analysis shows that the differences seen for the 10% changes in the mean runoff are not significant.

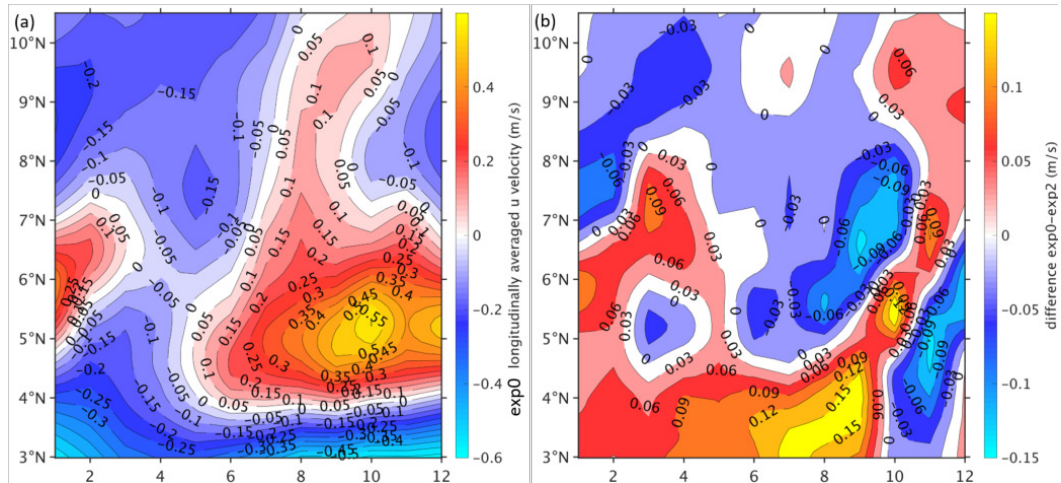


Figure 5.18: (a) The longitudinally-averaged zonal velocity (m/s) for exp0 and (b) the difference exp0-exp2 of longitudinally-averaged zonal velocity over the region of the retroflection (3-12°N, 45-48°W) are shown.

The significant differences are seen in case of the other experiments, with maximum differences in case of extreme experiments and least of all significant differences seen in case of experiments with a 40% change in the amplitude of the seasonal cycle. In case of the KE, MKE and EKE, in the non-linear region of the retroflection and the NECC, the differences are significant for the extreme cases of exp3cm2 and exp0m2, and for exp4m2. For other experiments the magnitude of the differences in this region are more or less similar to exp2bm2.

In the last section it was seen that in presence of more freshwater, the top 50 m volume transports of the western boundary currents at the three sections, Caribbean Sea, Yucatan Channel and Florida Strait, have larger amplitudes of interannual fluctuations. The time mean of those transports showed mostly a positive linear relation with runoff change. On the other hand, the top-to-bottom FCT is smaller for larger runoff and BLT. The mean FCT is highest for exp5b, and smallest for exp3b. There is an anti-correlation between BLT and FCT and BLT could predict FCT 9 months in advance. The largest correlation between the FCT and the FCT reconstructed with the lagged BLT is for exp6 (-0.74), followed by exp2. There is a negative linear relation between the runoff and the AMOC, as well as the BLT and the AMOC. The detrended and deseasoned time series of the AMOC and the BLT in each experiment revealed that an increase in BLT precedes a decrease in the AMOC by 23 months. Exp3b, exp3c, exp5b and exp6 all showed an anti-correlation of 0.8 or larger. However, more investigation is needed to explain the BLT as a possible predictor of the FCT and the AMOC.

Thus my study supports the conclusion of Mignot and Frankignoul (2010), Jahfer et al. (2017) and Jahfer et al. (2020), that the AMOC intensifies when there is less freshwater in the tropics or no Amazon runoff, as an anti-correlation was seen to exist between the runoff and AMOC, and additionally, BLT and AMOC. It was seen that

exp6 has a high correlation with the BLT leading the FCT and the AMOC in general. Therefore, if there is a future reduction in the amplitude of the runoff, it would probably lead to a better prediction of FCT and AMOC based on BLT. Also a drought condition which is predicted over the Amazon region (Koirala et al., 2014; Dai, 2016), as for instance simulated in exp5b, exp6 and exp0, would potentially also lead to a good prediction of the AMOC from BLT.

Chapter 6

Conclusions and outlook

In this thesis I looked at two aspects of the tropical Atlantic barrier layers. Their growth and decay mechanisms were first identified and later their response to changes in the Amazon river discharge was investigated, along with the ocean's response triggered by changes in the runoff. Eddy-resolving 4 km and 8 km resolution numerical simulations forced by atmospheric reanalyses facilitated this study. The simulations reproduced the temporal and spatial patterns of BLT estimated with Argo and CTD profiles fairly well, giving confidence on the suitability of the model to study the physical processes behind barrier layers. Below I summarize the conclusions reached in the present work, answering the two primary questions posed in the thesis, and give an outlook on possible future extensions of this work.

6.1 What are the mechanisms responsible for the BLT variability in the tropical Atlantic?

The physical mechanisms defined by different terms of the vertical gradient of the salinity and temperature balance equations have been studied to understand the growth and decay of barrier layers in the tropical Atlantic Ocean. Specifically, the impact of small-scale processes embedded in the regional circulation on the evolution of barrier layers was investigated using output from an eddy-resolving numerical simulation at 4 km resolution forced by an atmospheric reanalysis. It was seen that different mechanisms play a main role in the four different localized regions of the tropical Atlantic, all of which have different seasonality in barrier layer evolution.

In this study the NBC rings have been identified to play a major role in advecting conditions that support the existence of barrier layers towards the northwest, by transporting freshwater originating from the Amazon and Orinoco rivers and from ITCZ precipitation. The dynamics intrinsic to the NBC rings and to their formation are per se capable of growing barrier layers. The localized barrier layers larger than 80 m

inside NBC rings during late June to July (summer) are mainly due to a deepening of the ILD by a stretching of the isotherms, caused by horizontal temperature advection, tilting of temperature fronts and stretching mechanisms. The decay of the BLT in the NBC rings is also mainly due to stretching of the isotherms due to horizontal temperature advection, stretching, tilting and turbulent mixing mechanisms which cause the ILD to reduce. The seasonal ILD increase in June to July in the NBC rings is due to the reduction in the net heat flux forcing in the middle of peak net heat forcing in summer, causing a short period of reduction in SST, which brings about an increase in ILD, that is isolated in the NBC rings. The ILD increases and reduces moreover due to the internal eddy dynamics as explained above. Overall, the BLT in NBC rings is more determined by changes in ILD rather than by changes in MLD. Non-typically, combined with the deepening of the ILD, the BLT in summer sometimes grows when the MLD shoals in the eddy due to horizontal advection and turbulent mixing of freshwater on the surface and the tilting of salinity fronts. All the NBC rings have barrier layers during their lifetime, either in their core or in their periphery. In autumn these barrier layers are thin. In winter, the shoaling of the MLD by horizontal advection and turbulent mixing of freshwater in the periphery of the NBC rings and a tilting of the salinity fronts is rather responsible for growing the barrier layers, than an increase in ILD. But in the decay phase, an increase of MLD and a decrease of ILD both are equally responsible. The BLT in the NBC rings during winter is larger at the periphery than at the core of the ring.

Further north in the western tropical Atlantic, in the region along the NEC there are quasi-permanent barrier layers. Winter convection and turbulent mixing cause the deepening of MLD and ILD in winter, but the rate of deepening of MLD is smaller than that of ILD. The largest barrier layers (>90 m) form and grow in winter during January to early-March due to stretching of isohalines caused by tilting of salinity fronts (with small contributions from stretching, horizontal advection and turbulent mixing), which shoals the MLD, making it lie above the deeper seasonal winter ILD. The tilting of salinity fronts is caused by the northward and northwestward flow of fresh equatorial water at the surface, and the equatorward flow of the SMW at the subsurface "entering" into the isothermal layer. The decay of the local barrier layers in the NEC region is mainly caused by compression and shifting down of isohalines that deepen the mixed layer. This winter BLT is completely eroded in spring due to the shallowing of the isothermal and mixed layers by surface temperature stratification. The ILD shoals in spring by compression of isotherms due to turbulent surface heat mixing. In summer there is thin BLT due to shoaling of MLD by again mainly tilting of salinity fronts and a slight deepening of ILD due to turbulent heat mixing. This thin BLT decays in September due to shoaling of ILD by turbulent heat mixing. Overall, the formation and evolution of barrier layers in the NEC area is mostly depending on changes in the MLD.

In the open ocean of the central tropical Atlantic, the migrating ITCZ causes episodes of strong rainfall. The precipitation due to the ITCZ causes local freshwater

lenses on the surface. Turbulent mixing of surface rainwater drastically reduces the MLD over a deeper seasonal ILD, forming the large sporadic barrier layers in the open ocean. In this case, the barrier layers decay by a deepening of the MLD. Turbulent salt mixing and a tilting of salinity fronts into the vertical deepen the MLD causing the barrier layers to decay. In most of the cases in this region, there is no local ILD change in the growth or decay of the BLT. The thickest barrier layers (~60 m) form here in December-January, September-October and around June. The short timescale episodes of BLT have a large amplitude, dominating completely over the seasonal cycle.

At the eastern limit of the tropical Atlantic, the largest BLT (~60 m) exists from September to October and the second largest in February. Barrier layers in September and October form and grow by the shoaling of the mixed layer due to the tilting of salinity fronts at the Niger river plume edge and turbulent mixing of freshwater from the ITCZ precipitation, along with a deepening of the ILD due to turbulent heat mixing. The comparatively smaller BLT in February grows when the MLD shoals due to mainly tilting and partly stretching mechanisms, thus indicating no prominent influence of local rainfall. Tilting here takes place at the salinity fronts formed when the river plume is adjacent to the saline ocean water, as the heavier saline water subducts penetrating into the isothermal layer. Tilting of salinity fronts also happens as the Niger discharge freshwater is advected westward and comes in contact with the saline open-ocean water being carried eastward. The freshwater is carried westward by the SEC and the saline water is carried eastward by the GC2 (currents demarcated in Figure 2.1c) at the subsurface. Shoaling of the ILD mostly decays the BLT due to an upward shifting of isotherms by turbulent mixing in most of the events throughout the year.

The semi-annual behavior of wind stress and of the net heat flux forcing the SST are important factors in determining the seasonal variability of ILD and MLD in all the above regions in the tropical Atlantic. The western tropical sector under the influence of the Amazon river plume (like the NBC and NEC regions) have larger BLT values than the rest of the tropical Atlantic (like the ITCZ and ETA regions). The strong current dynamics at the river plume edge and the eddy dynamics of the NBC rings cause the magnitude of the physical mechanisms of growth and decay of barrier layers to be larger at the Amazon plume, the NBC rings region, and at the ETA Niger plume region, as compared to the regions of the NEC and the ITCZ.

6.2 What is the impact of changing the Amazon river runoff on BLT and larger-scale circulation?

In order to find the impact of variations in the Amazon river discharge (the world's largest river discharge) on the tropical Atlantic Ocean, a series of numerical experiments were performed. Exp0 had no Amazon runoff. Exp1 had a constant mean river runoff

of 0.2 Sv for all months. Exp2, the control experiment, had the same mean runoff as exp1 but included an idealized seasonal cycle. An experiment just like exp2 but with $10^{-4}\%$ increase in mean runoff was conducted to test the statistical significance of the results. To check the impact of increasing/decreasing the mean runoff, there was exp3/exp5 with 10% increased/decreased mean runoff and exp3b/exp5b with 20% increased/decreased mean runoff. An extreme case (exp3c) had 100% increased mean runoff. To check the impacts of variations in just the seasonal amplitude of the runoff, there was exp4/exp6, where the seasonal cycle was amplified/attenuated by 40%, while the same mean runoff as in exp1 and exp2 was retained. Exp2, exp3, exp3b, exp4, exp5, exp5b and exp6 are based on actual observations of the Amazon river runoff (Dai, 2016; Dai, 2017), so these situations are realistic. The extreme cases of exp0, exp1 and exp3c were designed to test and understand the maximal response of the ocean, but realism in those is not claimed.

The best linear positive correlation between the runoff (imposed in the model as a virtual salt flux added to the Evaporation-minus-Precipitation forcing) and BLT exists in the area covering the Amazon mouth and its periphery. A positive difference relative to exp2 in SST (maximum $\sim +0.5^\circ\text{C}$) and BLT (maximum $\sim +42$ m), and a negative difference in SSS (maximum ~ -10 psu), ILD (maximum ~ -42 m) and MLD (maximum ~ -50 m) are maintained throughout the year in the experiments with a larger mean runoff (exp3, exp3b and exp3c). The opposite behavior of the variables takes place throughout the year for the experiments with smaller mean runoff (exp5, exp5b) or no runoff (exp0). The changes in the spatial reach of the differences depend on the spread of the plume in that month. The above maximum values of differences are seen between exp2 and the extreme experiments, exp0 and exp3c, in summer and autumn, around the Amazon mouth. The signs of the differences in the experiments forced with a change in the seasonal amplitude (exp4, exp6) and the sign of the difference in the experiment with constant runoff (exp1), change during a year, since they have a smaller runoff than exp2 in one half of the year and a larger runoff than exp2 in the other half. Exp6 shows the same behavior as exp1, while exp4 displays the opposite. The salinity and density in the top 50 m behave like the SSS, while the temperature in the top 50 m behaves much like the SST in the plume.

The impacts on currents and the eddy activity in the tropical Atlantic were also analyzed. The MKE explains a large part of the KE differences, with EKE changes being present only in the highly nonlinear areas of the NBC rings, the retroflexion into the NECC and the LC (currents demarcated in Figure 2.1c). The western boundary surface currents and KE increase in magnitude with an increase in runoff. The largest KE difference (~ -0.6 m²/s²) is found between exp0 and exp2 in the NBC in May-June. However, the contrary is true for the NBC retroflexion and the NECC. The retroflexion and NECC become stronger with smaller runoff and weaker with larger runoff. The differences in KE (exp0-exp2) have a maximum magnitude of ~ 0.6 m²/s² in the monthly mean for October at the NBC retroflexion into the NECC. Also, with more freshwater there is more meandering of the retroflexion into the NECC and the

NECC is therefore shifted marginally northward. In exp2 the retroflection and the NECC gain later in strength than in exp0. It was further found that exp3b and exp3c behave more like exp2, and exp5b more like exp0. The retroflection and NECC develop from July onward and intensify in August-October. At this time of the year exp4 has a smaller runoff than exp2, and exp6 has a larger runoff than exp2. Therefore at the retroflection and the NECC, in the overall time mean and climatology, it was seen that exp6 behaves more like exp2 and exp4 like exp0. The impacts of small changes in mean runoff (exp3 and exp5) are insignificant at the non-linear regions of the retroflection and NECC.

Overall, exp3c and exp0 showed extreme opposite impacts. Among the experiments with realistic runoff, the experiments with 20% (exp3b and exp5b) change in mean discharge have a larger impact on the tropical Atlantic than the experiments with 40% change in the seasonal amplitude of the runoff (exp4 and exp6). Only in the region of the NBC rings and at the eastern extent of the Amazon plume the BLT was marginally more impacted in exp4 and exp6 than in exp3b and exp5b, because of more freshwater being transported northwestward and eastward in the months of large runoff and BLT (June and August, respectively) due to NBC and NECC currents being stronger, respectively.

After finding the impact of the changes in Amazon discharge on the above physical variables and dynamical quantities, it was interesting to investigate if the generated barrier layers can be linked to the large-scale circulation. The top 50 m volume transports of the western boundary currents through three sections (Caribbean Sea, Yucatan Channel and Florida Strait) have larger amplitudes of interannual fluctuations and has mostly a linear positive relation with increased runoff. Furthermore, BLT and the top-to-bottom FCT, as well as BLT and the AMOC were anti-correlated. Therefore, the larger the runoff and BLT, the weaker is the FCT and the AMOC. The BLT leads the FCT by 9 months and the AMOC by 23 months. The correlations are significantly the highest in both cases in the control run and exp6. Therefore, a drought condition, which is predicted over the Amazon region (Koirala et al., 2014; Dai, 2016) (for instance exp5b, exp6 and exp0 here), may lead to a good prediction of the AMOC from BLT. Also, a flood condition (exp3b, exp3c) would also lead to a good prediction of AMOC. BLT as a possible predictor of the FCT and the AMOC deserves therefore further investigation.

6.3 Future work

With the growing availability of comprehensive observational datasets of ocean temperature, salinity and currents, resolved spatially and in depth (also in the coastal regions) it will be interesting to apply my findings from model to observations. At present, it is only possible to study the detailed mechanisms of growth and decay in four dimensions with high resolution model output. Results from this thesis give an insight into the mechanisms governing the formation, evolution and erosion of the barrier layers throughout the year, in the tropical Atlantic and help bridge the knowledge gap in times of insufficient observational data. Extending this study to a longer period could enhance the robustness of the conclusions.

The processes involved in the growth and decay of barrier layers can be translated into other regions of the world, where similar physical conditions are prevalent, e.g., in the subtropical and equatorial Pacific, in other river plume regions like in the Bay of Bengal in the Indian Ocean, other regions in the tropics which have ITCZ rainfall. These mechanisms can be applied to study even the barrier layers at the farthest northern or southern latitudes (Pan et al., 2018) where the freshwater influx is due to ice melt. In this case, tilting of the salinity fronts at the ice melt freshwater plume edge could lead to the barrier layer formation, apart from turbulent mixing of the freshwater capping the surface.

This work highlights that a barrier layer is a localized and dynamic phenomenon, and that its growth and decay depend not only on the freshwater influx, but also largely on the local dynamics. Salinity and temperature fronts formed due to local surface and subsurface currents, eddies and filaments are seen to play a major role in the evolution of barrier layers. It shows that at some places and instances, the barrier layer forms/grows because of just the dynamics without a local surface freshwater influx. A resolution finer than 4 km could reveal eddies, fronts and filaments at the submesoscale regime, which would help explain barrier layer features in more detail. Very high vertical resolution in the upper ocean would be a benefit for studying upper ocean stratification due to freshwater lenses or freshwater advection and could give more realistic estimates. Having a higher temporal and spatial resolution of the atmospheric forcing in the model simulation could also create more realistic forcing conditions, and thus give a better understanding of the characteristics of the resulting barrier layers. River runoff implemented as a lateral boundary condition in the model simulation instead of a surface forcing could be more realistic. It would also be interesting to investigate the diurnal variability in BLT in this region with hourly simulated and observed data.

The presented sensitivity of the ocean to extreme decrease or increase in Amazon runoff and also to changes based on the past behavior of the Amazon discharge, gives an idea of the ocean's response during the future predicted drought scenario in the Amazon basin, according to which the freshwater discharged into the Atlantic would

decrease. The resulting impacts on the upper ocean salinity, temperature, BLT, regional and large-scale Atlantic circulation, due to changes of the runoff in every possible scenario seen in this study, can help to better predict the other quantities involved in air-sea interaction and dynamics, which have been shown in literature so far to have a relation with Amazon runoff (Mignot and Frankignoul, 2010; Jahfer et al., 2017; Jahfer et al., 2020), e.g. the AMOC and atmospheric teleconnections. Furthermore, barrier layers are known to trap heat as they prevent surface fluxes from penetrating below the mixed layer and hinder the entrainment of colder water from the thermocline below. It usually harbors a temperature inversion within it, also noticed to exist within the simulated barrier layers in this thesis. Known from literature, barrier layers facilitate the initiation and intensification of tropical cyclones in the northwestern tropical Atlantic, due to the large amount of trapped heat. Knowing the formation/growth and erosion/decay mechanisms, and the very nature and behavior of the barrier layers, as well as the response of these barrier layers to the different scenarios of Amazon runoff, as addressed in the present work, can help to improve the prediction of tropical cyclone intensification.

To study the biogeochemical impacts of barrier layers on phytoplankton blooms, algal blooms and fisheries, simulations at high resolution with a biogeochemical model could be conducted. Another interesting extent of the present work could be to integrate high resolution coupled or earth system models with all the components, allowing to study the relation between barrier layers and ecosystems. One could also study the feedbacks between each climate compartment in the presence and absence of barrier layers being resolved. This could also help to predict many other processes, like nutrient rise in the mixed layer due to the entrainment of cool nutrient-rich water from greater depths when the barrier layer is breached, increasing primary production. In addition, impacts of the turbidity at the river plume on barrier layers could be investigated. Ocean color monitoring satellite data could also help study the biological, geological and physical impacts of barrier layers in the Amazon and Niger plumes, or biological and physical impacts in the central ITCZ region.

Results in this work consolidate in my opinion the knowledge about barrier layers, especially in the tropical Atlantic, adding to the knowledge by identifying in detail the processes responsible for the formation, evolution and decay of barrier layers in the northern tropical and equatorial Atlantic, which were not defined comprehensively enough before. The work gives a clear understanding of the characteristics of seasonal and short-term BLT evolution, along with the behavior of barrier layers and other variables under changes in the Amazon river runoff. This knowledge can aid in future analysis of the role of barrier layers in air-sea interaction, salt/heat budgets, prediction of tropical cyclones and their intensification, AMOC, shifting of ITCZ patterns and other atmospheric teleconnections and biogeochemical impacts.

References

- Agarwal, N., Sharma, R., Parekh, A., Basu, S., Sarkar, A., and Agarwal, V. K. (2012). Argo observations of barrier layer in the tropical Indian Ocean. *Advances in Space Research*, 50(5):642–654.
- Arnault, S. (1987). Tropical Atlantic geostrophic currents and ship drifts. *Journal of Geophysical Research: Oceans*, 92(C5):5076–5088.
- Balaguru, K., Chang, P., Saravanan, R., and Jang, C. J. (2012a). The barrier layer of the Atlantic warmpool: formation mechanism and influence on the mean climate. *Tellus A: Dynamic Meteorology and Oceanography*, 64(1):18162.
- Balaguru, K., Chang, P., Saravanan, R., Leung, L. R., Xu, Z., Li, M., and Hsieh, J.-S. (2012b). Ocean barrier layers’ effect on tropical cyclone intensification. *Proceedings of the National Academy of Sciences*, 109(36):14343–14347.
- Biri, S., Serra, N., Scharffenberg, M. G., and Stammer, D. (2016). Atlantic sea surface height and velocity spectra inferred from satellite altimetry and a hierarchy of numerical simulations. *Journal of Geophysical Research: Oceans*, 121(6):4157–4177.
- Blanke, B., Arhan, M., Lazar, A., and Prévost, G. (2002). A Lagrangian numerical investigation of the origins and fates of the salinity maximum water in the Atlantic. *Journal of Geophysical Research: Oceans*, 107(C10):27–1–27–15.
- Bourlès, B., Gouriou, Y., and Chuchla, R. (1999a). On the circulation in the upper layer of the western equatorial Atlantic. *Journal of Geophysical Research: Oceans*, 104(C9):21151–21170.
- Bourlès, B., Molinari, R. L., Johns, E., Wilson, W. D., and Leaman, K. D. (1999b). Upper layer currents in the western tropical north Atlantic (1989–1991). *Journal of Geophysical Research: Oceans*, 104(C1):1361–1375.
- Boyer, T., Levitus, S., Garcia, H., Locarnini, R. A., Stephens, C., and Antonov, J. (2005). Objective analyses of annual, seasonal, and monthly temperature and salinity for the World Ocean on a 0.25° grid. *International Journal of Climatology*, 25(7):931–945.

- Breugem, W. P., Chang, P., Jang, C. J., Mignot, J., and Hazeleger, W. (2008). Barrier layers and tropical Atlantic SST biases in coupled GCMs. *Tellus A: Dynamic Meteorology and Oceanography*, 60(5):885–897.
- Camara, I., Kolodziejczyk, N., Mignot, J., Lazar, A., and Gaye, A. T. (2015). On the seasonal variations of salinity of the tropical Atlantic mixed layer. *Journal of Geophysical Research: Oceans*, 120(6):4441–4462.
- Chelton, D. B., Schlax, M. G., and Samelson, R. M. (2011). Global observations of nonlinear mesoscale eddies. *Progress in Oceanography*, 91(2):167–216.
- Coles, V. J., Brooks, M. T., Hopkins, J., Stukel, M. R., Yager, P. L., and Hood, R. R. (2013). The pathways and properties of the Amazon river plume in the tropical north Atlantic Ocean. *Journal of Geophysical Research: Oceans*, 118(12):6894–6913.
- Collins, M., Knutti, R., Arblaster, J., Dufresne, J. L., Fichet, T., Friedlingstein, P., Gao, X., Gutowski, W. J., Johns, T., Krinner, G., Shongwe, M., Tebaldi, C., Weaver, A. J., and Wehner, M. (2013). Long-term climate change: Projections, commitments and irreversibility. In *Climate Change 2013: The Physical Science Basis, Contribution of Working Group I to the Fifth Assessment Report of the Intergovernmental Panel on Climate Change* (eds. T. F. Stocker et al.), 1029–1136. Cambridge University Press.
- Cronin, M. F. and McPhaden, M. J. (2002). Barrier layer formation during westerly wind bursts. *Journal of Geophysical Research: Oceans*, 107(C12):8020.
- Da-Allada, C. Y., Alory, G., du Penhoat, Y., Kestenare, E., Durand, F., and Hounkonnou, N. M. (2013). Seasonal mixed-layer salinity balance in the tropical Atlantic Ocean: Mean state and seasonal cycle. *Journal of Geophysical Research: Oceans*, 118(1):332–345.
- Da-Allada, C. Y., du Penhoat, Y., Jouanno, J., Alory, G., and Hounkonnou, N. M. (2014). Modeled mixed-layer salinity balance in the Gulf of Guinea: Seasonal and interannual variability. *Ocean Dynamics*, 64(12):1783–1802.
- Dai, A. (2016). Historical and future changes in streamflow and continental runoff. In *Terrestrial Water Cycle and Climate Change* (eds. Q. Tang and T. Oki), 2:17–37. Washington, DC: American Geophysical Union.
- Dai, A. (2017). Dai and Trenberth global river flow and continental discharge dataset. *Research Data Archive at the National Center for Atmospheric Research, Computational and Information Systems Laboratory*.
- Dave, A. C. and Lozier, M. S. (2013). Examining the global record of interannual variability in stratification and marine productivity in the low-latitude and mid-latitude ocean. *Journal of Geophysical Research: Oceans*, 118(6):3114–3127.

- de Boyer Montégut, C., Madec, G., Fischer, A. S., Lazar, A., and Iudicone, D. (2004). Mixed layer depth over the global ocean: An examination of profile data and a profile-based climatology. *Journal of Geophysical Research: Oceans*, 109(C12):C12003.
- de Boyer Montégut, C., Mignot, J., Lazar, A., and Cravatte, S. (2007). Control of salinity on the mixed layer depth in the world ocean: 1. General description. *Journal of Geophysical Research: Oceans*, 112(C6):C06011.
- Dee, D. P., Uppala, S. M., Simmons, A. J., Berrisford, P., Poli, P., Kobayashi, S., Andrae, U., Balmaseda, M. A., Balsamo, G., Bauer, P., Bechtold, P., Beljaars, A. C. M., van de Berg, L., Bidlot, J., Bormann, N., Delsol, C., Dragani, R., Fuentes, M., Geer, A. J., Haimberger, L., Healy, S. B., Hersbach, H., Hólm, E. V., Isaksen, L., Kållberg, P., Köhler, M., Matricardi, M., McNally, A. P., Monge-Sanz, B. M., Morcrette, J.-J., Park, B.-K., Peubey, C., de Rosnay, P., Tavolato, C., Thépaut, J.-N., and Vitart, F. (2011). The ERA-Interim reanalysis: Configuration and performance of the data assimilation system. *Quarterly Journal of the Royal Meteorological Society*, 137(656):553–597.
- Defant, A. (1961). *Physical Oceanography*, 1:1–729. Pergamon Press, New York.
- Delcroix, T., Eldin, G., and Henin, C. (1987). Upper ocean water masses and transports in the western tropical Pacific (165°E). *Journal of Physical Oceanography*, 17(12):2248–2262.
- Denman, K. L. (1973). A time-dependent model of the upper ocean. *Journal of Physical Oceanography*, 3(2):173–184.
- Doney, S. C. (2006). Plankton in a warmer world. *Nature*, 444(7120):695–696.
- Dossa, A. N., Da-Allada, C. Y., Herbert, G., and Bourlès, B. (2019). Seasonal cycle of the salinity barrier layer revealed in the northeastern Gulf of Guinea. *African Journal of Marine Science*, 41(2):163–175.
- Drushka, K., Sprintall, J., and Gille, S. T. (2014). Subseasonal variations in salinity and barrier-layer thickness in the eastern equatorial Indian Ocean. *Journal of Geophysical Research: Oceans*, 119(2):805–823.
- Elliott, G. W. (1974). Precipitation signatures in sea-surface-layer conditions during BOMEX. *Journal of Physical Oceanography*, 4(3):498–501.
- Enfield, D. B. and Lee, S.-K. (2005). The heat balance of the western hemisphere warm pool. *Journal of Climate*, 18(14):2662–2681.
- Fekete, B., Vorosmarty, C., and Grabs, W. (1999). Global, composite runoff fields based on observed river discharge and simulated water balances. *Technical Report 22*. Global Runoff Data Centre.

- Ferry, N. and Reverdin, G. (2004). Sea surface salinity interannual variability in the western tropical Atlantic: An ocean general circulation model study. *Journal of Geophysical Research: Oceans*, 109(C5):C05026.
- Ffield, A. (2007). Amazon and Orinoco river plumes and NBC rings: Bystanders or participants in hurricane events? *Journal of Climate*, 20(2):316–333.
- Foltz, G. R., Grodsky, S. A., Carton, J. A., and McPhaden, M. J. (2004). Seasonal salt budget of the northwestern tropical Atlantic Ocean along 38°W. *Journal of Geophysical Research: Oceans*, 109(C3):C03052.
- Foltz, G. R. and McPhaden, M. J. (2008). Seasonal mixed layer salinity balance of the tropical north Atlantic Ocean. *Journal of Geophysical Research: Oceans*, 113(C2):C02013.
- Fonseca, C., Goni, G., E. Johns, W., and Campos, E. (2004). Investigation of the North Brazil Current retroflection and North Equatorial Countercurrent variability. *Geophysical Research Letters*, 31(21):L21304.
- Fournier, S., Vandemark, D., Gaultier, L., Lee, T., Jonsson, B., and Gierach, M. M. (2017). Interannual variation in offshore advection of Amazon-Orinoco plume waters: Observations, forcing mechanisms, and impacts. *Journal of Geophysical Research: Oceans*, 122(11):8966–8982.
- Fratantoni, D. M. and Glickson, D. A. (2002). North Brazil Current ring generation and evolution observed with SeaWiFS. *Journal of Physical Oceanography*, 32(3):1058–1074.
- Fratantoni, D. M., Johns, W. E., Townsend, T. L., and Hurlburt, H. E. (2000). Low-latitude circulation and mass transport pathways in a model of the tropical Atlantic Ocean. *Journal of Physical Oceanography*, 30(8):1944–1966.
- Fratantoni, D. M. and Richardson, P. L. (2006). The evolution and demise of North Brazil Current rings. *Journal of Physical Oceanography*, 36(7):1241–1264.
- Godfrey, J. S. and Lindstrom, E. J. (1989). The heat budget of the equatorial western Pacific surface mixed layer. *Journal of Geophysical Research: Oceans*, 94(C6):8007–8017.
- Goelzer, H., Mignot, J., Levermann, A., and Rahmstorf, S. (2006). Tropical versus high latitude freshwater influence on the Atlantic circulation. *Climate Dynamics*, 27(7):715–725.
- Good, S. A., Martin, M. J., and Rayner, N. A. (2013). EN4: Quality controlled ocean temperature and salinity profiles and monthly objective analyses with uncertainty estimates. *Journal of Geophysical Research: Oceans*, 118(12):6704–6716.

- Gouretski, V. and Reseghetti, F. (2010). On depth and temperature biases in bathythermograph data: Development of a new correction scheme based on analysis of a global ocean database. *Deep Sea Research Part I: Oceanographic Research Papers*, 57(6):812–833.
- Gu, G. and Adler, R. F. (2013). Interdecadal variability/long-term changes in global precipitation patterns during the past three decades: Global warming and/or pacific decadal variability? *Climate Dynamics*, 40(11):3009–3022.
- Hellweger, F. L. and Gordon, A. L. (2002). Tracing Amazon river water into the Caribbean Sea. *Journal of Marine Research*, 60(4):537–549.
- Isern-Fontanet, J., Font, J., García-Ladona, E., Emelianov, M., Millot, C., and Taupier-Letage, I. (2004). Spatial structure of anticyclonic eddies in the Algerian basin (Mediterranean Sea) analyzed using the Okubo-Weiss parameter. *Deep Sea Research Part II: Topical Studies in Oceanography*, 51(25):3009–3028.
- Jahfer, S., Vinayachandran, P. N., and Nanjundiah, R. S. (2017). Long-term impact of Amazon river runoff on northern hemispheric climate. *Scientific Reports*, 7(1):10989.
- Jahfer, S., Vinayachandran, P. N., and Nanjundiah, R. S. (2020). The role of Amazon river runoff on the multidecadal variability of the Atlantic ITCZ. *Environmental Research Letters*, 15(5):054013.
- Jochum, M. and Malanotte-Rizzoli, P. (2003). On the generation of North Brazil Current rings. *Journal of Marine Research*, 61(2):147–173.
- Kalnay, E., Kanamitsu, M., Kistler, R., Collins, W., Deaven, D., Gandin, L., Iredell, M., Saha, S., White, G., Woollen, J., Zhu, Y., Chelliah, M., Ebisuzaki, W., Higgins, W., Janowiak, J., Mo, K. C., Ropelewski, C., Wang, J., Leetmaa, A., Reynolds, R., Jenne, R., and Joseph, D. (1996). The NCEP/NCAR 40-Year Reanalysis Project. *Bulletin of the American Meteorological Society*, 77(3):437–472.
- Katsura, S., Oka, E., and Sato, K. (2015). Formation mechanism of barrier layer in the subtropical Pacific. *Journal of Physical Oceanography*, 45(11):2790–2805.
- Katsura, S. and Sprintall, J. (2020). Seasonality and formation of barrier layers and associated temperature inversions in the eastern tropical north Pacific. *Journal of Physical Oceanography*, 50(3):791–808.
- Kirchner, K., Rhein, M., Hüttl-Kabus, S., and Böning, C. W. (2009). On the spreading of south Atlantic water into the northern hemisphere. *Journal of Geophysical Research: Oceans*, 114(C5):C05019.
- Köhl, A. and Serra, N. (2014). Causes of decadal changes of the freshwater content in the Arctic Ocean. *Journal of Climate*, 27(9):3461–3475.

- Koirala, S., Hirabayashi, Y., Mahendran, R., and Kanae, S. (2014). Global assessment of agreement among streamflow projections using CMIP5 model outputs. *Environmental Research Letters*, 9(6):064017.
- Koldunov, N. V., Serra, N., Köhl, A., Stammer, D., Henry, O., Cazenave, A., Prandi, P., Knudsen, P., Andersen, O. B., Gao, Y., and Johannessen, J. (2014). Multimodel simulations of Arctic Ocean sea surface height variability in the period 1970-2009. *Journal of Geophysical Research: Oceans*, 119(12):8936–8954.
- Kraus, E. B. and Turner, J. S. (1967). A one-dimensional model of the seasonal thermocline II. The general theory and its consequences. *Tellus*, 19(1):98–106.
- Latif, M., Böning, C., Willebrand, J., Biastoch, A., Dengg, J., Keenlyside, N., Schweckendiek, U., and Madec, G. (2006). Is the thermohaline circulation changing? *Journal of Climate*, 19(18):4631–4637.
- Lindstrom, E., Lukas, R., Fine, R., Firing, E., Godfrey, J., Meyers, G., and Tsuchiya, M. (1987). The western equatorial Pacific Ocean circulation study. *Nature*, 330(6148):533–537.
- Liu, H., Wang, C., Lee, S.-K., and Enfield, D. (2012). Atlantic warm-pool variability in the IPCC AR4 CGCM simulations. *Journal of Climate*, 25(16):5612–5628.
- Lukas, R. and Lindstrom, E. (1991). The mixed layer of the western equatorial Pacific Ocean. *Journal of Geophysical Research: Oceans*, 96(S01):3343–3357.
- Maes, C. and O’Kane, T. J. (2014). Seasonal variations of the upper ocean salinity stratification in the Tropics. *Journal of Geophysical Research: Oceans*, 119(3):1706–1722.
- Marshall, J., Adcroft, A., Hill, C., Perelman, L., and Heisey, C. (1997). A finite-volume, incompressible Navier Stokes model for studies of the ocean on parallel computers. *Journal of Geophysical Research: Oceans*, 102(C3):5753–5766.
- Masson, S. and Delecluse, P. (2001). Influence of the Amazon river runoff on the tropical Atlantic. *Physics and Chemistry of the Earth, Part B: Hydrology, Oceans and Atmosphere*, 26(2):137–142.
- Mignot, J., de Boyer Montégut, C., Lazar, A., and Cravatte, S. (2007). Control of salinity on the mixed layer depth in the world ocean: 2. Tropical areas. *Journal of Geophysical Research: Oceans*, 112(C6):C06011.
- Mignot, J. and Frankignoul, C. (2010). Local and remote impacts of a tropical Atlantic salinity anomaly. *Climate Dynamics*, 35(7-8):1133–1147.
- Mignot, J., Lazar, A., and Lacarra, M. (2012). On the formation of barrier layers and associated vertical temperature inversions: A focus on the northwestern tropical Atlantic. *Journal of Geophysical Research: Oceans*, 117(C2):C02010.

- Miller, J. (1976). The salinity effect in a mixed layer ocean model. *Journal of Physical Oceanography*, 6(1):29–35.
- Moura, R. L., Amado-Filho, G. M., Moraes, F. C., Brasileiro, P. S., Salomon, P. S., Mahiques, M. M., Bastos, A. C., Almeida, M. G., Silva, J. M., Araujo, B. F., Brito, F. P., Rangel, T. P., Oliveira, B. C. V., Bahia, R. G., Paranhos, R. P., Dias, R. J. S., Siegle, E., Figueiredo, A. G., Pereira, R. C., Leal, C. V., Hajdu, E., Asp, N. E., Gregoracci, G. B., Neumann-Leitão, S., Yager, P. L., Francini-Filho, R. B., Fróes, A., Campeão, M., Silva, B. S., Moreira, A. P. B., Oliveira, L., Soares, A. C., Araujo, L., Oliveira, N. L., Teixeira, J. B., Valle, R. A. B., Thompson, C. C., Rezende, C. E., and Thompson, F. L. (2016). An extensive reef system at the Amazon river mouth. *Science Advances*, 2(4):e1501252.
- Pailler, K., Boulès, B., and Gouriou, Y. (1999). The barrier layer in the western tropical Atlantic Ocean. *Geophysical Research Letters*, 26(14):2069–2072.
- Pan, L., Zhong, Y., Liu, H., Zhou, L., Zhang, Z., and Zhou, M. (2018). Seasonal variation of barrier layer in the Southern Ocean. *Journal of Geophysical Research: Oceans*, 123(3):2238–2253.
- Qu, T., Gao, S., and Fukumori, I. (2011). What governs the north Atlantic salinity maximum in a global GCM? *Geophysical Research Letters*, 38(7):L07602.
- Reul, N., Quilfen, Y., Chapron, B., Fournier, S., Kudryavtsev, V., and Sabia, R. (2014). Multisensor observations of the Amazon-Orinoco river plume interactions with hurricanes. *Journal of Geophysical Research: Oceans*, 119(12):8271–8295.
- Romanova, V., Köhl, A., and Stammer, D. (2011). Seasonal cycle of near-surface freshwater budget in the western tropical Atlantic. *Journal of Geophysical Research: Oceans*, 116(C7):C07009.
- Rudzin, J. E., Shay, L. K., Jaimes, B., and Brewster, J. K. (2017). Upper ocean observations in eastern Caribbean Sea reveal barrier layer within a warm core eddy. *Journal of Geophysical Research: Oceans*, 122(2):1057–1071.
- Sarmiento, J. L., Slater, R., Barber, R., Bopp, L., Doney, S. C., Hirst, A. C., Kleypas, J., Matear, R., Mikolajewicz, U., Monfray, P., Soldatov, V., Spall, S. A., and Stouffer, R. (2004). Response of ocean ecosystems to climate warming. *Global Biogeochemical Cycles*, 18(3):GB3003.
- Sato, K., Suga, T., and Hanawa, K. (2006). Barrier layers in the subtropical gyres of the world’s oceans. *Geophysical Research Letters*, 33(8):L08603.
- Schiller, R. V. and Smith, R. B. (2018). On extreme surface and sub-surface currents driven by North Brazil Current rings offshore Suriname. *Offshore Technology Conference*, OTC-29023-MS.

- Schmitt, R. W. and Blair, A. (2015). A river of salt. *Oceanography*, 28(1):40–45.
- Schott, F. A., Fischer, J., and Stramma, L. (1998). Transports and pathways of the upper-layer circulation in the western tropical Atlantic. *Journal of Physical Oceanography*, 28(10):1904–1928.
- Sena Martins, M., Serra, N., and Stammer, D. (2015). Spatial and temporal scales of sea surface salinity variability in the Atlantic Ocean. *Journal of Geophysical Research: Oceans*, 120(6):4306–4323.
- Serra, N., Käse, R. H., Köhl, A., Stammer, D., and Quadfasel, D. (2010). On the low-frequency phase relation between the Denmark Strait and the Faroe-Bank Channel overflows. *Tellus A: Dynamic Meteorology and Oceanography*, 62(4):530–550.
- Silva, A., Araujo, M., Medeiros, C., Silva, M., and Bourlès, B. (2005). Seasonal changes in the mixed and barrier layers in the western equatorial Atlantic. *Brazilian Journal of Oceanography*, 53(3-4):83–98.
- Sommer, A., Reverdin, G., Kolodziejczyk, N., and Jacqueline, B. (2015). Sea surface salinity and temperature budgets in the north Atlantic subtropical gyre during SPURS experiment: August 2012–August 2013. *Frontiers in Marine Science*, 2:107.
- Sprintall, J. and Tomczak, M. (1992). Evidence of the barrier layer in the surface layer of the tropics. *Journal of Geophysical Research: Oceans*, 97(C5):7305–7316.
- Stramma, L., Rhein, M., Brandt, P., Dengler, M., Böning, C. W., and Walter, M. (2005). Upper ocean circulation in the western tropical Atlantic in boreal fall 2000. *Deep Sea Research Part I: Oceanographic Research Papers*, 52(2):221–240.
- Stramma, L. and Schott, F. (1999). The mean flow field of the tropical Atlantic Ocean. *Deep Sea Research Part II: Topical Studies in Oceanography*, 46(1-2):279–303.
- Thadathil, P., Thoppil, P., Rao, R. R., Muraleedharan, P. M., Somayajulu, Y. K., Gopalakrishna, V. V., Murtugudde, R., Reddy, G. V., and Revichandran, C. (2008). Seasonal variability of the observed barrier layer in the Arabian Sea. *Journal of Physical Oceanography*, 38(3):624–638.
- van der Boog, C. G., Pietrzak, J. D., Dijkstra, H. A., Brüggemann, N., van Westen, R. M., James, R. K., Bouma, T. J., Riva, R. E. M., Slobbe, D. C., Klees, R., Zijlema, M., and Katsman, C. A. (2019). The impact of upwelling on the intensification of anticyclonic ocean eddies in the Caribbean Sea. *Ocean Science*, 15(6):1419–1437.
- Varona, H. L. (2018). Circulation, transport and dispersion of hydrocarbon plumes in the north Brazilian equatorial broadband. *PhD thesis*. Federal University of Pernambuco, Recife, PE, Brazil.

- Varona, H. L., Veleda, D., Silva, M., Cintra, M., and Araujo, M. (2019). Amazon river plume influence on western tropical Atlantic dynamic variability. *Dynamics of Atmospheres and Oceans*, 85:1–15.
- Veneziani, M., Griffa, A., Garraffo, Z., and Mensa, J. A. (2014). Barrier layers in the tropical south Atlantic: Mean dynamics and submesoscale effects. *Journal of Physical Oceanography*, 44(1):265–288.
- Vialard, J. and Delecluse, P. (1998). An OGCM study for the TOGA decade. Part II: Barrier-layer formation and variability. *Journal of Physical Oceanography*, 28(6):1089–1106.
- Waliser, D. E. and Gautier, C. (1993). A satellite-derived climatology of the ITCZ. *Journal of Climate*, 6(11):2162–2174.
- Wang, C. and Enfield, D. B. (2003). A further study of the tropical western hemisphere warm pool. *Journal of Climate*, 16(10):1476–1493.
- Wang, C., Lee, S.-K., and Enfield, D. B. (2007). Impact of the Atlantic warm pool on the summer climate of the western hemisphere. *Journal of Climate*, 20(20):5021–5040.
- Wang, H. and Fu, R. (2007). The influence of Amazon rainfall on the Atlantic ITCZ through convectively coupled Kelvin Waves. *Journal of Climate*, 20(7):1188–1201.
- Wilson, W. D., Johns, E., and Molinari, R. L. (1994). Upper layer circulation in the western tropical north Atlantic Ocean during August 1989. *Journal of Geophysical Research: Oceans*, 99(C11):22513–22523.
- Xie, S.-P. and Carton, J. A. (2004). Tropical Atlantic variability: Patterns, mechanisms, and impacts. In *Earth’s Climate: The Ocean-Atmosphere Interaction, Geophysical Monograph Series* (eds. C. Wang, S. Xie and J. Carton), 147:121–142. Washington, DC: American Geophysical Union.
- You, Y. (1995). Salinity variability and its role in the barrier-layer formation during TOGA-COARE. *Journal of Physical Oceanography*, 25(11):2778–2807.

List of Abbreviations

AC1	Antilles Current
AC2	Angola Current
AMOC	Atlantic Meridional Overturning Circulation
Argo	Array for Real-time Geostrophic Oceanography
AOGCM	Atmosphere-Ocean General Circulation Model
ATL	Atlantic Ocean Simulation
AWP	Atlantic Warm Pool
BLT	Barrier Layer Thickness
BOMEX	Barbados Meteorological and Oceanographic Experiment
CC1	Caribbean Current
CC2	Canary Current
CMIP	Climate Model Intercomparison Project
CTD	Conductivity, Temperature and Depth
ECMWF	European Centre for Medium-Range Weather Forecasts
ECMWF ERA	ECMWF Re-Analysis
EKE	Eddy Kinetic Energy
E-P-R	Evaporation-minus-Precipitation-minus-Runoff
ETOPO2	Global Digital Elevation Model
EUC	Equatorial Undercurrent
FC	Florida Current
FCT	Florida Current Transport
GC1	Guiana Current
GC2	Guinea Current
HYCOM	HYbrid Coordinate Ocean Model
IFREMER	Institut français de recherche pour l'exploitation de la mer, English: French Research Institute for Exploitation of the Sea
ILD	Isothermal Layer Depth

IPCC	The Intergovernmental Panel on Climate Change
ITCZ	Intertropical Convergence Zone
KE	Kinetic Energy
KPP	K-profile parameterization
LC	Loop Current
MLD	Mixed layer Depth
MITgcm	Massachusetts Institute of Technology general circulation model
MKE	Mean Kinetic Energy
NBC	North Brazil Current
NBC-r	North Brazil Current retroflexion
NBUC	North Brazil Undercurrent
NCEP	National Centers for Environmental Prediction
NEC	North Equatorial Current
NECC	North Equatorial Countercurrent
OGCM	Ocean General Circulation Model
ROMS	Regional Ocean Modeling System
SEC	South Equatorial Current
nSEC	northern branch of SEC
cSEC	central branch of SEC
SMW	Salinity Maximum Water
SSS	Sea Surface Salinity
SST	Sea Surface Temperature
TOGA	Tropical Ocean and Global Atmosphere
WEPOCS	Western Equatorial Pacific Ocean Study

List of Figures

- 1.1 Schematic of the upper ocean processes and its external forcings along a salinity section at 15°N in the Atlantic Ocean (observations from the EN4 database). Adapted and expanded from an illustration by Jayne Doucette, Woods Hole Oceanographic Institution. 2
- 1.2 Examples of vertical stratification in the tropical Atlantic Ocean (a) without and (b) with a barrier layer. The profiles were taken from Simple Ocean Data Assimilation (SODA) reanalysis at the location of the red dot in the insert (25°N, 30°W and 15°N, 50°W, respectively). The black, red and blue lines depict, respectively, potential density (kg/m^3), potential temperature ($^{\circ}\text{C}$), and salinity (psu). Reproduced from Breugem et al. (2008). 4
- 1.3 (a) Annual maximum of the monthly BLT, showing the maximum BLT in meters and (b) number of months during which the percentage of the BLT relative to ILD exceeds 10%. Areas where the relative thickness never exceeds 10% are in light grey. Areas where data are not available over a whole annual cycle are hatched. Adapted from de Boyer Montégut et al. (2007). 5
- 1.4 Seasonal distribution of profile data obtained with Argo floats from January 2000 to June 2005: (a) January-March and (b) July-September. The BLT at each profile is denoted by colored points. Background shadings denote the BLT calculated from the corresponding seasonal World Ocean Atlas 2001. Adapted from Sato et al. (2006). 8
- 1.5 Multimodel mean long-term percentage changes from 1970-1999 to 2070-2099 (under a moderate RCP4.5 scenario) over land in annual (a) precipitation, (b) soil moisture content in the top 10 cm layer, (c) surface evapotranspiration, and (d) total runoff, from 31-33 CMIP5 models. The stippling indicates at least 80% of the models agree on the sign of change. The change patterns are similar to those shown by Collins et al. (2013). Figure adapted from Dai (2016). 11

2.1	Climatology of simulated mixed-layer salinity (psu) and simulated flow at 20 m depth for the months of (a) February, (b) May, (c) July, (d) September, (e) October and (f) December. The flow trajectories result from a 30-day integration of particles using the climatological three-dimensional ocean velocity of the respective month. Labeled are the North Brazil Current (NBC), the North Brazil Current retroflection (NBC-r), the North Equatorial Countercurrent (NECC), the North Brazil Current ring (NBC ring), the Guiana Current (GC1), the Caribbean Current (CC1), the Loop Current (LC), the Florida Current (FC), the Antilles Current (AC1), the North Equatorial Current (NEC), the Canary Current (CC2), the Guinea Current (GC2), the South Equatorial Current (SEC) with the northern (nSEC) and central (cSEC) branches, the Equatorial Undercurrent (EUC) and the Angola Current (AC2).	18
2.2	Climatology of simulated E-P-R ($\times 10^{-7}$ m/s) for the months of (a) February, (b) May, (c) July, (d) September, (e) October and (f) December.	19
3.1	Spatial variability of BLT in February (top-left), May (top-right), July (bottom-left) and October (bottom-right) computed from monthly EN4 objective analyzed fields (a,e,i,m), in situ profiles (b,f,j,n) and ATL4km daily model output (c,g,k,o). The average number of days BLT was present in the period 2003-2011 is shown (d,h,l,p). The black boxes delimit the areas of large BLT studied in the present work: NBC-box (6-10°N, 51-59°W), NEC-box (14-20°N, 46-58°W), ITCZ-box (4°S-13°N, 6-30°W) and ETA-box (1°S-7°N, 11°E-1°W).	25
3.2	Spatial variability of the difference in MLD (a,c,e,g) and ILD (b,d,f,h) between ATL4km and EN4 in February (top-left), May (top-right), July (bottom-left) and October (bottom-right).	27
3.3	Spatial variability of the largest simulated BLT (average over values of the BLT larger than 2 standard deviations) in (a) February (top-left), (c) May (top-right), (e) July (bottom-left) and (g) October (bottom-right). The corresponding average number of days in the period 2003-2011 is shown in (b,d,f,h).	29
3.4	Monthly variability of area-averaged BLT in the (a) NBC-box (6-10°N, 51-59°W), (b) NEC-box (14-20°N, 46-58°W), (c) ITCZ-box (4°S-13°N, 6-30°W) and (d) ETA-box (1°S-7°N, 11°E-1°W) from EN4 objective analyzed data (2003-2011, blue), observational profiles (2003-2011, green), DeBoyer climatology (1961-2008, yellow), ATL4km daily output (2003-2011, violet) and ATL4km monthly output (2003-2011, red). The values at the bottom of the error bars represent the percentage of the number of profiles with barrier layers (top value) with respect to the total number of profiles present (bottom value) for that month in the period 2003-2011.	31
4.1	Histogram of the number of occurrences (in terms of model grid points) of BLT values (in meters) during the years 2003-2011 for (a) NBC rings and NEC regions, (b) ITCZ and ETA regions.	34

- 4.2 Schematics of (a) horizontal advection, (b) tilting, (c) stretching and (d) turbulent mixing, the mechanisms responsible for barrier layer formation and growth. The black and grey dashed lines are, respectively, the initial and the resulting mixed layer depth (MLD). The black and grey solid lines depict, respectively, the initial and the resulting isothermal layer depth (ILD). Hatched regions are the initial barrier layers and the blue shaded regions depict the resulting barrier layers. Adapted and expanded from Cronin and McPhaden (2002). 36
- 4.3 Hovmöller diagram of Okubo-Weiss parameter (s^{-2}) showing the NBC rings passing through $51^{\circ}W$ in the years 2003-2011. 39
- 4.4 (a) Simulated NBC rings shown as an instantaneous mask, defined using a criteria which uses the Okubo-Weiss parameter and relative vorticity. (b) Percentage of the nine years (2003-2011) when NBC rings are present. The black box encloses the studied NBC rings region ($6-10^{\circ}N$, $51-59^{\circ}W$). 39
- 4.5 Daily time series of area-averaged ILD (black), MLD (yellow) and BLT (blue) (in meters) in the region of NBC rings ($6-10^{\circ}N$, $51-59^{\circ}W$). Red circles depict events when the eddies have large summer BLT; green circles show events when the eddies have large winter BLT; grey circles correspond to the remaining eddies which have significant BLT. 40
- 4.6 Relation of ILD and MLD in NBC eddy cores: (a) eddies generated in June-July (marked with red circles in Figure 4.5) and (b) all other eddies except those in (a) (marked with grey and green circles in Figure 4.5). 42
- 4.7 Relation of BLT and ILD in cores of NBC rings generated in: (a) April-July, (b) August-March. Relation of BLT and MLD in cores of NBC rings generated in: (c) January-early March and (d) May-July. 43
- 4.8 Monthly variability of area-averaged ILD, MLD and BLT (meters) for eddy cores in the two regions (a) $56-61^{\circ}W$, $7-13^{\circ}N$ and (b) $51-56^{\circ}W$, $7-13^{\circ}N$, respectively. 44
- 4.9 (a) NBC meridional non-recirculated transport (Sv); (b) NBC meridional non-recirculated freshwater transport (Sv), both monthly for 2003-2011 from ATL4km simulation. 45
- 4.10 Time series of ILD, MLD, BLT, net surface heat flux and SST low-pass filtered with a 60 days cut-off filter. Red circles depict events when the eddies have large summer BLT; green circles show events when the eddies have large winter BLT; grey circles correspond to the remaining eddies which have significant BLT. 46
- 4.11 Daily anomalies of ILD, MLD and BLT (meters) after high-pass filtering (cut-off 60 days). Red circles depict events when the eddies have large summer BLT resulting in a peak in the BLT time series, green circles depict events when the eddies have large winter BLT and grey circles depict events when the remaining eddies have BLT resulting in a peak in the years 2003-2011. 47

- 4.12 Snapshots from 17-06-2007 to 26-07-2007 showing the growth and decay of the maximum BLT on 30-06-2007 (summer) (black box delineates the NBC region): (row 1 and 2) BLT (meters) with vectors showing surface currents and (row 3 and 4) ILD (meters). 48
- 4.13 Snapshots for 30-06-2007 (summer) of (a) MLD (meters), (b) SSS (psu) with vectors showing surface currents, (c) top 152.5 m horizontal transport magnitude (Sv) and direction, (d) salinity (psu) at 82.5 m with corresponding currents, (e) SST ($^{\circ}\text{C}$) and (f) E-P-R ($\times 10^{-7}$ m/s). 49
- 4.14 Vertical section at 52.32°W through the core of the NBC ring present on 30-06-2007 in the NBC-box. Temperature gradient balance terms (a) LHS; (b) Term 1: horizontal advection; (c) Term 2: vertical advection; (d) Term 3: tilting; (e) Term 4: stretching; (f) Term 5: turbulent mixing, averaged from 28-06-2007 to 30-06-2007, units ($\times 10^{-7}$ $^{\circ}\text{C}/\text{m}\cdot\text{s}$). Temperature vertical gradient ($^{\circ}\text{C}/\text{m}$) with contours being isotherms ($^{\circ}\text{C}$) are shown for (g) 28-06-2007 and (h) 30-06-2007. Black (green) solid line correspond to the ILD, black (green) dashed line corresponds to the MLD for 30-06-2007 (28-06-2007). 51
- 4.15 Vertical section at 8.95°N through the core of a NBC ring on 30-06-2011 of salinity and temperature gradient balance terms: (a,b) LHS, (c,d) Term 1: horizontal advection, (e,f) Term 2: vertical advection, (g,h) Term 3: Tilting, (i,j) Term 4: stretching; (k,l) Term 5: turbulent mixing, averaged from 28-06-2011 to 30-06-2011 (units are $\times 10^{-7}$ psu/m.s and $\times 10^{-7}$ $^{\circ}\text{C}/\text{m}\cdot\text{s}$, respectively). Black (green) solid lines correspond to ILD and black (green) dashed lines to MLD for 30-06-2011 (28-06-2011). 52
- 4.16 Vertical section at 8.95°N through the core of a NBC ring on 30-06-2011: (a,b) salinity vertical gradient (psu/m), with isohalines (psu) superimposed; (c,d) temperature vertical gradient ($^{\circ}\text{C}/\text{m}$) with isotherms ($^{\circ}\text{C}$) superimposed, (e,f) density, (g,h) salinity and (i,j) temperature stratification ($\times 10^{-4}/\text{s}^2$) for 28-06-2011 and 30-06-2011, respectively. Black (green) solid lines are ILD, black (green) dashed lines are MLD for 30-06-2011 (28-06-2011). 54
- 4.17 Same as Figure 4.14, but for a vertical section at 58.31°W through the core of the NBC ring present on 07-03-2009 and here salinity gradient balance terms are averaged from 05-03-2009 to 07-03-2009 (units are $\times 10^{-7}$ psu/m.s) and (g,h) are salinity vertical gradient (psu/m), with isohalines (psu) superimposed. Black (green) solid lines correspond to the ILD, black (green) dashed lines to the MLD for 07-03-2009 (05-03-2009). 56
- 4.18 Same as Figure 4.14, but for a vertical section at 56.12°W through the core of the NBC ring present on 11-07-2003. Temperature gradient balance terms are averaged from 11-07-2003 to 13-07-2003 ($\times 10^{-7}$ $^{\circ}\text{C}/\text{m}\cdot\text{s}$) and (g,h) are temperature vertical gradient ($^{\circ}\text{C}/\text{m}$) with isotherms ($^{\circ}\text{C}$) superimposed. Black (green) solid lines correspond to the ILD, black (green) dashed lines to the MLD for 11-07-2003 (13-07-2003). 57

- 4.19 Daily time series of area-averaged ILD (black), MLD (yellow) and BLT (blue) in the NEC region (14-20°N, 46-58°W). Red circles denote the large peak events of BLT. Green circles indicate the events when the winter barrier layer peaks before getting eroded in spring. 58
- 4.20 Same as Figure 4.15, but vertical section at 53.72°W through the maximum climatological BLT in February. Salinity and temperature gradient balance terms are averaged from November to February (units are $\times 10^{-7}$ psu/m.s and $\times 10^{-7}$ °C/m.s, respectively). Black (green) solid line is ILD, black (green) dashed line is MLD for February (November). 60
- 4.21 Same as Figure 4.15, but vertical section at 53.72°W through the maximum climatological BLT. Salinity and temperature gradient balance terms are averaged from March to April (units are $\times 10^{-7}$ psu/m.s and $\times 10^{-7}$ °C/m.s, respectively). Black (green) solid line is ILD, black (green) dashed line is MLD for March (April). 62
- 4.22 Snapshots from 13-02-2009 to 23-02-2009 showing the growth and decay of the maximum BLT on 17-02-2009 (winter) (black box delineates the NEC region): (row 1) BLT (meters) with vectors showing surface currents, (row 2) ILD (meters), (row 3) MLD (meters) and (row 4) SSS (psu) with vectors showing surface currents. 64
- 4.23 Snapshots for 17-02-2009 (winter) of (a) top 152.5 m horizontal transport magnitude (Sv) and direction, (b) salinity (psu) at 82.5 m with corresponding currents, (c) SST (°C) and (d) E-P-R ($\times 10^{-7}$ m/s). 65
- 4.24 Same as Figure 4.15, but in a vertical section at 17.69°N through the maximum BLT present on 17-02-2009. Black (green) solid lines correspond to the ILD, black (green) dashed lines correspond to the MLD for 17-02-2009 (14-02-2009). 66
- 4.25 Vertical section at 17.69°N through the maximum BLT on 17-02-2009. Salinity vertical gradient (psu/m) with isohalines (psu) superimposed for (a) 14-02-2009 and (b) 17-02-2009. (c) Density, (d) salinity and (e) temperature stratification ($\times 10^{-4}$ /s²) for 17-02-2009 are shown. Black (green) solid lines correspond to the ILD, black (green) dashed lines to the MLD for 17-02-2009 (14-02-2009). 67
- 4.26 Same as Figure 4.14, but vertical section at 14.23°N through the maximum BLT of 06-01-2006, and salinity gradient balance terms are averaged from 06-01-2006 to 10-01-2006 (units are $\times 10^{-7}$ psu/m.s). The salinity vertical gradient (psu/m) with isohalines (psu) superimposed are shown for (g) 06-01-2006 and (h) 10-01-2006. Black (green) solid lines correspond to the ILD, black (green) dashed lines to the MLD for 06-01-2006 (10-01-2006). 69
- 4.27 Same as Figure 4.15, but vertical section at 54.87°W through the maximum BLT on 19-03-2003, and the gradient balance terms are averaged from 19-03-2003 to 23-03-2003. Black (green) solid line is ILD, black (green) dashed line is MLD for 19-03-2003 (23-03-2003). 70

4.28	Same as Figure 4.16, but vertical section at 54.87°W through the maximum BLT on 19-03-2003. (a,b) salinity vertical gradient (psu/m), with isohalines (psu) superimposed; (c,d) temperature vertical gradient ($^\circ\text{C}/\text{m}$) with isotherms ($^\circ\text{C}$) superimposed, (e,f) density, (g,h) salinity and (i,j) temperature stratification ($\times 10^{-4}/\text{s}^2$) for 19-03-2003 and 23-03-2003, respectively. Black (green) solid line is ILD, black (green) dashed line is MLD for 19-03-2003 (23-03-2003).	71
4.29	Daily time series of area-averaged ILD (meters, black), MLD (meters, yellow) and BLT (meters, blue) in the central tropical Atlantic in the ITCZ region (4°S - 13°N , 6 - 30°W). Red circles are the events of large BLT.	73
4.30	Time series of ILD, MLD, BLT, net surface heat flux, SST and wind stress magnitude low-pass filtered with a 60 days cut-off filter. Red circles depict events with large BLT.	74
4.31	Snapshots from 29-12-2004 to 01-01-2005 showing the growth and decay of the maximum BLT on 30-12-2004 (black box delineates the ITCZ region): (row 1) BLT (meters), with vectors showing surface currents, (row 2) ILD (meters), (row 3) MLD (meters), (row 4) SSS (psu), with vectors showing surface currents and (row 5) E-P-R ($\times 10^{-7}$ m/s).	75
4.32	Vertical section at 20.72°W of the salinity gradient balance terms averaged from 28-12-2004 to 30-12-2004 (units are $\times 10^{-7}$ psu/m.s). Black (green) solid lines correspond to the ILD, black (green) dashed lines to the MLD for 30-12-2004 (28-12-2004). Salinity vertical gradient (psu/m) with isohalines (psu) superimposed for (g,h) both days. Corresponding (i) density, (j) salinity and (k) temperature stratification ($\times 10^{-4}/\text{s}^2$) on 30-12-2004.	76
4.33	Same as Figure 4.31 for an event with maximum BLT on 05-09-2011	78
4.34	Same as Figure 4.32, but vertical section at 25.56°W of the salinity gradient balance terms averaged from 03-09-2011 to 05-09-2011. Black (green) solid lines correspond to the ILD, black (green) dashed lines to the MLD for 05-09-2011 (03-09-2011). Corresponding (i) density, (j) salinity and (k) temperature stratification on 05-09-2011.	79
4.35	Vertical section at 25.56°W of the salinity gradient balance terms averaged from 05-09-2011 to 07-09-2011 (units are $\times 10^{-7}$ psu/m.s). Salinity vertical gradient (psu/m) with isohalines (psu) superimposed for (g,h) both days. Black (green) solid lines correspond to the ILD, black (green) dashed lines to the MLD for 07-09-2011 (05-09-2011).	80
4.36	Daily time series of area-averaged ILD (meters, black), MLD (meters, yellow) and BLT (meters, blue) in the Niger river plume in the eastern tropical Atlantic (1°S - 7°N , 11°E - 1°W). Red circles are the events of large BLT.	81
4.37	Time series of ILD, MLD, BLT, net surface heat flux, SST and wind stress magnitude low-pass filtered with a 60 days cut-off filter. Red circles depict events with large BLT.	82

- 4.38 Vertical section at 1.7°N through the maximum climatological BLT in September, of salinity and temperature gradient balance terms averaged from July to September (units are $\times 10^{-7}$ psu/m.s and $\times 10^{-7}$ $^{\circ}\text{C}/\text{m.s}$, respectively). Black (green) solid line is ILD, black (green) dashed line is MLD for September (July). 83
- 4.39 Same as 4.38 but salinity and temperature gradient balance terms averaged from September to December (units are $\times 10^{-7}$ psu/m.s and $\times 10^{-7}$ $^{\circ}\text{C}/\text{m.s}$, respectively). Black (green) solid line is ILD, black (green) dashed line is MLD for September (December). 85
- 4.40 Same as 4.38 but salinity and temperature gradient balance terms averaged from December to February (units are $\times 10^{-7}$ psu/m.s and $\times 10^{-7}$ $^{\circ}\text{C}/\text{m.s}$, respectively). Black (green) solid line is ILD, black (green) dashed line is MLD February (December). 86
- 4.41 Same as 4.38 but salinity and temperature gradient balance terms averaged from February to April (units are $\times 10^{-7}$ psu/m.s and $\times 10^{-7}$ $^{\circ}\text{C}/\text{m.s}$, respectively). Black (green) solid line is ILD, black (green) dashed line is MLD February (April). 87
- 4.42 Snapshots from 14-10-2003 to 21-10-2003 showing the growth and decay of the maximum BLT on 18-10-2003 (black box delineates the ETA region) of (row 1) BLT (meters) with vectors showing surface currents, (row 2) ILD (meters), (row 3) MLD (meters), (row 4) SSS (psu) with vectors showing surface currents and (row 5) E-P-R ($\times 10^{-7}$ m/s). 89
- 4.43 Same as Figure 4.15, but in a vertical section at 1.8°N through the maximum BLT present on 18-10-2003. Salinity and temperature gradient balance terms are averaged from 14-10-2003 to 18-10-2003 (units are $\times 10^{-7}$ psu/m.s and $\times 10^{-7}$ $^{\circ}\text{C}/\text{m.s}$, respectively). Black (green) solid lines correspond to the ILD, black (green) dashed lines correspond to the MLD for 18-10-2003 (14-10-2003). 90
- 4.44 Vertical section at 1.8°N through the maximum BLT on 18-10-2003. Salinity vertical gradient (psu/m) with isohalines (psu) superimposed and Temperature vertical gradient ($^{\circ}\text{C}/\text{m}$) with isotherms ($^{\circ}\text{C}$) superimposed for (a,c) 14-10-2003 and (b,d) 18-10-2003. (e,f) Density, (g,h) salinity and (i,j) temperature stratification ($\times 10^{-4}/\text{s}^2$) for 14-10-2003 and 18-10-2003 are also shown. Black (green) solid lines correspond to the ILD, black (green) dashed lines to the MLD for 18-10-2003 (14-10-2003). 91
- 4.45 Same as Figure 4.15, but in a vertical section at 2°N through the maximum BLT present on 12-02-2010. Salinity and temperature gradient balance terms are averaged from 09-02-2010 to 12-02-2010 (units are $\times 10^{-7}$ psu/m.s and $\times 10^{-7}$ $^{\circ}\text{C}/\text{m.s}$, respectively). Black (green) solid lines correspond to the ILD, black (green) dashed lines correspond to the MLD for 12-02-2010 (09-02-2010). 93
- 4.46 Salinity vertical gradient (psu/m) at 2°N with isohalines (psu) superimposed for (a) 09-02-2010, (b)12-02-2010 (day of the largest BLT) and (c) 15-02-2010. Black (green) solid lines correspond to the ILD, black (green) dashed lines correspond to the MLD. 94

4.47	Same as Figure 4.43, but only the temperature gradient balance terms are averaged from 18-10-2003 to 21-10-2003 (units are $\times 10^{-7}$ °C/m.s). Black (green) solid lines correspond to the ILD, black (green) dashed lines to the MLD for 18-10-2003 (21-10-2003). The temperature vertical gradient (°C/m) with isotherms (°C) superimposed for both dates are shown in (g,h).	95
5.1	(a) Observed Amazon river discharge from Dai (2017). (b) Idealized Amazon discharge imposed in the model for different experiments. (c) Idealized model discharges of different experiments shown relative to that of exp2.	106
5.2	2008-2015 time mean (a,b) SSS (psu) and (c,d) BLT (meters) from (a,c) EN4 observations and (b,d) exp2 simulation. Black solid boxes: Box A (3°S-5.5°N, 40-51°W) represents the Amazon river mouth, Box B (3°S-7°N, 40-52°W), Box C (6-10°N, 51-59°W), Box D (14-20°N, 46-58°W) and Box E (4-10°N, 28-40°W) are the four areas having localized large BLT and are under the influence of the Amazon plume. The black dashed Box F (3°S-20°N, 28-80°W) delineates the entire area in the western tropical Atlantic featuring barrier layers.	107
5.3	(a) Time mean and (b) monthly mean (the number of the calendar month is shown next to the exp2 symbol) relationship between SSS (psu) and runoff (Sv). Exp0 and exp1 both are forced with constant runoff. Monthly mean (c) SSS (solid) and runoff (dashed) and (d) E-P-R (solid) and precipitation (dashed) ($\times 10^{-7}$ m/s), area-averaged at the Amazon mouth (3°S-5.5°N, 40-51°W - Box A in Figure 5.2a) over the period 2008-2015.	108
5.4	Relationship over the period 2008-2015 between monthly-mean runoff (Sv) (area-averaged in Box A directly at the Amazon mouth) and monthly means of BLT (meters) area-averaged in (a) mouth-Box B, (b) NBC-Box C, (c) NEC-Box D and (d) east-Box E.	111
5.5	Monthly means over the period 2008-2015 of area-averaged (a,c,e) SSS (psu, solid) and precipitation ($\times 10^{-7}$ m/s, dashed), and (b,d,f) ILD (meters, solid) and MLD (meters, dashed) over (a,b) NBC-Box C, (c,d) NEC-Box D, (e,f) east-Box E, for different experiments.	112
5.6	Time mean over the period 2008-2015 of (a,c,e,g,i,k,m) SSS (psu) and (b,d,f,h,j,l,n) SST (°C) differences (a,b) exp0-exp2 (exp0m2), (c,d) exp1m2, (e,f) exp3bm2, (g,h) exp3cm2, (i,j) exp4m2, (k,l) exp5bm2, (m,n) exp6m2.	115
5.7	Time mean over the period 2008-2015 of the differences (a,b,c) exp0-exp2 (exp0m2), (d,e,f) exp1m2, (g,h,i) exp3bm2, (j,k,l) exp3cm2, (m,n,o) exp4m2, (p,q,r) exp5bm2, (s,t,u) exp6m2 in (a,d,g,j,m,p,s) ILD, (b,e,h,k,n,q,t) MLD, and (c,f,i,l,o,r,u) BLT (meters).	116
5.8	Mean over the period 2008-2015 for June of the differences (a,b,c) exp0-exp2 (exp0m2), (d,e,f) exp1m2, (g,h,i) exp3bm2, (j,k,l) exp3cm2, (m,n,o) exp4m2, (p,q,r) exp5bm2, (s,t,u) exp6m2 in (a,d,g,j,m,p,s) SSS (psu), (b,e,h,k,n,q,t) MLD and (c,f,i,l,o,r,u) BLT (meters).	118

5.9	Monthly means over 2008-2015 of the area-averaged differences: exp0-exp2 (exp0m2), exp1m2, exp3bm2, exp3cm2, exp4m2, exp5bm2, exp6m2 for (a,d,g,j) SSS (psu), (b,e,h,k) MLD and (c,f,i,l) BLT (meters) over (a,b,c) mouth-Box B, (d,e,f) NBC-Box C, (g,h,i) NEC-Box D and (j,k,l) east-Box E.	119
5.10	Mean over the period 2008-2015 for January of the differences (a,b,c) exp0-exp2 (exp0m2), (d,e,f) exp1m2, (g,h,i) exp3bm2, (j,k,l) exp3cm2, (m,n,o) exp4m2, (p,q,r) exp5bm2, (s,t,u) exp6m2 in (a,d,g,j,m,p,s) SSS (psu), (b,e,h,k,n,q,t) MLD and (c,f,i,l,o,r,u) BLT (meters).	121
5.11	Time mean over the period 2008-2015 of the differences (a,b,c) exp0-exp2 (exp0m2), (d,e,f) exp1m2, (g,h,i) exp3bm2, (j,k,l) exp3cm2, (m,n,o) exp4m2, (p,q,r) exp5bm2, (s,t,u) exp6m2 of (a,d,g,j,m,p,s) KE (m^2/s^2), (b,e,h,k,n,q,t) MKE (m^2/s^2) and (c,f,i,l,o,r,u) EKE (m^2/s^2).	123
5.12	Monthly mean over the period 2008-2015 of the area-average of the differences exp0-exp2 (exp0m2), exp1m2, exp3bm2, exp3cm2, exp4m2, exp5bm2, exp6m2 for (a,c,e,g) KE and (b,d,f,h) EKE (m^2/s^2) over (a,b) mouth-Box B, (c,d) NBC-Box C, (e,f) NEC-Box D, and (g,h) east-Box E.	125
5.13	Monthly mean KE (m^2/s^2) for (a,c,e,g,i) exp0 from July-November and (b,d,f,h,j) differences exp0-exp2 (exp0m2) of KE. Black lines show sections studied later: (a) Caribbean Sea section, (b) Yucatan Channel section, (c) Florida Strait section.	127
5.14	Relation between time mean runoff (Sv) area-averaged in Box A and time mean top 50 m transport (Sv) through (a) Caribbean Sea section, (b) Yucatan Channel section and (c) Florida Strait section for all experiments.	129
5.15	Power Spectral Density (PSD) ($Sv^2/months^{-1}$) estimation for top 50 m transports through the (a,b) Caribbean Sea section, (c,d) Yucatan Channel section and (e,f) Florida Strait section for all experiments. PSD for exp3b and exp5b are divided by a factor of 10.	131
5.16	Relation between time mean FCT (Sv) and (a) time mean runoff (Sv) area-averaged in Box A, and (b) time mean BLT (m) area-averaged in Box F. Exp0, exp3c, exp4 and exp6 are not included in the regression line. Monthly time series (2008-2015) of FCT and FCT predicted from BLT (leading the FCT by 9 months) are shown for (c) exp2 and (d) exp6.	133
5.17	Relation between time mean AMOC (Sv) and (a) time mean runoff (Sv) area-averaged in Box A, and (b) time mean BLT (meters) area-averaged in Box F (dashed in Figure 5.2a). Exp0, exp3c, exp4 and exp6 are not included in the regression line. Monthly time series (2008-2015) of the AMOC and of the AMOC predicted from BLT (leading the AMOC by 23 months) are shown for (c) exp2, (d) exp3b, (e) exp5b and (f) exp6.	135
5.18	(a) The longitudinally-averaged zonal velocity (m/s) for exp0 and (b) the difference exp0-exp2 of longitudinally-averaged zonal velocity over the region of the retroflection (3-12°N, 45-48°W) are shown.	140

List of Tables

4.1	Monthly generation of NBC rings in 2003-2011	40
5.1	Summary of experiments performed at 8 km resolution including different idealized Amazon river discharge time series.	105

Acknowledgements

Firstly, I would like to express my deepest gratitude to my supervisor Prof. Dr. Detlef Stammer, for giving me the opportunity to conduct research in his group at the Institute of Oceanography (IfM), turning my aspiration to further delve into oceanography, into a reality. I thank him for his sterling guidance, patience and for supporting my ideas. I am very grateful to my co-supervisor Dr. Nuno Serra, for being patient and encouraging, for his timely suggestions, constructive criticisms and for the insightful discussions. Also, I am thankful to him for his expertise in high resolution modeling and for providing the eddy resolving simulation I analyzed in this work. I owe my sincere gratitude to both of them, Prof. Dr. Detlef Stammer and Dr. Nuno Serra, for their confidence in me.

I would like to thank the Deutsche Forschungsgemeinschaft (DFG) for funding the project “Atlantic Freshwater Cycle” FOR1740 which supported this work at the Universität Hamburg. All model simulations were performed at the German Climate Computing Centre (Deutsches Klimarechenzentrum, DKRZ). Thanks to the Center for Earth System Research and Sustainability CEN-IT for their IT support. I acknowledge Met Office Hadley Centre (<https://www.metoffice.gov.uk/hadobs/>) for the observational EN4.2.1 dataset. The barrier layer climatology is available from the IFREMER website (www.ifremer.fr/cerweb/deboyer/mld).

I am grateful to Prof. Dr. Inga Hense, my advisory panel chair, for her valuable time and helpful advices. I would like to thank the panel members of my examination commission, Prof. Dr. Detlef Stammer, Dr. Nuno Serra, Prof. Dr. Dirk Notz, Prof. Dr. Stefan Bühler and Prof. Dr. Eva-Maria Pfeiffer, for their valuable time.

Special thanks go to each member of the Remote Sensing & Assimilation group at IfM. I am delighted to have been a part of a caring working group and appreciate the warm, friendly and motivating atmosphere they created. I thank all the colleagues at IfM, for the thriving environment. I would like to thank the administrative staff for their assistance. My gratitude goes to all the colleagues I met during conferences.

I would like to acknowledge School of Integrated Climate System Sciences (SICSS) for organizing some interesting, relevant and enjoyable courses and retreats. Thanks also to my fellow graduate students I befriended during the course of my PhD.

My sincere gratitude goes to my former advisors, and teachers, from the School of Earth, Ocean and Climate Sciences, Indian Institute of Technology (IIT) Bhubaneswar, India, and from the Geology Department, St. Xavier’s College, Mumbai, India, for supporting my interest and guiding me, especially during my initial steps in the beautiful field of Earth, ocean and climate sciences. I express my gratitude to my teachers from all my alma maters.

A very warm token of thanks to my dear family, friends, and my wonderful parents.

Aus dieser Dissertation hervorgegangene Veröffentlichungen

Publication related to this dissertation

Saha, A., Serra, N., and Stammer, D. (2020). Growth and decay of northwestern tropical Atlantic barrier layers. (*Submitted*).

Versicherung an Eides statt

Declaration on Oath

Hiermit versichere ich an Eides statt, dass ich die vorliegende Dissertation mit dem Titel: „Barrier layers in the tropical Atlantic Ocean: Growth and decay mechanisms and impact of Amazon river runoff“ selbstständig verfasst und keine anderen als die angegebenen Hilfsmittel – insbesondere keine im Quellenverzeichnis nicht benannten Internet-Quellen – benutzt habe. Alle Stellen, die wörtlich oder sinngemäß aus Veröffentlichungen entnommen wurden, sind als solche kenntlich gemacht. Ich versichere weiterhin, dass ich die Dissertation oder Teile davon vorher weder im In- noch im Ausland in einem anderen Prüfungsverfahren eingereicht habe und die eingereichte schriftliche Fassung der auf dem elektronischen Speichermedium entspricht.

I hereby declare an oath that I have written the present dissertation on my own with the title: "Barrier layers in the tropical Atlantic Ocean: Growth and decay mechanisms and impact of Amazon river runoff" and have not used other than the acknowledged resources and aids. All passages taken literally or analogously from other publications are identified as such. I further declare that this thesis has not been submitted to any other German or foreign examination board and that the submitted written version corresponds to that on the electronic repository.

Hamburg, August 2020

Aurpita Saha